frontiers | Research Topics

Novel nuclear reactors and research reactors

Edited by
Shichang Liu, Lianjie Wang, Jingang Liang, Yang Zou
and Jiankai Yu

Published in
Frontiers in Energy Research

ISSN 1664-8714
ISBN 978-2-8325-6746-3
DOI 10.3389/978-2-8325-6746-3

Generative AI statement
Any alternative text (Alt text) provided alongside figures in the articles in this ebook has been generated by Frontiers with the support of artificial intelligence and reasonable efforts have been made to ensure accuracy, including review by the authors wherever possible. If you identify any issues, please contact us.

About Frontiers

Frontiers is more than just an open access publisher of scholarly articles: it is a pioneering approach to the world of academia, radically improving the way scholarly research is managed. The grand vision of Frontiers is a world where all people have an equal opportunity to seek, share and generate knowledge. Frontiers provides immediate and permanent online open access to all its publications, but this alone is not enough to realize our grand goals.

Frontiers journal series

The Frontiers journal series is a multi-tier and interdisciplinary set of open-access, online journals, promising a paradigm shift from the current review, selection and dissemination processes in academic publishing. All Frontiers journals are driven by researchers for researchers; therefore, they constitute a service to the scholarly community. At the same time, the *Frontiers journal series* operates on a revolutionary invention, the tiered publishing system, initially addressing specific communities of scholars, and gradually climbing up to broader public understanding, thus serving the interests of the lay society, too.

Dedication to quality

Each Frontiers article is a landmark of the highest quality, thanks to genuinely collaborative interactions between authors and review editors, who include some of the world's best academicians. Research must be certified by peers before entering a stream of knowledge that may eventually reach the public - and shape society; therefore, Frontiers only applies the most rigorous and unbiased reviews. Frontiers revolutionizes research publishing by freely delivering the most outstanding research, evaluated with no bias from both the academic and social point of view. By applying the most advanced information technologies, Frontiers is catapulting scholarly publishing into a new generation.

What are Frontiers Research Topics?

Frontiers Research Topics are very popular trademarks of the *Frontiers journals series*: they are collections of at least ten articles, all centered on a particular subject. With their unique mix of varied contributions from Original Research to Review Articles, Frontiers Research Topics unify the most influential researchers, the latest key findings and historical advances in a hot research area.

Find out more on how to host your own Frontiers Research Topic or contribute to one as an author by contacting the Frontiers editorial office: frontiersin.org/about/contact

Novel nuclear reactors and research reactors

Topic editors
Shichang Liu — North China Electric Power University, China
Lianjie Wang — Nuclear Power Institute of China (NPIC), China
Jingang Liang — Tsinghua University, China
Yang Zou — Shanghai Institute of Applied Physics, Chinese Academy of Sciences (CAS), China
Jiankai Yu — Massachusetts Institute of Technology, United States

Citation
Liu, S., Wang, L., Liang, J., Zou, Y., Yu, J., eds. (2025). *Novel nuclear reactors and research reactors*. Lausanne: Frontiers Media SA. doi: 10.3389/978-2-8325-6746-3

Table of contents

frontiers | Frontiers in Energy Research

TYPE Editorial
PUBLISHED 12 August 2025
DOI 10.3389/fenrg.2025.1673172

Check for updates

OPEN ACCESS

EDITED AND REVIEWED BY
Shripad T. Revankar,
Purdue University, United States

*CORRESPONDENCE
Shichang Liu,
✉ liu-sc@ncepu.edu.cn

RECEIVED 25 July 2025
ACCEPTED 04 August 2025
PUBLISHED 12 August 2025

CITATION
Liu S, Liang J, Yu J, Wang L and Zou Y (2025) Editorial: Novel nuclear reactors and research reactors.
Front. Energy Res. 13:1673172.
doi: 10.3389/fenrg.2025.1673172

Editorial: Novel nuclear reactors and research reactors

Shichang Liu[1]*, Jingang Liang[2], Jiankai Yu[3], Lianjie Wang[4] and Yang Zou[5]

[1]North China Electric Power University, Beijing, China, [2]Tsinghua University, Beijing, China, [3]Massachusetts Institute of Technology Cambridge, Cambridge, MA, United States, [4]Nuclear Power Institute of China (NPIC), Chengdu, China, [5]Shanghai Institute of Applied Physics, Chinese Academy of Sciences (CAS), Shanghai, China

KEYWORDS

novel nuclear reactors, research reactors, reactor physics, thermal-hydraulics, reactor safety, nuclear fuel and materials

Editorial on the Research Topic
Novel nuclear reactors and research reactors

The advancement of nuclear energy technology has brought significant attention to next-generation reactor systems, including Generation IV reactors, small modular reactors (SMRs), and fusion reactors. Generation IV designs—such as ultra-high temperature reactors, liquid metal-cooled fast reactors, and molten salt reactors—demonstrate marked improvements in sustainability, safety, cost efficiency, and proliferation resistance (Li et al., 2025; Mochizuki, 2025; Liu et al., 2018). Meanwhile, SMRs offer distinct advantages, including versatility in application, deployment flexibility, enhanced safety, and reduced environmental impact. Research reactors also play a pivotal role in nuclear innovation, serving critical functions such as material irradiation testing, isotope production, and theoretical/experimental studies in nuclear technology (Colvin and Palmer, 2025; Jin et al., 2025). Compared to conventional nuclear power plants, these advanced and research reactors exhibit unique design and operational characteristics, making their simulation and engineering processes notably more complex and multidisciplinary.

In recent years, with the continuous innovation of Generation IV nuclear systems, small modular reactors, and research reactors, nuclear reactor modeling and simulation have been evolving toward higher accuracy, multi-scale, and multi-physics coupling approaches (Weng et al., 2021; Fiorina et al., 2022). The design and application of novel reactors exhibit greater complexity and diversity, placing higher demands on thermal-hydraulic characteristics and safety, while also introducing new challenges in fuel behavior and material evolution. To address these needs, researchers are actively advancing the use of sophisticated numerical methods, coupled simulation tools, and high-performance computing, while also strengthening model validation and uncertainty analysis.

Meanwhile, neural network methods are increasingly being integrated into the analysis and optimization of reactor systems, providing strong support for the design and safe operation of next-generation nuclear technologies (Zou et al., 2023; Elhareef and Wu, 2023; Wang et al., 2025). Consequently, the nuclear engineering field continues to advance modeling and simulation technologies to address the complex and diverse challenges posed by novel reactor development, driving nuclear technology toward higher levels of performance and innovation.

We have collected four papers on reactor thermal-hydraulics and safety analysis for *novel nuclear reactors and research reactors* by Geng et al., Cui and Cai, Wu et al., and Lu et al. Geng et al. model transient behavior in the NHR-200-II passive residual heat removal system using RELAP5, identifying flow oscillations during valve failures and proposing design mitigations. Cui and Cai develop a novel degassing system for the HPR1000 pressurizer, improving shutdown performance via steady-state and transient simulations. Wu et al. couple ARSAC and ATHROC codes to simulate CPR1000 containment dynamics under TMLB' accidents, resolving pressure evolution and hydrogen distribution. Lu et al. employ Eulerian–Lagrangian CFD to analyze spray-induced depressurization in multicompartment containments, validating against OECD SETH-2 experiments.

We have collected three papers on nuclear fuel and materials, as well as the nuclear fuel cycle for *novel nuclear reactors and research reactors*, by Wan et al., Changbin et al., and Jiang et al. Wan et al. use cluster dynamics to model defect evolution in proton-irradiated RPV steels, linking solute clustering to embrittlement. Changbin et al. simulate blister formation in UMo/Zr monolithic fuel under annealing, revealing cladding creep's role in bubble growth. Jiang et al. investigate radioactive particle migration in liquid effluents, informing post-operation fuel treatment and environmental monitoring.

We have collected two papers on the conceptual design of *novel nuclear reactors and research reactors* by Qi et al. and Yang et al. Qi et al. propose a graphene-enhanced nanofluid heat exchanger for lead-bismuth reactors, optimized via genetic algorithms for thermal efficiency and compactness. Yang et al. analyze fuel rod vibration to enhance core integrity under dynamic loads.

We have collected two papers on uncertainty quantification, sensitivity analysis, and optimization by Cacuci. Cacuci introduces the nth-order adjoint sensitivity methodology (nth-FASAM-L) for exact high-order sensitivity computation in linear systems, later applying it to neutron slowing-down problems to demonstrate optimization efficacy.

This Research Topic focuses on the key aspects of design, simulation, and analysis for *novel nuclear reactors and research reactors*. The collected studies span thermal-hydraulic behavior, fuel and material evolution, conceptual innovations, and high-order sensitivity analyses. By employing multiphysics coupling, high-fidelity modeling, and advanced numerical techniques, these works demonstrate recent progress in enhancing the safety, efficiency, and engineering viability of next-generation nuclear energy systems.

Looking ahead, balancing computational accuracy with practical applicability remains a central challenge for advanced modeling and simulation technologies. Continued efforts in model validation, algorithm optimization, and integration with artificial intelligence will provide essential support for the industrial application of novel nuclear reactor systems.

Author contributions

SL: Writing – original draft, Writing – review and editing. JL: Writing – review and editing. JY: Writing – review and editing. LW: Writing – review and editing. YZ: Writing – review and editing.

Funding

The author(s) declare that financial support was received for the research and/or publication of this article. This work was partially supported by Project U2330117/12175067 of the National Natural Science Foundation of China, the Beijing Nova Program (20240484596/20250484805), and the Fundamental Research Funds for the Central Universities (2024MS046).

Conflict of interest

The authors declare that the research was conducted in the absence of any commercial or financial relationships that could be construed as a potential conflict of interest.

Generative AI statement

The author(s) declare that no Generative AI was used in the creation of this manuscript.

Any alternative text (alt text) provided alongside figures in this article has been generated by Frontiers with the support of artificial intelligence and reasonable efforts have been made to ensure accuracy, including review by the authors wherever possible. If you identify any issues, please contact us.

Publisher's note

References

Colvin, E., and Palmer, T. S. (2025). High-fidelity multiphysics modeling of pulsed reactor heat generation in the annular core research reactor fuel using serpent 2. *Ann. Nucl. Energy* 211 (000), 110954. doi:10.1016/j.anucene.2024.110954

Elhareef, M. H., and Wu, Z. (2023). Physics-informed neural network method and application to nuclear reactor calculations: a pilot study. *Nucl. Sci. Eng.* 197 (4), 601–622. doi:10.1080/00295639.2022.2123211

Fiorina, C., Clifford, I., Kelm, S., and Lorenzi, S. (2022). On the development of multi-physics tools for nuclear reactor analysis based on OpenFOAM®: state of the art, lessons learned and perspectives. *Nucl. Eng. Des.* 387, 111604. doi:10.1016/j.nucengdes.2021.111604

Jin, C., Liu, S., Zhang, M., Wang, X., Li, M., Yan, X., et al. (2025). Application of similarity analysis method in neutronics design of multi-purpose experimental reactor. *Prog. Nucl. Energy* 180 (000), 105604. doi:10.1016/j.pnucene.2025.105604

Li, R., Liu, S., Wang, L., Chen, L., and Chen, Y. (2025). Criticality safety analysis of space reactor falling accident based on unstructured mesh monte carlo neutron transport. *Prog. Nucl. Energy* 189, 105921. doi:10.1016/j.pnucene.2025.105921

Liu, S., Li, Z., Wang, K., Cheng, Q., and She, D. (2018). Random geometry capability in rmc code for explicit analysis of polytype particle/pebble and applications to htr-10 benchmark. *Ann. Nucl. Energy* 111, 41–49. doi:10.1016/j.anucene.2017.08.063

Mochizuki, H. (2025). Summary of researches on operational characteristics and safety of molten salt fast reactors based on neutronics and thermal-hydraulics coupling analysis. *Nucl. Eng. Des.* 435, 113941. doi:10.1016/j.nucengdes.2025.113941

Wang, Z., Gou, J., Jiang, D., and Yun, D. (2025). A data-driven multi-physics coupling analysis method for multi-objective optimization design of an innovative heat pipe reactor core. *Comput. Phys. Commun.* 311, 109551. doi:10.1016/j.cpc.2025.109551

Weng, M., Liu, S., Liu, Z., Qi, F., and Chen, Y. (2021). Development and application of monte carlo and comsol coupling code for neutronics/thermohydraulics coupled analysis. *Ann. Nucl. Energy* 161 (5), 108459. doi:10.1016/j.anucene.2021.108459

Zou, J., Liu, S., Jin, C., Chen, Y., Cai, Y., and Wang, L. (2023). Optimization method of burnable poison based on genetic algorithm and artificial neural network. *Ann. Nucl. Energy* 192. doi:10.1016/j.anucene.2023.109985

frontiers | Frontiers in Energy Research

TYPE Original Research
PUBLISHED 19 January 2024
DOI 10.3389/fenrg.2024.1352706

OPEN ACCESS

EDITED BY
Shichang Liu,
North China Electric Power University, China

REVIEWED BY
Zhaoming Meng,
Harbin Engineering University, China
Yuanyuan Xue,
Northwest Institute of Nuclear Technology,
China

*CORRESPONDENCE
Shuhua Yin,
✉ yinshuhua@cgnpc.com.cn
Yihong Yan,
✉ yihong@stu.xjtu.edu.cn

RECEIVED 08 December 2023
ACCEPTED 02 January 2024
PUBLISHED 19 January 2024

CITATION
Jiang Z, Xiong J, Pan Y, Hu J, Chen Y, Yin S and Yan Y (2024), Study on the actual particle size, activity concentration, and migration process adsorption behavior of radioactive substances in liquid effluents from nuclear power plants.
Front. Energy Res. 12:1352706.
doi: 10.3389/fenrg.2024.1352706

Study on the actual particle size, activity concentration, and migration process adsorption behavior of radioactive substances in liquid effluents from nuclear power plants

Zhenyu Jiang[1], Jun Xiong[2], Yuelong Pan[1], Jie Hu[3], Yujia Chen[2], Shuhua Yin[2]* and Yihong Yan[3]*

[1]State Key Laboratory of Nuclear Power Safety Technology and Equipment, China Nuclear Power Engineering Co., Ltd., Shenzhen, Guangdong, China, [2]China Nuclear Power Engineering Co., Ltd., Shenzhen, Guangdong, China, [3]Xi'an Jiaotong University, Xi'an, Shaanxi, China

Radionuclides emitted by nuclear power plants may have effects on the environment and public health. At present, research on radioactive material effluent in the industry mainly focuses on the treatment of radioactive effluent and the particle size distribution of the primary circuit. There is little research on the particle size of radioactive material during the migration process outside the primary circuit system, as well as the flocculation precipitation and other enrichment phenomena during the collection process of effluent. Therefore, this study relies on the sampling of effluent from an in-service nuclear power plant to measure its radioactivity level by particle size range. At the same time, the mixing process of effluent is simulated in the laboratory to simulate the adsorption behavior of effluent during the migration process. It was found that in the activity concentration of detectable radioactive nuclides in the effluent samples, more than 95% of radioactive nuclides exist in the liquid with particle sizes less than 0.1μm, while particle sizes greater than 0.45 μm account for less than 5%. After the sample was filtered by the demineralizer, the radioactive activity decreased. The flocculation precipitation in the waste liquid of the waste water recovery system has a certain contribution to the enrichment of nuclides. With the extension of time, the enrichment of transition elements such as cobalt and manganese is particularly obvious, so that it is distributed in the liquid again with a large particle size. In addition, large particle size substances such as colloids in seawater have a certain adsorption effect on radionuclides, which will lead to its aggregation effect again.

KEYWORDS

pressurized water reactor, radioactive effluent, γ measurement, particle size, adsorption effect

1 Introduction

The study of the safety of nuclear reactor facilities is of great significance (Qi et al., 2023; Cao et al., 2024). The radioactive nuclides produced by nuclear power plants mainly come from the fission of nuclear fuel and the activation corrosion of Primary circuit structural materials. In terms of effluent, the liquid radioactive nuclides emitted during conventional operation of nuclear power plants include ^{137}Cs, ^{51}Cr, ^{54}Mn, ^{110m}Ag, ^{124}Sb, ^{134}Cs, ^{131}I, ^{90}Sr, ^{103m}Rh, ^{58}Co, ^{58}Co (Kong et al., 2017). The discharge of liquid effluents from nuclear power plants into the environment under national regulations and standards means that the effluents are safe from a legal perspective (National Nuclear Energy Agency, 2011; Ministry of Environmental and Forestry, 2016; Yuniarto et al., 2016).

However, companies around nuclear power plants hold a questioning attitude towards the safety of effluent, especially those involved in the large-scale use of seawater technology. During the process of seawater reuse in the ocean, radioactivity is trapped and enriched again on the filtering equipment, causing radiation effects on workers. According to theoretical estimation, if the source term of the effluent is measured at a radioactive concentration of 1,000 Bq/L, under extremely conservative assumptions (radioactive nuclides in the effluent are all trapped by the filters of the enterprise's seawater extraction facilities), the contact dose rate of the filter can reach approximately the level of 10 μSv/h, which corresponds to the dose rate level in the control area (green area) of the nuclear power plant, and is indeed unacceptable for civil enterprises.

It should be pointed out that due to overly conservative assumptions, the possibility of the aforementioned conclusion occurring is unlikely. However, the crux still lies in the lack of understanding of the actual particle size distribution of radioactive substances in the effluent, and the assessment can only conservatively assume that all radioactive substances have been trapped on the filter core. On the other hand, according to feedback from the operation of in-service nuclear power plants, sampling and testing before effluent discharge can indeed detect radioactive hot particles. It should be pointed out that the liquid effluent of nuclear power plants is treated by multiple purification methods such as filtration and desalination of radioactive waste liquid from nuclear power plants. Therefore, it is believed that the effluent is basically non-radioactive. The actual phenomenon of measuring radioactive hot particles indicates that radioactive enrichment may have occurred during the collection process of the effluent, which may have resulted in the regeneration of particles.

Therefore, combining the monitoring methods of effluent (Kang and Cheong, 2022; Wang et al., 2023) and the treatment methods of radioactive nuclides in effluent (Attallah et al., 2019; Bashir et al., 2019; Ahmed et al., 2020; Ma et al., 2020; Tofighy et al., 2020; Gul et al., 2021; Thakur et al., 2022; Nivetha et al., 2023; Oh et al., 2023), mastering the particle size of radioactive substances in effluent, and studying whether the collection process of effluent will produce particulate thermal particles, is the key to more accurate evaluation and reducing the impact of effluent on environmental radiation. The relationship route is shown in Figure 1.

This study relied on the sampling of effluent from an in-service nuclear power plant to measure its radioactive levels in particle size intervals. However, it is also necessary to consider the migration process of effluent into the ocean. At present, research on the particle size distribution and adsorption behavior of radioactive nuclides in seawater has focused on seawater measurement. For example, Yuki Kamidaira et al. established an ocean diffusion model for radioactive nuclides, considering the interaction between dissolved radioactive nuclides and suspended particles and multi-scale seabed sediments (Kamidaira et al., 2021). P. G. Appleby et al. believed that radioactive nuclides are soluble in water and adhere to colloidal sized particles (<0.4 μm) The upper part is basically transported with the water

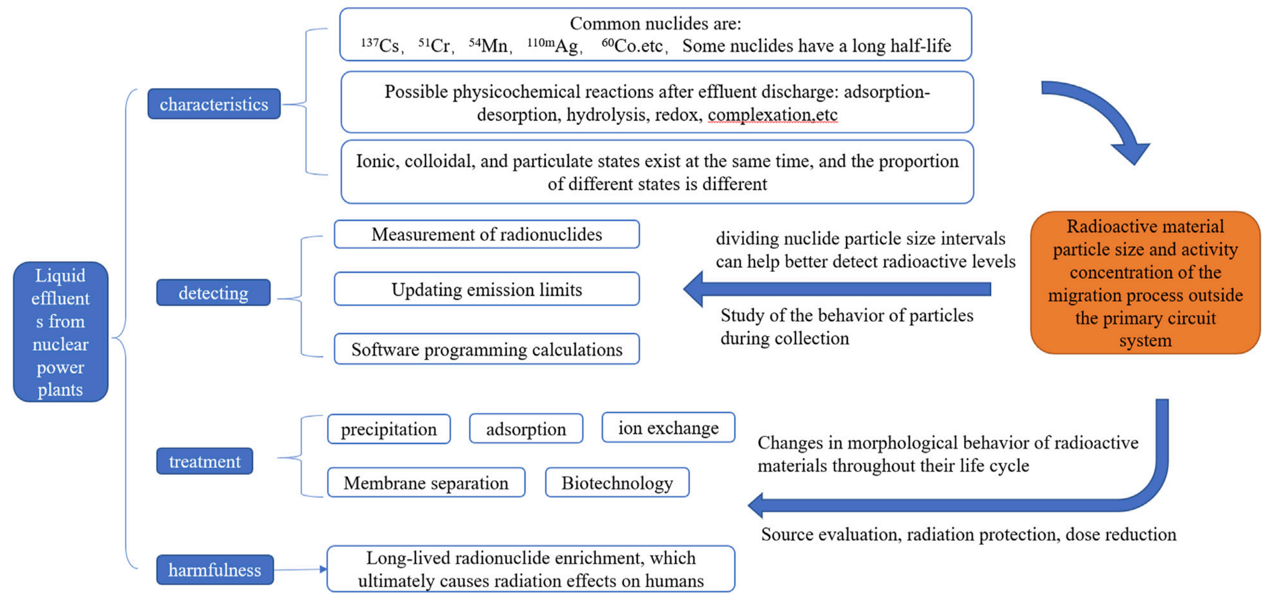

FIGURE 1
Characteristics, hazards, monitoring and treatment of liquid effluents from nuclear power plants, and study on particle size behavior.

phase. The deposition or outflow of particulate matter largely depends on factors that control the transportation of suspended sediment through water bodies, including particle size distribution, residence time, etc. (Appleby et al., 2019). Therefore, this study also utilized laboratory simulations of the mixing process of effluent to simulate the adsorption behavior of effluent during migration.

It should be pointed out that the research on the particle size of radioactive substances in the industry mainly focuses on the primary circuit (Geraldo et al., 2019; Li et al., 2019; Tessaro et al., 2020; Guo et al., 2022), while there is very little research on the particle size of radioactive substances during the migration process outside the primary circuit system. Studying and analyzing the changes in particle size morphology of radioactive materials throughout the entire life cycle of nuclear power plants is a prerequisite for constructing a full life cycle source term evaluation and radiation protection. It helps to further improve the level of source term management in nuclear power plants, reduce collective doses, and select more favorable and suitable environmental conditions to cope with radiation effects. Therefore, research has long-term significance.

2 Material design and manufacture

2.1 The object of study

Effluent from the nuclear Island building of a pressurized water reactor nuclear power plant is collected in the liquid waste storage tank of the Nuclear Island Liquid Waste Discharge System (TER) before discharge. The effluent to be discharged is received in the TER system effluent temporary tank from the Radioactive Effluent Treatment System (TEU), the Boron Recovery System (TEP), and the radioactive effluent Recovery System (SRE). In this study, the effluent from a nuclear power unit during the shutdown overhaul in March 2023 was selected for sampling and measurement. Before sampling, the TER waste liquid temporary storage tank was decontaminated to avoid radioactive mixing. Then each strand of waste liquid discharged from TEU, TEP and SRE systems into TER waste liquid temporary storage tank was sampled, and a total of two groups of waste liquid samples were collected. The sampling information is in Table 1.

The sample size of each sample is about 5L, and the sample container is taken from a 1L glass bottle. The inner wall of the bottle is soaked with dilute hydrochloric acid with pH = 1 in advance to reduce the adsorption loss of radionuclides. Seven kinds of radionuclides were measured, including ^{58}Co、^{60}Co、^{134}Cs、^{137}Cs、^{110m}Ag、^{54}Mn、^{124}Sb, etc. For particle size, five intervals were separated, respectively: $d < 0.1\ \mu m$, $0.1\ \mu m \le d < 0.45\ \mu m$, $0.45\ \mu m \le d < 1\ \mu m$, $1\ \mu m \le d < 5\ \mu m$ and $d \ge 5\ \mu m$.

2.2 Equipment material

The nuclide in the sample was analyzed by using the high-purity germanium gamma spectrometer system produced by ORTEC and CANBERRA. There are 3 sets of measuring instruments (the equipment models are GEM40P4-76, GC4019 and BE3830 respectively), and the drying oven produced by Nabertherm (the model is TR240) was used for sample pretreatment. The sample particle size was separated by microporous filter membrane produced by Hangzhou Anuo Filtration Equipment Co., LTD. (Material was polypropylene, diameter was 75 mm, pore size was 0.1, 0.45, 1.0, and 5.0 μm, respectively). All the devices are used within the verification validity period and can be traced to the national standard.

2.3 Sample particle size separation and measurement methods

The colloids or clusters that may exist in different particle size ranges in the sample are separated by microporous filtration membrane combined with the extraction filtration device, as shown in Figure 2. The process is as follows:

(1) The filter membrane is dried in a drying oven at 110°C to constant weight, and the quality of the filter membrane is numbered and recorded;
(2) According to the filter membrane aperture from large to small in the order of separation, the filter membrane with the corresponding aperture is fixed on the G1 sand core funnel with a clamp, the sample is pumped with a constant pressure filtration device, the pressure is set at 0.7 MPa, and the filter membrane is replaced once every 500 mL sample pumped;
(3) The beaker containing the sample is cleaned more than 3 times with distilled water, and the cleaning liquid is also pumped and filtered, and the volume of distilled water used is recorded;

TABLE 1 Sampling information of waste liquid discharged into the TER waste liquid temporary storage tank by TEU, TEP, and SRE systems.

Group	Sample number of TEU	Sampling time of TEU	Sample number for TEP	Sampling time of TEP	Sample number of TER	Sampling time of TER
Group 1	A1TEU003	8/03/23	A1TEP001	7/03/23	A1TER001	22/03/23
	A1TEU004	3/03/23	A1TEP005	7/03/23		
			A1TEP003	7/03/23		
Group 2	A2TEU001	19/04/23	A1TEP006	23/05/23	A1TER002	30/05/23
	A2TEU002	19/04/23	A1TEP002	23/05/23		
			A1TEP004	23/05/23		

FIGURE 2
Photo of the filter extraction unit.

(4) After the filtration is completed, the same group of filter membranes with the same particle size are placed on the surface dish and numbered, dried at 110°C in the oven to constant weight, and four groups of filter membranes with the particle size of 0.1–0.45 μm, 0.45~1 μm, 1–5 μm and >5 μm are obtained. After weighing the filter membranes, they are pressed into the sample box of φ75 × 10 and sealed. Put into the specified high purity germanium gamma spectrometer for measurement;
(5) The filtrate after pumping and filtering is shaken and measured 200 mL, weighed and put into the sample bottle and put into the specified high purity germanium gamma spectrometer for measurement;
(6) After filtration, nuclide activity concentrations with particle size distribution less than 0.1 μm can be measured in the filtrate. On microporous filter membranes with pore sizes of 0.1, 0.45, 1.0, and 5.0 μm, four sets of nuclide activity concentrations with particle sizes of 0.1–0.45 μm, 0.45–1 μm, 1–5 μm, and >5 μm can be measured, respectively;
(7) After the separation of each sample was completed, the filtration device was cleaned with dilute hydrochloric acid solution with pH = 1, and washed with distilled water before it could be used for the separation of subsequent samples.

2.4 Measurement and treatment of radionuclides adsorbed on the inner wall of the sample container

Although the inner wall of the sample container was treated with anti-adsorption treatment, there were still a small number of nuclides adsorbed on the inner wall of the container. In order to determine the activity of the nuclides adsorbed on the inner wall of the container, the measurement efficiency of the sample container and the corresponding nuclides was established by using LABSOCS software in this experiment, and the results were verified by using Monte-Carlo simulation and different γ spectrometer. The sample container is fully rinsed with distilled water and drained after being placed in the instrument for measurement. The common desorption methods can be roughly divided into physical methods and chemical methods, among which the common physical method is ultrasonic vibration, but the effect is not very good. In chemical methods, acid washing can be used for desorption, and its desorption effect is better than ultrasonic vibration.

After the measurement, 1L of 2 mol/L dilute nitric acid solution was added to each sample container and soaked for about 150 h. The

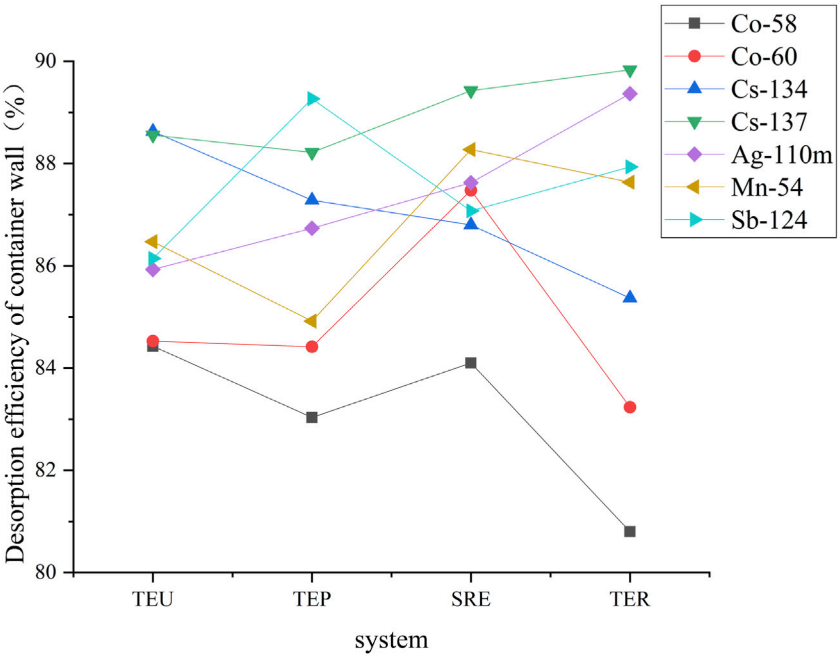

FIGURE 3
Desorption efficiency of each nuclide container wall in each system.

TABLE 2 Initial activity concentrations of nuclides in each sample unit: Bq/kg.

Sample number	Activity concentration of nuclides						
	^{58}Co	^{60}Co	^{134}Cs	^{137}Cs	^{110m}Ag	^{54}Mn	^{124}Sb
A1TEU003	13.6 ± 0.6	33.7 ± 1.6	3.19 ± 0.17	3.56 ± 0.16	7.04 ± 0.32	8.81 ± 0.27	1.62 ± 0.13
A1TEU004	11.7 ± 0.6	38.9 ± 1.7	3.61 ± 0.17	3.17 ± 0.15	9.10 ± 0.34	6.13 ± 0.25	2.01 ± 0.14
A2TEU001	94.6 ± 2.2	111 ± 4	7.88 ± 0.30	6.87 ± 0.27	31.3 ± 1.2	24.5 ± 1.1	5.09 ± 0.18
A2TEU002	5.05.044 ± 0.15	6.88 ± 0.21	2.66 ± 0.30	2.90 ± 0.61	3.62 ± 0.16	1.25 ± 0.08	2.17 ± 0.10
A1TEP001	96.7 ± 3.1	110 ± 4	3.78 ± 0.17	4.01 ± 0.19	3.16 ± 0.14	29.5 ± 1.4	2.35 ± 0.10
A1TEP005	3.12 ± 0.26	29.2 ± 0.7	2.30 ± 0.28	2.51 ± 0.56	1.45 ± 0.42	1.13 ± 0.34	1.42 ± 0.46
A1TEP003	3.43 ± 0.29	30.1 ± 0.6	<0.56	2.58 ± 0.26	2.57 ± 0.34	1.44 ± 0.26	<0.76
A1TEP006	88.988.9 ± 1.1	104 ± 2	2.07 ± 0.24	2.94 ± 0.22	2.78 ± 0.24	31.4 ± 0.80	3.16 ± 0.20
A1TEP002	1.65 ± 0.24	15.2 ± 0.6	1.37 ± 0.50	1.74 ± 0.24	1.55 ± 0.37	1.07 ± 0.32	1.17 ± 0.12
A1TEP004	2.07 ± 0.28	14.6 ± 0.6	1.49 ± 0.52	1.74 ± 0.24	1.55 ± 0.37	1.07 ± 0.32	1.17 ± 0.12
A1TER001	<0.47	1.04 ± 0.43	<0.59	<0.71	<0.81	<0.63	<0.99
A1TER002	<0.38	2.69 ± 0.17	<0.41	<0.68	<0.66	<0.50	<0.71
SRE	<0.47	3.56 ± 0.37	<0.52	<0.66	<0.80	<0.57	<0.91

Note: After "<" in the table, it represents the actual detection limit of the sample, indicating that the measurement result of the sample is below the detection limit.

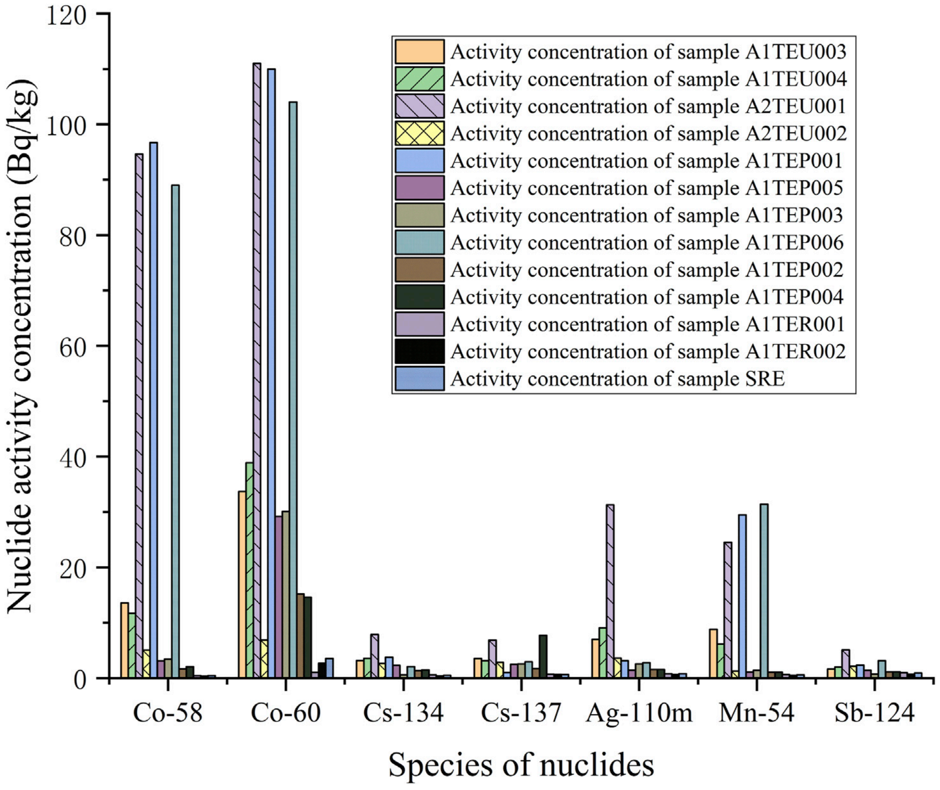

FIGURE 4
Histogram of initial activity concentration of radionuclides in each sample.

acid solution after soaking was taken for measurement to determine the nuclide activity of the desorbed container wall. After the pH of the acid solution was adjusted to 7~8 with sodium hydroxide, the particle size was separated and measured. The average desorption efficiency of each nuclide ranged from 80.8% to 90.2%, as shown in Figure 3.

TABLE 3 Activity concentrations of different nuclides with different particle sizes in each system.

Sample number	Size distribution (μm)	Nuclide activity concentration (Bq/kg)						
		^{58}Co	^{60}Co	^{134}Cs	^{137}Cs	^{110m}Ag	^{54}Mn	^{124}Sb
A1TEU003	d < 0.1	11.1 ± 0.4	27.3 ± 0.7	1.33 ± 0.06	1.79 ± 0.07	6.23 ± 0.20	7.51 ± 0.25	<0.87
	0.1 ≤ d < 0.45	/	3.02 ± 0.15	/	/	/	/	/
	0.45 ≤ d < 1.0	/	/	/	/	/	/	/
	1.0 ≤ d < 5.0	/	/	/	/	/	/	/
	d ≥ 5.0	/	/	/	/	/	/	/
A1TEU004	d < 0.1	9.82 ± 0.28	32.7 ± 1.3	2.20 ± 0.14	2.41 ± 0.13	7.12 ± 0.27	3.88 ± 0.20	<0.91
	0.1 ≤ d < 0.45	/	2.72 ± 0.15	/	/	/	/	/
	0.45 ≤ d < 1.0	/	/	/	/	/	/	/
	1.0 ≤ d < 5.0	/	/	/	/	/	/	/
	d ≥ 5.0	/	/	/	/	/	/	/
A2TEU001	d < 0.1	86.1 ± 2.0	102 ± 4	6.52 ± 0.28	6.33 ± 0.26	27.4 ± 1.1	20.8 ± 1.1	3.11 ± 0.16
	0.1 ≤ d < 0.45	2.61 ± 0.13	4.19 ± 0.27	/	/	/	/	/
	0.45 ≤ d < 1.0	/	/	/	/	/	/	/
	1.0 ≤ d < 5.0	/	/	/	/	/	/	/
	d ≥ 5.0	/	/	/	/	/	/	/
A1TEP001	d < 0.1	91.8 ± 2.5	104 ± 4	2.39 ± 0.14	2.86 ± 0.15	2.08 ± 0.12	24.3 ± 1.2	1.75 ± 0.09
	0.1 ≤ d < 0.45	1.89 ± 0.11	3.27 ± 0.22	/	/	/	/	/
	0.45 ≤ d < 1.0	/	/	/	/	/	/	/
	1.0 ≤ d < 5.0	/	/	/	/	/	/	/
	d ≥ 5.0	/	/	/	/	/	/	/
A1TEP005	d < 0.1	2.37 ± 0.20	26.7 ± 0.6	1.77 ± 0.23	1.98 ± 0.29	1.17 ± 0.10	0.96 ± 0.07	<0.88
	0.1 ≤ d < 0.45	/	/	/	/	/	/	/
	0.45 ≤ d < 1.0	/	/	/	/	/	/	/
	1.0 ≤ d < 5.0	/	/	/	/	/	/	/
	d ≥ 5.0	/	/	/	/	/	/	/
A1TEP003	d < 0.1	2.58 ± 0.23	27.7 ± 0.6	<0.62	2.01 ± 0.19	2.12 ± 0.25	1.01 ± 0.17	<0.84
	0.1 ≤ d < 0.45	/	/	/	/	/	/	/
	0.45 ≤ d < 1.0	/	/	/	/	/	/	/
	1.0 ≤ d < 5.0	/	/	/	/	/	/	/
	d ≥ 5.0	/	/	/	/	/	/	/
A1TEP006	d < 0.1	81.0 ± 1.0	93.5 ± 1.8	1.75 ± 0.18	2.47 ± 0.20	2.35 ± 0.25	28.9 ± 0.9	2.45 ± 0.20
	0.1 ≤ d < 0.45	/	/	/	/	/	/	/
	0.45 ≤ d < 1.0	/	/	/	/	/	/	/
	1.0 ≤ d < 5.0	/	/	/	/	/	/	/
	d ≥ 5.0	/	/	/	/	/	/	/
A1TEP002	d < 0.1	1.23 ± 0.14	12.7 ± 0.4	1.07 ± 0.12	1.05 ± 0.12	1.27 ± 0.25	0.87 ± 0.06	<0.89
	0.1 ≤ d < 0.45	/	/	/	/	/	/	/

(Continued on following page)

TABLE 3 (*Continued*) Activity concentrations of different nuclides with different particle sizes in each system.

Sample number	Size distribution (μm)	Nuclide activity concentration (Bq/kg)						
		^{58}Co	^{60}Co	^{134}Cs	^{137}Cs	^{110m}Ag	^{54}Mn	^{124}Sb
	0.45 ≤ d < 1.0	/	/	/	/	/	/	/
	1.0 ≤ d < 5.0	/	/	/	/	/	/	/
	d ≥ 5.0	/	/	/	/	/	/	/
A1TEP004	d < 0.1	1.64 ± 0.17	11.2 ± 0.3	1.21 ± 0.20	1.49 ± 0.18	1.12 ± 0.12	0.79 ± 0.06	<0.90
	0.1 ≤ d < 0.45	/	/	/	/	/	/	/
	0.45 ≤ d < 1.0	/	/	/	/	/	/	/
	1.0 ≤ d < 5.0	/	/	/	/	/	/	/
	d ≥ 5.0	/	/	/	/	/	/	/
A1TER001	d < 0.1	/	0.77 ± 0.05	/	/	/	/	/
	0.1 ≤ d < 0.45	/	/	/	/	/	/	/
	0.45 ≤ d < 1.0	/	/	/	/	/	/	/
	1.0 ≤ d < 5.0	/	/	/	/	/	/	/
	d ≥ 5.0	/	/	/	/	/	/	/
A1TER002	d < 0.1	/	2.28 ± 0.23	/	/	/	/	/
	0.1 ≤ d < 0.45	/	/	/	/	/	/	/
	0.45 ≤ d < 1.0	/	/	/	/	/	/	/
	1.0 ≤ d < 5.0	/	/	/	/	/	/	/
	d ≥ 5.0	/	/	/	/	/	/	/
SRE	d < 0.1	/	1.18 ± 0.21	/	/	/	/	/
	0.1 ≤ d < 0.45	/	/	/	/	/	/	/
	0.45 ≤ d < 1.0	/	/	/	/	/	/	/
	1.0 ≤ d < 5.0	/	/	/	/	/	/	/
	d ≥ 5.0	/	1.87 ± 0.30	/	/	/	/	/

Note: "/" in the table indicates that the sample measurement result is below the detection limit.

2.5 Experimental simulation

In order to observe the behavior of radioactive particles adsorbed by colloid in seawater during the migration and mixing process of liquid effluent after discharge, the laboratory used SRE waste liquid with low radioactivity to mix with TEP and TEU waste liquid respectively to simulate the mixing process of waste liquid of different systems in TER waste liquid temporary storage tank. Because the SRE waste liquid contains a certain number of surfactants, the colloidal composition inside the solution is more complex than the natural seawater, and this simulation process also simply represents the mixing process of the effluent and seawater.

A total of six groups of simulated samples were prepared in this experiment, including three groups of SRE and A1TEP001 simulated samples and three groups of SRE and A2TEU001 simulated samples, each group was composed of 500 mL SRE waste liquid and 500 mL TEP and TEU waste liquid. Each group of simulated samples was stirred for 1 min in the morning and evening every day. The simulation duration was 5, 10 and 20 days, respectively. After reaching the simulation time, use the above method to separate and measure the particle size of the sample.

3 Result and discussion

3.1 Measurement results of each nuclide in the effluent sample

The measurement results of each nuclide in the initial state of the sample are shown in Table 2. The extracted information is plotted as a column chart, as shown in Figure 4. The activity concentration of radioactive nuclides in TEU and TEP wastewater is reduced to varying degrees after being filtered by a desalination device. The measurement results of all nuclides in TER and SRE wastewater, except for ^{60}Co, are below the detection limit.

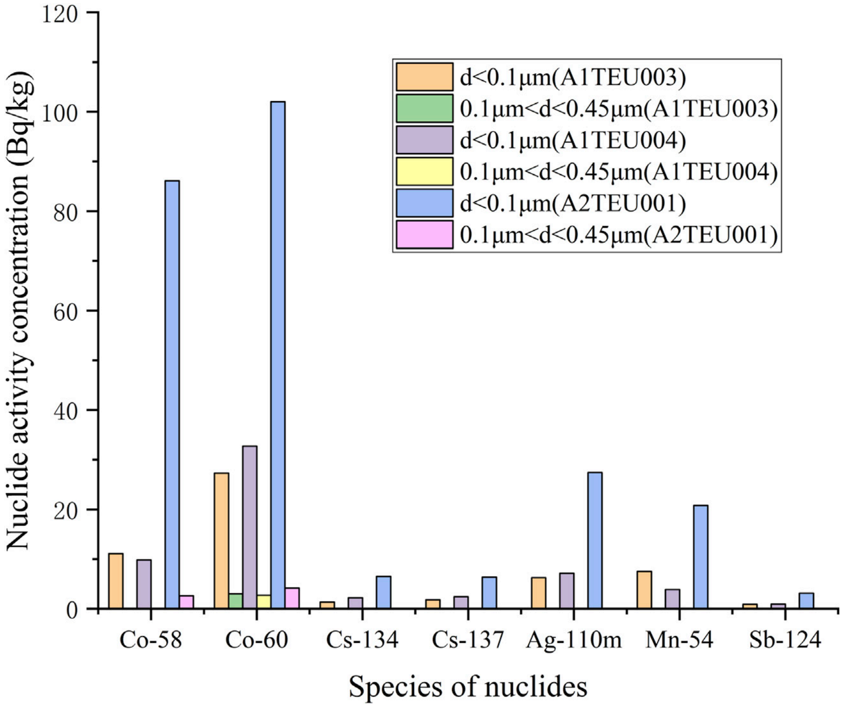

FIGURE 5
Column diagram of activity concentration of different particle sizes of each nuclide.

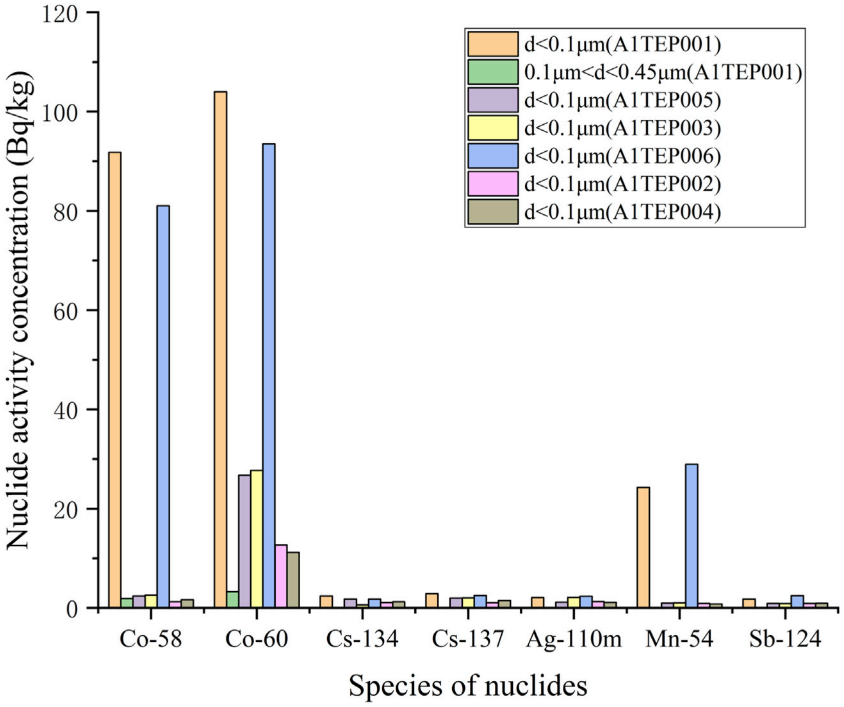

FIGURE 6
Histogram of activity concentration of different particle sizes of each nuclide in TEU.

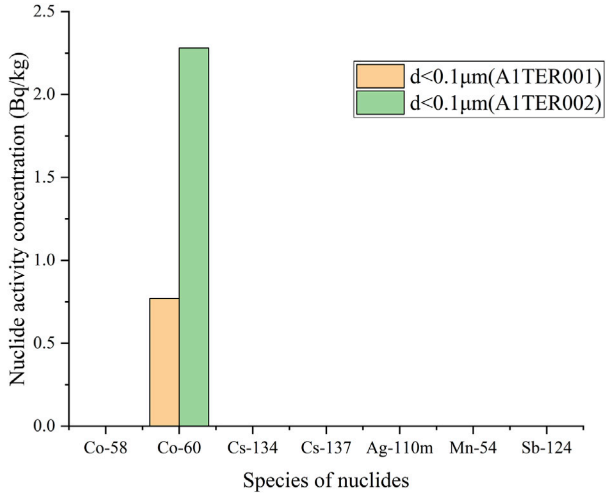

FIGURE 7
Histogram of activity concentration of different particle sizes of each nuclide in TER.

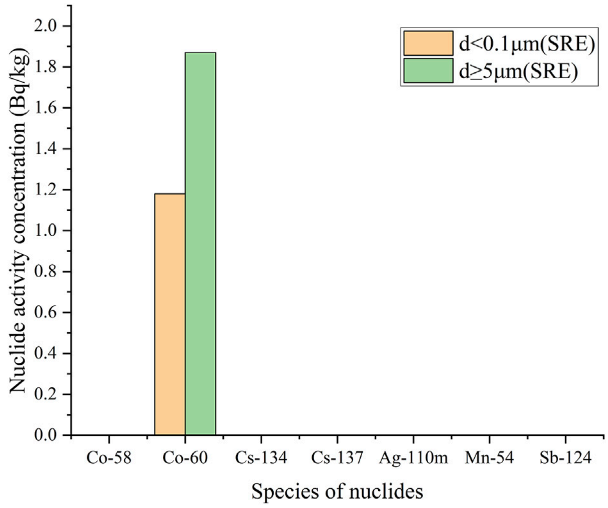

FIGURE 8
Histogram of activity concentration of different particle sizes of each nuclide in SRE.

You may insert up to five heading levels into your manuscript as can be seen in "Styles" tab of this template. These formatting styles are meant as a guide, as long as the heading levels are clear, Frontiers style will be applied during typesetting.

3.2 Measurement results of activity concentration distribution of various nuclides with different particle sizes in each sample

The activity concentration distribution results of various nuclides with different particle sizes in each sample are shown in Table 3, and plotted as a column chart as shown in Figures 5–8. Except for the SRE system, the measurement results of all other systems with d ≥ 0.45 μm are less than the detection limit. In order to better express the relationship between the main particle size and activity concentration, samples below the detection value in the sample results are omitted from the bar graph.

FIGURE 9
Flocculent precipitation at the bottom of the SRE system sample.

According to Table 3, The proportion of nuclide activity concentrations with particle size distribution less than 0.1 μm in sample A1TEU003 is:

$$p = \frac{\text{Particle size distribution less than } 0.1\mu m}{\text{The total activity concentration of all detectable nuclides in the sample}} = 0.95$$

The calculation process for other samples is the same as above, and the calculation results are as follows: $p_{\mathrm{A1TEU004}} = 0.956$, $p_{\mathrm{A2TEU001}} = 0.971$, $p_{\mathrm{A1TEP001}} = 0.978$, $p_{\mathrm{A1TEP005}} = 1$ $p_{\mathrm{A1TEP003}} = 1$, $p_{\mathrm{A1TEP006}} = 1$, $p_{\mathrm{A1TEP002}} = 1$, $p_{\mathrm{A1TEP004}} = 1$, $p_{\mathrm{A1TER001}} = 1$, $p_{\mathrm{A1TER002}} = 1$, $p_{\mathrm{SRE}} = 0.387$. Obviously, for most samples, the proportion of nuclide activity concentrations with particle size distribution less than 0.1 μm is over 95%.

The reason for the distribution of nuclides within the d ≥ 5.0 μm in the SRE system is that the surfactant in the liquid produces a small amount of flocculent precipitation, which adsorbs a small number of nuclides. The flocculent precipitation at the bottom of the SRE system sample is shown in Figure 9.

In addition, all nuclides in other systems are concentrated within the particle size range of d < 0.45 μm, mainly within the particle size

TABLE 4 Activity concentrations of different nuclides with different particle sizes in simulated samples.

Enrichment duration	Size distribution (μm)	Nuclide activity concentration (Bq/kg)						
		^{58}Co	^{60}Co	^{134}Cs	^{137}Cs	^{110m}Ag	^{54}Mn	^{124}Sb
TEU 5days	$d < 0.1$	50.0 ± 1.3	53.2 ± 1.6	3.17 ± 0.18	3.01 ± 0.19	3.22 ± 0.18	12.4 ± 0.6	1.46 ± 0.10
	$0.1 \le d < 0.45$	0.97 ± 0.08	1.32 ± 0.10	/	/	/	/	/
	$0.45 \le d < 1.0$	/	/	/	/	/	/	/
	$1.0 \le d < 5.0$	/	/	/	/	/	/	/
	$d \ge 5.0$	/	1.12 ± 0.09	/	/	/	/	/
TEU 10 days	$d < 0.1$	41.3 ± 1.3	47.2 ± 1.6	3.62 ± 0.16	3.41 ± 0.16	3.05 ± 0.15	10.8 ± 0.6	1.16 ± 0.10
	$0.1 \le d < 0.45$	1.28 ± 0.10	1.81 ± 0.12	/	/	/	/	/
	$0.45 \le d < 1.0$	/	/	/	/	/	/	/
	$1.0 \le d < 5.0$	/	/	/	/	/	/	/
	$d \ge 5.0$	/	2.82 ± 0.14	/	/	/	/	/
TEU 20 days	$d < 0.1$	39.8 ± 1.3	41.5 ± 1.4	3.26 ± 0.15	3.08 ± 0.14	2.87 ± 0.14	9.73 ± 0.71	1.15 ± 0.10
	$0.1 \le d < 0.45$	1.26 ± 0.10	1.53 ± 0.13	/	/	/	/	/
	$0.45 \le d < 1.0$	/	/	/	/	/	/	/
	$1.0 \le d < 5.0$	/	/	/	/	/	/	/
	$d \ge 5.0$	0.86 ± 0.08	3.12 ± 0.16	/	/	/	0.91 ± 0.08	/
TEP 5 days	$d < 0.1$	46.7 ± 2.0	57.3 ± 2.0	1.30 ± 0.10	1.17 ± 0.09	1.12 ± 0.10	12.7 ± 1.0	0.94 ± 0.27
	$0.1 \le d < 0.45$	1.89 ± 0.11	3.27 ± 0.22	/	/	/	/	/
	$0.45 \le d < 1.0$	/	/	/	/	/	/	/
	$1.0 \le d < 5.0$	/	/	/	/	/	/	/
	$d \ge 5.0$	/	1.26 ± 0.10	/	/	/	/	/
TEP 10 days	$d < 0.1$	42.8 ± 2.0	52.2 ± 2.0	1.27 ± 0.11	1.28 ± 0.10	1.04 ± 0.20	11.3 ± 0.9	<0.92
	$0.1 \le d < 0.45$	1.94 ± 0.11	3.45 ± 0.22	/	/	/	/	/
	$0.45 \le d < 1.0$	/	/	/	/	/	/	/
	$1.0 \le d < 5.0$	/	/	/	/	/	/	/
	$d \ge 5.0$	/	3.11 ± 0.24	/	/	/	/	/
TEP 20 days	$d < 0.1$	37.7.±1.9	46.1 ± 1.9	1.39 ± 0.12	1.10 ± 0.19	1.15 ± 0.22	9.88 ± 0.87	<0.92
	$0.1 \le d < 0.45$	1.75 ± 0.10	3.04 ± 0.21	/	/	/	/	/
	$0.45 \le d < 1.0$	/	/	/	/	/	/	/
	$1.0 \le d < 5.0$	/	/	/	/	/	/	/
	$d \ge 5.0$	/	4.58 ± 0.26	/	/	/	/	/

Note: "/" in the table indicates that the sample measurement result is below the detection limit.

range of $d < 0.1$ μm. It is worth noting that the sum of activity concentrations for each particle size is not the same as the activity concentration in the initial state of the sample, and each nuclide has a certain loss, possibly due to:

(1) There are a small amount of radioactive nuclides present in the interval $d > 0.45$ μm, but the activity concentration is lower than the judgment limit measured by the instrument;

(2) During the separation and measurement process, a small number of nuclides are adsorbed on the container wall, causing losses.

3.3 Simulate the measurement results of each nuclide in the sample

The activity concentration distribution of various nuclides with different particle sizes in the simulated sample is shown in Table 4,

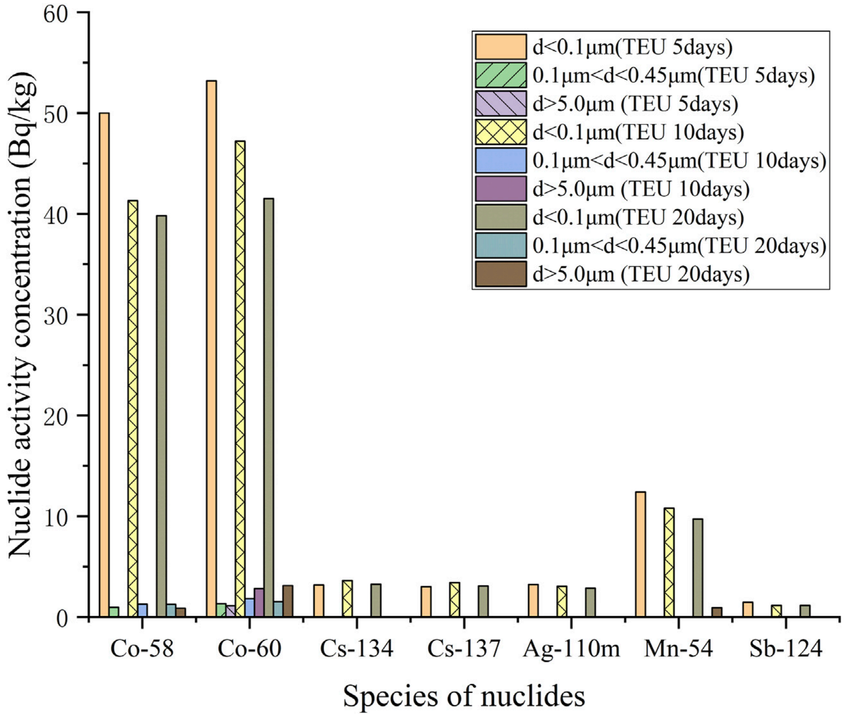

FIGURE 10
Histogram of activity concentration of TEU samples at different enrichment times with different particle sizes of nuclides.

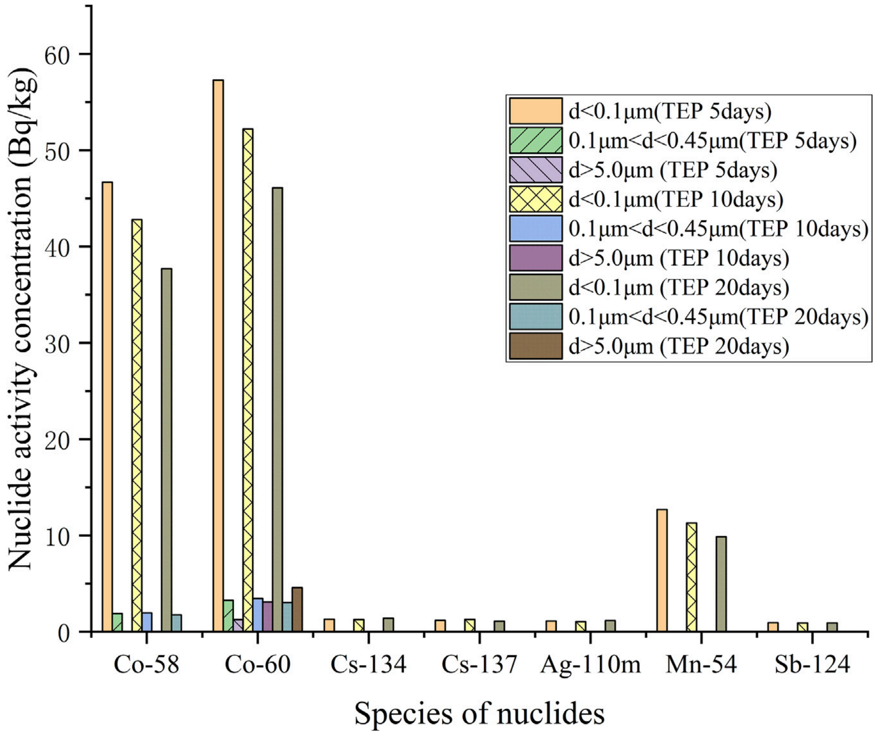

FIGURE 11
Histogram of activity concentration of each nuclide with different particle sizes at different enrichment times of TEP samples.

and the column plots are shown in Figure 10 and Figure 11. With the extension of mixing time, the simulated samples of TEU and TEP showed different degrees of radioactive enrichment in the range of d ≥ 5.0 μm, indicating that the flocculent precipitates and colloids in the SRE waste liquid have a certain degree of enrichment effect on Co and Mn. However, the overall activity of radioactive nuclides in the sample shows a decreasing trend, mainly due to a certain amount of wall adsorption during the mixed enrichment process, resulting in a small amount of nuclide loss.

4 Conclusion

The radioactive nuclides in the effluent samples mostly exist in the liquid with a particle size of d < 0.1 μm, and are almost not distributed in the form of d > 0.45 μm particle size. After the sample is filtered by a desalination device, the radioactive activity is greatly reduced, and the filtering effect of the desalination device on radioactive nuclides cannot be ignored.

The flocculent precipitation in the waste liquid of the SRE system has a certain contribution to the enrichment of nuclides. With the extension of time, its enrichment of transition elements such as cobalt and manganese is particularly significant, causing nuclides to be distributed again in larger particle size forms in the liquid. It can be inferred that after the liquid effluent is discharged into the receiving water body, large particle sized substances such as colloids in the seawater have a certain adsorption effect on radioactive nuclides, which will lead to their aggregation effect again.

Although the liquid effluents from pressurized water reactor nuclear power plants are mainly dispersed in small particle sizes in the TEP and TEU systems, after they merge with SRE liquids containing complex colloids and particles in the TER tank and are stirred by external forces, transition metals such as cobalt and manganese will undergo a small amount of aggregation effect again within a certain period of time. With the extension of time and environmental conditions, after the effluent is discharged into the sea, A small amount of radioactive nuclides will inevitably accumulate in seawater, but the ocean is an extremely complex medium, and nuclides will undergo complex particle size changes as seawater migrates and exchanges with sediment and marine organisms.

Data availability statement

The original contributions presented in the study are included in the article/Supplementary Material, further inquiries can be directed to the corresponding authors.

Author contributions

ZJ: Conceptualization, Methodology, Writing–review and editing. JX: Formal Analysis, Software, Validation, Writing–original draft. YP: Supervision, Validation, Writing–original draft. JH: Supervision, Validation, Writing–review and editing. YC: Data curation, Formal Analysis, Writing–original draft. SY: Conceptualization, Methodology, Writing–original draft. YY: Conceptualization, Methodology, Writing–review and editing.

Funding

The author(s) declare financial support was received for the research, authorship, and/or publication of this article. This research is supported by the National Natural Science Foundation Projects under Grant (11975182).

Conflict of interest

Authors ZJ, JX, YP, YC, and SY were employed by China Nuclear Power Engineering Corporation.

The remaining authors declare that the research was conducted in the absence of any commercial or financial relationships that could be construed as a potential conflict of interest.

Publisher's note

References

Ahmed, D. S., Mohammed, M. R., and Mustafa, K. A. M. (2020). Synthesis of multi-walled carbon nanotubes decorated with ZnO/Ag nanoparticles by co-precipitation method. *Nanosci. Nanotechnology-Asia* 10 (2), 127–133. doi:10.2174/2210681208666181005145644

Appleby, P. G., Semertzidou, P., Piliposian, G. T., Chiverrell, R. C., Schillereff, D. N., and Warburton, J. (2019). The transport and mass balance of fallout radionuclides in Brotherswater, Cumbria (UK). *J. Paleolimnol.* 62 (4), 389–407. doi:10.1007/s10933-019-00095-z

Attallah, M. F., Hassan, H. S., and Youssef, M. A. (2019). Synthesis and sorption potential study of Al2O3ZrO2CeO2 composite material for removal of some radionuclides from radioactive waste effluent. *Appl. Radiat. Isotopes* 147, 40–47. doi:10.1016/j.apradiso.2019.01.015

Bashir, A., Malik, L. A., Ahad, S., Manzoor, T., Bhat, M. A., Dar, G. N., et al. (2019). Removal of heavy metal ions from aqueous system by ion-exchange and biosorption methods. *Environ. Chem. Lett.* 17, 729–754. doi:10.1007/s10311-018-00828-y

Cao, A., Hua, Y., Sun, Z., Meng, Z., Guo, Z., and Zhang, N. (2024). Study on reduction of pressure oscillation in low-velocity steam jet condensation. *Ann. Nucl. Energy* 197 (2024), 110271. doi:10.1016/j.anucene.2023.110271

Geraldo, B., de Araujo, L. G., Taddei, M. H. T., Ferreira, M. T., Máduar, M. F., Vicente, R., et al. (2019). Radiochemical characterization of spent filter cartridges from the primary circuit of a research reactor. *J. Radioanalytical Nucl. Chem.* 322, 1941–1951. doi:10.1007/s10967-019-06864-4

Gul, A., Hruza, J., and Yalcinkaya, F. (2021). Fouling and chemical cleaning of microfiltration membranes: a mini-review. *Polymers* 13 (6), 846. doi:10.3390/polym13060846

Guo, J., Wang, Y., Zhou, Z., Xie, F., Tong, J., Wang, K., et al. (2022). "Summary of methods for studying the chemical states of nuclides in nuclear Energy systems," in International Conference on Nuclear Engineering, August 8–12, 2022. V015T16A032.

Kamidaira, Y., Uchiyama, Y., Kawamura, H., Kobayashi, T., and Otosaka, S. (2021). A modeling study on the oceanic dispersion and sedimentation of radionuclides off the coast of Fukushima. *J. Environ. Radioact.* 238, 106724. doi:10.1016/j.jenvrad.2021.106724

Kang, J. S., and Cheong, J. H. (2022). New methodologies to derive dischargelimits considering operational flexibility of radioactive effluents from Korean nuclear power plants based on historical discharge data. *Nucl. Eng. Technol.* 54 (3), 1003–1015. doi:10.1016/j.net.2021.09.007

Kong, T. Y., Kim, S., Lee, Y., Son, J. K., and Maeng, S. J. (2017). Radioactive effluents released from Korean nuclear power plants and the resulting radiation doses to members of the public. *Nucl. Eng. Technol.* 49 (8), 1772–1777. doi:10.1016/j.net.2017.07.021

Li, C., Li, W., Sun, L., Xing, H., and Fang, C. (2019). Chemical forms of important fission products in primary circuit of HTR-PM under conditions of normal operation and overpressure and water ingress accidents: a study with a chemical thermodynamics approach. *Sci. Technol. Nucl. Installations* 2019, 1–12. doi:10.1155/2019/4251280

Ma, F., Gui, Y., Liu, P., Xue, Y., and Song, W. (2020). Functional fibrous materials-based adsorbents for uranium adsorption and environmental remediation. *Chem. Eng. J.* 390, 124597. doi:10.1016/j.cej.2020.124597

Ministry of Environmental and Forestry (2016). *Decree of changes in environmental permits for operational activities of the serpong nuclear area and irradiators and other facilities. Jakarta, Indonesia.*

National Nuclear Energy Agency (2011). *Emergency and preparedness plan. ‖ safety analysis report of G.A. Siwabessy multipurpose reactor, rev 10.1 p 20, tangerang selatan, Indonesia.*

Nivetha, N., Srivarshine, B., Sowmya, B., Rajendiran, M., Saravanan, P., Rajeshkannan, R., et al. (2023). A comprehensive review on bio-stimulation and bio-enhancement towards remediation of heavy metals degeneration. *Chemosphere* 312 (2023), 137099. doi:10.1016/j.chemosphere.2022.137099

Oh, M., Lee, K., Jeon, M. K., Foster, R. I., and Lee, C. H. (2023). Chemical precipitation–based treatment of acidic wastewater generated by chemical decontamination of radioactive concrete. *J. Environ. Chem. Eng.* 11, 110306. doi:10.1016/j.jece.2023.110306

Qi, X., Yu, F., Meng, Z., Sun, Z., Zhang, N., and Guo, Z. (2023). Preliminary design of the suppressive containment system based on HPR1000. *Nucl. Eng. Des.* 415 (2023), 112743. doi:10.1016/j.nucengdes.2023.112743

Tessaro, A. P. G., de Araujo, L. G., and Vicente, R. (2020). Inventorying the radionuclides in spent cartridge filters from the primary circuit of a nuclear research reactor by the dose-to-activity method. *Radiat. Phys. Chem.* 171, 108710. doi:10.1016/j.radphyschem.2020.108710

Thakur, D. A., Sonar, N. L., Shukla, R., Valsala, T. P., Sathe, D. B., Bhatt, R. B., et al. (2022). Evaluation of cerium–zirconium mixed oxides for separation of 125Sb from radioactive liquid waste. *J. Radioanalytical andNuclear Chem.* 331 (7), 2903–2909. doi:10.1007/s10967-022-08369-z

Tofighy, M. A., and Mohammadi, T. (2020). "Carbon nanotubes-polymer nanocomposite membranes for pervaporation," in *Polymer nanocomposite membranes for pervaporation*. Editor S. Thomas (Elsevier), 105–133.

Wang, X. W., Wang, R. D., Liang, M. C., He, S. J., Zhang, C., Li, K., et al. (2023). High-temperature catalytic oxidation preparation and liquid scintillation counting determination of the carbon-14 in liquid effluent samples from nuclear power plants. *Chin. J. Anal. Chem.* 51 (4), 100218. doi:10.1016/j.cjac.2022.100218

Yuniarto, A. N., Winansi, A., and Ritayanti, (2016). "—Application of radioactivity release boundary values to water bodies in the serpong nuclear area," in *Proc. National seminar of waste management Technology XIV* (Jakarta: Pusat Teknologi Limbah Radioaktif - BATAN), 43–53.

frontiers | Frontiers in Energy Research

TYPE Original Research
PUBLISHED 06 March 2024
DOI 10.3389/fenrg.2024.1374751

EDITED BY
Shichang Liu,
North China Electric Power University, China

REVIEWED BY
Hong Zhong,
China Institute of Water Resources and Hydropower Research, China
Shuli Fan,
Dalian University of Technology, China
Xunqiang Yin,
Dalian University, China

*CORRESPONDENCE
Yong Zhang,
✉ yong.zhang@fds.org.cn

RECEIVED 22 January 2024
ACCEPTED 16 February 2024
PUBLISHED 06 March 2024

CITATION
Yang G, Zhang Y, Fan T, Song Y and Bai Y (2024), An analytical method for free vibrations of the fuel rod with non-uniform mass of small modular reactor.
Front. Energy Res. 12:1374751.
doi: 10.3389/fenrg.2024.1374751

An analytical method for free vibrations of the fuel rod with non-uniform mass of small modular reactor

Guowei Yang[1,2], Yong Zhang[3,4]*, Tiandi Fan[1,2], Yong Song[1,3] and Yunqing Bai[4,5,6]

[1]Hefei Institutes of Physical Science, Chinese Academy of Sciences, Hefei, China, [2]University of Science and Technology of China, Hefei, China, [3]International Academy of Neutron Science, Qingdao, China, [4]National Institute of Neutronic Energy Co., Ltd., Qingdao, China, [5]Shandong Key Laboratory of Neutron Science and Technology, Qingdao, China, [6]Institute of Nuclear Science and Technology, Shandong University, Jinan, China

The intricate internal structure of fuel rods results in a non-uniform mass distribution, making it imperative to employ analytical methods for accurate assessment. The study utilizes Euler beam theory to derive the transverse vibration equation for beams with varying mass distribution. The approach involves transforming the non-uniform mass beam into a multi-segment beam with concentrated mass points. Modal function relationships between adjacent uniform segments are established based on continuous conditions at connection points. This transformation leads to the conversion of the variable coefficient differential equation into a nonlinear matrix equation. The Newton-Raphson method is then applied to calculate the characteristic equation and mode shapes, essential for determining natural frequencies. To validate precision, the results obtained are compared with those derived from the finite element method. Furthermore, the developed method is employed to assess the impact of gas plenum location and length on the natural frequency of fuel rods. The proposed methodology serves as a rapid design tool, particularly beneficial during the design phase of fuel rods with non-uniform mass distribution, aiding in configuring structural aspects effectively.

KEYWORDS

lead-based fast reactor, fuel rod, free vibration, non-uniform mass, Newton-Raphson iteration method

1 Introduction

Small modular reactor (SMR) has aroused extensive attention because of the low-cost and high fitness (Hussein, 2020). Among various Gen IV reactors, the Lead-based Fast Reactor (LFR) is known for its favorable neutron properties, superior heat transfer capability (Bandini et al., 2011), excellent fuel breeding performance, and inherent safety. These characteristics make LFR particularly promising for miniaturized applications (Takahashi and Sekimoto, 2007; OECD Nuclear Energy Agency, 2014). Recent years have seen the proposal of various Lead-based Fast Reactor (LFR) concepts worldwide. These include the SVBR-100 (Grape et al., 2014) and BREST-OD-300 projects (Zrodnikov et al., 2011) in Russia, the MYRRHA project (Orlov et al., 2005) in Belgium, the ELFR and ALFRED projects (Hamid et al., 2001) in the European Union, and the CLEAR-I project in China (Roberto et al., 2014; Wang et al., 2015; Wu, 2016a; Wu, 2016b; Wu et al., 2016).

The fuel rod is a crucial component in a nuclear reactor, primarily serving to contain nuclear fuel, regulate neutron flux, induce nuclear fission reactions, and generate heat energy. Within fuel rods, Fission Gases (FG) are continuously generated during burn-up, escaping to the fuel-to-cladding gap and eventually reaching the gas plenum. The release of FG increases the internal pressure, potentially accelerating the degradation of the mechanical properties of the cladding that surrounds the fuel. The gas plenum serves as a crucial component in the fuel rod design, intended to mitigate pressure changes and minimize their impact. The mass of the gas plenum section is significantly lighter than the other parts of the fuel rod, resulting in an uneven axial distribution of mass in the fuel rod. The fuel rod is a typical beam model with variable cross-sectional parameters.

Numerous scholars have extensively delved into theoretical and numerical investigations concerning beams with arbitrary variable cross-sectional parameters. Early researchers predominantly explored diverse methodologies to address the natural frequencies of specific configurations of such beams. Heidebrecht (Ramesh and Rao, 2013), for instance, extended the vibration equation of variable cross-sectional parameters beams into a Fourier series, thereby deriving approximate natural frequencies and modes for simply supported instances. Bailey (Bailey, 1978), by integrating the Hamiltonian principle with numerical methods, resolved the frequency equation and determined the natural frequencies of cantilevered variable cross-sectional parameters beams. Gupta (Gupta, 1985) employed the finite element method to obtain numerical solutions for the natural frequencies and modes of circular beams with linearly varying diameters. Olver (Olver, 1974), utilizing the WKB (Wentzel, Kramers, Brillouin (Avdoshka and Mikhasev, 2001)) method, addressed the natural frequencies and modes of free vibrations in variable cross-sectional parameters Euler beams. Given that the WKB method fundamentally relies on a small parameter, introducing a parameter representing the reciprocal of the natural frequency, its limitations become apparent when dealing with beams of low natural frequencies, leading to inaccuracies in frequency solutions. Consequently, the WKB method is best suited for variable cross-sectional parameters Euler beams characterized by substantial stiffness; however, for beams with low stiffness, significant errors arise in the computations. Moreover, numerous studies have scrutinized circular cone beams with linearly varying cross-sectional radii, employing methodologies such as orthogonal analysis (Spigler and Vianello, 2007), Bessel equations (Caruntu, 1996; Auciello and Nolè, 1998), infinite series (Rosa and Auciello, 1996), Frobenius power exponent method (Ö and Kaya, 2006), and Differential Transform Method (DTM) (BanerjeeSuJackson, 2006).

Upon analyzing the current research landscape regarding the calculation of vibration characteristics in beams with variable cross-sectional parameters, it becomes evident that diverse methods are employed. The utilization of these mathematical approaches for calculating the vibration characteristics of such beams entails a cumbersome and intricate solving process, making it less conducive to engineering applications. Additionally, the establishment and computation process of finite element models require a considerable amount of time.

This paper investigates the calculation method for the transverse vibration characteristics of Euler beams with non-uniform mass. Based on Euler beam theory, non-uniform mass is equivalently represented as a uniform mass beam with multiple concentrated mass points. The transverse vibration equations for beams with concentrated masses are derived, and the resulting equations are validated through comparisons with results obtained using the finite element software ANSYS in various instances. The accuracy of the method is confirmed through these comparisons. Additionally, the study explores the impact of mass distribution on the natural frequencies of fuel rods.

2 General theoretical formulations for non-uniform beam

Assuming the length of the beam is L, the mass per unit length is ρ, and the bending stiffness is a constant EI. Consider the beam as a Bernoulli-Euler beam. The Euler-Bernoulli beam theory satisfies some fundamental assumptions, including a length-to-thickness ratio greater than 10, neglecting shear deformation of the beam, as well as ignoring the influence of the rotational inertia of the cross-section about the neutral axis.

The bending equation of the beam can be used to describe the behavior of lateral bending. For free vibration, neglecting external loads, the bending equation is given by Eq. 1.

$$\frac{\partial^2 y}{\partial x^2}\left(EI\frac{\partial^2 y(x,t)}{\partial x^2}\right)+\rho\frac{\partial^2 y(x,t)}{\partial t^2}=0 \tag{1}$$

Where $y(x, t)$ represents the lateral displacement at point x of the beam at time t.

The free vibration of the curved beam is a fourth-order partial differential equation. To solve the differential equation, the separation variable method can be employed resulting in Eq. 2:

$$y(x,y)=Y(x)T(t) \tag{2}$$

In Eq. 2, $T(t)$ is a sinusoidal function, which can be expressed as given in Eq. 3.

$$T(t)=\sin(\omega t-\varphi) \tag{3}$$

In Eq. 3, ω represents the natural frequency of the system. ω signifies the natural circular frequency of lateral vibrations, and φ represents the phase angle determined by the initial conditions of the vibration.

$Y(x)$ is the mode function of the transverse vibration of the beam, which can be expressed in Eq. 4.

$$Y(x)=A_1\sinh\lambda x+A_2\cos\lambda x+A_3\sinh\lambda x+A_4\cosh\lambda x \tag{4}$$

In Eq. 5, λ is the eigenvalue, typically represented as a solution to the modal equation and can be obtained through Eq. 5.

$$\lambda^4=\frac{\rho}{EI}\omega^2 \tag{5}$$

A_1, A_2, A_3, and A_4 are undetermined coefficients determined by the boundary conditions at the left and right ends of the beam. For an equal cross-section beam under specified boundary conditions. The analytical solution of its mode functions can be obtained from Eq. 4, and the characteristic equation for calculating its natural frequencies can be derived from Eq. 4.

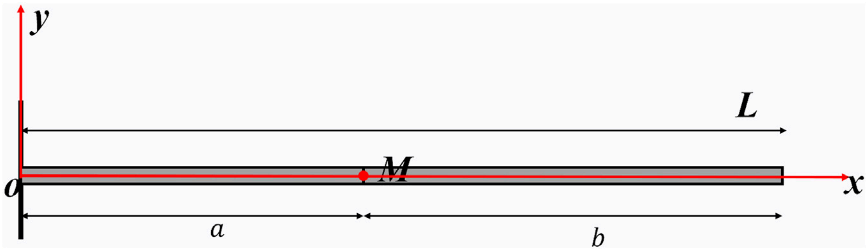

FIGURE 1
Single concentrated mass point model.

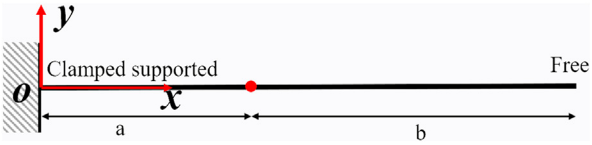

FIGURE 2
Cantilever beam model with a single concentrated mass point.

The fuel rod contains internal fillers with non-uniform mass distribution, making it impractical to calculate using the above-mentioned methods. By simplifying the internal fillers into concentrated mass points, the fuel rod is then modeled as a beam with concentrated mass points.

2.1 Theory formula for beam with single concentrated mass point

The beam is divided into two parts at a concentrated mass point, as shown in Figure 1. The lengths of the two beam segments are denoted as a and b. Both beams have consistent density ρ, bending stiffness EI, and a concentrated mass M.

Assume that the two beams have different vibration mode functions, denoted as $Y_1x)$ and $Y_2x)$, as shown in Eq. 6 and Eq. 7).

$$Y_1(x) = C_1 \cosh\lambda x + C_2 \sinh\lambda x + C_3 \cos\lambda x + C_4 \sinh\lambda x \tag{6}$$

$$Y_2(x) = D_1 \cosh\lambda x + D_2 \sinh\lambda x + D_3 \cos\lambda x + D_3 \sinh\lambda x \tag{7}$$

Each mode function involves four parameters to be determined. The presence of concentrated mass points influences the boundary conditions of the two equations. Taking a cantilever beam as an example (as shown in Figure 2), the boundary conditions are expressed as Eqs 8–15:

1) At the clamped support, both the deflection and the rotation of the beam are zero. The boundary conditions for the fixed end are written as Eq. 8 and Eq. 9:

$$\text{Deflection: } Y_1(0) = 0 \tag{8}$$

$$\text{Rotation: } Y_1'(0) = 0 \tag{9}$$

2) At the concentrated mass point, both beams exhibit the same deflection, rotation, bending moment. The sum of the generated shear forces is zero. The boundary conditions of the concentrated mass point are written as Eqs 10–13:

$$\text{Deflection: } Y_1(a) - Y_2(0) = 0 \tag{10}$$

$$\text{Rotation: } Y_1'(a) - Y_2'(0) = 0 \tag{11}$$

$$\text{Bending moment: } Y_1''(\mathrm{a}) - Y_2''(0) = 0 \tag{12}$$

$$\text{Shear force: } EI\left[Y_1'''(a) - Y_2'''(0)\right] - MY_1''(a) = 0 \tag{13}$$

3) At the free end, both the bending moment and shear force of the beam are zero. The boundary conditions of the free end are written as Eq. 14, Eq. 15:

$$\text{Bending moment: } Y_2''(\mathrm{b}) = 0 \tag{14}$$

$$\text{Shear force: } Y_2'''(\mathrm{b}) = 0 \tag{15}$$

Bring the boundary conditions into Eq. 6 and Eq. 7 to get Eq. 16, and the final coefficient matrix is given as shown in Eq. 17.

$$\begin{cases} C_1 + C_3 = 0 \\ C_2 + C_4 = 0 \\ C_1(\cosh\lambda a - \cos\lambda a) + C_2(\sinh\lambda a - \sin\lambda a) - D_1 - D_3 = 0 \\ C_1\lambda(\sinh\lambda a + \sin\lambda a) + C_2\lambda(\cosh\lambda a - \cos\lambda a) - D_2 - D_4 = 0 \\ C_1\lambda^2(\cosh\lambda a + \cos\lambda a) + C_2\lambda^2(\sinh\lambda a + \sin\lambda a) - D_1 + D_3 = 0 \\ C_1\left[EI\lambda^3(\sinh\lambda a - \sin\lambda a) - M\lambda^2(\cosh\lambda a + \cos\lambda a)\right] + \\ C_1\left[EI\lambda^3(\cosh\lambda a + \cos\lambda a) - M\lambda^2(\sinh\lambda a + \sin\lambda a)\right] - D_2 + D_4 = 0 \\ D_1 \cosh\lambda b + D_2 \sinh\lambda b - D_3 \cos\lambda b - D_4 \sin\lambda b = 0 \\ D_1 \sin \mathrm{h}\lambda b + D_2 \cosh\lambda b + D_3 \sin\lambda b - D_4 \cos\lambda b = 0 \end{cases} \tag{16}$$

$$A = \begin{bmatrix} 1 & 0 & 1 & 0 & 0 & 0 & 0 & 0 \\ 0 & 1 & 0 & 1 & 0 & 0 & 0 & 0 \\ 0 & 0 & 0 & 0 & \cosh\lambda b & \sinh\lambda b & -\cos\lambda b & -\sin\lambda b \\ 0 & 0 & 0 & 0 & \sinh\lambda b & \cosh\lambda b & \sin\lambda b & -\cos\lambda b \\ \cosh\lambda a & \sinh\lambda a & \cos\lambda a & \sin\lambda a & -1 & 0 & -1 & 0 \\ \lambda\sinh\lambda a & \lambda\cos\lambda a & -\lambda\sin\lambda a & \lambda\cos\lambda a & 0 & -1 & 0 & -1 \\ \lambda^2\cosh\lambda a & \lambda^2\cos\lambda a & -\lambda^2\cos\lambda a & -\lambda^2\cos\lambda a & -1 & 0 & 1 & 0 \\ \begin{matrix} EI\lambda^3\sinh\lambda a \\ -M\lambda^2\cosh\lambda a \end{matrix} & \begin{matrix} EI\lambda^3\cosh\lambda a \\ -M\lambda^2\sinh\lambda a \end{matrix} & \begin{matrix} EI\lambda^3\sin\lambda x \\ +M\lambda^2\cosh\lambda x \end{matrix} & \begin{matrix} EI\lambda^3\cos\lambda a \\ +M\lambda^2\sin\lambda a \end{matrix} & 0 & -EI\lambda^2 & 0 & EI\lambda^2 \end{bmatrix} \tag{17}$$

The coefficient matrix Eq. (17) in row-column form must be zero, resulting in the characteristic equation of a simply supported beam with non-uniform mass.

$$\det(A) = 0 \tag{18}$$

Organize the determinant and get Eq. 19

FIGURE 3
Simply supported beam model with a single concentrated mass point.

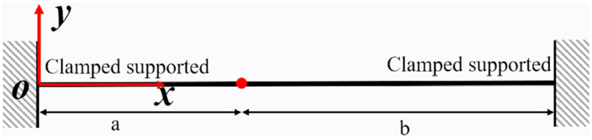

FIGURE 4
Clamped supported beam model with a single concentrated mass point.

$$-\frac{M}{4EI}=\frac{\lambda\left(1+\cosh\lambda l\cos\lambda l\right)}{\begin{aligned}(\sinh\lambda a+\sin\lambda a)[(\sinh\lambda l-\cosh\lambda l)(\cos\lambda b+\sin\lambda b)\\+(\sin\lambda l-\cos\lambda l)(\cosh\lambda b+\sinh\lambda b)]\end{aligned}} \tag{19}$$

The same method can be used to derive the eigenvalue matrix equations for simply supported beams and clamped supported beams with a concentrated mass point.

In the simply supported beam model depicted in Figure 3, the boundary conditions at the clamped end and the positions of the concentrated mass point are consistent with those of the cantilever beam. The distinction lies in the boundary conditions at the simply supported end, where deflection and bending moment are both zero, as illustrated in Eq. 20 and 21.

$$\text{Deflection: } Y_2(\mathrm{b})=0 \tag{20}$$

$$\text{Bending moment: } Y_2''(\mathrm{b})=0 \tag{21}$$

By introducing the boundary conditions into Eq. 6 and 7 is obtained, and the final coefficient matrix is given as shown in Eq. 22.

$$A=\begin{bmatrix}
1 & 0 & 1 & 0 & 0 & 0 & 0 & 0\\
0 & 1 & 0 & 1 & 0 & 0 & 0 & 0\\
0 & 0 & 0 & 0 & \cosh\lambda b & \sinh\lambda b & \cos\lambda b & \sin\lambda b\\
0 & 0 & 0 & 0 & \lambda^2\cosh\lambda b & \sinh\lambda b & -\lambda^2\cos\lambda b & -\lambda^2\sin\lambda b\\
\cosh\lambda a & \sinh\lambda a & \cos\lambda a & \sin\lambda a & -1 & 0 & -1 & 0\\
\lambda\sinh\lambda a & \lambda\cos\lambda a & -\lambda\sin\lambda a & \lambda\cos\lambda a & 0 & -1 & 0 & -1\\
\lambda^2\cosh\lambda a & \lambda^2\cos\lambda a & -\lambda^2\cos\lambda a & -\lambda^2\cos\lambda a & -1 & 0 & 1 & 0\\
\begin{matrix}EI\lambda^3\sinh\lambda a\\-M\lambda^2\cosh\lambda a\end{matrix} & \begin{matrix}EI\lambda^3\cosh\lambda a\\-M\lambda^2\sinh\lambda a\end{matrix} & \begin{matrix}EI\lambda^3\sin\lambda x\\+M\lambda^2\cosh\lambda x\end{matrix} & \begin{matrix}EI\lambda^3\cos\lambda a\\+M\lambda^2\sin\lambda a\end{matrix} & 0 & -EI\lambda^2 & 0 & EI\lambda^2
\end{bmatrix} \tag{22}$$

The coefficient matrix Eq. 22 in row-column form must be zero, resulting in the characteristic equation of a simply supported beam with non-uniform mass.

$$\det(A)=0 \tag{23}$$

In the clamped supported beam model depicted in Figure 4, the boundary conditions at the clamped end and the positions of the concentrated mass point are consistent with those of the cantilever beam. The distinction lies in the boundary conditions at the another clamped supported end. These conditions entail the deflection of 0 and the Rotation of 0, as illustrated in Eq. 24 and 25.

$$\text{Deflection: } Y_2(\mathrm{b})=0 \tag{24}$$

$$\text{Bending moment: } Y_2'(\mathrm{b})=0 \tag{25}$$

By introducing the boundary conditions into Eq. 6 and 7 is obtained, and the final coefficient matrix is given as shown in Eq. 26.

$$A=\begin{bmatrix}
1 & 0 & 1 & 0 & 0 & 0 & 0 & 0\\
0 & 1 & 0 & 1 & 0 & 0 & 0 & 0\\
0 & 0 & 0 & 0 & \cosh\lambda b & \sinh\lambda b & \cos\lambda b & \sin\lambda b\\
0 & 0 & 0 & 0 & \lambda\sinh\lambda b & \lambda\cosh\lambda b & -\lambda\sin\lambda b & \lambda\cos\lambda b\\
\cosh\lambda a & \sinh\lambda a & \cos\lambda a & \sin\lambda a & -1 & 0 & -1 & 0\\
\lambda\sinh\lambda a & \lambda\cos\lambda a & -\lambda\sin\lambda a & \lambda\cos\lambda a & 0 & -1 & 0 & -1\\
\lambda^2\cosh\lambda a & \lambda^2\cos\lambda a & -\lambda^2\cos\lambda a & -\lambda^2\cos\lambda a & -1 & 0 & 1 & 0\\
\begin{matrix}EI\lambda^3\sinh\lambda a\\-M\lambda^2\cosh\lambda a\end{matrix} & \begin{matrix}EI\lambda^3\cosh\lambda a\\-M\lambda^2\sinh\lambda a\end{matrix} & \begin{matrix}EI\lambda^3\sin\lambda x\\+M\lambda^2\cosh\lambda x\end{matrix} & \begin{matrix}EI\lambda^3\cos\lambda a\\+M\lambda^2\sin\lambda a\end{matrix} & 0 & -EI\lambda^2 & 0 & EI\lambda^2
\end{bmatrix} \tag{26}$$

The coefficient matrix Eq. 26 in row-column form must be zero, resulting in the characteristic equation of a simply supported beam with non-uniform mass.

$$\det(A)=0 \tag{27}$$

The characteristic Eq. 19 and (23 and Eq. 27 is a nonlinear function of the λ. The Newton-Raphson iteration method can be employed to solve for λ.

Firstly, while ensuring that the total mass and geometric dimensions remain unchanged, the non-uniform mass Bernoulli-Euler beam is equivalently transformed into a uniform mass Bernoulli-Euler beam. Subsequently, the natural frequency of the uniform mass Bernoulli-Euler beam is calculated to obtain an analytical solution. This analytical solution serves as the initial approximate solution (x_0) to initiate the iterative process.

Updating the initial guess using the Newton-Raphson iteration formula Eq. 28.

$$x_n=x_{n-1}-\frac{f\left(x_{n-1}\right)}{f'\left(x_{n-1}\right)} \tag{28}$$

Check whether the new guessed value satisfies the predetermined convergence criteria. If satisfied, consider the root of the equation found; if not, go back to the previous step and repeat the iteration process.

2.2 Theoretical formulations for beam with multiple centralized mass points

The internal filling of the fuel element is complex, and the fuel rod is divided into multiple sections. As shown in Figure 5, the beam model is segmented into N sections with concentrated mass points

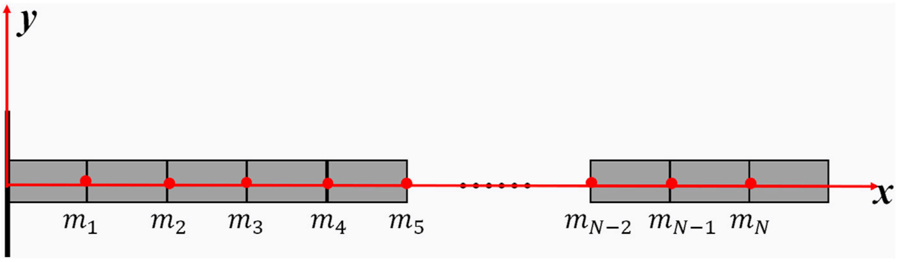

FIGURE 5
Skech of Bernoulli–Euler cantilever beam.

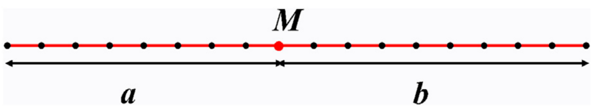

FIGURE 6
Skech of Bernoulli–Euler cantilever beam.

TABLE 1 Main parameters of cantilever beam.

L (m)	I (m^4)	S (m^2)	ρ (kg/m^3)	E (Pa)	m (kg)
2	1/12 × 10^{-8}	0.0001	7,850	2 × 1,011	1.57

TABLE 2 The value of the first five characteristic roots λ

n	1	2	3	4	5
Λn	0.69	1.72	4.09	4.94	7.37

TABLE 3 First 5 natural frequency of beam with single concentrated mass.

n	1	2	3	4
Numerical calculation (Hz)	1.08	6.74	38.18	55.780
Theoretical calculation (Hz)	1.10	6.86	38.79	56.59
Error (%)	1.9	1.7	1.5	1.4

as endpoints. It is simplified into a Bernoulli-Euler beam with *N-1* concentrated mass points, each with a concentrated mass value of m_a.

As shown in Eq. (29), it is simplified to the free vibration equation of a Bernoulli-Euler beam with *N-1* concentrated masses m_a.

$$\frac{\partial^2}{\partial x^2}\left[EI\frac{\partial^2 y(x,t)}{\partial x^2}\right]+\sum\nolimits_{a=1}^{N-1} m_a\delta\left(x-x_a^m\right)\frac{\partial^2 y(x,t)}{\partial t^2}+\rho A\frac{\partial^2 y(x,t)}{\partial t^2}$$
$$=0 \tag{29}$$

where, EI is the bending stiffness of the beam section; A is the beam section area; ρ is density; δ is the Dirac function; x_a^m is the horizontal coordinate of a concentrated mass point;

The free vibration of the curved beam is a fourth-order partial differential equation. To solve the differential equation, the separation variable method can be employed resulting in Eq. (30):

$$y(x,t)=\bar{\varphi}(x)\bar{T}(t) \tag{30}$$

In the equation, $\bar{\varphi}(x)$ represents the shape of the vibration; $\bar{T}(t)$ represents the amplitude that varies with time. By substituting Eqs 16 into Eq. 15 and rearranging, Eq. 31 is obtained:

$$EI\frac{\partial^4\bar{\varphi}(x)}{\partial x^4}+\bar{\lambda}_i\sum\nolimits_{a=1}^{N-1} m_a\delta\left(x-x_a^m\right)\bar{\varphi}(x)+\bar{\lambda}\rho A\bar{\varphi}(x)=0 \tag{31}$$

In this equation, $\bar{\lambda}=\omega^2$ represents the eigenvalues of the Bernoulli-Euler beam with concentrated mass. Obtaining an analytical solution for the variable coefficient differential equation is relatively challenging.

Consider the Euler beam with concentrated mass as a new system obtained by adding concentrated mass to a uniform mass Euler beam through system modification. The primary mode functions and eigenvalues of this new system can be obtained by perturbation calculations using the mode functions of a uniform mass beam.

$$\bar{\varphi}_i(x)=\varphi_i(x)+\Delta\varphi_i(x) \tag{32}$$

$$\bar{\lambda}_i=\lambda_i+\Delta\lambda_i \tag{33}$$

$\bar{\varphi}_i(x)$ and $\bar{\lambda}_i$ represent the *i* order mode function and eigenvalue of the new system beam with concentrated mass; $\varphi_i(x)$ and λ_i represent the *i* order mode function and eigenvalue of the uniform mass beam; $\Delta\lambda_i$ is the *i*th order eigenvalue correction of the new system with a concentrated mass point relative to the uniform mass beam. $\Delta\varphi_i(x)$ is the correction of the primary mode function of the new system with a concentrated mass point relative to the uniform mass beam, and it is a linear combination of the other retained primary mode functions of the uniform mass beams, excluding $\varphi_i(x)$.

$$\Delta\varphi_i(x)=\sum\nolimits_{j=1,j\neq i}^{n}\varphi_j(x)q_j \tag{34}$$

In the equation, q_j are coefficients of the modal linear combination. As long as $\delta\lambda_i$ and is q_j obtained, there are η unknowns, and by using Eqs 32 and 33, the *i* order main modal function $\bar{\varphi}_i(x)$ and eigenvalue $\bar{\lambda}_i$ of the beam with **concentrated mass**es can be obtained. According to the theory of dynamics, the equivalent beam in Eq. (34) has an infinite number of main modes. However, in practical calculations,

TABLE 4 Natural frequency of single-mass cantilever beam with different mass position.

Mass	Position (m)	Method	1	2	3	4
Concentrated mass of 1.57 kg	a = 1	FEA (Hz)	1.08	6.74	38.18	55.78
		analytical solution (Hz)	1.10	6.86	38.79	56.59
	b = 1	error %	1.9	1.7	1.5	1.4
	a = 0.5	FEA (Hz)	2.06	6.62	20.42	55.47
		analytical solution (Hz)	2.09	6.70	20.73	56.36
	b = 1.5	error %	1.5	1.2	1.5	1.5
	a = 1.5	FEA (Hz)	0.64	13.36	28.41	63.02
		analytical solution (Hz)	0.65	13.58	28.89	64.16
	b = 0.5	error %	1.7	1.6	1.6	1.7
Concentrated mass of 15.7 kg	a = 1	FEA (Hz)	0.382	6.179	38.187	55.080
	b = 1	Theoretical calculation (Hz)	0.389	6.313	39.171	56.590
		error %	2.5	2.1	02.5	2.6
	a = 0.5	FEA (Hz)	1.01	3.60	21.68	61.41
	b = 1.5	analytical solution (Hz)	1.04	3.68	22.28	62.94
		error %	2.2	2.3	2.7	2.4
	a = 1.5	FEA (Hz)	0.210	13.333	27.883	62.693
	b = 0.5	analytical solution (Hz)	0.215	13.693	28.618	64.550
		error %	2.6	2.6	2.5	2.8

taking a finite number of low-order modes for approximation in perturbation solution can achieve results with sufficient accuracy.

Substituting Eqs 32 and 33 into Eq. 29, and simplifying using Eq. 31, yields the expression for Eq. 35:

$$\begin{aligned} &EI\frac{\partial^4 \Delta\varphi(x)}{\partial x^4} - \left[\lambda_i \rho A \Delta\varphi_i(x) + \Delta\lambda_i \rho A \varphi_i(x) + \Delta\lambda_i \rho A \Delta\varphi_i(x)\right] \\ &- \sum_{a=1}^{N-1} m_a \delta\left(x - x_a^m\right) \times \left[\lambda_i \varphi_i(x) + \lambda_i \Delta\varphi_i(x) + \Delta\lambda_i \varphi_i(x) + \Delta\lambda_i \Delta\varphi_i(x)\right] \\ &= 0 \end{aligned} \tag{35}$$

Substitute Eq. 34 into Eq. 35, then multiply both sides by $\varphi_k(x)$ (k = 1,2, . . . , η), integrate along the length L of the beam, and simplify using the modal orthogonality of the equivalent beam, resulting in Eq. (36):

$$\begin{aligned} &\Delta\lambda_i\left(m_k \delta_{ki} + \Delta m_{ki}\right) + \Delta\lambda_i \sum_{j=1, j\neq i}^{n} \left(m_k \delta_{kj} + \Delta m_{kj}\right) q_j \\ &+ \sum_{j=1, j\neq i}^{n} \left[\left(\lambda_i - \lambda_j\right) m_k \delta_{kj} + \lambda_i \Delta m_{kj}\right] q_j \\ &= -\lambda_i \Delta m_{ki} \end{aligned} \tag{36}$$

Where

$$m_k = \int_0^L \rho A \varphi_k^2(x) dx \tag{37}$$

$$\delta m_k = \int_0^L \sum_{a=1}^{N-1} m_a \delta\left(x - x_a^m\right) \varphi_k(x) \varphi_i(x) dx = 0 \tag{38}$$

Eq. 37 and Eq. 38 can be directly obtained using numerical integration. Letting $k = 1, 2, \ldots, \eta$ in Eq. 36 yields η nonlinear algebraic equations involving unknowns $\Delta\lambda_i$ and q_j. After organization and simplification, these equations can be expressed in matrix form as Eq. (39):

$$\left[A + \lambda_i B + \lambda_i C + q_i\right] q = p \tag{39}$$

Where

$$A = \begin{bmatrix} m_1(\lambda_i - \lambda_1) & \cdots & \cdots & 0 \\ \vdots & m_1(\lambda_i - \lambda_2) & \cdots & \vdots \\ \vdots & \vdots & \ddots & \vdots \\ 0 & \cdots & \cdots & m_\eta\left(\lambda_i - \lambda_\eta\right) \end{bmatrix}_{\eta\times\eta} \tag{40}$$

$$B = \begin{bmatrix} \Delta m_{11} & \Delta m_{12} & \cdots & \Delta m_{1\eta} \\ \Delta m_{21} & \Delta m_{22} & \cdots & \Delta m_{2\eta} \\ \vdots & \vdots & \vdots & \vdots \\ \Delta m_{\eta 1} & \Delta m_{\eta 2} & \cdots & \Delta m_{\eta\eta} \end{bmatrix}_{\eta\times\eta} \tag{41}$$

$$C = \begin{bmatrix} \delta m_{11} + m_1 & \delta m_{12} & \cdots & 0 & \cdots & \delta m_{1\eta} \\ \delta m_{21} & \delta m_{22} + m_2 & \cdots & 0 & \cdots & \delta m_{2\eta} \\ \vdots & \vdots & \vdots & \vdots & \vdots & \vdots \\ \delta m_{i1} & \delta m_{11} & \cdots & 0 & \cdots & \delta m_{i\eta} \\ \vdots & \vdots & \vdots & \vdots & \vdots & \vdots \\ \delta m_{\eta 1} & \delta m_{\eta 2} & \cdots & 0 & \cdots & \delta m_{\eta\eta} + m_\eta \end{bmatrix}_{\eta\times\eta} \tag{42a}$$

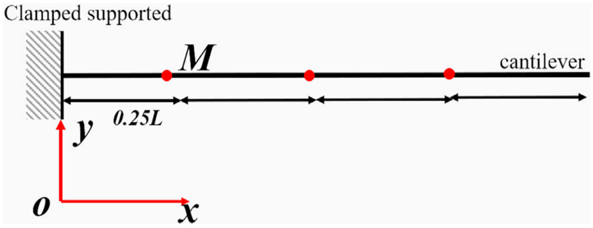

FIGURE 7
The Bernoulli-Euler beam model with three Concentrated mass.

$$p = \begin{bmatrix} -\lambda_i \delta m_{1i} \\ -\lambda_i \delta m_{2i} \\ \vdots \\ -\lambda_i \delta m_{\eta i} \end{bmatrix}_{\eta \times 1} \tag{43a}$$

$$q = \begin{bmatrix} q_1 & q_2 & \cdots & q_\eta \end{bmatrix}_{1\times\eta} \tag{44a}$$

Where the i of q is $q_i = \Delta\lambda_i / \lambda_i$.This transforms the variable coefficient differential Eq. (29) into a nonlinear matrix Eq. 39. λ_i represents the eigenvalues of the free vibration of a uniform mass beam. The study of the free vibration characteristics of uniform mass beams under different boundary conditions is well-established, with standard analytical solutions available.

The nonlinear matrix Eq. (39) can be solved using the Newton-Raphson method or intelligent algorithms. The Newton-Raphson method is highly dependent on the choice of initial values. Providing reasonable initial values can not only reduce the number of iterations but also achieve more accurate convergence results. Given the meaning of the various combination coefficients within the vector q, initial values for q are specified.

$$q = 0 \tag{42b}$$

The termination criteria for iteration can be adopted as follows:

$$\left| q_i^{(\varepsilon)} - q_i^{(\varepsilon-1)} \right| / \left| q^{(\varepsilon)} \right| \le \xi \tag{43b}$$

In Eq. 43b: the superscript ε denotes the number of equation iterations; ξ is the convergence error, $\xi = 1 \times 10^{-8}$. After obtaining the unknown vector q, substitute it into Eq. 32 and 33 to obtain the i natural frequency and mode shape of the beam with concentrated masses.

3 Benchmark verification of the proposed analytical method

3.1 Single concentrated mass point

By comparing with the natural frequency of the non-uniform mass fuel rod obtained through finite element analysis (FEA) in ANSYS, the correctness of the rapid method is verified.

The finite element model is modeled using beam3 elements. The Beam3 element is a uniaxial element capable of withstanding tension, compression, and bending. Each node of this element has three degrees of freedom: linear displacements along the x and y directions, as well as angular displacement about the Z-axis.

As shown in Figure 6, the finite element model is divided into 17 elements, featuring a concentrated mass point with a mass of M. The lengths of the beams on either side of the concentrated mass are a and b. The key parameters governing the behavior of the system are detailed in Table 1, providing essential insights into the structural dynamics.

There is a concentrated mass in the middle of the beam (x = 1) with a concentrated mass of 1.57 kg. Under this condition, the relevant parameters in Eq. (19) can be expressed as a = 1, b = 1, M = 1.57kg, EI = 1/6 × 103, and solved Eq. 19 to obtain λn. The calculation results were shown in Table 2.

The natural frequency is calculated by Eq.44b and 45.

$$\omega_n = \lambda_n^2 \sqrt{\frac{EI}{\rho S l^4}} \tag{44b}$$

$$f_n = \frac{\lambda_n^2}{2\pi} \sqrt{\frac{EI}{\rho S l^4}} \tag{45}$$

The first four natural frequencies were determined using Eq. 44b and 44and the results are presented in Table 3. The theoretical calculations closely align with the simulation results, confirming the accuracy of the formula.

To evaluate the sensitivity of the formula to variations in the weight and position of the concentrated mass point, an additional analysis was performed. This involved altering both the location and weight of the concentrated mass point, and the corresponding results are provided in Table 4.

Eq. 19 is applicable to a cantilever Bernoulli–Euler beam with a single concentrated mass of varying weight. Across different parameter settings, the deviation between the theoretical formula and simulation results is consistently below 3%.

3.2 Multiple concentrated mass points

The parameters of the beam model remain consistent with Section 3.1. Three concentrated mass points are introduced onto the beam, dividing the beam model into four segments. Each concentrated mass has a mass of M, and each segment has a length of 0.25, as shown in Figure 7.

Table 5 presents the first four natural frequency values of the cantilever beam with concentrated mass points calculated using the finite element method and the proposed method. The study investigates the influence of the concentrated mass values on the computational accuracy. From Table 5, it can be observed that the number of concentrated mass points has a limited impact on the calculation error. However, as the weight of the concentrated mass increases, the calculation error also rises. Under various parameter settings, the deviation between the results obtained using Eq. 29 and the ANSYS simulation results is consistently below 3%.

To validate the impact of fixation methods on computational accuracy, three different fixation methods are considered (as shown in Figure 8): simply supported beam (CS), cantilever beam (CA) and clamped-supported beam (CC). The mass of concentrated mass point is 1.57/4 kg, and the length is L/4. The parameters of the beam model remain consistent with Section 3.1.

TABLE 5 First 4 natural frequencies of the beam with different concentrated mass points.

Concentrated mass (kg)	Methods	1st	2nd	3rd	4th
M1 = M2 = M3 = M4 = 1.57/4	FEA (Hz)	1.92	5.88	15.97	28.30
	analytical solution (Hz)	1.94	5.97	16.27	28.72
	error %	1.03	1.51	1.84	1.46
M1 = M2 = M3 = M4 = 15.7/4	FEA (Hz)	0.31	2.07	5.59	23.94
	analytical solution (Hz)	0.318	2.12	5.74	24.64
	error %	2.58	2.415	2.683	2.924

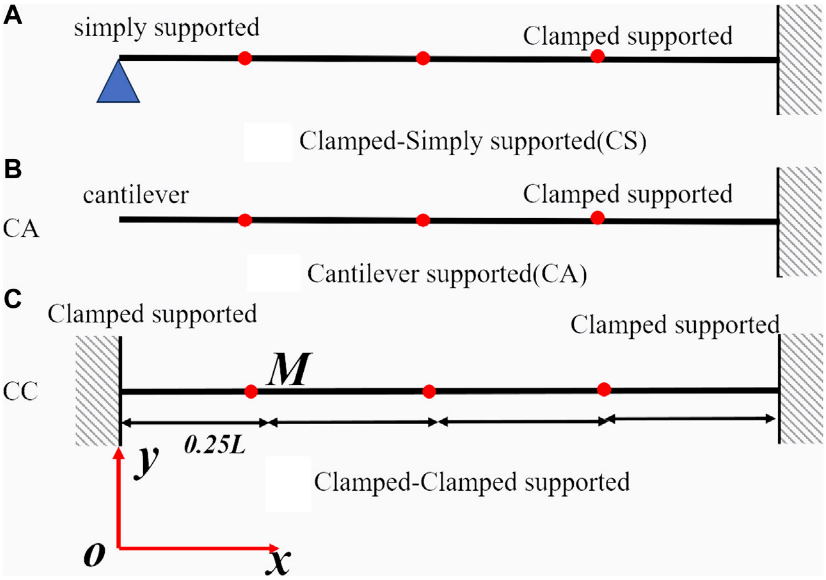

FIGURE 8
The Bernoulli-Euler beam model under different boundary conditions.

TABLE 6 First 4 natural frequencies of the beam with concentrated mass points under different constraints.

Fixation method	Methods	1st	2nd	3rd	4th
CS	FEA (Hz)	1.92	5.88	15.97	28.30
	analytical solution (Hz)	1.95	5.98	16.26	28.85
	error %	2.03	1.81	1.84	1.96
CA	FEA (Hz)	3.04	7.08	16.18	29.76
	analytical solution (Hz)	3.09	7.17	16.45	30.20
	error %	1.53	1.31	1.69	1.46
CC	FEA (Hz)	4.84	9.83	22.35	36.38
	analytical solution (Hz)	4.89	9.92	22.55	37.09
	error %	1.03	0.91	0.89	1.96

Table 6 lists the natural frequencies of non-uniform mass fuel rods under different boundary conditions. After segmenting the fuel rod based on internal filling, the analytical solutions obtained are generally similar to the results obtained through finite element calculations, with errors less than 3%. Among them, the fixed-supported beam has the smallest calculation error, while the cantilever beam has the largest. The stronger the constraint, the smaller the error in

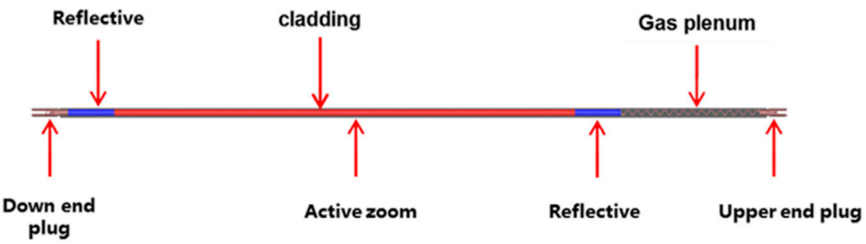

FIGURE 9
Typeical conpostion of fuel rod.

the analytical solution. First 4natural frequencies of segmented beams with different fixing methods.

Under various parameter settings, the deviation between the results obtained using the fast method and ANSYS simulation results consistently remains below 3%.

In summary, the model demonstrates accuracy in analyzing both single concentrated mass points and multi-concentrated mass points in the beam.

4 Validation of fast methods in modal analysis of fuel rod

4.1 Structural characteristics of fuel rod

The fuel rod is one of the most important components in a nuclear reactor core. Typically, a fuel rod comprises enriched cylindrical ceramic pellets, gas plenums, and a reflector located at both ends of the fuel rod. These components are sealed within a stainless-steel cladding through the upper and lower end plugs. The length of the internal structure is tailored based on the specific service environment of the fuel rod in different reactors. Figure 9 illustrates the typical structure of fuel rods in a small lead-based reactor. The fuel rod has a length of 850 mm and a diameter of 9.3 mm. The fuel element includes upper and down end plugs, upper and down reflectors, the active zone, and a gas plenum, all enclosed by cladding. The materials, lengths, and masses of each section are detailed in Table 7.

TABLE 7 Type size and mass distribution of fuel rod.

	Material	L mm	M kg
Upper end plug	316L	50	0.0207
Upper reflective	316L	50	0.0186
Active zoom	UO_2	500 mm	0.00523
Lower reflective	316L	50	0.0186
Gas plenum	316L	150	0
Lower end plug	316L	50	0.0207
cladding	316L	800	0.036

As shown in Figure 10, finite element models for two different constraint methods are established. The finite element model is divided into 17 elements, and the linear density of each element is set based on the distribution of the filling material inside the fuel rod.

The natural frequency of the fuel rod is determined using the finite rod software ANSYS. In the model analysis, filler is introduced to the beam model in the form of attached mass. The first four natural frequencies of the fuel rod are then calculated using ANSYS, and the results are presented in Table 8.

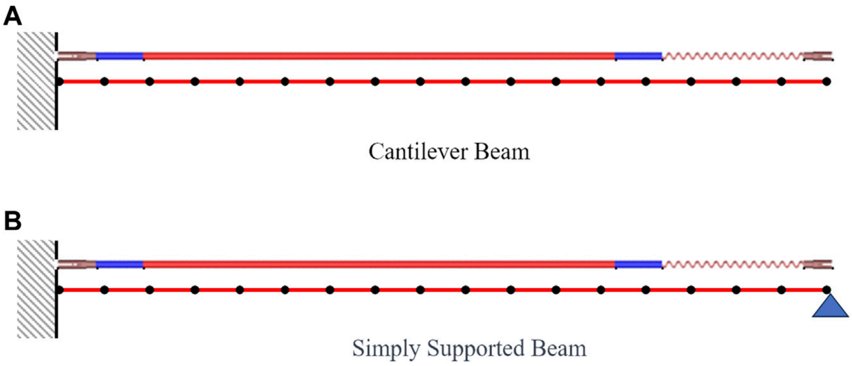

FIGURE 10
Finite element model of fuel rod.

TABLE 8 First fourth natural frequency of non-uniform fuel rod using FEA method.

n	1	2	3	4
Numerical calculation Hz	5.5653	35.514	106.89	223.91

4.2 Calculation results and analysis

To simplify the internal structure, the contents of the fuel rod are represented as concentrated mass points. This representation allows the fuel rod to be treated as a Bernoulli-Euler cantilever beam, with the concentrated mass points illustrated in Figure 11. The distribution of these concentrated mass points is based on the center-of-gravity of the internal fill.

Uniform mass distribution (Simplified Model 1): This assumes an even distribution of the filler's mass within the fuel rod in the beam model. The natural frequency is then calculated using the vibration motion of a uniform mass cantilever beam.

Three concentrated mass points (Simplified Model 2): The internal filling of the fuel rod is organized into three concentrated mass points. The upper-end plug and the gas plenum are considered one concentrated mass point, the active zoom and the reflection are another concentrated mass point, and the lower end plug and the lower reflection form the third concentrated mass point. These mass points are distributed based on the center of gravity.

Five concentrated mass points (Simplified Model 3): Organize the internal filling of the fuel rod into 5 concentrated mass points, considering the upper plug, upper reflective, active zoom, lower end plug, and lower reflective as individual concentrated mass points. These mass points are distributed based on the center of gravity.

The natural frequencies of the three simplified models are presented in Table 9. In comparison with the simplified method using a uniform mass model (Simplified Model 1), the natural frequencies calculated using the new method (Simplified Model 2 and Simplified Model 3) exhibit increased accuracy. As depicted in Figure 12, the number of mass points influences the calculation accuracy with the new method. Setting a greater number of concentrated mass points results in more accurate calculations. For a model with five concentrated mass points, the error is less than 3% when compared with the calculation results obtained using ANSYS.

Moreover, this method demonstrates a faster calculation speed than ANSYS. By utilizing five concentrated mass points, the calculations equivalent to 17 nodes in ANSYS can be efficiently performed. In addition, when there are changes in the structure of the fuel rod, this method eliminates the need for remodeling; instead, it only requires the modification of relevant parameters to complete the modal analysis.

5 The impact of fuel rod structural on natural frequencies

The traditional fixing method for lead-based reactor fuel rods often adopts a configuration where one end is clamped while the other end is simply supported. To minimize the reactor core volume, the fuel rods of small LFR are short and arranged densely. Consequently, the mounting space is small. For ease of installation in a small vessel, the fuel rod is designed with a cantilevered structure, fixed only at the upper end plug rather than employing two-end fixation. In contrast to the traditional fixing method, the natural frequency of the cantilevered structural fuel rod exhibits higher sensitivity to mass distribution.

Lead-based reactor fuel rods have high fuel consumption, requiring longer gas plenums to accommodate fission gas pressure. The gas plenum can result in non-uniform axial distribution of fuel rod mass. The length of the gas plenum is a crucial parameter in the design of fuel rods.

Four fuel rods with different structures are designed (as shown in Figure 13). Figure 13A is a traditional fuel element fixing method with one end clamped and one end simply supported, and the gas chamber is close to the clamped end. Figure 13B is a fixed method for fuel elements with one end clamped and one end simply supported, with the gas chamber located near the simply supported end. Figure 13C is a cantilever fuel rod with one end clamped and one end free, and the gas chamber is close to the clamped end. Figure 13D is a cantilever fuel rod with one end clamped and one end free, and the gas chamber is close to the free end.

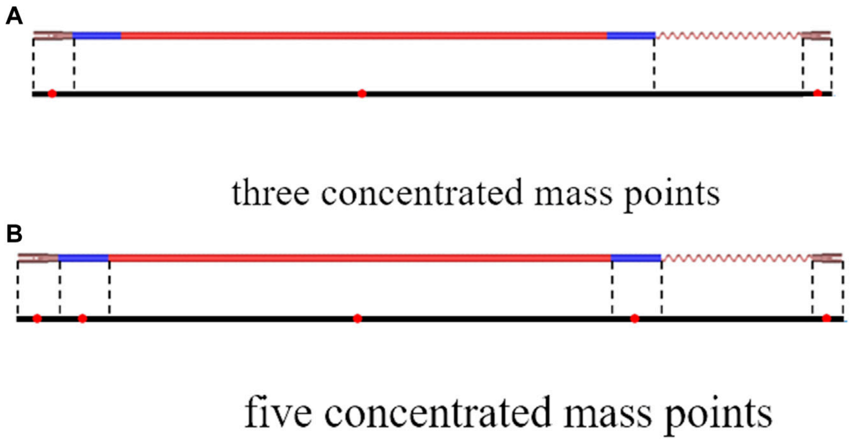

FIGURE 11
Concentrated mass model for analytical method.

TABLE 9 First fourth natural frequency of fuel rod by FEA method and analytical method.

	n	1	2	3	4
Cantilever Beam	FEA (Hz)	5.56	35.51	106.89	223.91
	Simplified model 1 (Hz)	6.28	35.38	98.14	193.54
	error %	5.5	5.2	6.2	5.7
	Simplified model 2 (Hz)	6.14	36.14	98.47	197.57
	error %	3.2	3.2	3.1	3.8
	Simplified model 3 (Hz)	6.08	36.53	102.17	199.88
	error %	2.2	2.2	2.4	2.7
Simply Supported Beam	FEA (Hz)	15.31	56.99	130.34	240.15
	Simplified model 1 (Hz)	16.02	59.55	136.59	250.71
	error %	4.7	4.5	4.8	4.4
	Simplified model 2 (Hz)	15.74	58.76	134.50	247.35
	error %	2.9	3.1	3.2	3.0
	Simplified model 3 (Hz)	15.57	57.92	132.59	244.55
	error %	1.7	1.6	1.7	1.8

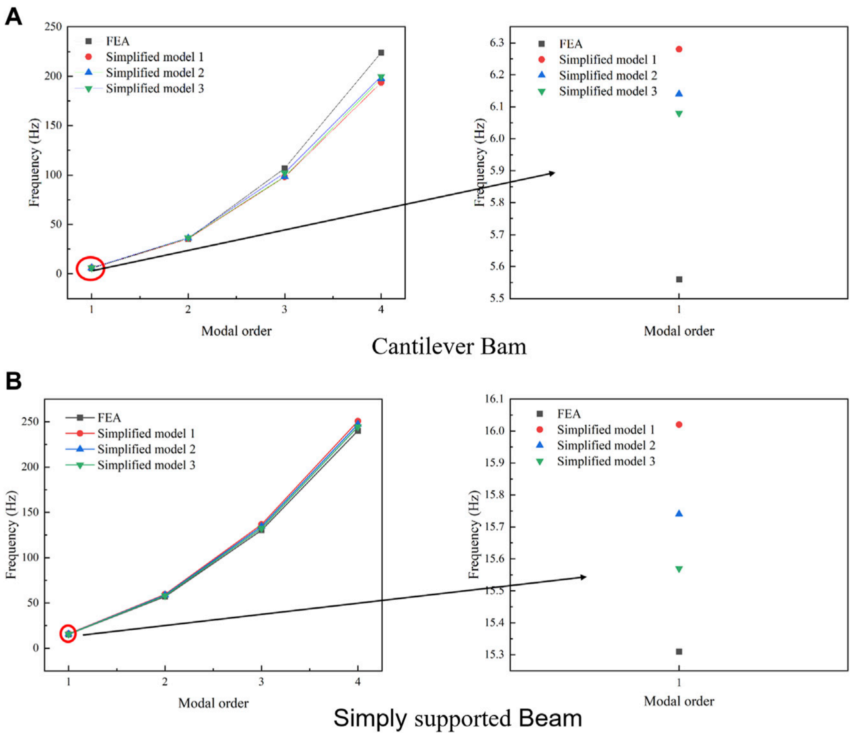

FIGURE 12
First 4 natural frequency using different calculation model.

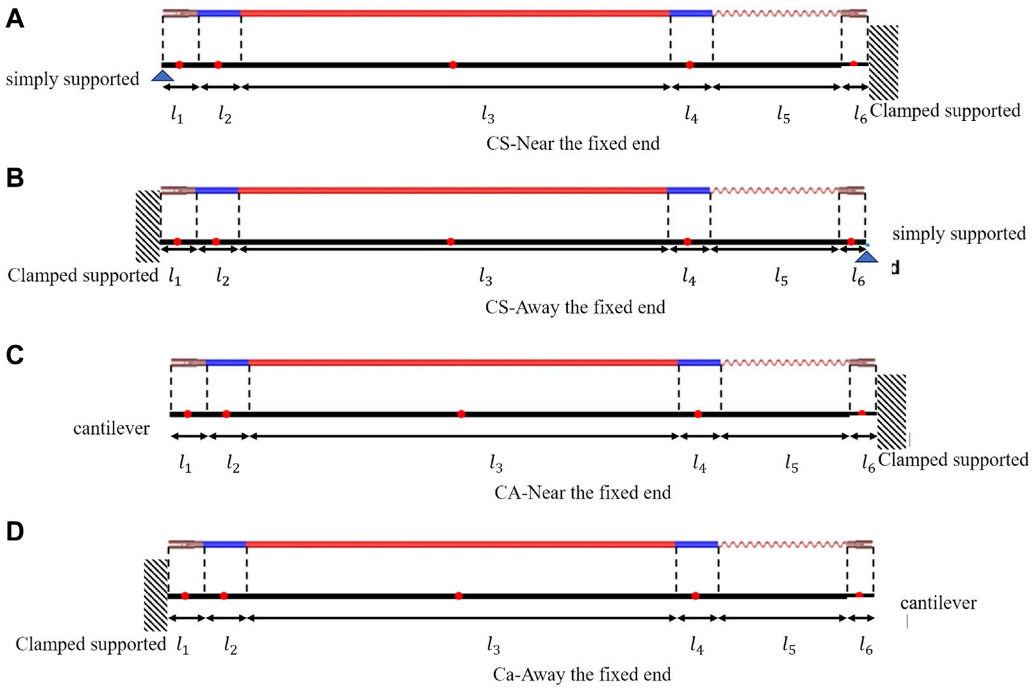

FIGURE 13
Different structural models of fuel rods.

TABLE 10 First fourth natural frequency for differential fuel rods.

	n	1	2	3	4
CS	Near the fixed end (Hz)	15.57	57.92	132.59	244.55
	Away from fixed end (Hz)	16.19	61.97	139.25	253.10
CA	Near the fixed end (Hz)	6.08	36.53	102.17	199.88
	Away from fixed end (Hz)	6.75	35.02	101.06	213.99

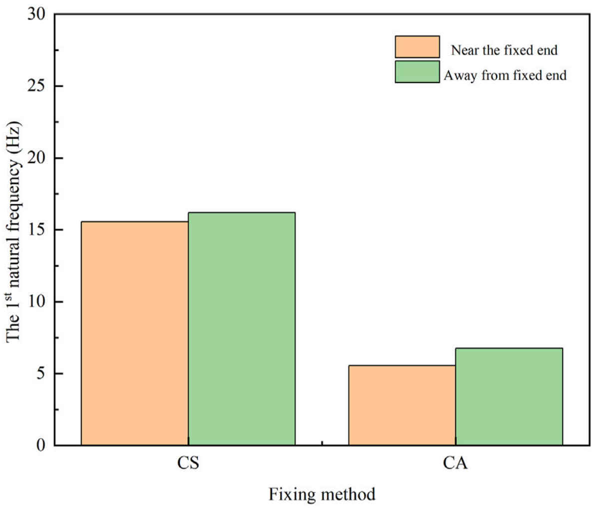

FIGURE 14
Comparison of first frequencies for different structural fuel rod models.

TABLE 11 Structural parameters of different fuel rods.

Parameter mm	Case1	Case2	Case3	Case4
Fuel rod length	800	850	900	950
Gas Plenum length	100	150	200	250
ratio	12.5%	17.6%	22.2%	26.3%

5.1 Effect of the gas plenum position on natural frequency

In general, the design lifespan for a fuel rod is typically set at 30 years. The fuel rod has a length of 850 mm and an uneven mass distribution. The weight of the gas pressurization chamber is significantly lighter than the other sections. By analyzing the position of the gas pressurization chamber and considering different constraint methods, the study investigates the impact of mass distribution on the natural frequencies of the fuel rod.

From Table 10 and Figure 14, In the case of fuel rods clamped at one end and simply supported at the other, this is the most commonly used fixing method in current reactors. Due to the asymmetric fixing method, when the gas chamber is near the simply supported end, there is a slight increase in the natural frequency of the fuel rod, with an increase of approximately 7%. This adjustment is made to reduce installation difficulty. In the case of fuel rods clamped at one end and free at the other, forming a cantilever beam structure, the sensitivity of the fuel rod to the position of the gas chamber is significant. When the gas chamber is close to the free end, there is a substantial increase in the natural frequency of the fuel rod, with a maximum increase of up to 17%.

TABLE 12 First fifth natural frequency of differential length fuel rods.

	N		1	2	3	4
CS	Near the fixed end (Hz)	Case1	17.57	65.38	149.68	276.07
		Case2	15.57	57.92	132.59	244.55
		Case3	13.88	64.93	148.64	274.16
		Case4	12.46	46.36	106.14	195.77
	Away from fixed end (Hz)	Case1	18.38	70.38	158.15	287.46
		Case2	16.19	61.97	139.25	253.10
		Case3	14.61	55.91	125.64	228.35
		Case4	13.70	52.45	117.85	214.21
CA	Near the fixed end (Hz)	Case1	6.29	39.47	115.08	237.08
		Case2	5.56	35.51	106.89	223.91
		Case3	4.76	32.31	100.37	211.65
		Case4	3.77	29.68	94.869	198.96
	Away from fixed end (Hz)	Case1	7.24	39.55	108.68	233.03
		Case2	6.75	35.02	101.06	213.99
		Case3	6.30	31.64	92.846	202.42
		Case4	5.87	28.77	87.235	187.10

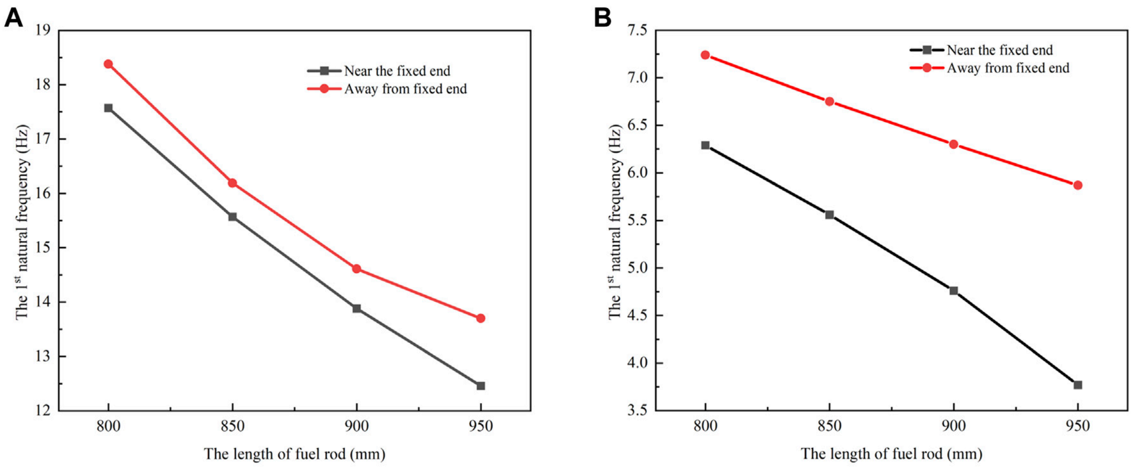

CS

CA

FIGURE 15
First natural frequency of different length fuel rods with fixed and free end.

5.2 Effect of the gas plenum length on natural frequency

As the lifespan of the fuel rod increases, it is necessary to increase the length of the gas plenum, to reduce the internal pressure of the fuel rod.

The effect of length on the natural frequency of the fuel rod is determined by varying the length of the gas plenum. The length of the gas plenum is 100mm, 150mm, 200mm, and 250 mm.Four cases with different length were established (In Table 11).

The first 4 natural frequencies for four scenarios were calculated using the fast computation model. The results are presented in Table 12 and Figure 15.

The research findings indicate a negative correlation between the natural frequency of the fuel rod and the length of the gas chamber. From Figure 15, in the case of clamped one end of the fuel rod and simply supporting the other, as the gas chamber length increases, the influence of the gas chamber position on the natural frequency gradually becomes more pronounced, especially when the gas chamber is close to the clamped end. The rate at which the natural frequency decreases with an increase in length becomes significantly more pronounced. In the scenario where one end of the fuel rod is clamped while the other end is free, this trend is even more noticeable. When the gas chamber length is near the clamped end, the decrease in the natural frequency of the fuel rod becomes more significant with an increase in the gas chamber length.

Therefore, if there is a need to increase the length of the plenum, it is recommended to place the plenum at the free end to enhance the first-order n*/atural frequency.

Compared to traditional fixing methods, the cantilever beam structure of the fuel rod exhibits a significantly lower natural frequency and higher sensitivity to mass, posing certain safety risks. However, the establishment of this fuel rod structure is designed to facilitate in-depth research for optimization.

6 Conclusion

This paper explores the vibration issues of fuel rods with non-uniform mass distribution. We introduce a simplified analytical model to solve the free vibration problem of an Euler-Bernoulli beam with non-uniform mass distribution. The results obtained from this model align well with those computed using ANSYS. Additionally, we analyze the impact of the position and length of the gas plenum on the natural frequency of the fuel rod.

The non-uniform mass distribution in the beam is treated by dividing it into several parts, with concentrated mass points serving as demarcation points. Employing Euler beam theory, the transverse vibration equation is derived for beams with varying mass distribution. Through equivalent means, the non-uniform mass beam is transformed into a multi-segment beam with concentrated mass points, establishing modal function relationships between adjacent uniform segments based on continuous conditions at connection points. The variable coefficient differential equation is then transformed into a nonlinear matrix equation.

The analytical method is validated against a benchmark beam problem, and when compared to fine Finite Element Method (FEM) calculations, it demonstrates high accuracy, approximately 5%. The natural frequency of the fuel rod calculated using the proposed method aligns well with fine FEM results. By simplifying the internal filling of the fuel rod into 5 concentrated mass points, the model's calculation differs from the finite element model by only 2%, showcasing a significant acceleration in computation speed.

The natural frequency of the fuel rod proves to be highly sensitive to the position of the gas plenum. Specifically, the fuel rod's natural frequency is higher when the gas plenum is closer to the free end compared to when it is closer to the fixed end, with a notable 17.6% difference in natural frequencies between the two configurations. As the length of the gas plenum increases, the structural stability of the fuel rod with the gas plenum close to the free end becomes more apparent.

The method proposed in this paper has been preliminarily applied to the design analysis of fuel rods and has proven to be highly useful in evaluating the vibration characteristics of fuel rods with non-uniform structural configurations.

Data availability statement

The raw data supporting the conclusion of this article will be made available by the authors, without undue reservation.

Author contributions

GY: Data curation, Formal Analysis, Writing–original draft. YZ: Methodology, Supervision, Writing–review and editing. TF: Validation, Writing–review and editing. YS: Resources, Writing–review and editing. YB: Funding acquisition, Writing–review and editing.

Funding

The author(s) declare that no financial support was received for the research, authorship, and/or publication of this article. This work was supported and funded by National Key Research and Development Plan of China with Grant Nos. 2020YFB1902102 and 2020YFB1901901.

Acknowledgments

The authors would further thank the great help from other members of FDS Consortium in this research.

Conflict of interest

Authors YZ and YB were employed by National Institute of Neutronic Energy Co., Ltd.

The remaining authors declare that the research was conducted in the absence of any commercial or financial relationships that could be construed as a potential conflict of interest.

Publisher's note

References

Auciello, N. M., and Nolè, G. (1998). VIBRATIONS OF A CANTILEVER TAPERED BEAM WITH VARYING SECTION PROPERTIES AND CARRYING A MASS AT THE FREE END. *J. Sound Vib.* 214 (1), 105–119. doi:10.1006/jsvi.1998.1538

Avdoshka, I. V., and Mikhasev, G. I. (2001). Wave packets in a thin cylindrical shell under a non-uniform axial load. *J. Appl. Math. Mech.* 65 (2), 301–309. doi:10.1016/s0021-8928(01)00034-x

Bailey, C. D. (1978). Direct analytical solutions to non-uniform beam problems. *J. Sound Vib.* 56 (4), 501–507. doi:10.1016/0022-460x(78)90292-4

Bandini, G., Meloni, P., and Polidori, M. (2011). Thermal-hydraulics analyses of ELSY lead fast reactor with open square core option. *Nucl. Eng. Des.* 241 (4), 1165–1171. doi:10.1016/j.nucengdes.2010.04.034

BanerjeeSuJackson, J. R. H. D. R. (2006). Free vibration of rotating tapered beams using the dynamic stiffness method. *J. Sound Vib.* 298 (4-5), 1034–1054. doi:10.1016/j.jsv.2006.06.040

Caruntu, D. I. (1996). *On bending vibrations of some kinds of beams of variable cross-section using orthogonal polynomials*. Singapore: Springer Nature.

Grape, S., Jacobsson, S., Hellesen, C., Jansson, P., and Åberg Lindell, M. (2014). New perspectives on nuclear power-Generation IV nuclear energy systems to strengthen nuclear non-proliferation and support nuclear disarmament. *Energy Policy* 73, 815–819. doi:10.1016/j.enpol.2014.06.026

Gupta, A. K. (1985). Vibration of tapered beams. *J. Struct. Eng.* 111 (1), 19–36. doi:10.1061/(asce)0733-9445(1985)111:1(19)

Hamid, A., Kupschus, P., Malambu, E., Benoit, P., Van Tichelen, K., Arien, B., et al. (2001). MYRRHA: a multipurpose accelerator driven system for research and development. *Nucl. Instrum. methods Phys. Res. Sect. A Accel. Spectrom. Detect. Assoc. Equip.* 463 (3), 487–494. doi:10.1016/s0168-9002(01)00164-4

Hussein, E. M. A. (2020). Emerging small modular nuclear power reactors: a critical review. *Phys. Open*, 5, 100038. doi:10.1016/j.physo.2020.100038

OECD Nuclear Energy Agency (2014). *OECD nuclear Energy agency for the generation IV international forum, Technology roadmap update for generation IV nuclear Energy systems*.

Olver, F. W. J. (1974). *Asymptotics and special functions. Introduction to asymptotics and special functions*.

Ö, Ö., and Kaya, M. (2006). Flapwise bending vibration analysis of a rotating tapered cantilever Bernoulli–Euler beam by differential transform method. *J. Sound Vib.* 289, 413–420. doi:10.1016/j.jsv.2005.01.055

Orlov, V. V., Filin, A. I., Lopatkin, A. V., Glazov, A., Sukhanov, L., Volk, V., et al. (2005). The closed on-site fuel cycle of the BREST reactors. *Prog. Nucl. Energy* 47 (1-4), 171–177. doi:10.1016/j.pnucene.2005.05.017

Ramesh, M. N. V., and Rao, N. M. (2013). Free vibration analysis of pre-twisted rotating FGM beams. *Int. J. Mech. Mater. Des.* 9 (4), 367–383. doi:10.1007/s10999-013-9226-x

Roberto, P., Andrea, B., Antonio, C., Lorenzi, S., and Luzzi, L. (2014). Object-oriented modelling and simulation for the ALFRED dynamics. *Prog. Nucl. Energy* 71, 15–29. doi:10.1016/j.pnucene.2013.10.013

Rosa, M. A. D., and Auciello, N. M. (1996). Free vibrations of tapered beams with flexible ends. *Comput. Struct.* 60 (2), 197–202. doi:10.1016/0045-7949(95)00397-5

Spigler, R., and Vianello, M. (2007). Liouville–Green asymptotic approximation for a class of matrix differential equations and semi-discretized partial differential equations. *J. Math. Analysis Appl.* 325 (1), 69–89. doi:10.1016/j.jmaa.2006.01.050

Takahashi, M., and Sekimoto, H. (2007). OS8-6 status and prospect of development of lead-alloy-cooled fast reactor. *Jpn. Soc. Mech. Eng.* 2007.12, 201–204. doi:10.1299/jsmepes.2007.12.201

Wang, M., Lian, C., Li, Y., Wang, Y., Jiang, J., and Wu, Y. C. (2015). Preliminary conceptual design of a lead–bismuth cooled small reactor (CLEAR-SR). *Int. J. Hydrogen Energy* 40, 15132–15136. doi:10.1016/j.ijhydene.2015.03.097

Wu, Y. C. (2016a). Design and R&D progress of China lead-based reactor for ADS research facility. *Engineering* 2 (1), 124–131. doi:10.1016/j.eng.2016.01.023

Wu, Y. C. (2016b). CLEAR-S: an integrated non-nuclear test facility for China lead-based research reactor. *Int. J. Energy Res.* 40 (14), 1951–1956. doi:10.1002/er.3569

Wu, Y. C., Bai, Y. Q., Song, Y., Huang, Q., Zhao, Z., and Hu, L. (2016). Development strategy and conceptual design of China lead-based research reactor. *Ann. Nucl. Energy* 87, 511–516. doi:10.1016/j.anucene.2015.08.015

Zrodnikov, A. V., Toshinsky, G. I., Komlev, O. G., Stepanov, V., and Klimov, N. (2011). SVBR-100 module-type fast reactor of the IV generation for regional power industry. *J. Nucl. Mater.* 415 (3), 237–244. doi:10.1016/j.jnucmat.2011.04.038

frontiers | Frontiers in Energy Research

TYPE Original Research
PUBLISHED 28 March 2024
DOI 10.3389/fenrg.2024.1379747

OPEN ACCESS

EDITED BY
Shichang Liu,
North China Electric Power University, China

REVIEWED BY
Jie Li,
Sun Yat-sen University, China
Chenglong Wang,
Xi'an Jiaotong University, China
Xiang Chai,
Shanghai Jiao Tong University, China

*CORRESPONDENCE
PengCheng Zhao,
✉ pengcheng.zhao@usc.edu.cn

RECEIVED 31 January 2024
ACCEPTED 14 March 2024
PUBLISHED 28 March 2024

CITATION
Qi J, Ai Q, Zhao P, Yang J and Wang G (2024), Design and optimization analysis of a new double-layer tube type heat exchanger for lead-bismuth reactors.
Front. Energy Res. 12:1379747.
doi: 10.3389/fenrg.2024.1379747

Design and optimization analysis of a new double-layer tube type heat exchanger for lead-bismuth reactors

JingWen Qi[1,2], QingSong Ai[1,2], PengCheng Zhao[1,2]*, Junkang Yang[1] and GuiMei Wang[3]

[1]School of Nuclear Science and Technology, University of South China, Hengyang, Hunan, China, [2]Key Lab of Advanced Nuclear Energy Design and Safety, Ministry of Education, Hengyang, Hunan, China, [3]China Nuclear Industry Huawei Engineering Design and Research Co., Ltd, Nanjing, Jiangsu, China

Double-layer heat tubes have been designed to effectively reduce the occurrence of heat pipe rupture accidents. However, inter-tube thermal contact resistance can decrease heat transfer efficiency, thus hampering the heat dissipation in the primary loop system of lead-bismuth reactors. Therefore, optimizing the design of double-layer heat tubes is necessary. This work focuses on the double-layer heat exchanger of a lead-bismuth reactor and utilizes gallium-based graphene nanofluids as a thermal interface material to fill the gap between the heat tubes. Furthermore, the impact of the length, wall thickness, outer diameter, and spacing of heat tubes on the heat transfer performance of the double-layer heat exchanger with and without the nanofluids has been analyzed. The study aims to optimize the JF factor and cost-effectiveness ratio (CER). Genetic algorithms are employed to optimize and evaluate the heat transfer performance of the main heat exchanger based on the four aforementioned parameters. Consequently, a new design scheme is obtained for the double-layer heat exchanger, which increases the optimized overall heat transfer coefficient of the main heat exchanger by 5.79%, pressure drop in the primary loop by 2.32%, JF factor by 5%, and CER by 24.62%. These results demonstrate that the gallium-based graphene nanofluids can effectively enhance the heat transfer performance of the double-layer heat exchanger while reducing the likelihood of steam generator tube rupture accidents.

KEYWORDS

gallium-based graphene nanofluids, thermal interface material, double-layer heat exchanger tube, lead-bismuth reactor, optimized design

1 Introduction

Lead-bismuth reactors have garnered considerable attention due to their favorable neutron kinetics, thermal-hydraulics, and safety characteristics. According to the Generation IV International Forum (GIF), these reactors are poised to be the first commercially viable Generation IV reactors (Alemberti et al., 2014). The main heat exchanger plays a critical role in heat transport within lead-bismuth reactors, thus significantly impacting their economic viability and safety. However, their operating environment is harsh and characterized by high temperatures, substantial pressure differentials, high density, and rapid corrosion rates. Consequently, the heat exchange tubes in the main heat exchanger tend to be the weakest point in the primary loop system of lead-bismuth reactors. Thus, developing new heat exchange tubes that can exhibit superior heat transfer performance and exceptional reliability is necessary to mitigate the relatively high probability of failures, such as heat exchanger tube rupture and corrosion-induced flow blockage (Iskhakov et al., 2018). Closely bonded double-layer heat tube structures offer distinct advantages when applied to lead-bismuth reactors; for example, they prevent continuous crack propagation in the event of a rupture. Unlike single-layer tubes, cracks in double-layer heat tubes terminate at the interface between the two layers. Consequently, double-layer heat tubes can significantly reduce the likelihood of heat tube failure accidents (Jeltsov et al., 2018), making them an appealing design choice. However, the inter-tube thermal contact resistance decreases heat transfer efficiency, which is detrimental to the smooth dissipation of heat within the primary loop system of lead-bismuth reactors. Therefore, there is an imperative need to optimize heat tube design, mitigate inter-tube thermal contact resistance, and enhance heat transfer efficiency.

To effectively enhance the heat transfer performance of double-layer heat exchangers in lead-bismuth reactors, researchers from different countries have performed extensive exploratory studies and provided valuable insights. Guimei (WANG, 2014) investigated the impact of inter-tube thermal contact resistance on the heat transfer performance of a heat exchanger based on factors such as wall temperature difference, materials, tolerance fit, and surface roughness while proposing optimized fabrication schemes for double-layer tubes. Rozzia et al. (Rozzia et al., 2015) performed experimental research to investigate the impact of filling the gap between double-layer tubes with the AISI-316 powder on the heat transfer performance of the main heat exchanger. Meanwhile, Liu et al. (Liu et al., 2018) discovered that adding diamond powder inside double-layer tubes yielded superior heat transfer performance compared to that obtained by adding the 316L powder. The existing research has primarily concentrated on enhancing the heat transfer performance of heat exchangers in double-layer tubes by utilizing solid metal powders as fillers between the layers. However, the increase in heat transfer efficiency has been limited, thus significantly restricting the widespread application of double-layer heat exchangers in lead-bismuth reactors. Xiaohong et al. (Wang et al., 2021) proposed that by blending high-thermal-conductivity nanoparticles with ambient liquid metals such as gallium, rubidium, cesium, and mercury, high-performance metal thermal interface materials can be obtained, which tend to significantly reduce the thermal conductivity resistance between adjacent contacting objects and have broad application prospects in the design of double-layer tube-type heat exchangers for lead-bismuth reactors.

Gallium has stable chemical properties and can remain in liquid form under atmospheric pressure within the temperature range of 29.8°C–2,403°C. It also boasts high thermal conductivity, electrical conductivity, good fluidity, and a certain level of corrosion resistance. Importantly, it is non-toxic, making its use safer and more reliable. Therefore, it is considered an ideal liquid metal matrix material (Zhang et al., 2023). Nanoparticles are key to achieving excellent thermomechanical performance in nanofluids. Compared to other added nanoparticles, graphene is a two-dimensional layered structure material with high thermal conductivity, consisting of a single layer of carbon atoms arranged in a hexagonal lattice. As one of the best-known thermal conductive materials, it exhibits outstanding electrical, thermal, and mechanical properties (Kuang and Hu, 2013). Combining nanoscale graphene sheets with gallium particles results in nanofluids with a larger specific surface area, increasing the heat transfer interface, and thereby enhancing heat transfer efficiency. The stable properties of metallic gallium, along with its corrosion resistance, endow gallium-based graphene nanofluids with good stability, making them less prone to sedimentation or aggregation, which is beneficial for long-term stable thermal management.

This work focuses on improving the heat transfer performance associated with the main heat exchanger of a double-layer heat tube used in a lead-bismuth reactor. The gap between the double-layer heat tubes is filled with gallium-based graphene nanofluids, which serve as a thermal interface material. To assess the impact of this modification, the influence of heat tube length, wall thickness, outer diameter, and spacing on the heat transfer performance of the double-layer heat exchanger with and without the gallium-based graphene nanofluids filling is analyzed. This study aims to optimize the JF factor and cost-effectiveness ratio (CER). By utilizing a genetic algorithm, the four aforementioned parameters have been considered as optimization variables to evaluate and optimize the heat transfer performance of the main heat exchanger. Consequently, a new design scheme is obtained for the double-layer heat exchanger used in lead-bismuth reactors.

2 Theoretical model of the main heat exchanger

Currently, lead-bismuth reactors in several countries have entered the engineering and construction phase. The secondary loop of these reactors utilizes water and employs either flow boiling heat transfer or high-pressure single-phase heat transfer. This work primarily aims to explore the use of gallium-based graphene nanofluids as a thermal interface material, which can fill the gap between double-layer heat tubes. The study also involves the design and optimization of the proposed double-layer heat exchanger. To simplify the computational process, it is considered that the secondary loop in the main heat exchanger implements high-pressure single-phase heat transfer.

2.1 Heat transfer calculation of the double-layer heat exchange tube

Based on the heat balance, the coolant flow on both sides of the heat exchange tube is countercurrent; thus, the heat transfer relationship is as follows:

$$Q = K \cdot A \cdot \Delta t_m \tag{1}$$

Where Q is the heat exchange power of the main heat exchanger $[W]$, K is the total heat transfer coefficient for the outer surface of the heat exchange tube $[W/(m^2 \cdot K)]$, A is the total heat transfer area for the outer surface of the heat exchange tube $[m^2]$, and Δt_m is the countercurrent logarithmic mean temperature difference [°C].

The total heat transfer coefficient K is calculated as follows:

$$K = \frac{1}{\frac{1}{h_1} \cdot \frac{d_4}{d_1} + \frac{d_4}{2\lambda_1} \ln \frac{d_2}{d_1} + \frac{d_4}{2\lambda_0} \ln \frac{d_3}{d_2} + \frac{d_4}{2\lambda_1} \ln \frac{d_4}{d_3} + \frac{1}{h_2} + R_F} \tag{2}$$

$$h_1 = \frac{q'_{(1)}}{\pi d_4 \left(T_{d_4} - T_{1(f)} \right)} \tag{3}$$

$$h_2 = \frac{q'_{(2)}}{\pi d_1 \left(T_{d1} - T_{2(f)} \right)} \tag{4}$$

Where h_1 and h_2 are the convective heat transfer coefficients on the lead-bismuth alloy and pressurized water side, respectively $[W/(m^2 \cdot K)]$; d_1, d_2, d_3, and d_4 represent the inner diameter of the inner tube, the outer diameter of the inner tube, the inner diameter of the outer tube, and outer diameter of the outer tube, respectively $[m]$; λ_0 and λ_1 are the inter-tube thermal conductivity and tube-wall thermal conductivity, respectively, $[W/(m \cdot K)]$; R_F is the fouling resistance $[(m^2 \cdot K)/W]$; $q'_{(1)}$ and $q'_{(2)}$ are the linear power density of the outer wall of the outer tube d_4 and the inner wall of the inner tube d_1 $[W/m]$; T_{d_4}, T_{d_1}, $T_{1(f)}$ and $T_{2(f)}$ represent the temperature of the outer wall of the outer tube, the inner wall of the inner tube, the lead-bismuth alloy and pressurized water [°C].

The heat flow transfer within the heat tube bundle, which contains liquid lead-bismuth, bears similarities to the flow heat transfer occurring within the fuel rods of the reactor core. Consequently, the heat transfer occurring on the shell side of the heat tube is computed using the flow heat transfer correlation proposed by Cheng et al. (Cheng and Tak, 2006) from the Karlsruhe Institute of Technology (KIT) in Germany; this correlation considers the heat transfer between the liquid heavy metal and the fuel rods.

For calculating the heat transfer coefficient in the fluid flow inside a circular channel under forced convection, the Dittus-Boelter correlation is employed.

2.2 Pressure drop calculation of the double-layer heat exchange tube

Since liquid coolants are considered incompressible fluids, their density can be considered to be the same at each point in the flow field. Since the coolant on both sides of the heat exchange tubes in the main heat exchanger does not undergo phase change during the flow process, the Darcy formula has been used to calculate the pressure drop along the single-phase flow:

$$\Delta P_f = f \frac{L}{d} \frac{\rho v^2}{2} \tag{5}$$

$$\frac{1}{\sqrt{f}} = -2 \log \left(\frac{\varepsilon}{3.7d} + \frac{2.51}{\mathrm{Re}\sqrt{f}} \right), \quad 2300 < \mathrm{Re} \leq 10^5 \tag{6}$$

Where ΔP_f is the frictional pressure drop $[Pa]$, L is the length of the flow channel $[m]$, ρ is the fluid density $[kg/m^3]$, d is the hydraulic diameter of the flow channel $[m]$, A is the cross-sectional area of the fluid $[m^2]$, v is the fluid velocity $[m/s]$, the calculation of frictional resistance coefficient f is based on the Colebrook equation, Re is Reynolds number of the fluid, ε is the absolute roughness of the tube.

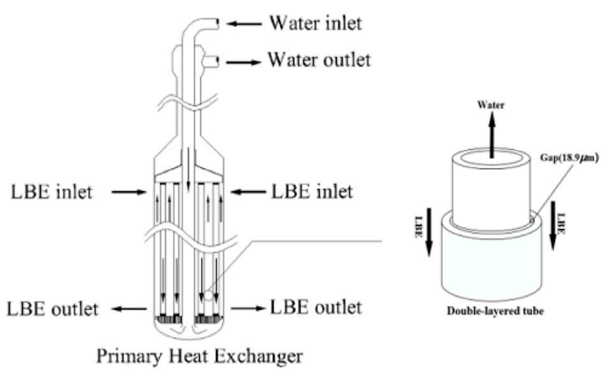

FIGURE 1
Schematic of the heat exchanger.

Owing to the sudden change in the cross-section of the flow channel at the inlet and outlet of the heat exchanger tube as well as at the inlet and outlet windows of the lead-bismuth reactor, a local pressure drop occurs, which can be calculated as follows:

$$\Delta P_{form} = k \frac{\rho v^2}{2} \tag{7}$$

Where ΔP_{form} is the form-resistance pressure drop $[Pa]$, and k is the form-resistance pressure drop coefficient, taking 0.7 (Yu et al., 2002).

2.3 JF factor

To optimize the design of the main heat exchanger, it is desirable to obtain the best results at the least cost and ensure that the heat exchanger tube does not undergo breakage; this can be achieved by designing a main heat exchanger with the highest possible heat transfer efficiency and the lowest possible shell process pressure drop. The JF factor compares the heat transfer performance of the main heat exchanger with 1/3rd power of the pressure drop; the larger the JF factor, the better the overall performance of the main heat exchanger. Therefore, this study utilizes the JF factor as the evaluation index:

$$JF = \frac{K/K_o}{(\Delta P/\Delta P_o)^{1/3}} \tag{8}$$

$$\Delta P = \Delta P_{outlet} - \Delta P_{inlet} \tag{9}$$

Where K is the overall heat transfer coefficient $[W/(m^2 \cdot K)]$ and ΔP is the pressure loss $[Pa]$; the subscript o indicates the calculation reference value; ΔP_{inlet} and ΔP_{outlet} are the inlet and outlet of the shell-side pressure drop $[Pa]$.

2.4 Cost-effectiveness ratio

The JF factor is used as an evaluation criterion only for the performance of the main heat exchanger; however, it does not consider the actual engineering construction costs. Therefore, CER has been used to practically optimize the structural parameters of the main heat exchanger:

TABLE 1 Parameters of the main heat exchanger during steady-state operation.

Thermal hydraulic parameters	Values
Design thermal power/MW	3
Pressurized water mass flow/kg·s-1	40.21
Lead-bismuth mass flow/kg·s-1	158.844
Pressurized water inlet and outlet temperature/°C	215/230
Liquid lead-bismuth inlet and outlet temperature/°C	390/260

Based on these parameters, the preliminary design parameters of the main heat exchanger are determined and shown in Table 2.

TABLE 2 Preliminary design parameters of the main heat exchanger.

Parameter	L/m	d4/mm	c/mm	P/mm
Initial value	2.985	26	4	32

$$CER = \frac{JF}{C} \tag{10}$$

$$C = \frac{M_t P_t + M_s P_s}{M_s P_s} = \frac{V_t + V_s}{V_s} \tag{11}$$

Where C is the average cost ratio per unit heat exchange area for the main heat exchanger; M and P represent the mass $[kg]$ and material costs, respectively; V denotes the volume $[m^3]$; and subscripts t and s denote the heat exchanger tube and shell, respectively. Since the main heat exchanger structure used in this study is all made of 316L stainless steel, C can be expressed as the volume ratio.

2.5 Physical property model

The physical property models used in this work include the liquid lead-bismuth alloy, pressurized water, heat exchange tubes, and gallium-based graphene nanofluids. The main physical parameters of the liquid lead-bismuth alloy and pressurized water have been sourced from Fazio et al. (Fazio et al., 2015) and Wagner et al. (Wagner and Kretzschmar, 2008), respectively. Since the heat exchange tube is made of 316L stainless steel, the physical parameters of stainless steel data are used (Kim, 1975). Meanwhile, the physical properties of gallium-based graphene nanofluids are sourced from Xuan et al. (Xuan et al., 2003).

3 Research on the factors affecting the performance of the main heat exchanger

This study focuses on the main heat exchanger of China LEAd-based Reactor (CLEAR-I) (Wu et al., 2015). The flow direction of the coolant on the primary and secondary sides of the main heat exchanger is shown in Figure 1. The main heat exchanger has a tube-shell structure and comprises straight double-layered heat tubes arranged in a triangular pattern. The gap between the tubes is filled with the gallium-based graphene nanofluids.

The parameters of the main heat exchanger during steady-state operation are shown in Table 1.

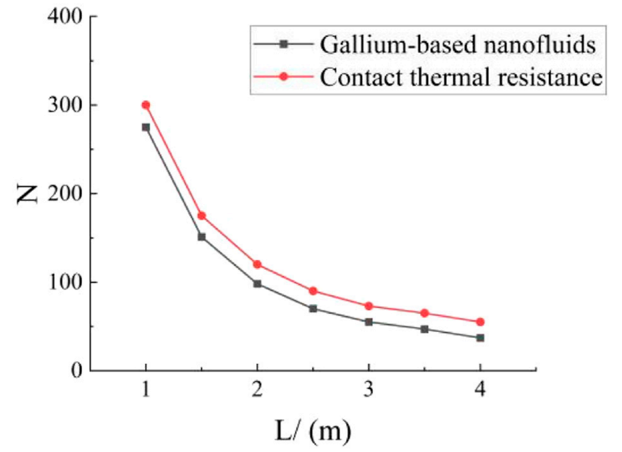

FIGURE 2
Variation in the number of heat exchange tubes with the length.

The arithmetic mean deviation Ra of the heat exchanger tube surface profile is taken as 6.3 μm and the double-layer tube gap is considered as 3 Ra. The gallium-based graphene nanofluids exhibit a graphene nanoparticle volume fraction of 20% and a particle radius of 20 nm. The average contact thermal resistance of the double-layer tube without nanofluids filling is 0.00003 $(m^2 \cdot K)/W$ (WANG, 2014). The effect that the length L, outer diameter d_4, wall thickness c, and tube spacing P of the heat exchanger have on the total heat transfer coefficient K and the pressure drop loss ΔP is determined for the main heat exchanger with and without the addition of the gallium-based graphene nanofluids.

3.1 Length of the heat exchange tube

The length of the heat exchanger tube L is based on the initial value shown in Table 2 and several typical lengths are selected: 1, 1.5, 2, 2.5, 3, 3.5, and 4 m. The remaining parameters shown in Table 2 are used to investigate the effect of the heat exchanger tube length on the performance of the two main heat exchangers.

Figure 2 shows that as the length L increases, the heat transfer area of a single heat exchanger tube also increases; however, the total heat transfer remains the same. Thus, the number of heat exchanger tubes N decreases non-linearly for both the main heat exchangers. Nevertheless, since the gallium-based graphene nanofluids have

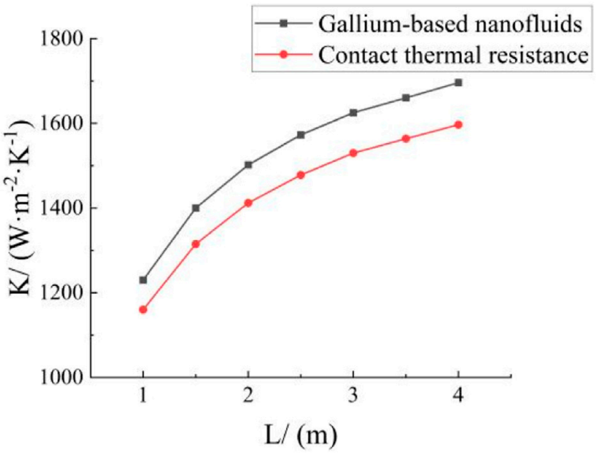

FIGURE 3
Variation in the total heat transfer coefficient with the length.

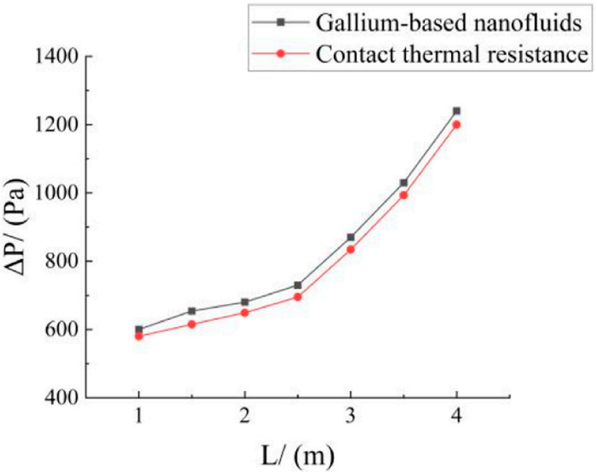

FIGURE 4
Effect of heat exchange tube length on shell-side pressure drop.

high thermal conductivity, the main heat exchanger with gallium-based graphene nanofluids requires fewer heat exchanger tubes N for total heat transfer and is more economical.

Figure 3 shows that the total heat transfer coefficient K increases with a rise in the heat exchanger tube length L. When L increases, the number of heat exchanger tubes decreases along with the coolant flow cross section. This increases flow velocity, turbulence intensity, and thermal conductivity; hence, K increases. However, as the nanofluids have higher thermal conductivity, the total heat transfer coefficient K of the double-layer heat exchanger tube with the nanofluids tends to be greater, which leads to a better heat transfer performance. Figures 4, 5 show that increasing the length L of the heat exchanger tube increases the frictional pressure drop as well as the pressure drop observed in both the shell and tube coolant, thereby increasing the operating cost. For the same case, the pressure drop in the shell and tube coolant of the main heat exchanger with gallium-based graphene nanofluids is greater and the required operating cost is higher.

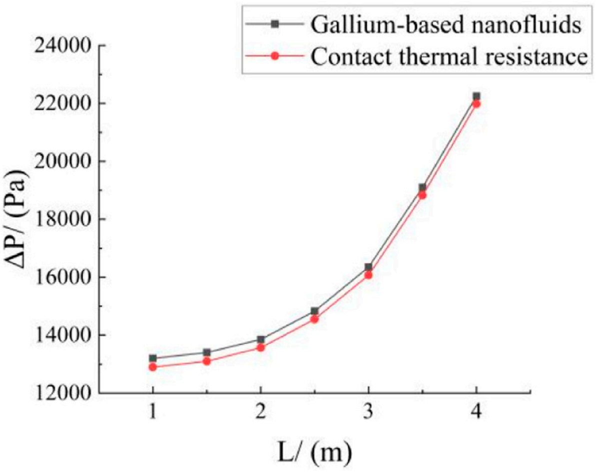

FIGURE 5
Effect of heat exchange tube length on tube-side pressure drop.

Figure 6 shows that when the secondary coolant flow rate remains the same, the JF factor decreases with increasing L. Under the same conditions, the JF factor of the double-layer heat exchanger tube with the nanofluids always exceeds that of the double-layer heat exchanger tube without the nanofluids. This result is mainly observed because K and shell pressure drop rise as L increases; however, the increase in shell pressure drop in the main heat exchanger is less than the increase in K. The total heat transfer coefficient of the double-layer heat exchanger tube with the nanofluids undergoes a larger increase when compared to that of the unmodified heat exchanger tube.

3.2 Outer diameter and inner/outer diameter ratio of the heat exchange tube

The inner diameter d_1 and the outer diameter d_4 are based on the initial value in Table 2 and several typical heat exchanger tube outer diameters have been selected: 15, 20, 25, 30, and 35 mm, and the increase of the outer diameter leads to the increase of the inner/outer diameter ratio. The remaining parameters shown in Table 2 are used to investigate the effect of the outer diameter and the inner/outer diameter ratio of the heat exchanger tube on the exchanger performance.

Figures 7, 8 show that when the rest of the structural parameters of the heat exchanger bundle remain unchanged, increasing the outer diameter d_4 and the inner/outer diameter ratio d_1/d_4 reduce the heat transfer capacity due to a rise in the heat exchanger tube cross-section, a decrease in the flow velocity of the tube course coolant, and a decrease in the turbulence intensity. A reduction in the circulation cross-section and an increase in the flow velocity of the first circuit increases the heat transfer capacity; however, this effect is more pronounced in the second circuit. Thus, K decreases almost linearly. The total heat transfer coefficient of the heat exchanger tube comprising the interstitially filled gallium-based graphene nanofluids is consistently higher than that of the unmodified heat exchanger tube, owing to the better thermal conductivity of the nano-liquid metal.

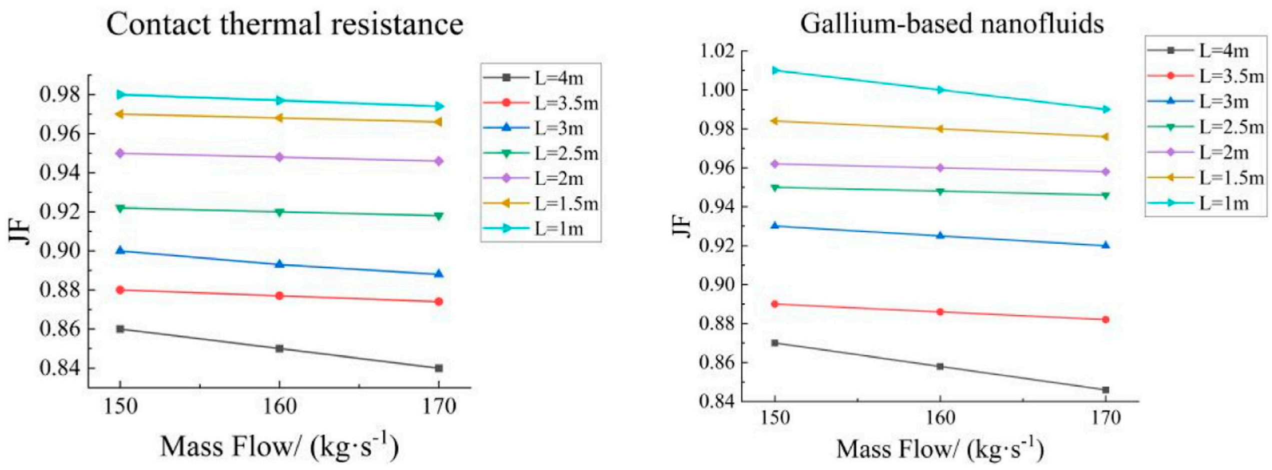

FIGURE 6
Effect of heat exchange tube length on JF factor.

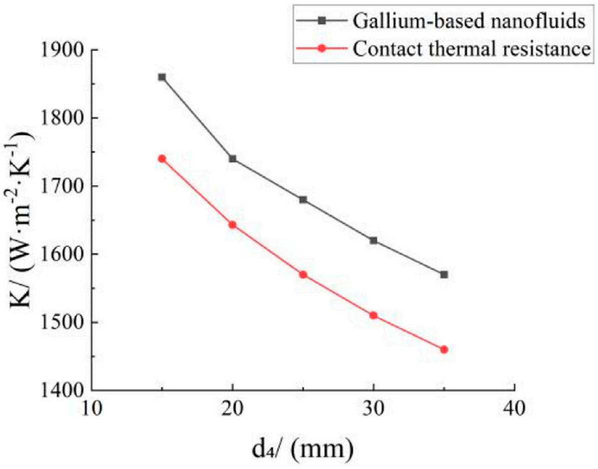

FIGURE 7
Variation in the total heat transfer coefficient with outer diameter.

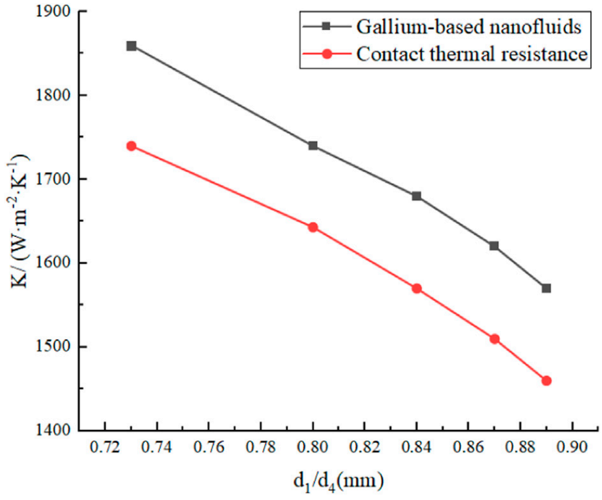

FIGURE 8
Variation in the total heat transfer coefficient with inner/outer diameter ratio.

Figures 9–12 show that augmenting the outer diameter d_4 and the inner/outer diameter ratio d_1/d_4 can increase the shell pressure drop and decrease the tube pressure drop; this is because when all other parameters are held constant and d_4 and d_1/d_4 increase, the flow cross-section in the first and second circuit decreases and increases, respectively, while the flow velocity decreases. Thus, the shell pressure drop increases, and the tube pressure drop decreases. However, the shell pressure drop in the heat exchanger tube filled with nanofluids tends to be higher than that in the unfilled heat exchanger tube under the same circumstances, and the same result is observed for the tube pressure drop. The heat exchanger tube comprising the nanofluids is less likely to exhibit natural circulation in its first circuit while being more costly to operate than a normal double-layer heat exchanger tube.

Figure 13 shows that at a constant secondary coolant flow rate, the JF factor decreases with increasing d_4. However, the JF factor of the heat exchanger tube comprising the gallium-based graphene nanofluids is always greater than that of the heat exchanger tube with no nanofluids under the same circumstances. This is mainly because as d_4 increases, the shell pressure drop increases, K decreases, and the JF factor decreases. The shell pressure drop and K of the tube filled with the nanofluids are both greater than those of the double-layer heat exchanger tube; however, the increase in K is greater than one-third of the increased shell pressure drop.

3.3 Wall thickness of the heat exchange tube

Several typical heat exchanger tubes with wall thicknesses of 3, 3.5, 4, 4.5, and 5 mm are used in this study, and the remaining parameters are shown in Table 2. As the outer diameter and tube spacing of the heat exchanger remain the same, the coolant flow

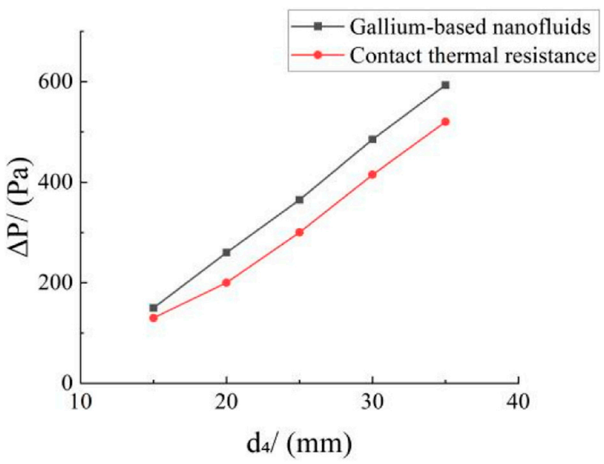

FIGURE 9
Effect of the outer diameter of the heat exchange tube on shell-side pressure drop.

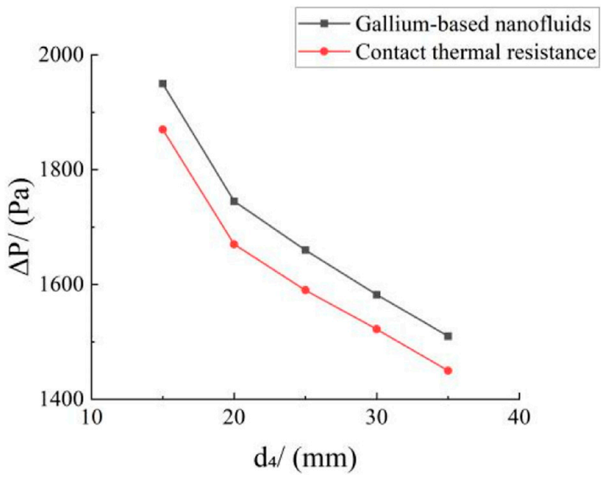

FIGURE 10
Effect of the outer diameter of the heat exchange tube on tube-side pressure drop.

cross section in a single circuit also remains constant; therefore, the shell pressure drop does not change much. These conditions allowed us to effectively study the influence of the wall thickness of the heat exchanger tube on the total heat transfer coefficient and the pressure drop in the tube for both main heat exchangers.

Figures 14, 15 show the variations in the total heat transfer coefficient and the pressure drop that occur across the tube due to a change in the wall thickness of the main heat exchanger. Figures 14, 15 show that as *c* increases, *K* decreases and the pressure drop across the tube increases; however, the *K* and pressure drop for the tube filled with the nanofluids tends to be higher than that observed for a normal double-layer heat exchanger under the same conditions. Overall, although the proposed double-layer heat exchanger tube is costlier than its conventional counterparts, its heat transfer performance is better.

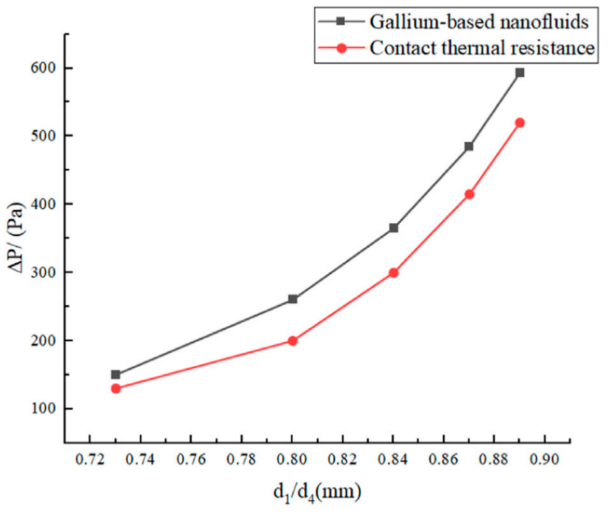

FIGURE 11
Effect of the inner/outer diameter ratio of the heat exchange tube on shell-side pressure drop.

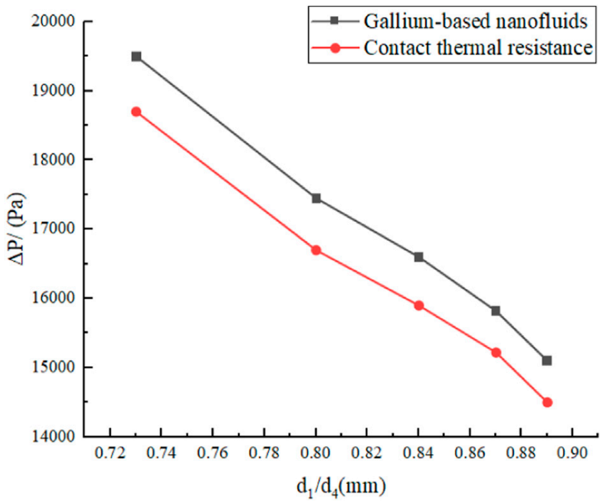

FIGURE 12
Effect of the inner/outer diameter ratio of the heat exchange tube on tube-side pressure drop.

Figure 16 shows the effect that the heat exchanger tube wall thickness has on the JF factor: when the outer diameter of the heat exchanger tube remains constant, *c* increases and JF factor decreases; this is mainly because *c* increases, *K* decreases, and the shell pressure drop remains constant, which decreases the JF factor.

3.4 Spacing of the heat exchanger tubes

Tube spacing has a greater impact on the shell pressure drop than on the tube pressure drop; thus, this work studies the effect of tube spacing on the shell pressure drop of the two heat exchangers.

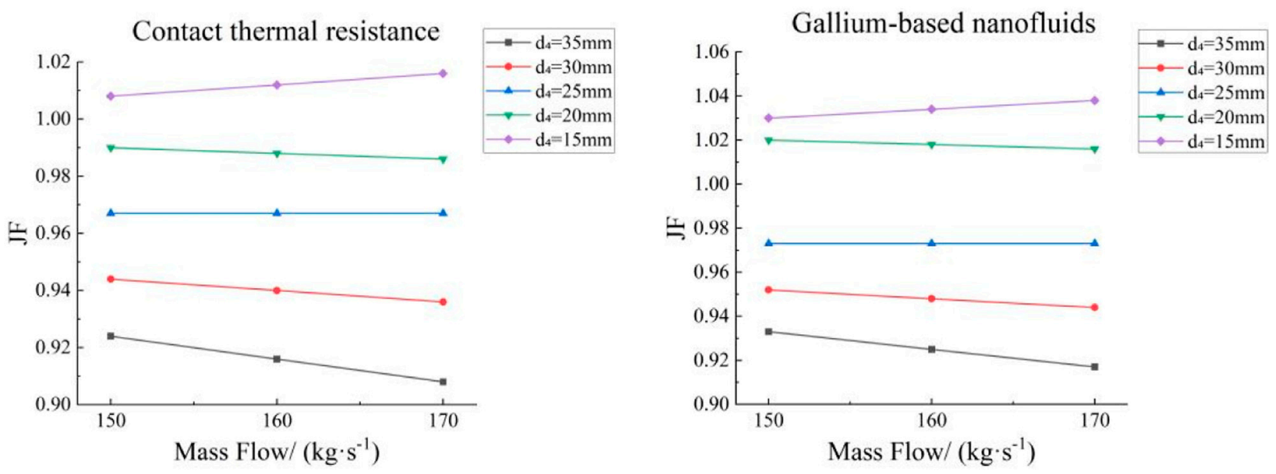

FIGURE 13
Effect of the outer diameter of heat exchanger tube on JF factor.

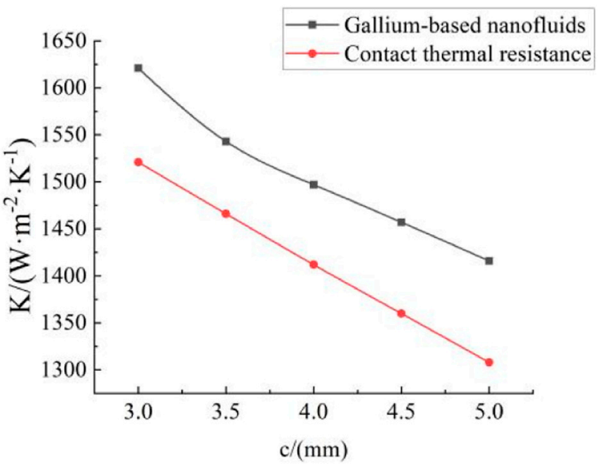

FIGURE 14
Variation in total heat transfer coefficient with wall thickness.

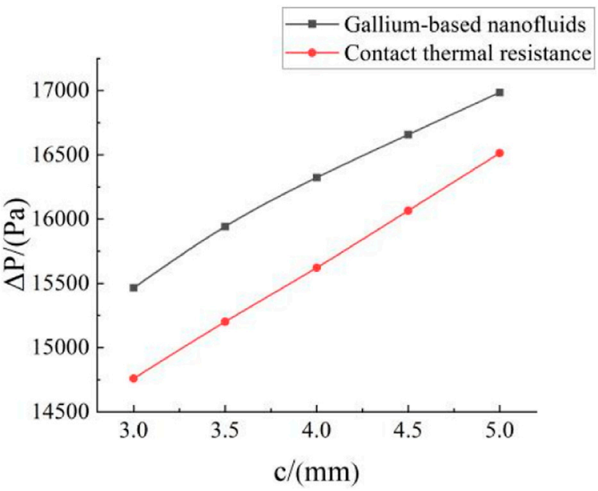

FIGURE 15
Effect of heat exchanger tube wall thickness on tube-side pressure drop.

The following heat exchanger tube spacings have been used in this study: 32, 34, 36, 38, 40, 42, 44, and 50 mm; the remaining parameters are shown in Table 2.

The effect of heat exchanger tube spacing on shell pressure drop and JF factor is shown in Figures 17, 18, respectively. Figure 17 shows that the shell pressure drop decreases non-linearly with increasing heat exchanger tube spacing *P*. However, the shell pressure drop in the heat exchanger tube filled with the nanofluids tends to be higher than that in the double-layer heat exchanger tube without any nanofluids under the same circumstances, which is not conducive to natural circulation in one circuit. Figure 18 shows that the JF factor decreases with an increase in the tube spacing *P*, which shows that *P* has a relatively small effect on the heat exchanger performance.

In summary, for the same structural parameters, the JF factor of the heat exchanger tube with the nanofluids tends to be greater than that of the tube without any nanofluids, thereby ensuring that the main heat exchanger exhibits the best results at lower costs without causing any tube ruptures. Therefore, the geometry of the heat exchanger tube interstitially filled with the gallium-based graphene nanofluids has been optimized in the next section.

4 Optimization of the main heat exchanger size

4.1 Genetic algorithm

A genetic algorithm is an adaptive global optimization probabilistic search algorithm that simulates the evolutionary process of living organisms in nature and performs objective optimization based on size adaptation to find the optimal solution (Gen and Cheng, 1999). The genetic algorithm is based on the natural

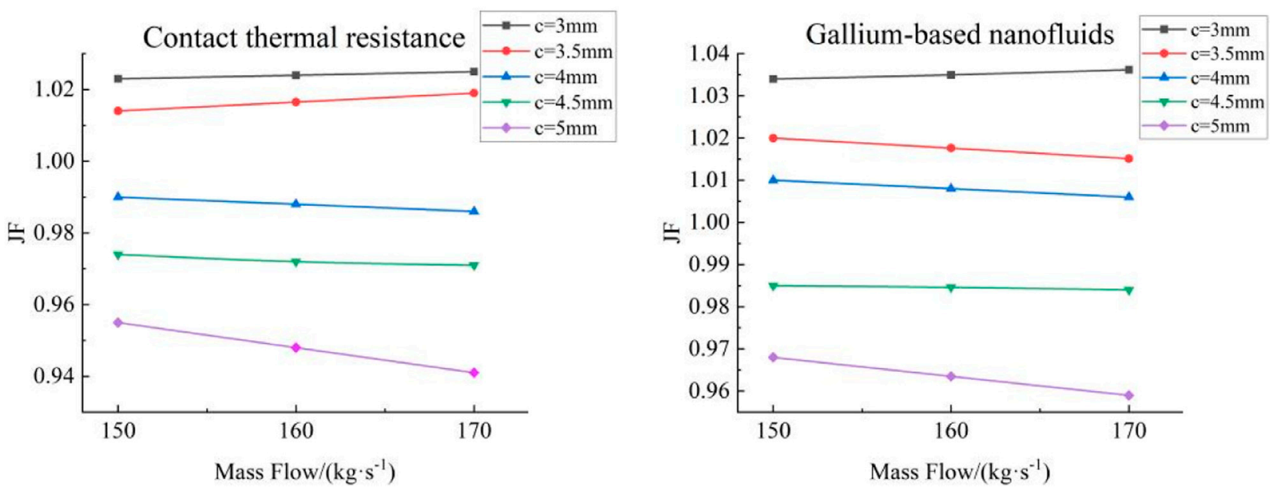

FIGURE 16
Effect of the heat exchanger tube wall thickness on the JF factor.

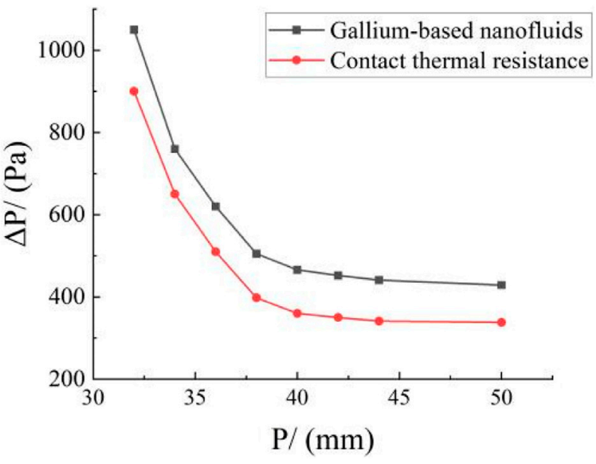

FIGURE 17
Effect of heat exchanger tube spacing on shell-side pressure drop.

selection principle of "survival of the fittest and elimination of the unfit", where genes are passed and varied among a group of individuals through genetic manipulation (e.g., selection, crossover, and mutation) to produce better-performing offspring. The algorithm repeats this process until a termination condition is met, such as reaching the maximum number of iterations or obtaining a sufficiently good solution. The genetic algorithm is widely used because it starts searching from multiple initial points, converges faster, covers a large area, and provides a globally optimal solution. Yang et al. (Yang et al., 2014) optimized the structural parameters in a shell and tube heat exchanger based on the genetic algorithm, such as tube diameter, wall thickness, and number of tubes, which significantly reduced the total heat exchanger cost. Mirzaei et al. (Mirzaei et al., 2017) used a multi-objective genetic algorithm to optimize the structural parameters of a heat exchanger, thereby improving its thermal efficiency by more than 28%.

In this work, the heat exchanger tube length, wall thickness, outer diameter, and spacing are coded as individuals, while the JF factor and CER are used as fitness functions. The maximum values are used as the target to continuously select, cross, and mutate, remove some individuals with low fitness, and generate the same number of individuals to maintain the total number of individuals; the iteration is stopped when the individual with the highest fitness is generated.

4.2 Variable scope

To more effectively select the variation range of parameters and speed up the convergence of optimal design, this work uses contribution ratio (CR) to evaluate the influence of each parameter on the comprehensive performance, which provides the optimization range of each structural parameter design according to its contribution level (Yun and Lee, 2000); CR is calculated as follows:

$$CR_i = \frac{SN_{\max,i} - SN_{\min,i}}{\sum\limits_{i=1}^{n} \left(SN_{\max,i} - SN_{\min,i}\right)} \tag{12}$$

$$\begin{cases} SN = 10\log\left(\dfrac{1}{r} \times \dfrac{(S_m - V_e)}{V_e}\right) \\ r = \sum\limits_{j=1}^{n} u_j^2, S_m = \dfrac{\left(\sum\limits_{j=1}^{n} u_j \cdot JF_j\right)^2}{r} \\ V_e = \dfrac{S_e}{n-1}, S_e = S_T - S_m, S_T = \sum\limits_{j=1}^{n} JF_j^2 \end{cases} \tag{13}$$

Where $SN_{\max,i}$ and $SN_{\min,i}$ are the maximum and minimum signal-to-noise ratios for the i th parameter, respectively; u_j is the j th coolant flow; and JF_j is the j th JF factor.

The calculated CR of each parameter is shown in Figure 19, which reveals that spacing P has a negligible contribution when

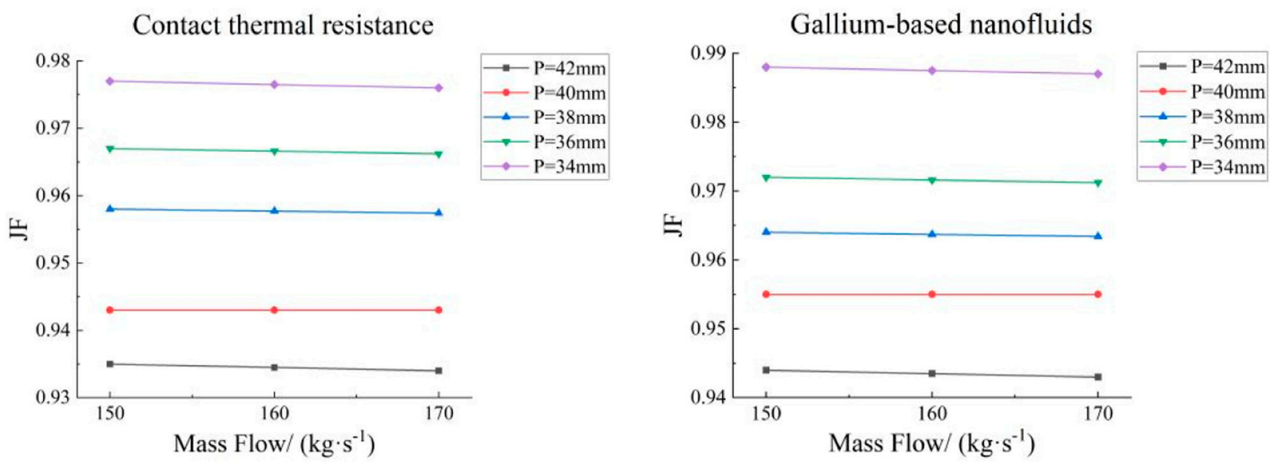

FIGURE 18
Effect of heat exchanger tube spacing on the JF factor.

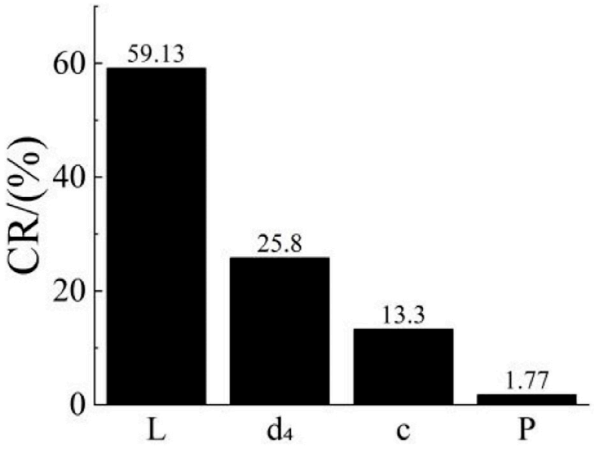

FIGURE 19
Contribution ratio (CR) of each parameter.

TABLE 3 Design parameter ranges of the heat exchange tube.

Design parameters	Ranges
d4/mm	[19,33]
c/mm	[3.5,4.5]
L/m	[1.2,4.8]
P/mm	[41,43]

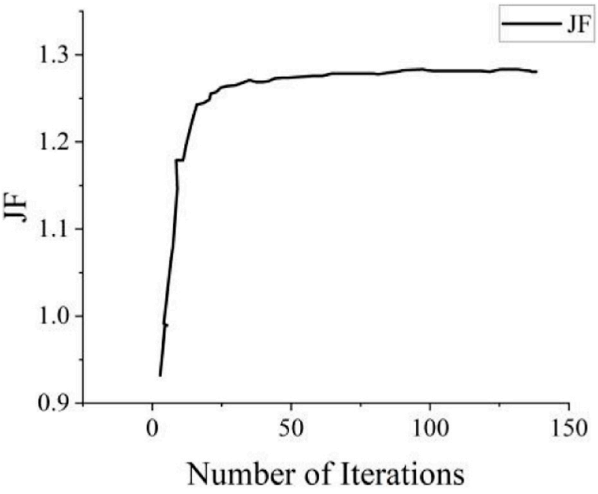

FIGURE 20
Variation curve of the JF factor with the number of iterations.

compared to the other three factors that influence the heat exchanger performance. This indicates that the tube length L, outer diameter d_4, and wall thickness c significantly impact the heat exchanger's performance. Since L has the greatest impact, it is imperative to choose a reasonable heat exchanger tube length when designing the heat exchanger. According to the CR and the processing technology of the heat exchange tube, based on the preliminary design parameters in Table 2, the parameter range is shown in Table 3.

4.3 Optimization results

By using the maximum values of the JF factor and CER as objective functions, the outer diameter, wall thickness, length, and tube spacing of heat exchange tubes have been optimized using the genetic algorithm. The convergence process of the objective function value is depicted in Figures 20, 21 based on the number of iterations. The comparison of optimization results is shown in Table 4.

This table provides valuable insights into the optimization results for Scheme 1 and Scheme 2 of the main heat exchanger.

In Scheme 1, optimization was performed to maximize the JF factor. Compared to the pre-optimization values, the overall heat

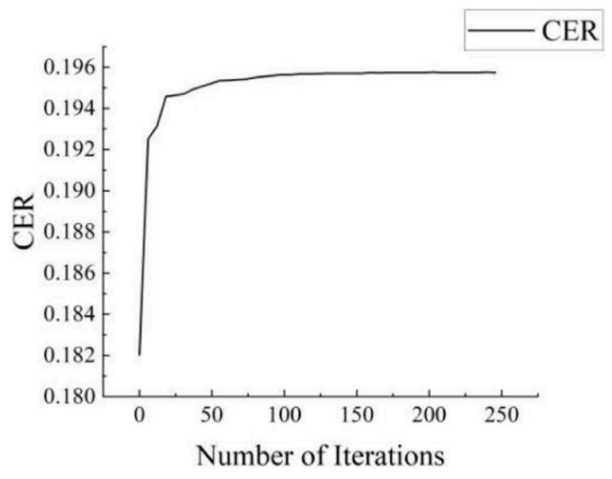

FIGURE 21
Variation curve of CER with the number of iterations.

transfer coefficient increased by 4.04%. Additionally, the pressure drop in the primary loop decreased by 23.01%, while the JF factor increased by 14%. This optimization approach aimed to improve the overall performance of the main heat exchanger by maximizing the heat transfer capacity while minimizing the pressure drop.

In Scheme 2, optimization was conducted to maximize CER. The overall heat transfer coefficient increased by 5.79% when compared to the pre-optimization value. However, the pressure drop in the primary loop increased slightly (by 2.32%). Nevertheless, CER significantly improved by 24.62%, which indicates that the heat transfer performance per unit cost is enhanced.

Compared with the double-tube heat exchanger with the same bundle structure optimization parameters but without using gallium-based graphene nanofluids, there is no significant change in the primary circuit pressure drop. For Scheme 1 and Scheme 2, the overall heat transfer coefficients are reduced by 42.32 W/(m^2·K) and 59.67 W/(m^2·K), respectively. Comparatively, the heat transfer capacity of the double-tube heat exchanger without gallium-based graphene nanofluid added in the gap decreases by approximately 2.70% and 3.56%. It can be seen that adding gallium-based graphene nanofluids in the gap between the double-layer heat exchange tubes can improve the heat transfer capability of the reactor, thereby reducing the temperature difference between different components of the reactor, and enhancing its safety and operational efficiency.

A comprehensive comparative analysis reveals that Scheme 2 strikes an optimal balance between heat transfer performance and cost-effectiveness. Although the pressure drop only slightly increases in Scheme 2, a greater improvement in heat transfer performance is achieved and the average cost ratio is minimized. This balanced optimization approach enhances the overall economic feasibility of the heat exchanger.

Based on the heat transfer performance and average cost, it can be established that Scheme 2 is the preferred design for the main heat exchanger. This design choice ensures a significant enhancement in heat transfer performance while exhibiting the best cost-effectiveness.

5 Conclusion

In this work, we propose to fill the gap between the double-layer heat exchanger tubes in a lead-bismuth reactor with a thermal interface material (gallium-based graphene nanofluids). Furthermore, the influence of the heat exchanger tube length, wall thickness, outer diameter, and spacing on the heat transfer performance is analyzed, and the results are compared to those obtained for the double-layer heat exchanger tube without the thermal interface material. Based on the optimization objectives of the genetic algorithm and the above-mentioned parameters, the heat transfer performance of the main heat exchanger is optimized and comprehensively evaluated; consequently, a new double-layer heat exchanger design scheme is obtained. The main research findings are as follows.

(1) For heat exchanger tubes with the same outer diameter, wall thickness, length, and spacing, adding the gallium-based graphene nanofluids leads to a better total heat transfer coefficient and higher heat transfer capacity; however, this addition increases the shell pressure drop, which is not conducive to achieving a natural circulation in the reactor. Nevertheless, the nanofluids increase the JF factor and lead to a better overall heat transfer performance.

TABLE 4 Comparison of heat exchanger performance before and after optimization.

Parameter	Initial parameters	Scheme 1	Scheme 2
Heat exchanger tube outer diameter/mm	26	32.48	32.08
Heat exchanger tube wall thickness/mm	4	3.5	3.5
Heat exchanger tube length/m	2.985	1.573	1.768
Heat exchanger tube spacing/mm	32	41.51	41.32
Overall heat transfer coefficient/W/(m2·K)	1,505	1,565.75	1,592.12
Primary circuit pressure drop/Pa	586.7	451.7	600.3
JF	1	1.14	1.05
CER	0.1576	0.1929	0.1964

(2) When other parameters are kept constant, increasing the heat exchanger tube length tends to increase the total heat transfer coefficient and the pressure drop in a single circuit, thereby strengthening the heat transfer capacity and weakening the natural circulation capacity. Furthermore, reducing the outer diameter of the heat exchanger tube can improve the total heat transfer coefficient and reduce the pressure drop in a single circuit, thus improving the heat transfer capacity and natural circulation capacity. Increasing the wall thickness of the heat exchanger tube tends to decrease the heat transfer capacity, while increasing the distance between tubes reduces the pressure drop in a single circuit, improves the natural circulation capacity, and reduces operation costs.

(3) The JF factor and CER are used as fitness functions and optimized using a genetic algorithm to obtain two solutions, which represent the maximum possible performance and the best overall performance of the main heat exchanger. The two solutions have been compared and the solution with the maximum CER value is selected as the optimal solution, which increased the total heat transfer coefficient by 5.79%, pressure drop in the first circuit by 2.32%, JF factor by 5%, and CER factor by 24.62%.

(4) The key technologies for optimizing the design of the double-layer heat exchanger include thermal performance optimization, improvement of bundle structure, and multi-objective optimization design. The aim is to enhance the overall heat transfer coefficient, reduce the pressure drop in the primary circuit, and improve economic feasibility while meeting optimization objectives.

Data availability statement

The original contributions presented in the study are included in the article/Supplementary material, further inquiries can be directed to the corresponding author.

Author contributions

JQ: Formal Analysis, Investigation, Methodology, Writing–original draft. QA: Investigation, Methodology, Validation, Writing–original draft. PZ: Conceptualization, Funding acquisition, Project administration, Supervision, Writing–review and editing. JY: Investigation, Methodology, Software, Validation, Writing–original draft. GW: Resources, Software, Validation, Writing–original draft.

Funding

The author(s) declare that financial support was received for the research, authorship, and/or publication of this article. This work is supported by Joint Fund of Ministry of Education for Equipment Pre-research (Grant No. 8091B032243). The authors would like to express their deepest gratitude to NEAL (Nuclear Engineering and Application Laboratory) Team for its help during this research.

Conflict of interest

Author GW was employed by China Nuclear Industry Huawei Engineering Design and Research Co., Ltd.

The remaining authors declare that the research was conducted in the absence of any commercial or financial relationships that could be construed as a potential conflict of interest.

Publisher's note

References

Alemberti, A., Frogheri, M., Hermsmeyer, S., Smirnov, L. A., Takahashi, M., Smith, C. F., et al. (2014). *Lead-cooled fast reactor (LFR) risk and safety assessment white paper*. Gen IV International Forum Online, Europe, UK

Cheng, X., and Tak, N. (2006). Investigation on turbulent heat transfer to lead–bismuth eutectic flows in circular tubes for nuclear applications. *Nucl. Eng. Des.* 236 (4), 385–393. doi:10.1016/j.nucengdes.2005.09.006

Fazio, C., Sobolev, V. P., Aerts, A., Gavrilov, S., Lambrinou, K., Schuurmans, P., et al. (2015). *Handbook on lead-bismuth eutectic alloy and lead properties, materials compatibility, thermal-hydraulics and technologies-2015 edition (No. NEA–7268)*. Organisation for Economic Co-Operation and Development. Paris, France

Gen, M., and Cheng, R. (1999). *Genetic algorithms and engineering optimization*, John Wiley and Sons. Hoboken, NY, USA.

Iskhakov, A., Melikhov, V., Melikhov, O., and Yakush, S. (2018). Steam generator tube rupture in lead-cooled fast reactors: estimation of impact on neighboring tubes. *Nucl. Eng. Des.* 341, 198–208. doi:10.1016/j.nucengdes.2018.11.001

Jeltsov, M., Villanueva, W., and Kudinov, P. (2018). Steam generator leakage in lead cooled fast reactors: modeling of void transport to the core. *Nucl. Eng. Des.* 328, 255–265. doi:10.1016/j.nucengdes.2018.01.006

Kim, C. S. (1975). Thermophysical properties of stainless steels. *U. S* 12, doi:10.2172/4152287

Kuang, D., and Hu, W. (2013). Research progress of graphene composites. *J. Inorg. Mater.* 28 (3):235–246. doi:10.3724/sp.j.1077.2013.12345

Liu, S., Jin, M., Lyu, K., Zhou, T., and Zhao, Z. (2018). Flow and heat transfer behaviors for double-walled-straight-tube heat exchanger of HLM loop. *Ann. Nucl. Energy* 120, 604–610. doi:10.1016/j.anucene.2018.06.016

Mirzaei, M., Hajabdollahi, H., and Fadakar, H. (2017). Multi-objective optimization of shell-and-tube heat exchanger by constructal theory. *Appl. Therm. Eng.* 125, 9–19. doi:10.1016/j.applthermaleng.2017.06.137

Rozzia, D., Fasano, G., Di Piazza, I., and Tarantino, M. (2015). Experimental investigation on powder conductivity for the application to double wall heat exchanger (NACIE-UP). *Nucl. Eng. Des.* 283, 100–113. doi:10.1016/j.nucengdes.2014.06.037

Wagner, W., and Kretzschmar, H. J. (2008). IAPWS industrial formulation 1997 for the thermodynamic properties of water and steam. *Int. steam tables Prop. water steam based industrial formulation IAPWS-IF97*, 52, 7–150. doi:10.1007/978-3-540-74234-0_3

Wang, G. M. (2014). *Thermal-hydraulic optimal design and study of primary heat exchanger for lead alloy cooled natural circulation reactor*. University of Science and Technology of China. Hebei, China.

Wang, X., Lu, C., and Rao, W. (2021). Liquid metal-based thermal interface materials with a high thermal conductivity for electronic cooling and bioheat-transfer applications. *Appl. Therm. Eng.* 192, 116937. doi:10.1016/j.applthermaleng.2021.116937

Wu, Y., Bai, Y., Song, Y., Huang, Q., Zhao, Z., and Hu, L. (2015). Development strategy and conceptual design of China lead-based research reactor. *Ann. Nucl. Energy* 87, 511–516. doi:10.1016/j.anucene.2015.08.015

Xuan, Y., Li, Q., and Hu, W. (2003). Aggregation structure and thermal conductivity of nanofluids. *AIChE J.* 49 (4), 1038–1043. doi:10.1002/aic.690490420

Yang, J., Oh, S. R., and Liu, W. (2014). Optimization of shell-and-tube heat exchangers using a general design approach motivated by constructal theory. *Int. J. heat mass Transf.* 77, 1144–1154. doi:10.1016/j.ijheatmasstransfer.2014.06.046

Yu, P., Zhu, R., and Yu, Z. (2002). *Thermal analysis of nuclear reactors*. Shanghai, China: Shanghai Jiao Tong University Press Publishing.

Yun, J., and Lee, K. (2000). Influence of design parameters on the heat transfer and flow friction characteristics of the heat exchanger with slit fins. *Int. J. Heat Mass Transf.* 43 (14), 2529–2539. doi:10.1016/S0017-9310(99)00342-7

Zhang, C., Cui, D., Du, Y., Xu, X., Zhong, J., and Ren, L. (2023). Structure and physical properties of gallium-based liquid metal. *Chin. J. Nat.* 45 (5), 340–354. doi:10.3969/j.issn.0253-9608.2023.05.003

Frontiers in Energy Research

TYPE Original Research
PUBLISHED 01 May 2024
DOI 10.3389/fenrg.2024.1343933

OPEN ACCESS

EDITED BY
Shichang Liu,
North China Electric Power University, China

REVIEWED BY
Di Wu,
Harbin Engineering University, China
Dali Yu,
Chinese Academy of Sciences (CAS), China

*CORRESPONDENCE
Geng Yiwa,
✉ eva_geng_1996@163.com
Huang Shuliang,
✉ huangsl@cnpe.cc

RECEIVED 24 November 2023
ACCEPTED 17 April 2024
PUBLISHED 01 May 2024

CITATION
Yiwa G, Xiongbin L, Ziyi L, Shuliang H, Lanyu Z, Yanfang X, Xiaotian L and Yajun Z (2024), Analysis of transient characteristics and design improvement of the passive residual heat removal system of NHR-200-II. *Front. Energy Res.* 12:1343933. doi: 10.3389/fenrg.2024.1343933

Analysis of transient characteristics and design improvement of the passive residual heat removal system of NHR-200-II

Geng Yiwa[1]*, Liu Xiongbin[2], Li Ziyi[3], Huang Shuliang[1]*, Zhou Lanyu[1], Xue Yanfang[1], Li Xiaotian[2] and Zhang Yajun[2]

[1]China Nuclear Power Engineering Co., Ltd., Beijing, China, [2]Institute of Nuclear and New Energy Technology of Tsinghua University, Beijing, China, [3]Shandong Institute of Advanced Technology, Jinan, Shandong, China

NHR-200-II is a small integrated pressurized water reactor with 200 MW core thermal power. The core heat is transferred to two independent intermediate circuits via fourteen in-vessel primary heat exchangers (PHE), and the heat in the intermediate circuits is transferred to feedwater by two steam generators (SG) in the two intermediate circuits respectively. A passive residual heat removal (PRHR) branch is connected to each intermediate circuit to remove core decay heat under postulated accidents. During normal operation, PRHR branches are isolated by valves while SG branches in intermediate circuits are open. The valves in PRHR branches will be opened and the isolation valves of SG branches will be closed during decay heat removal scenarios. The decay heat removal capacity of NHR-200-II PRHRS could be seriously deteriorated once the isolation valves for SG branches fail to close, which was confirmed in a scaled integral test loop previously. Current understanding of PRHRS's thermal-hydraulic characteristics with possible isolation failure in SG branches is limited. In this paper, the NHR-200-II PRHRS is modeled with RELAP5 considering the case of success and fail to isolate SG branches. A series of numerical simulations are carried out to study the impact of various parameters, such as the initial temperature, the size of the intermediate circuits' header, and the initial flow direction in the intermediate circuits. Oscillatory flow is found when SG branches fail to be isolated under certain parameters combinations. An improved PRHRS design is purposed to eliminate possible flow oscillations, and the purposed improved design are tested by numerical simulations.

KEYWORDS

NHR-200-II, passive residual heat removal system (PRHRS), RELAP5, intermediate circuits, numerical simulation

1 Introduction

An integrated pressurized water reactor (IPWR) integrates major primary components inside the pressure vessel. IPWR is generally more compact than traditional PWR, and has higher safety level since it eliminates possible failures of the main primary pipes (Liu et al., 2023). Research and design of integrated pressurized water

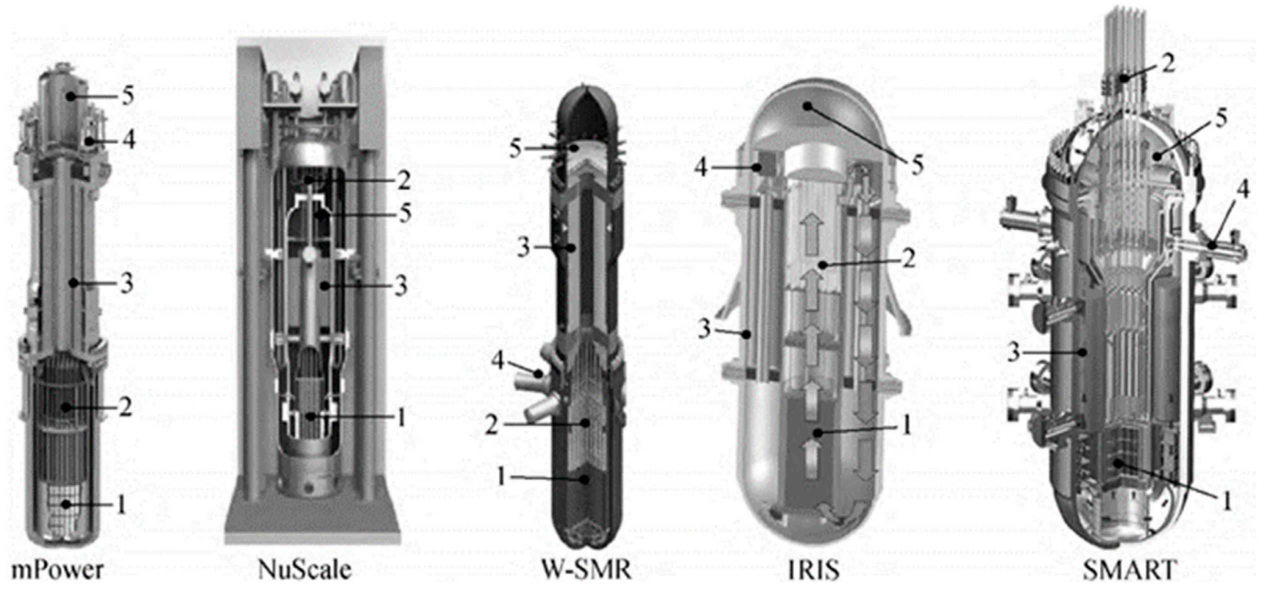

FIGURE 1
Small integrated pressurized water reactor under development in the worldwide. (*Copyright permission has been obtained before use*).

reactors is quite active in many countries, as shown in Figure 1. Korea's system-integrated modular advanced reactor (SMART) has a power rating 330 MW, and the system design of SMART includes both inherent and passive safety systems. In the United States, there are many IPWR designs such as mPower, NuScale, Westinghouse SMR, et al. In addition, CAREM-25 reactor in Argentina, Flexblue reactor by DCNS group in France and ABV-6M, RITM-200 reactors designed by Russia are integrated pressurized water reactor designs (IAEA, 2012).

NHR-200-II nuclear heating reactor is a multi-purpose small integrated pressurized water reactor developed by the Institute of Nuclear and New Energy Technology (INET) of Tsinghua University (Wang et al., 1993). The NHR-200-II design characteristics include a tri-circuits design, hydraulic control rod driving systems, in-vessel pressurizer with vapor and nitrogen, and passive residual heat removal systems (PRHRS). The NHR-200-II design has many advantages like higher safety, compact size, and controllable investment, make the reactor widely-deployable in many areas, like urban heating, seawater desalination, nuclear powered icebreakers, etc.

The PRHRS is an important safety system for NHR-200-II nuclear heating reactor. The PRHRS relies on three coupling natural circulations to remove core residual heat, namely the natural circulation of primary side in the reactor pressure vessel (RPV), the single-phase natural circulation in RHE branches of the intermediate circuits, and the natural circulation of air in the cooling tower (Zhang et al., 1993). However, flow instability in PRHRS was unexpectedly observed in a scaled integral test facility built for nuclear heating reactors, and the flow instability occurred when the isolation valves of SGs in the intermediate circuits failed to close (INET, 2018). Current understanding of the transient characteristics of NHR-200-II PRHRS with isolation failure in SG branch is quite limited.

The earliest studies on the instability of single-phase natural circulation loop (NCL) were focused on the oscillation mechanism in several typical simplified loops. Keller (Keller and Joseph, 1966) predicted the one-way oscillation without flow reversal by studying the rectangular loop with heat source and radiator in the center of the horizontal pipes at the bottom and top, and predicted the one-way instability flow in rectangular NCL with point-type heat source/sink. Keller first found that simplified rectangular loop flow have cyclic periodic motion theoretically. Welander (Welander, 1967) pointed out that a loop with two vertical branches, a point heat source at the bottom and a point heat sink at the top, may have unstable behavior at certain heat power inputs. Welander also provided a physical explanation for the instability by the motion of "warm and cold pockets of fluids." Welander's conclusion was validated by Creveling (Creveling et al., 1975), who first observed the instability in an annular water loop.

The initial flow direction in a closed NCL may have significant impact on the steady-state behavior of the NCL. Sen and Trevino (Sen and Trevino, 1982) proved that an NCL can have both positive and negative steady-state flow rates, depending on the initial NCL conditions. The heat input history and initial thermal condition will also affect the flow distribution in a NCL with multiple parallel branches. Takeda (Takeda et al., 1987) studied a parallel-channel NCL with different heat inputs experimentally and theoretically, and found that flow direction and flow rate of each channel depend on the historical effect of heat input in each channel. Gartia et al. (Gartia et al., 2006) studied a NCL with three non-uniformly heated parallel channels and a common cold leg by a RELAP5 model, the existence of a metastable state of the parallel-channel NCL was confirmed, and the influence of different parameters on the metastable state was studied theoretically and numerically.

In our related series research on NHR-200-II, it was found that the cold and hot ring header of PRHR system would have obvious

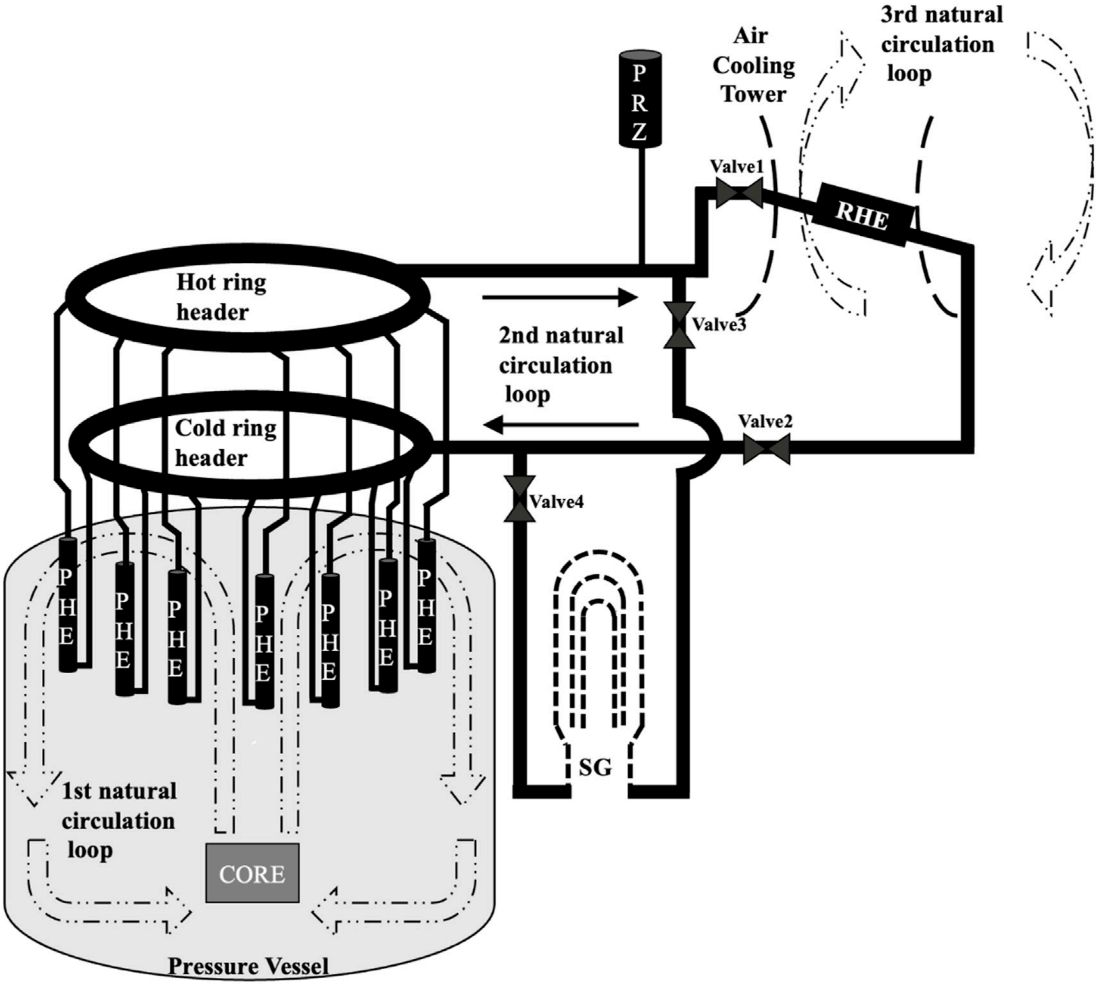

FIGURE 2
Schematic diagram of one column of PRHRS.

flow thermal stratification phenomenon (Geng et al., 2023), which would affect the flow stability and distribution. Thermal stratification effect in the headers of the PRHR system played an important role in the phenomenon of uneven outlet temperature distributions. In the previous study (Geng et al., 2023), the research focusses on reproducing the three-dimensional flow field effect of the cold and hot ring pipe. In this paper, the perspective of numerical model verification related research work also carried out, analyzes the influence of hot and cold ring pipe and Y-junction on the PRHR system, and an improved design was proposed.

In this paper, a RELAP5 model is built to study the transient characteristics of the PRHRS in a scaled integral test facility for nuclear heating reactors. The steady-state simulations under different core temperatures are performed first. Both the case of success and fail to isolate the SGs branches are investigated. Impact of various design parameters, such as header size of the intermediate circuits, initial flow direction of intermediate circuits, are studied numerically with the RELAP5 model. An improved PRHR design for the NHR-200-II reactor is proposed to suppress possible oscillatory flow in the original PRHR design.

2 Materials and methods

2.1 Design of PRHRS of NHR-200-II

The NHR-200-II PRHRS has two identical heat removal columns, and a simplified schematic diagram of PRHRS is shown in Figure 2. Each PRHR column consists of: (1) seven in-vessel primary heat exchanger (PHE) branches, (2) a residual heat exchanger (RHE) branch with the RHE placed in an air-cooling tower, (3) a pressurizer (PRZ), (4) a SG branch, (5) a hot ring header and a cold ring header above the pressure vessel, and (6) two isolation valves in the SG branch and another two isolation valves in the RHE branch.

The RHE is a finned-tube air cooler located in the air-cooling tower of NHR-200-II. The cold ring header and hot ring header are coaxially arranged above the reactor pressure vessel. PHEs are connected to the headers by T-shaped tees asymmetrically, and the RHE is connected to the headers by low resistance Y-shaped tees. The PRZ is placed at the highest location of the loop.

The PRHRS utilizes three coupled natural circulations loops to remove core residual heat passively. The first loop is natural

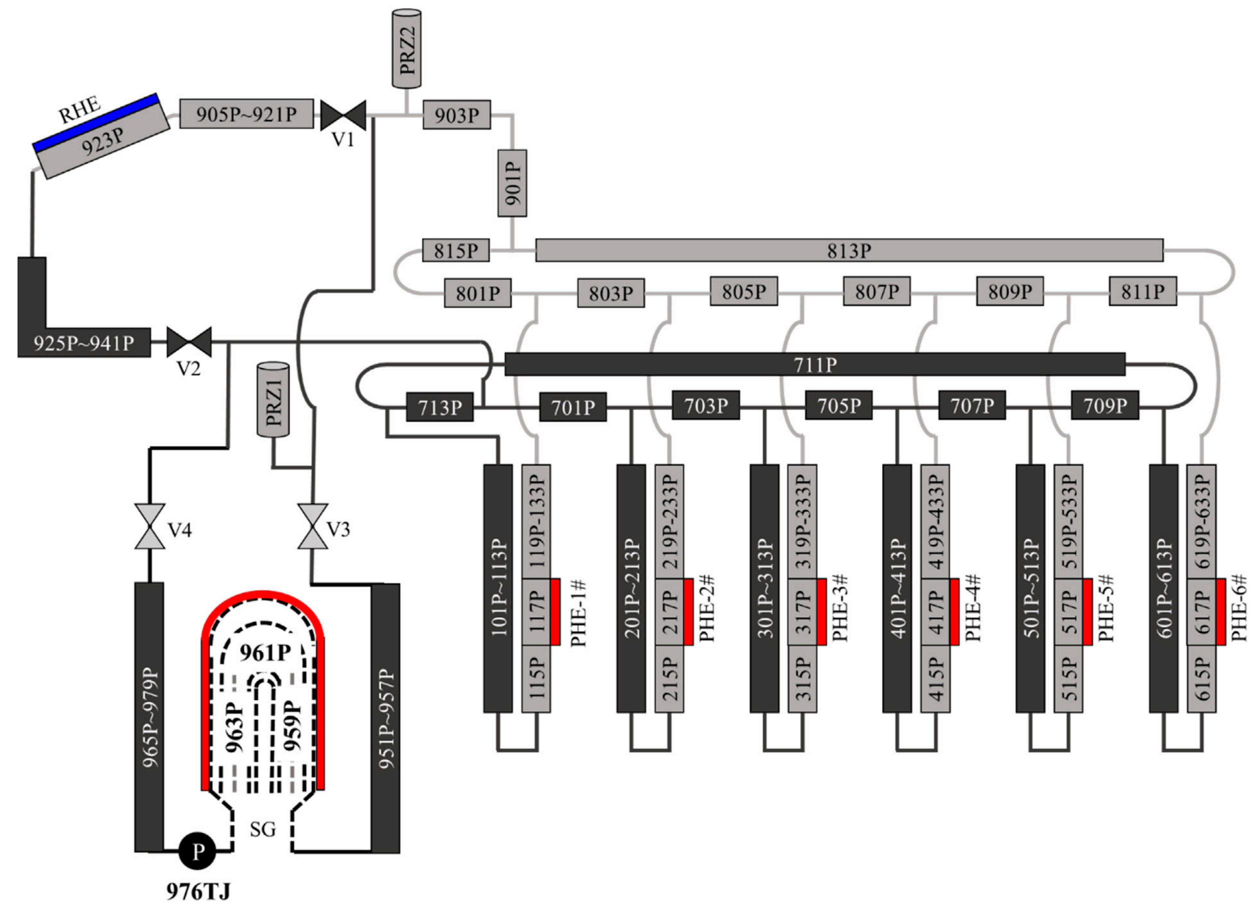

FIGURE 3
RELAP5 model of the PRHRS in integral test facility for NHR-200-II.

circulation of the primary fluid within the reactor pressure vessel. The second loop is the fluid circulation in the residual heat removal loop (Figure 2), and the third loop is natural circulation of air in the air-cooling tower.

Under normal operating conditions, valves in the RHE branch (Valve1 and Valve2 in Figure 2) are closed, and core heat is transferred from the seven in-vessel PHEs to the SG. Under reactor shutdown or postulated accidents, valves in the RHE branch (Valve3 and Valve4 in Figure 2) are opened, and decay heat is transferred from the PHEs to the RHE. However, the Valve1 and Valve2 may fail to close during PRHRS operation. In such scenarios, the RHE branch and SG branch will operate simultaneously to remove the core decay heat. The PRHRS should maintain the heat removal capacity upon isolation failure of Valve1 or Valve2 according to the single failure criteria.

2.2 The RELAP5 model

A RELAP5 model is developed for the PRHRS of the integral test facility. The model consists of six PHE branches (components number starting with 1–6 in the model), a cold ring header (components number starting with 7), a hot ring header (components number starting with 8), an RHE branch and a SG branch (components number starting with 9). The six PHE branches are evenly connected between the cold and hot ring headers in the circumferential direction. The RHE branch is connected to the cold ring header between PHE-1# and PHE- 2#. The RHE branch as well as SG branch is connected to the hot ring header between PHE-1# and PHE-6#, as shown in Figure 3. Four valves labeled as V1, V2, V3, and V4 are placed in the system, which can be switched on/off upon RELAP5 input cards.

RELAP5 input deck involves a variety of hydraulic components, including the initial calculation value, such as temperature, pressure, mass flow rate, and other thermal hydraulic parameters and calculation model. The facility design value was used as the initial state calculation value, and adjusted the input deck to the steady state before the calculation.

The PHE used in the NHR-200-II facility adopts a ring tube bundle structure with double casing. Simplified pipes are used in the Relap5 model to simulate the flow channel in the ring gap space of the tube bundle. The secondary side fluid flows in the middle gap of the ring tube, and the primary side fluid flows in the outsides and inside of the ring gap. Different constant temperatures are set as the thermal boundary in the heat structure, and different temperature values ranging from 533.15 to 327.15 K are used in different cases.

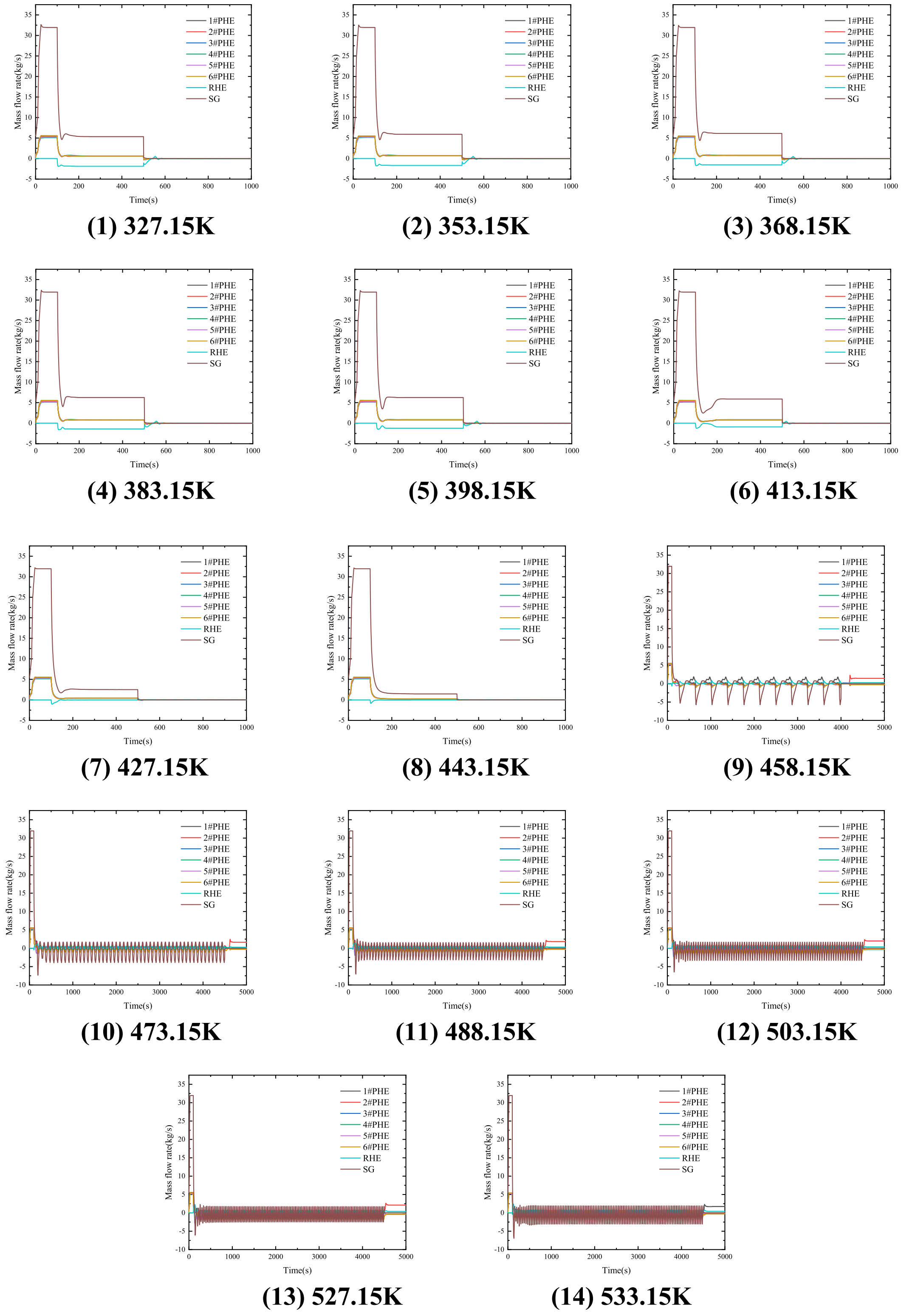

(1) 327.15K (2) 353.15K (3) 368.15K

(4) 383.15K (5) 398.15K (6) 413.15K

(7) 427.15K (8) 443.15K (9) 458.15K

(10) 473.15K (11) 488.15K (12) 503.15K

(13) 527.15K (14) 533.15K

FIGURE 4
Transient mass flow rate of each branch at different primary fluid temperature.

The U-shaped heat transfer tube bundle in SG is modeled by section, the secondary side is simulated by heat structure, and the thermal boundary is set as 453.15 K constant temperature.

The RHE heat transfer tube also uses a single pipe to simulate the heat transfer bundle, the heat structure simulates the secondary side, and the constant temperature thermal boundary 298.15 K is calculated.

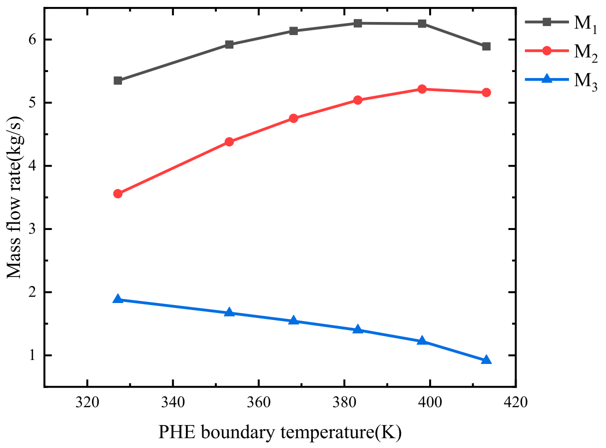

FIGURE 5
Mass flow rate with different PHE temperature in second stage Stable conditions.

3 Results

3.1 Impact of primary fluid temperature on the PRHRS transient characteristics

The transient characteristics of PRHRS is simulated with the primary fluid temperature varying from 327.15 K to 533.15 K. The RHE heat sink temperature is kept at 298.15 K and SG boundary temperature is kept at 453.15 K in all cases.

In this study, the operation curve of the PRHRS is divided into three stages. The first stage is the normal operation mode with all the PHE branches and the SG branch connected, where the valves of V1 and V2 are closed and the valves of V3 and V4 are opened. The SG branch is driven by the pump 976TJ, where the mass flow rate of pump is increased from zero to a maximum of approximately 31.95 kg/s and remained at the maximum for a period.

In the second stage, the RHE branch is put into operation by opening V1 and V2 while the V3 and V4 are kept open, the purpose

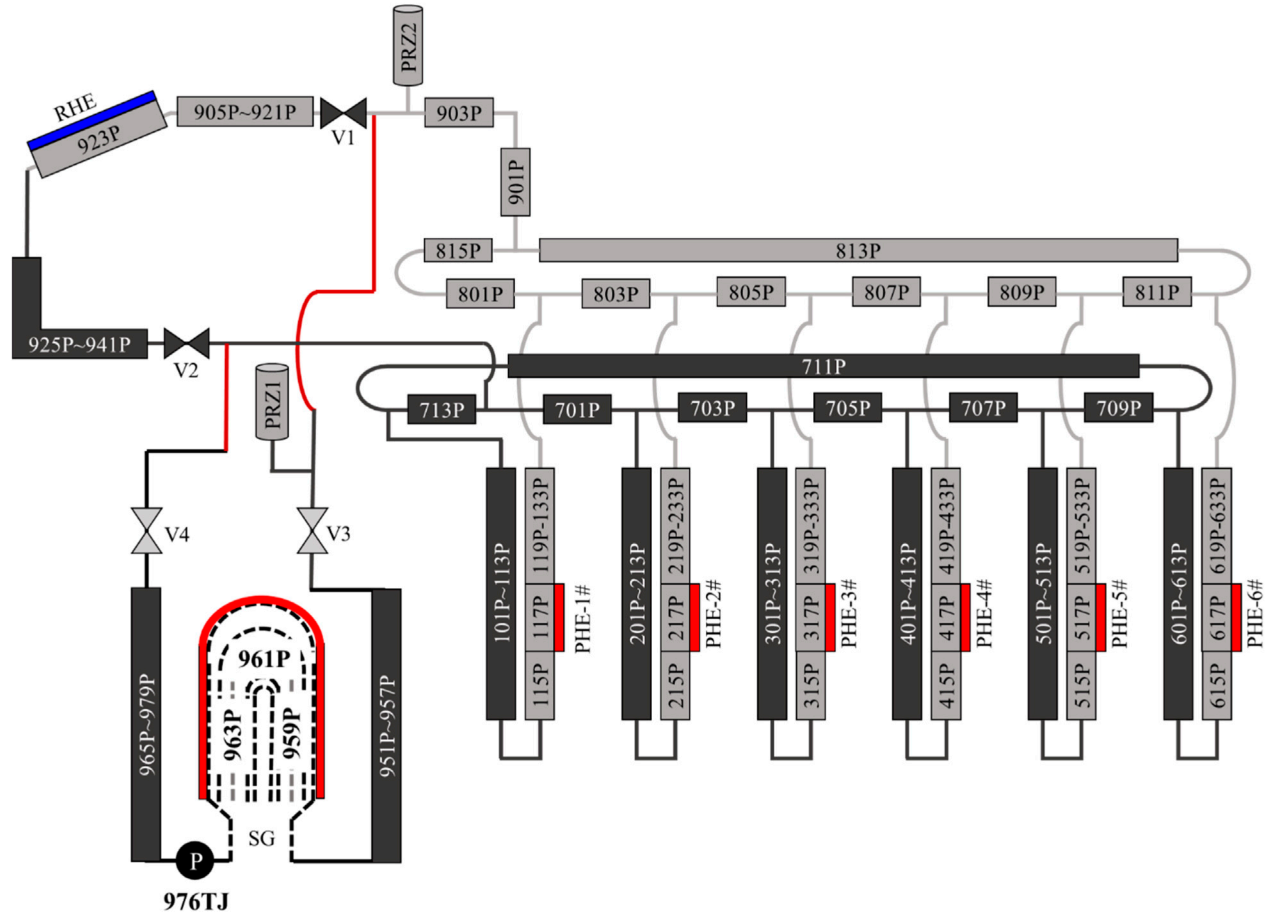

FIGURE 6
RELAP5 node diagram of the PRHRS of removing ring header.

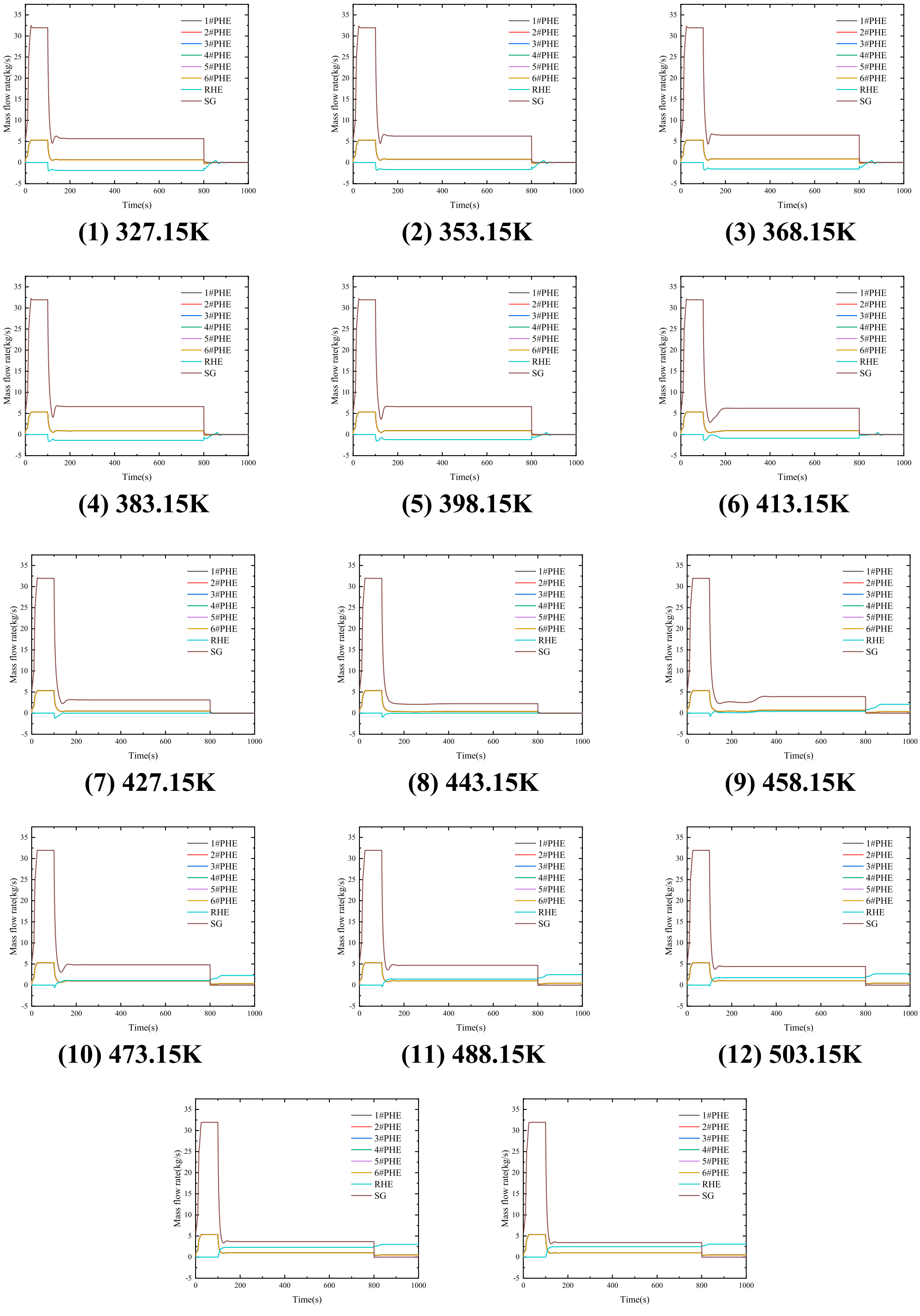

(1) 327.15K (2) 353.15K (3) 368.15K

(4) 383.15K (5) 398.15K (6) 413.15K

(7) 427.15K (8) 443.15K (9) 458.15K

(10) 473.15K (11) 488.15K (12) 503.15K

(13) 527.15K (14) 533.15K

FIGURE 7
Mass flow rate of each branch changing with Time at different PHE boundary temperature (removing the ring header).

of second stage is to simulate the transient characteristics of PRHRS in case of fail to isolate the SG branch.

In the third stage, the SG valves named V3 and V4 are closed and the SG branch is isolated successfully, and core decay heat is transferred from the PHEs to the RHE. The third stage is set to simulate the standard PRHRS operation mode.

A series of numerical simulations with different primary fluid temperature are conducted to simulate the impact of primary fluid

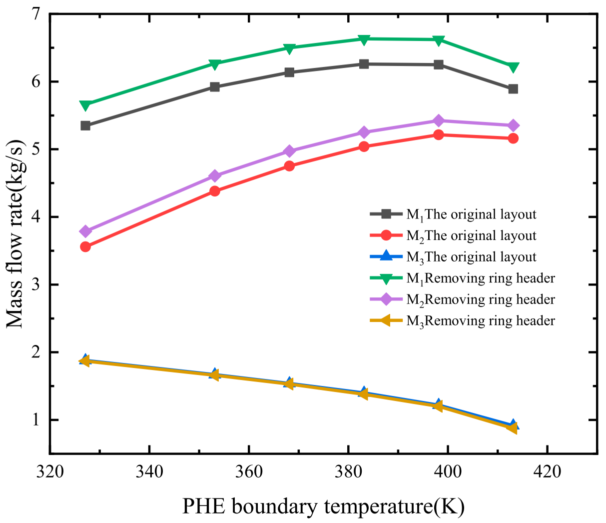

FIGURE 8
Mass flow rate at different primary fluid temperature under second stage (with the ring headers removed).

temperature on the PRHRS transient characteristics. Figure 4 shows the transient mass flow rate of each branch at different primary fluid temperatures.

When the core temperature is range between 327.15 K and 413.15 K, a steady-state flow distribution is achieved in the second stage. In this stage, the steady-state flow rates of each branch with the primary fluid temperature are shown in Figure 5, where the mass flow rate of SG branch is denoted as M1, the totally mass flow rate of six PHE branches is denoted as M2, and the mass flow rate of RHE branch is denoted as M3. With the increase of primary fluid temperature from 327.15 K to 413.15 K, the mass flow rate of RHE branch increases monotonically, while the mass flow rate of PHE branches and the SG branch first increase and then decrease.

For the middle temperature range of 413.15 K–458.15 K, the transient flow characteristics is different, where the flow in RHE branch is suppressed in the second stage completely.

For the core temperature range of 458.15 K–533.15 K, it can be seen from Figure 4 that unstable oscillating flow will occur in the second stage, which means the heat removal capacity of the PRHRS may be significantly deteriorated when the SG branch is failed to be isolated. In contrast, the PRHRS reaches a steady state in the third stage where the SG branch is isolated.

3.2 Effect of hot and cold ring header on the transient characteristics of PRHRS

The hot and cold ring header are important to the PRHRS hydraulic characteristics. In order to investigate the effect of ring headers on the oscillatory flow during the second stage, the ring headers in the original model (Figure 2) are replaced with small control volumes represented by the 714B and 814B (Figure 6). For the RELAP5 model of Figure 6, the transient flow rates of each branch at different primary fluid temperature are shown in Figure 7.

For the primary fluid temperature range of 327.15 K–413.15 K, steady-state flow distribution is also achieved in the second stage. The flow rate distribution without ring headers is compared to the flow rates of the original model in Figure 8. It can be seen from Figure 8 that the steady-state flow rate of each branch has the same trend for the two models with and without ring headers, the flow rate of SG branch and PHE branches of the model without ring headers is slightly higher than that of the original model, while the mass flow rate of RHE branch is not significantly changed.

For the temperature range of 413.15 K–458.15 K, the transient flow characteristics of the system model without ring headers is generally the same to the original RELAP5 model. However, in temperature range of 458.15 K–533.15 K, steady-state flow distributions are achieved instead of the oscillatory flow of the original model in the second stage, which indicates that removing ring headers can suppress the oscillatory flow when isolation valves of the SG branch fail to close. In the third phase, with the absence of ring header, the flow distribution of six PHE branches are uniform, and the reverse flow phenomena in the six PHE branches caused by the existence of ring headers is eliminated.

3.3 Effect of initial flow rates to the transient characteristics of PRHRS

In order to study the influence of the initial flow rates to the steady-state flow rate distribution of all PRHR branches, the flow direction of pump 976 TJ is set to the opposite direction in the first stage. The transient flow rate of each branch is shown in Figure 9.

For the primary fluid temperature range of 327.15 K–443.15 K, the steady-state flow rates of the second stage of the current model (Figure 9) are opposite to that of the original model (Figure 4). The absolute value of steady state flow rates of PRHR branches for the current model and the original model are plotted on Figure 10, where the flow rate of SG branch (M_1) and all PHE branches (M_2) are significantly higher than the flow rates of the original PRHRS model or the PRHRS model without ring headers, while the flow rate of RHE branch (M_3) is almost unchanged.

For higher primary fluid temperature ranges from 473.15 K to 533.15 K, oscillating flow also occurs in the second stage of PRHRS operation for the current model with initial SG pump flow direction reversed. However, it can be seen from Figure 10 that the pattern of oscillatory flow is very different compared to the transient flow rate of the original model (Figure 4). Therefore, the initial flow direction of PRHRS has a significant influence on the transient flow characteristics of PRHRS.

3.4 A preliminary PRHRS design improvement to suppress oscillatory flow

The flow oscillation phenomena, which may occur in PRHRS when the isolation valves of SG branch fail to close in certain temperature ranges, could significantly deteriorate the heat removal capacity of the PRHRS. A preliminary PRHRS design improvement to suppress the oscillatory flow is proposed and shown in Figure 11, where the tees of the SG branch are moved from the RHE branch (Figure 3) to the ring headers (Figure 11). The

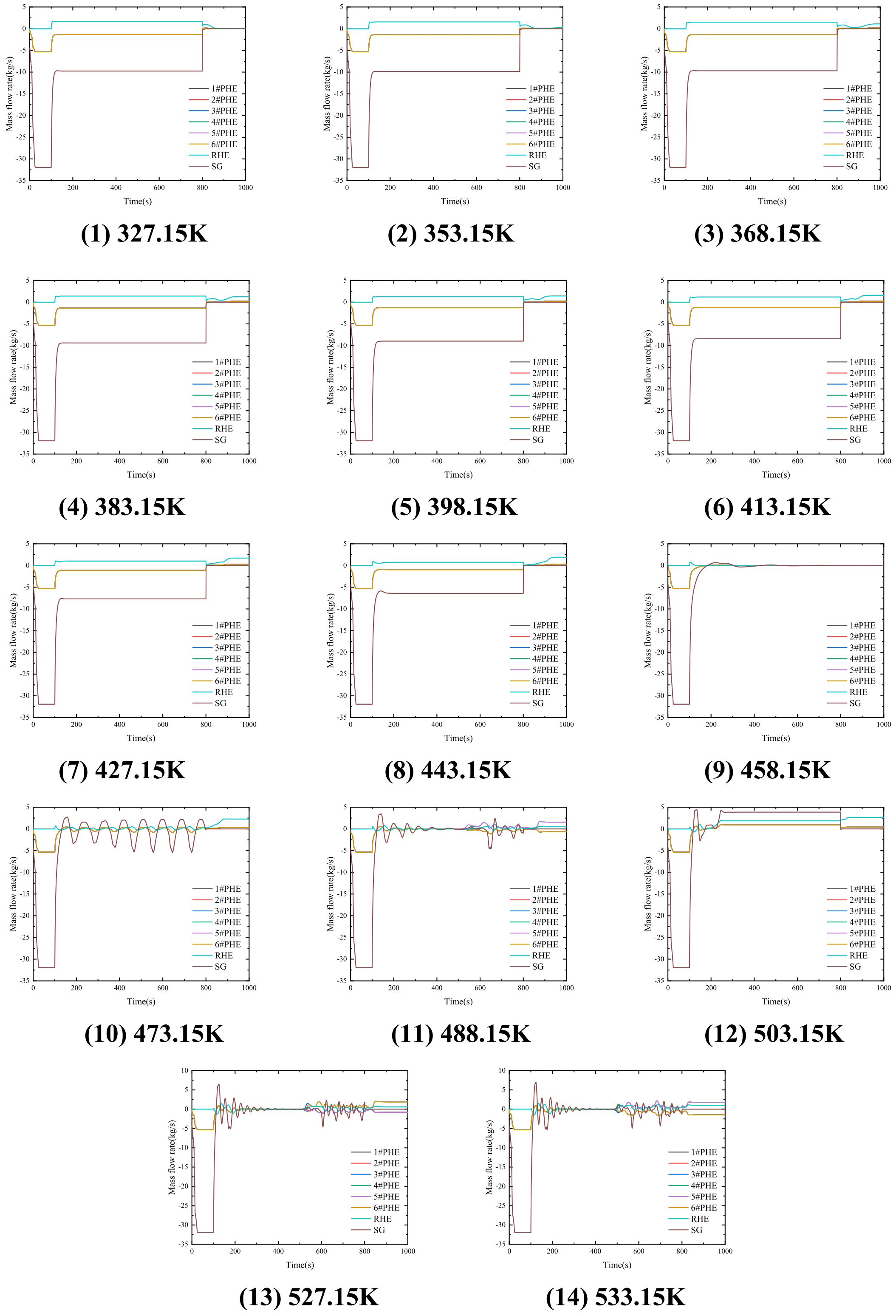

(1) 327.15K

(2) 353.15K

(3) 368.15K

(4) 383.15K

(5) 398.15K

(6) 413.15K

(7) 427.15K

(8) 443.15K

(9) 458.15K

(10) 473.15K

(11) 488.15K

(12) 503.15K

(13) 527.15K

(14) 533.15K

FIGURE 9
Transient flow rate of each branch at different primary fluid temperature (with reversed initial flow direction of SG pump).

general consideration behind this design improvement is to reduce the flow resistance from the six PHE branches to the SG branch, and to avoid early mixing of fluid with different temperatures from both the RHE branch and the SG branch.

The transient flow rate of the improved design is shown in Figure 12 with primary fluid temperature of 533.15 K. The operation curve of PRHRS used in this section is the same as previous sections, i.e., the first stage (0–50 s) with pump-driven circulation between SG and the six

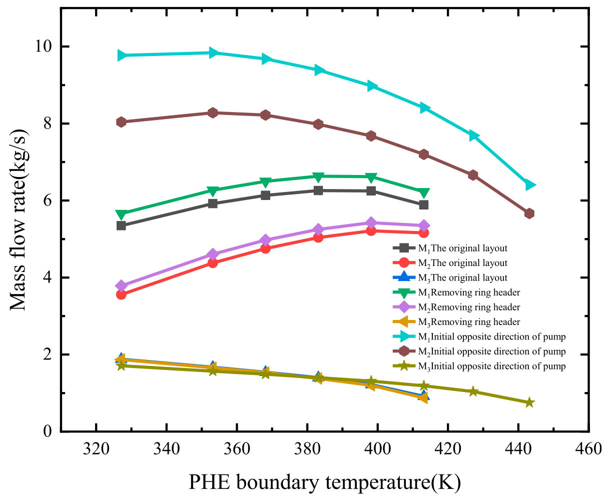

FIGURE 10
Steady-state flow rate at different primary fluid temperature in the second stage (with reversed initial flow direction of SG pump).

PHEs, and the second stage (50–550 s) with valves of RHE branch opened and valves of SG branch kept open (isolation failure), and for the third stage (550–1000 s), the SG branch is isolated.

As can be seen from Figure 12, the steady-state flow rate of all branches in the second stage (50–550 s) is the same as the third stage (550–1,000 s), which indicates that the improved PRHRS design can effectively suppress the flow oscillations during the period of isolation failure of SG valves. However, study of the purposed design improvement is preliminary and further numerical simulations and experiments are needed to confirm the effectiveness of the improved PRHRS design.

4 Discussion

In this paper, a RELAP5 model is established for the NHR-200-II nuclear heating reactor PRHRS integral test facility. The impact of various parameters on PRHRS transient flow characteristics are studied, the parameters include the primary fluid temperature, the existence of ring headers and the initial flow directions. Both the case of fail and success to isolate SG branch are considered. The main conclusions include:

(1) The flow rates in PRHR branches are always steady when success to isolate SG branch, and the flow in PRHRS is oscillatory when fail to isolate SG branch if the primary fluid temperature is larger than 458.15 K.
(2) The flow oscillation can be suppressed by replacing the ring headers with a small control volume in the RELAP5 model.

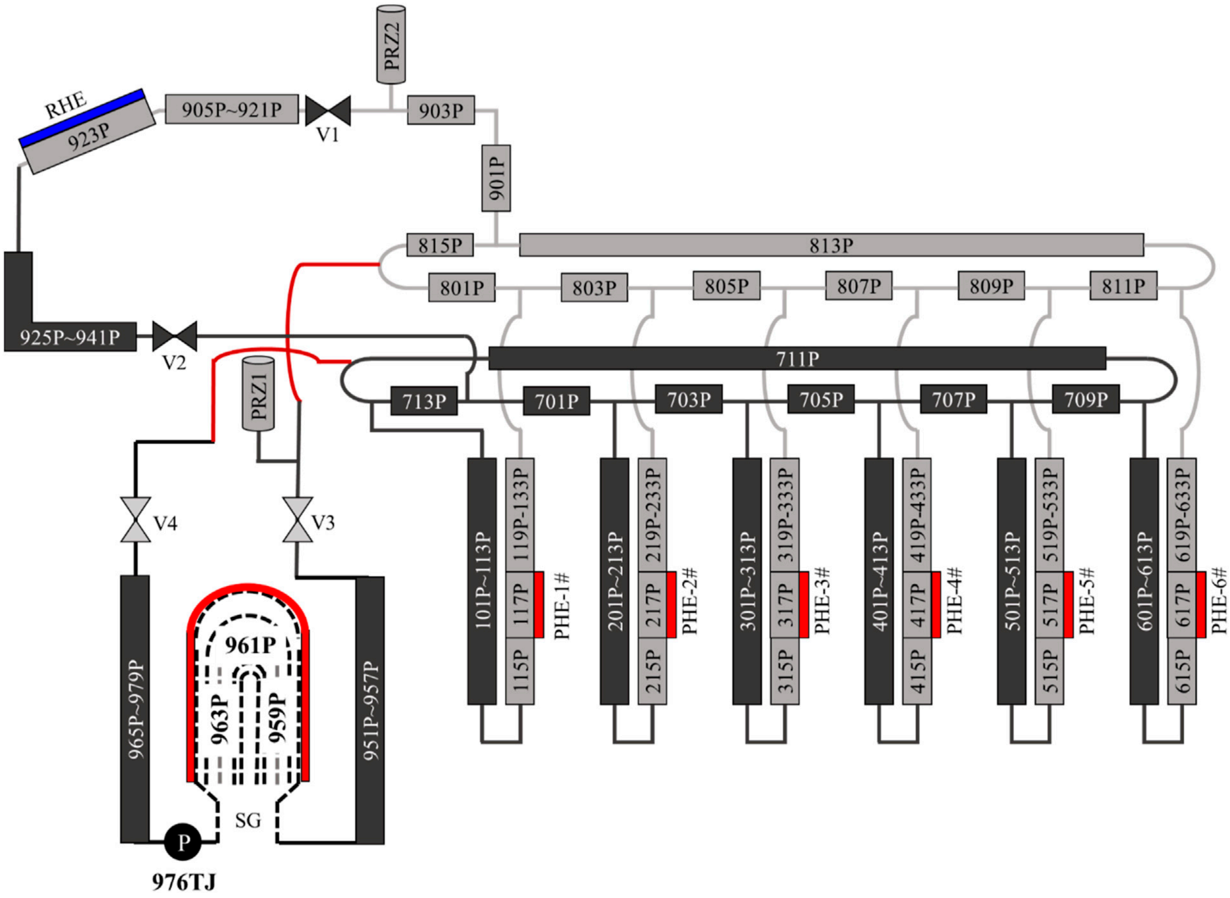

FIGURE 11
RELAP5 node figure of an improved PRHRS design.

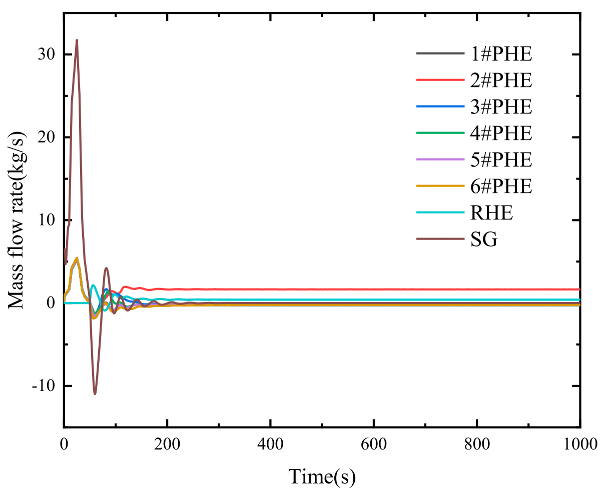

FIGURE 12
Transient flow rate of the improved design with primary fluid temperature of 533.15 K.

This means that the design of ring headers is an important cause on flow instability. In the RELAP5 model without ring headers, the steady-state flow rates of the SG branch and the six PHE branches are larger than that of the original model.

(3) The initial flow direction of PRHRS has a significant influence on the transient PRHRS flow characteristics. In a lower primary fluid temperature range of 327.15 K–443.15 K, the steady-state flow rates are opposite to the original model once the initial flow direction of SG branch is reversed. The SG branch and all PHE branches absolute value steady state flow rates increase when the initial flow direction of SG branch reversed, while the flow rate of RHE branch is almost unchanged.

(4) A preliminary improvement of PRHRS design is purposed, where the tees of SG branch are moved from the RHE branch to the ring headers. Preliminary numerical results show that the flow oscillations are effectively suppressed when fail to isolate SG branch. Further numerical simulations and experiments are planned to confirm the effectiveness of the improved PRHRS design.

Data availability statement

The original contributions presented in the study are included in the article/Supplementary material, further inquiries can be directed to the corresponding authors.

Author contributions

GY: Writing–review and editing, Writing–original draft, Visualization, Validation, Software, Methodology. LXb: Writing–review and editing, Resources, Funding acquisition, Conceptualization. LZ: Data curation, Formal Analysis, Writing–review and editing. HS: Writing–review and editing, Methodology, Investigation. ZL: Data curation, Writing–review and editing. XY: Writing–review and editing, Supervision. LXt: Writing–review and editing, Resources, Project administration. ZY: Funding acquisition, Project administration, Resources, Writing–review and editing.

Funding

The author(s) declare that no financial support was received for the research, authorship, and/or publication of this article.

Conflict of interest

Authors GY, HS, ZL, and XY were employed by China Nuclear Power Engineering Co., Ltd.

The remaining authors declare that the research was conducted in the absence of any commercial or financial relationships that could be construed as a potential conflict of interest.

Publisher's note

References

Creveling, H. F., Paz, J., Baladi, J. Y., and Schoenhals, R. J. (1975). Stability characteristics of a single-phase free convection loop. *J. Fluid. Mech.* 67 (1), 65–84. doi:10.1017/S0022112075000171

Gartia, M. R., Pilkhwal, D. S., Vijayan, P. K., and Saha, D. (2006). "Metastable regimes: a parametric study in reference to single-phase parallel channel natural circulation systems," in The Proceeding of 14th International Conference on Nuclear Engineering (ICONE 14), Miami, Florida, USA, July 17–20-2006 (IEEE).

Geng, Y., and Liu, X. (2023). "Numerical simulation of the transient flow characteristics and thermal stratification phenomena in the passive residual heat removal system of NHR-200-II," in *Proceedings of the 23rd pacific basin nuclear conference, volume 1. PBNC 2022. Springer proceedings in physics*. Editor C. Liu (Singapore: Springer), 283, 1031–1045. doi:10.1007/978-981-99-1023-6_87

IAEA (2012). *Status of small and medium reactor designs*. Vienna: IAEA.

INET (2018). *Test of passive residual heat removal system for low-temperature reactor (internal technical report), Institute of nuclear and New Energy Technology (INET)*. Beijing, China: Tsinghua University.

Keller, H., and Joseph, B. (1966). Periodic oscillations in a model of thermal convection. *J. Fluid. Mech.* 26 (03), 599–606. doi:10.1017/S0022112066001423

Liu, B., Liu, J., and Shen, Le (2023). Low-temperature nuclear heating reactors: characteristics and application of licensing law in China. *Front. Energy Res.* 10, 1060126. doi:10.3389/fenrg.2022.1060126

Sen, M., and Trevino, C. (1982). Dynamic analysis of a one-dimensional thermosyphon model. *J. Therm. Eng.* 3 (1), 15–20.

Takeda, T., Kawamura, H., and Seki, M. (1987). Natural circulation in parallel vertical channels with different heat inputs. *Nucl. Eng. Des.* 104 (2), 133–143. doi:10.1016/0029-5493(87)90294-9

Wang, D. Z., Lin, J. G., Ma, C. W., et al. (1993). Design of 200MW nuclear heating station. *Nucl. Power. Eng.* 14 (4), 289–295.

Welander, P. (1967). On the oscillatory instability of a differentially heated fluid loop. *J. Fluid. Mech.* 29 (1), 17–30. doi:10.1017/S0022112067000606

Zhang, Z. Y., Gao, Z. Y., Wang, Y. S., et al. (1993). Inherent safety of 200MW nuclear heating reactor. *Nucl. Power. Eng.*, 227–231+255.

frontiers | Frontiers in Energy Research

TYPE Methods
PUBLISHED 07 June 2024
DOI 10.3389/fenrg.2024.1407170

OPEN ACCESS

EDITED BY
Jiankai Yu,
Massachusetts Institute of Technology,
United States

REVIEWED BY
Wei Li,
Xi'an Jiaotong University, China
Muhammad Saeed,
University of Electronic Science and
Technology of China, China

*CORRESPONDENCE
Zhiyun Cai,
✉ 18200522011@163.com

RECEIVED 26 March 2024
ACCEPTED 10 May 2024
PUBLISHED 07 June 2024

CITATION
Cui H and Cai Z (2024), HPR1000 pressurizer degassing system design and analysis.
Front. Energy Res. 12:1407170.
doi: 10.3389/fenrg.2024.1407170

HPR1000 pressurizer degassing system design and analysis

Huaiming Cui and Zhiyun Cai*

Science and Technology on Reactor System Design Technology Laboratory, Nuclear Power Institute of China, Chengdu, Sichuan, China

In the Hualong-1 Unit (HPR1000), the hydrogen (H_2) concentration should be reduced to 15 mL (STP)/kg 24 h before reactor shutdown when the reactor vessel is scheduled to be opened. The traditional degassing method, i.e., letting down the reactor coolant through a chemical and volume control system, will take longer, and its operation is more complicated. To shorten the degassing time and simplify the operation, this paper proposes a pressurizer degassing system design for HPR1000 by applying the pressurizer as thermal degassing equipment. Then, the degassing system optimization analysis is carried out under a full range of steady operating conditions during shutdown, and the optimal size of the flow-limiting orifice plate is obtained. Meanwhile, in order to verify the transient characteristic during the degassing process to ensure operating safety, a dedicated transient degassing program based on an improved non-equilibrium multi-region pressurizer model and a transient degassing model is used to carry out a transient simulation analysis of this process. The transient simulation results show that, under bounding conditions of hot−zero-power operation, during the degassing process, the pressure of the pressurizer decreases by a maximum of 0.038 MPa and the water level increases by 0.016 m above the normal level. As can be seen, both the pressure and water level are within the normal operation band and shall not initiate any safety signal. Meanwhile, the entire transient process lasts approximately 24 min and then enters a stable degassing period. It takes approximately 5.2 h to remove the gas dissolved in the reactor coolant from 35 mL (STP)/kg to 15 mL (STP)/kg. The analysis shows that the pressurizer degassing system designed for HPR1000 is safe, effective, and reliable.

KEYWORDS

pressurizer degassing, Hualong-1 Unit, non-equilibrium multi-region model, degassing transient, degassing optimizer, system design

1 Introduction

The Hualong-1 Unit (HPR1000) is a third-generation nuclear power plant that is completely self-developed and designed by China using the highest international safety standards. It innovatively puts forward the safety concept of "active and passive safety," provides comprehensive measures for serious accident prevention and mitigation, and fully absorbs the experience feedback from the Fukushima accident. It has a core damage frequency (CDF) $\leq 10^{-6}$/reactor·year and a large release frequency (LRF) $\leq 10^{-7}$/reactor•year.

The HPR1000 reactor cooling system (RCS) consists of three parallel heat transfer loops, each with a reactor coolant pump, a steam generator, and associated pipes and valves. In addition, the RCS includes a pressurizer, a corresponding pressurizer spray subsystem, and an electric heating subsystem to control the pressure of the pressurizer. A 3D diagram of the HPR1000 RCS is shown in Figure 1.

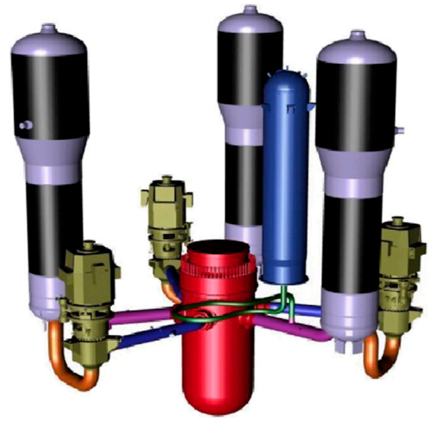

FIGURE 1
Three-dimensional (3D) diagram of the HPR1000 RCS.

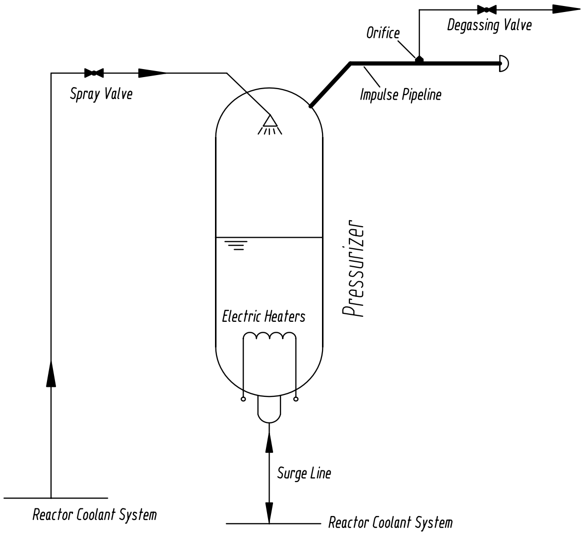

FIGURE 2
Schematic diagram of the HPR1000 regulator degassing system.

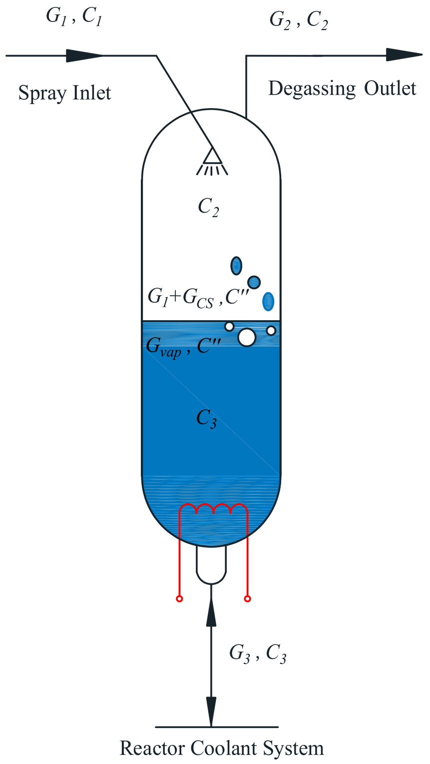

FIGURE 3
Degassing flow diagram.

The traditional degassing method is used to let down the reactor coolant through the chemical and volume control system under water–solid conditions. Engineering experience has shown that this traditional method is very complex and time-consuming.

To shorten the degassing time and simplify the operation, this paper proposes a pressurizer degassing system design for HPR1000 by applying the pressurizer as thermal degassing equipment. The pressurizer degassing system flow diagram is shown in Figure 2. The degassing pipeline of the pressurizer degassing system is connected to the pressurizer safety valve impulse pipeline, and a flow-limiting orifice plate is installed at the entrance of the degassing pipeline to limit the degassing flow. The degassing valve is selected as a remotely controlled, air-operated valve. During shutdown operation, when RCS degassing is required, the operator can manually open the degassing valve and modulate the spray-valve opening to adjust the charge/let-down flow rate according to the specific degassing procedure to degas the RCS continuously. The radioactive waste gas discharged from the RCS is then led into the radioactive gas treating system.

The principle for the degassing process is as follows.

First, the reactor coolant is pumped into the pressurizer vapor space through a pressurizer spray system by the reactor coolant pump (RCP). Since the concentration of non-condensing gas in the spray liquid is much higher than the equilibrium concentration of steam in the pressurizer vapor space, the non-condensing gas will then migrate from the spray liquid into the pressurizer vapor space. Therefore, the gas partial pressure of the pressurizer vapor space will increase. At the same time, mass exchange and gas migration occur continuously between the pressurizer vapor space and liquid space until the two-phase system achieves a new equilibrium. Then, the degassing valve is opened to discharge the pressurizer steam, whose gas partial pressure is increased, and the electric heater is put on to supplement the discharged gas and the lost heat, by which the pressure of the pressurizer and the corresponding saturation temperature are maintained within the allowed range. Repeating the above process can achieve the purpose of reducing the concentration of non-condensing gas in the primary coolant.

The pressurizer degassing system design can maximize the use of the pressurizer and is consistent with the principles of simplicity and economy for a small module reactor. At the same time, a reasonable system design can make degassing more efficient, the degassing time shorter, and operation safer. In this paper, the optimal system design of HPR1000 is first obtained by using the verified steady-state pressurizer degassing model and optimization algorithm. Then, to verify the safety of the optimized system design, a transient analysis of the process when opening the degassing valve is simulated based on the verified transient pressurizer model to ensure that the pressure and water level in the pressurizer do not fluctuate significantly to activate the safety protection device. The paper is structured as follows: Section 1 is the introduction; Section 2 provides the mathematical models for the steady-state and transient analysis of HPR1000; Section 3 describes the degassing system of HPR1000; and Section 4 provides the results and discussion.

2 Preliminaries

2.1 Steady degassing model

The degassing process is based on solution and mitigation theory, which can be described by Henry's Law (Henry, 1803). A typical pressurizer degassing model is shown in Figure 3.

In the figure, C_1, C_2, C_3, C', and C'' are the concentrations of non-condensable gas in the spray flow, discharging flow, coolant return from the surge line to the reactor loop, and evaporative gas in the pressurizer, respectively; G_1, G_2, G_3, G_{cs}, and G_{vap} are the corresponding mass flows.

Caldwell (1956) proposes a calculation model for steady-state hydrogen (H_2) removal efficiency for the pressurizer. Zhong et al. (2018) proposed a more accurate steady-state degassing model for the pressurizer, which can be used as the basis for theoretical research on degassing.

Based on the study by Zhong et al. (2018), the equation for the concentration of non-condensable gas in the pressurizer vs time is

$$C_1(t) = C_1(0)\exp\left(-\frac{G_1\varepsilon + G_2(1-\varepsilon)}{W}t\right), \tag{1}$$

where ε is the degassing efficiency.

Using this formula, the degassing time to reach a certain degassing concentration and the degassing concentration change curve in the coolant can be calculated under a given degassing efficiency.

2.2 Degassing optimization algorithm

The degassing efficiency can be influenced by different inherent characteristics of the pressurizer, degassing operating conditions, degassing flow rate, and degassing type. To obtain the optimal system design, a verified steady-state degassing optimization algorithm (Zhong et al., 2018) is adopted in this paper, and its main ideas are as follows.

2.2.1 Objective function

The degassing period T_d (Zhong et al., 2018) is defined as

$$T_d = \frac{C_1(t)}{\left|\frac{dC_1(t)}{dt}\right|}, \tag{2}$$

where T_d represents the time taken for the concentration of the non-condensable gas in the reactor coolant to decrease to $1/e$ of the initial concentration, reflecting the length of degassing time, and, therefore, serves as an objective function.

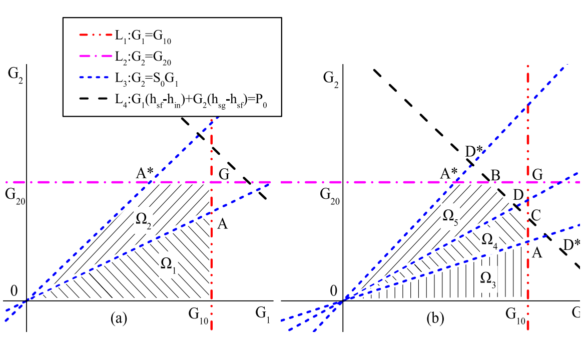

FIGURE 4
Optimization algorithm diagram (Zhong et al., 2018).

2.2.2 Constraints

To ensure the smooth operation of the degassing process, there are two constraints (Zhong et al., 2018):

1) The discharging flow rate must be less than the spray flow.
2) The electric heater cannot be overloaded and has a maximum limit value.

2.2.3 Optimization algorithm

Based on the constraints, the feasible region of the optimization objective is a linear constraint set, as shown in Figure 4 (Zhong et al., 2018). Since T_d (G_1, G_2) is a nonlinear function of G_1 and G_2, the optimization problem is a convex optimization problem.

The feasible region boundary in the figure above consists of four constraint lines, namely, L_1: $G1 = G10$, representing the maximum spray flow constraint line; L_2: $G2 = G20$, indicating the maximum discharging flow constraint line; L_3: $G2 = S0G_1$, which is the spray flow constraint line; and L_4: $G1\ (hsf\text{-}hin)+G2\ (hsg\text{-}hsf) = P0$, representing the electric heating power constraint line. Here, h_{sf} is the enthalpy of saturated water, h_{sg} is the enthalpy of saturated steam, and h_{in} is the enthalpy of spray flow.

2.3 Improved non-equilibrium multi-region pressurizer model

Typical pressure-level response models for pressurizer simulation include the non-equilibrium two-region model, the non-equilibrium tri-region model, and the non-equilibrium multi-region model. The two-region model was first proposed by Redfield and Margolis (Gunther and Kreith, 1950; Redfield et al., 1968; Nahavandi and Makkenchery, 1970; Baron, 1973; Kim et al., 2006). In this model, thermal stratification will be induced when cold water enters the pressurizer, which will affect its accuracy. The tri-region model was proposed first by Baggoura, Martin, and Baek (Abdallah et al., 1982), which divides the entire pressurizer into three regions, namely, vapor region, water region, and surge region. Since this model does not clearly define the surge region, the initial

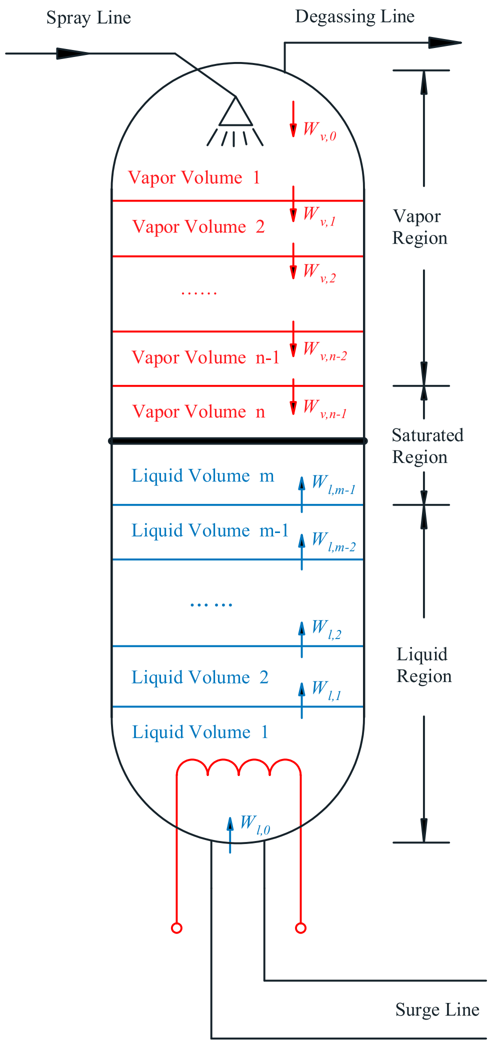

FIGURE 5
Multi-region non-equilibrium model.

volume is uncertain, and the dividing coefficient is also hard to determine, which is critical to the simulation accuracy.

The non-equilibrium multi-region model divides the entire pressurizer into three main regions (vapor region, liquid region, and saturated region), and each region is further subdivided into a number of control volumes, as shown in Figure 5. The mass and energy-exchanging processes can be more precisely simulated through this model, and it can overcome the problems that exist in two-region and tri-region models. Based on the multi-region model, an improved non-equilibrium multi-region model was proposed by Zhong et al. (2019), which is more applicable to the pressurizer degassing transient simulation analysis.

2.3.1 Control equations

From mass conservation and energy conservation, for liquid region i ($i = 1,2, \ldots ,m\text{-}1$),

$$\frac{d\left(\rho_{l,i}\frac{V_L}{m}\right)}{d_t} = W_{l,i-1} - W_{l,i} - W_{be,l,i}, \tag{3}$$

$$\frac{d\left(\left(\rho_{l,i}h_{l,i} - p\right)\frac{V_L}{m}\right)}{d_t} = W_{l,i-1}\tilde{h}_{l,i-1} - W_{l,i}\tilde{h}_{l,i-1} - W_{be,l,i}h_{sg} + P_{l,i} + Q_{tc,l,i}, \tag{4}$$

where p is the RCS pressure, Pa; V_L is the pressurizer volume, m^3; $W_{x,i}(x = 1,v)$ represents the mass flow rate between control volume i and i+1, kg/s; $\tilde{h}_{x,i}$ is the enthalpy between i and i+1, J/kg; $W_{be,l,i}$ is the flashing flow rate of volume i, kg/s; $P_{l,i}$ represents the heat power of liquid region volume i, W; and $Q_{tc,x,i}$ is the thermal conductivity of volume i, W.

For vapor region i ($i = 1,2, \ldots ,n\text{-}1$),

$$\frac{d\left(\rho_{v,i}\frac{V_T - V_L}{n}\right)}{d_t} = W_{v,i-1} - W_{v,i} - W_{bc,v,i} - W_{sc,v,i}, \tag{5}$$

$$\frac{d\left(\left(\rho_{v,i}h_{v,i} - p\right)\frac{V_T - V_L}{n}\right)}{d_t} = W_{v,i-1}\tilde{h}_{v,i-1} - W_{v,i}\tilde{h}_{v,i} - W_{bc,v,i}h_{sf} - W_{sc,v,i}h_{sg} + Q_{tc,v,i}, \tag{6}$$

where V_T is the pressurizer volume, m^3; $W_{bc,v,i}$ is the condensate flow rate of volume i, kg/s; and $W_{sc,v,i}$ is the spray flow rate of volume i, kg/s. For the saturated region,

$$\frac{d\left(\rho_{sf}\frac{V_L}{m} + \rho_{sg}\frac{V_T - V_L}{n}\right)}{d_t} = W_{be,sum} + W_{bc,sum} + W_{l,m-1} + W_{v,n-1} + W_{sp} + W_{sc,sum}, \tag{7}$$

$$\begin{aligned} \frac{d\left(\left(\rho_{sf}h_{sf} - p\right)\frac{V_L}{m} + \left(\rho_{sg}h_{sg} - p\right)\frac{V_T - V_L}{n}\right)}{d_t} &= W_{be,sum}h_{sg} + W_{bc,sum}h_{sf}, \\ &+ W_{l,m-1}\tilde{h}_{l,m-1} + W_{v,n-1}\tilde{h}_{v,n-1}, \\ &+ \left(W_{sp} + W_{sc,sum}\right)h_{sf} + Q_{tc,l,m} + Q_{tc,v,n}, \end{aligned} \tag{8}$$

where $W_{be,sum}$ represents the total flashing flow rate entering the vapor region from the liquid region, kg/s. $W_{be,sum}$ represents the total condensate flow rate entering the saturated region from the vapor region, kg/s, volume i and i+1, kg/s; Wsp is the pressurizer spray flow rate; and Wsc,sum is the total spray droplet flow rate, kg/s.

2.3.2 Physical models

During the pressurizer degassing process, two physical phenomena occur. One is flashing and steam condensation, while the other is spray condensation.

The flashing process occurring in the liquid region can be described as the process in which bubbles form and rise from the liquid region; the steam condensation process occurs when the droplets in the vapor region fall into the liquid region. Then, the flashing flow rate for volume i (i = 1, 2, . . . , m-1) in the liquid region is

$$W_{be,l,i} = \rho_{sg}\alpha_{l,i}AV_{br,l,i}, \tag{9}$$

where V_{br} is the bubble rising speed, m/s, which can be obtained by the Gunther–Kreith correlation (Gunther and Kreith, 1950).

Furthermore, the steam condensation flow rate for volume i (i = 1, 2, . . . , n-1) in the vapor region is

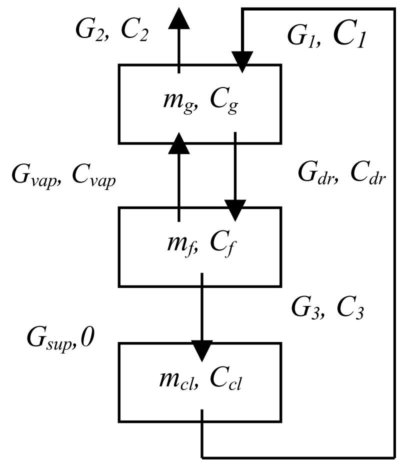

FIGURE 6
Degassing transient model diagram.

$$W_{bc,v,i} = \rho_{sf}\left(1-\alpha_{v,i}\right)AV_{cf,v,i}, \tag{10}$$

where V_{cf} is an experienced constant.

The homogeneous flow model is applied to both vapor and liquid regions; then,

$$\alpha = \frac{1}{1+\frac{\rho_{sg}}{\rho_{sf}}\left(\frac{1}{x}-1\right)}. \tag{11}$$

The spray condensation process occurs when the spray droplets condense the surrounding steam as they fall, and then the condensates enter the saturated region. From energy conservation, the total condensation flow rate is

$$W_{sc,sum} = W_{sp}\frac{h_{sf}-h_{sp}}{h_{sg}-h_{sf}}, \tag{12}$$

where h_{sp} is the enthalpy of the entrance spray liquid, J/kg.

2.4 Transient degassing model

During the degassing process, the pressure and water level in the pressurizer will fluctuate as the degassing valve opens, which can, in turn, affect the degassing efficiency. Thus, a pressurizer degassing transient model is required to simulate this process.

A lumped parameter method is applied in establishing the transient degassing model (Zhong et al., 2021), as shown in Figure 6.

From mass conservation,

$$\frac{d\left(m_g C_g\right)}{d_t} = G_1C_1 - G_2C_2 - G_{dr}C_{dr} + G_{vap}C_{vap}, \tag{13}$$

$$\frac{d\left(m_f C_f\right)}{d_t} = G_{dr}C_{dr} - G_{vap}C_{vap} - G_3C_3, \tag{14}$$

$$\frac{d\left(m_{cl}C_{cl}\right)}{d_t} = G_3C_3 - G_1C_1, \tag{15}$$

$$\frac{d\left(m_{cl}\right)}{d_t} = G_{sup} + G_3 - G_1, \tag{16}$$

where m_{cl} is the total mass of the RCS coolant, kg; C_{cl} is the gas concentration dissolved in the RCS coolant, kg/kg (H_2O); and G_{sup} is the makeup flow rate, kg/s.

For the gas concentration of the interface between the vapor and liquid regions,

$$C_{dr} = \left(K_i\frac{M_{H_2O}}{M_i}p_{H_2O}\right)C_g, \tag{17}$$

$$C_{vap} = \left(\frac{M_i}{K_iM_{H_2O}p_{H_2O}}\right)C_f, \tag{18}$$

where K_i is the Henry coefficient, which is the function of the saturated pressure p.

Before this model can be used to calculate the transient of the gas concentration of the pressurizer and the primary coolant, it is necessary to obtain the values of the thermal–hydraulic physical quantities of the pressurizer, such as pressure, mass, and mass flow rate. In this paper, the thermal–hydrodynamic calculations are given to the model proposed in Section 2.3, and then the calculated values are passed to this model to calculate the gas concentration. Zhong et al. (2021) provides the specific computational framework.

3 Degassing system analysis

3.1 Optimal size of the flow-restricting orifice

The optimal size of the flow-restricting office is calculated using the degassing optimization algorithm presented in Section 2.2. Seven pressure plateaus during plant shutdown operation are selected for the optimization calculation of pressurizer degassing (15.5 MPa–2.6 MPa [pressure of the steam bubble collapsed]), and the corresponding spray inlet temperature is the highest temperature allowed for each operating condition to maximize the degassing efficiency (Zhong et al., 2018). The available power of pressurizer electric heaters is 0–100%, and the maximum ratio of gas discharging flow to spray flow is set to be 1.0.

Based on the boundaries and conditions described above, the calculated results are shown in Table 1:

As shown in the optimization calculation results, the size of the flow-limiting orifice plate is in the range of 1.701 mm–2.343 mm. The larger the size of the flow-limiting orifice plate, the greater the system pressure fluctuations when the degassing valve is opened, especially under the high-pressure plateau. At the same time, for the low-pressure plateau, a larger flow-limiting orifice plate means more heat loss and a lower ratio of discharging and spray flow.

After comparative analysis, the size of the flow-limiting orifice plate is selected to be 1.7 mm. This selection not only ensures the stability of the system pressure fluctuations but also takes into account the degassing efficiency of the low-pressure plateau.

After using the 1.7-mm flow-limiting orifice plate. the hydrogen concentration vs. time curves when degassing at different pressure and temperature plateaus can be calculated using Equation 1, and the results are shown in Figure 7.

As shown in the figure, the lower the degassing pressure, the higher the degassing efficiency, and the shorter the degassing time required. The degassing time is shortest at the 2.6-MPa plateau, and

TABLE 1 Optimization calculation results.

Pressure/ MPa (abs)	Spray inlet temperature/°C	Electric heater power/%	Ratio of discharging flow to spray flow	Degassing period/h	Degassing efficiency(%)	Size of the orifice/mm
15.5	291.7	100	0.035	8.5	91.596	2.343
12	274.68	100	0.026	7.8	94.248	2.192
10	261.00	100	0.022	7.4	95.370	2.079
8	245.01	100	0.019	6.9	96.561	1.988
6	225.59	100	0.015	6.5	97.705	1.831
4	200.36	100	0.013	6.1	98.687	1.718
2.6	176.05	100	0.011	5.2	99.271	1.701

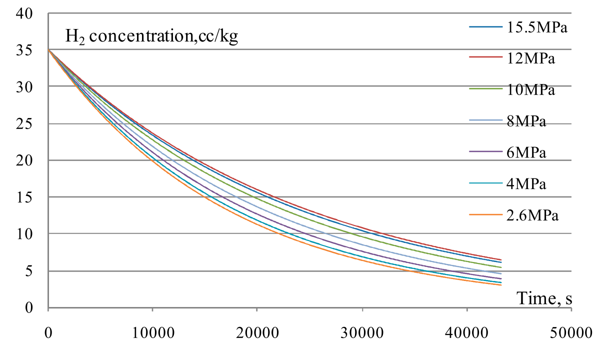

FIGURE 7
Hydrogen concentration vs. time curves.

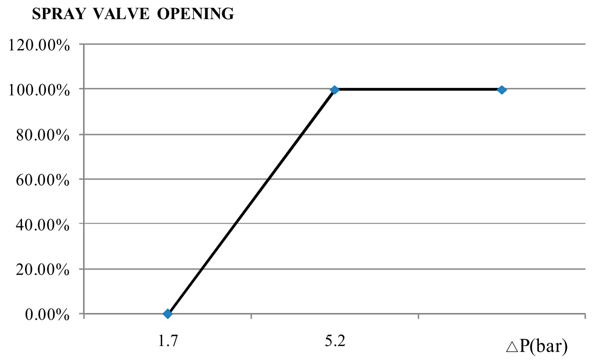

FIGURE 8
Opening of the spray valve vs. pressure difference.

TABLE 2 Degassing transient initial condition.

Item	Value	Unit
RCS pressure	15.5	MPa
RCS temperature	291.7	°C
Spray flow	3.582	kg/s
Water level	3.591	m
H_2 concentration	35	cc/kg

it takes approximately 5.2 h to remove the gas dissolved in the reactor coolant from 35 mL (STP)/kg to 15 mL (STP)/kg.

3.2 Degassing transient simulation analysis

3.2.1 Initial condition

Although the RCS can be degassed at any shutdown plateau, the bounding condition is the hot–zero-power operation. Prior to opening the degassing valve, the operator energizes all the pressurizer heaters and places the spray valve in automatic control mode, according to the operating procedure. When the plant enters a stable condition approximately 200 s later, the operator opens the degassing valve. Therefore, the initial condition parameters can be easily calculated through heat balance (see Table 2).

3.2.2 Boundary conditions

Boundary conditions are as follows:

i. Spray valve

The spray valve is placed into automatic control mode, whose opening is a function of the pressure difference between the measured pressure and the set pressure (see Figure 8).

ii. Surge line

The in-surge or out-surge flow rate in the surge line will vary with the spray flow and the thermal expansion of the RCS automatically.

iii. Electrical heaters

All the electrical heaters are energized according to the operating procedure and the optimized calculation result.

iv. Degassing valve

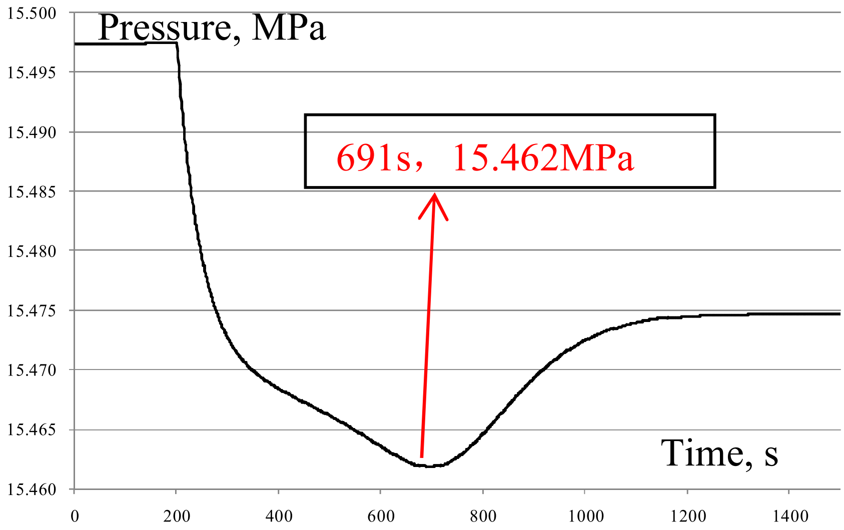

FIGURE 9
Pressure transient curve.

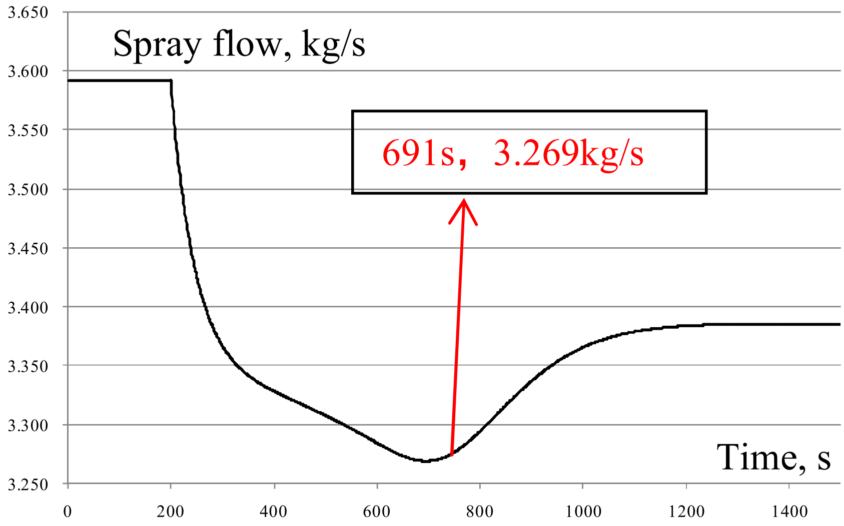

FIGURE 10
Spray flow-rate transient curve.

The degassing valve will be fully open at 200 s, and the flow will be limited by the downstream orifice plate with a size of 1.7 mm.

3.2.3 Transient simulation analysis

Transient simulation analysis is conducted using the improved non-equilibrium multi-region pressurizer model described in Section 2.3. The total simulation time is set at 3,000 s, and the time step is set to 0.1 s. By repeated trial calculation, when the grid number of the liquid region and vapor region reaches 300, a grid-independent solution can be obtained.

The degassing valve is opened 200 s later, and then the RCS begins to degas the hydrogen. In the degassing transient, the pressure and the spray flow versus time curves are given in Figure 9 and Figure 10, respectively.

From these two transient curves, at the moment of the degassing valve being opened, the pressure decreases rapidly, which will cause the control system to reduce the spray valve opening automatically; thus, the spray flow rate decreases quickly. However, at 263 s, since the spray flow, heater power, and degassing flow reach a heat-balance state gradually, the pressure and spray flow begin to decrease more slowly and eventually arrive at the lowest point at 691 s, with a pressure of 15.462 MPa and a spray flow rate of 3.269 kg/s. Then, the pressure begins to increase, and the spray flow starts to increase. After 1,230 s, the pressure reaches a stable value, which means that the degassing process enters the steady degassing condition.

The water level in the pressurizer is shown in Figure 11. In order to show more details, the section from 100 s to 300 s of the curve is partially enlarged (see Figure 12). As shown in Figure 11, the water

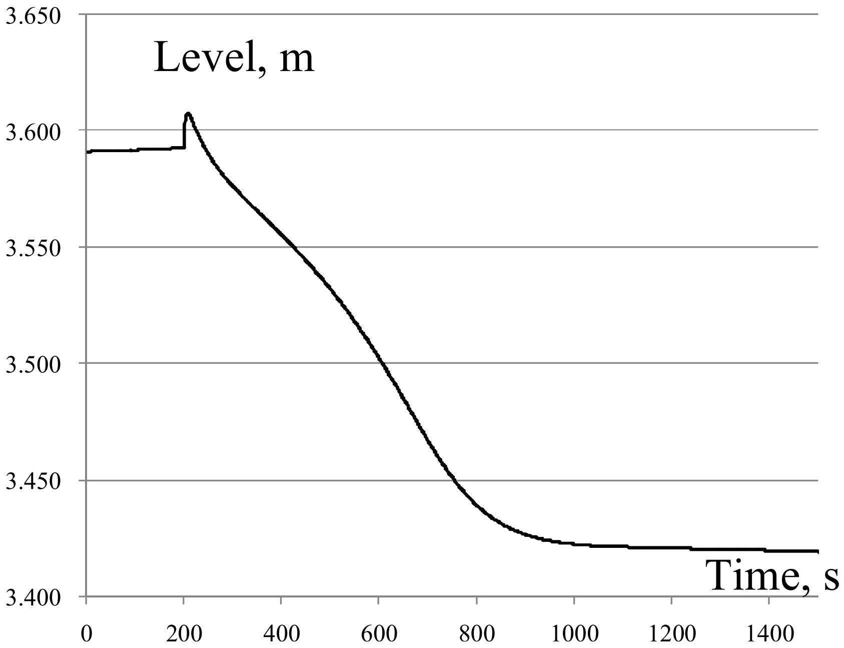

FIGURE 11
Water-level transient curve.

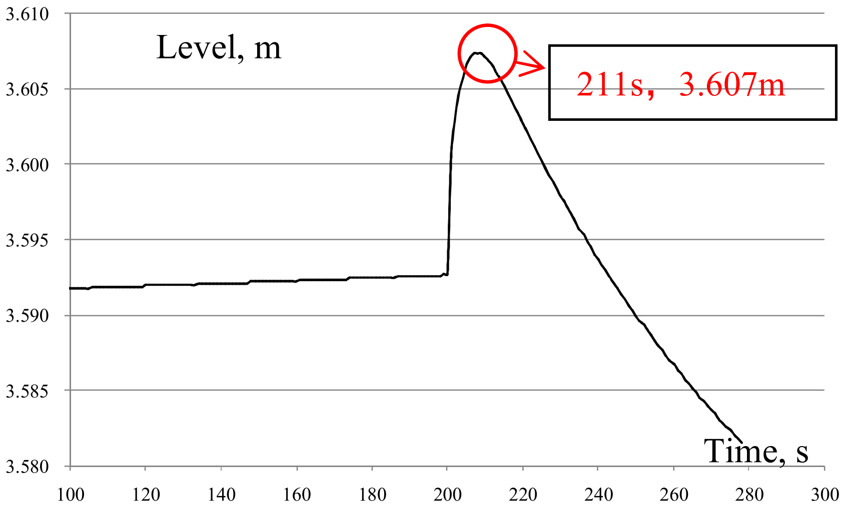

FIGURE 12
Partially enlarged water-level transient curve.

level does not change a lot due to opening the degassing valve. The eventual stable level is 3.421 m. From Figure 12, the partially enlarged water-level curve shows that, at the moment of opening the degassing valve, the water level increases to 3.607 m, which is because the condensation droplets in the vapor region increase quickly due to the pressure decreasing rapidly at this moment.

It can be seen that the HPR1000 regulator degassing system designed in this paper is stable and controllable in the transient process of degassing when opening the exhaust valve, and degassing is safe and effective and meets the safety design requirements.

4 Conclusion

To reduce the time taken to reduce the H_2 concentration from 35 mL (STP)/kg to 15 mL (STP)/kg, this paper designs a pressurizer degassing system by applying the pressurizer as thermal degassing equipment. Then, an optimization analysis is carried out under a full range of shutdown conditions, and the optimal size of the flow-limiting orifice plate is obtained.

Based on the optimal system design, the degassing steady analysis is performed for different degassing pressure plateaus. The analysis results show that the entire degassing process can be completed in as quickly as approximately 5.2 h, which shows a big advantage over the traditional degassing method, which removes non-condensable gas by letting down the reactor coolant to the chemical and volume control system.

To verify the safety features of the pressurizer degassing system designed for HPR1000, this paper performs an analysis of the transient when the degassing valve is opened with a dedicated computer application, which is developed based on the non-equilibrium multi-region model and pressurizer degassing transient model. Simulation results show that the pressure and water level in the pressurizer are within the normal operation band and will not initiate any safeguard signal and also have no effect on the degassing efficiency.

In conclusion, the pressurizer degassing system designed in HPR1000 is reasonable, feasible, safe, effective, and reliable.

Data availability statement

The original contributions presented in the study are included in the article/Supplementary Material; further inquiries can be directed to the corresponding author.

Author contributions

HC: conceptualization, data curation, formal analysis, funding acquisition, investigation, methodology, project administration, resources, software, supervision, validation, visualization, writing–original draft, and writing–review and editing. ZC: writing–original draft and writing–review and editing.

Funding

The author(s) declare that no financial support was received for the research, authorship, and/or publication of this article.

Conflict of interest

The authors declare that the research was conducted in the absence of any commercial or financial relationships that could be construed as a potential conflict of interest.

Publisher's note

References

Abdallah, A. M., Mariy, A. H., Rabie, M. A., and Nagy, M. E. (1982). Pressurizer transients dynamic model. *Nucl. Eng. Des.* 73 (3), 447–453. doi:10.1016/0029-5493(82)90018-8

Baggoura, B., and Martin, W. R. (1983). Transient analysis of the three Mile island unit 2 pressurizer system. *Nucl. Technol.* 62 (2), 159–171. doi:10.13182/nt83-a33215

Baron, R. C. (1973). Digital model simulation of a nuclear pressurizer. *Nucl. Sci. Eng.* 52 (3), 283–291. doi:10.13182/nse73-a19475

Caldwell, C. S. (1956) "RESULTS OF BETTIS TEST FACILITY HYDROGEN DEGASIFICATION TEST," in *BTF special test No. 4[R]. Westinghouse electric corp.* Pittsburgh: Atomic Power Div.

Gramer, G., and Korn, R. (1974). Thermal degassing of the primary coolant of nuclear reactors. *U.S. Pat.* 3 (789), 577.

Gunther, F. C., and Kreith, F. (1950) *Progress report*. California: Jet Propulsion Laboratory, California Institute of Technology.

Henry, W. (1803). Experiments on the quantity of gases absorbed by water, at different temperatures, and under different pressures. *Philosophical Trans. R. Soc. Lond.* (93), 29–276.

Kim, T. W., Kim, J. W., and Park, G. C. (2006). Development of non-equilibrium pressurizer model with non-condensable gas. *Nucl. Eng. Des.* 236 (4), 375–384. doi:10.1016/j.nucengdes.2005.09.003

Nahavandi, A. N., and Makkenchery, S. (1970). An improved pressurizer model with bubble rise and condensate drop dynamics. *Nucl. Eng. Des.* 12 (2), 135–147. doi:10.1016/0029-5493(70)90002-6

Redfield, J. A., Prescop, V., and Margolis, S. G. (1968). Pressurizer performance during loss-of-load tests at Shippingport: analysis and test. *Nucl. Appl.* 4 (3), 173–181. doi:10.13182/nt68-a26382

Zhong, X., Yu, J., Zhang, X., Saeed, M., Li, Y., Chen, Z., et al. (2021). Development of a lumped parameter dynamic degassing model for spray-heating degasser and its application in the pressurizer of a pressurized water reactor. *Nucl. Technol.* 207 (2), 228–246. doi:10.1080/00295450.2020.1763097

Zhong, X., Yu, J., Guo, X., and Saeed, M. (2018). Analysis of degassing time of pressurized water reactor pressurizer. *Nucl. Eng. Des.* 328, 301–308. doi:10.1016/j.nucengdes.2018.01.023

Zhong, X., Zhang, X., Yu, J., Saeed, M., Li, Y., Chen, Z., et al. (2019). Development of an improved non-equilibrium multi-region model for pressurized water reactor pressurizer. *Ann. Nucl. Energy* 126, 133–141. doi:10.1016/j.anucene.2018.11.010

Frontiers in Energy Research

TYPE Original Research
PUBLISHED 22 July 2024
DOI 10.3389/fenrg.2024.1439489

OPEN ACCESS

EDITED BY
Shichang Liu,
North China Electric Power University, China

REVIEWED BY
Chi Xu,
Beijing Normal University, China
Shi Wu,
China Institute of Atomic Energy, China
Baoqin Fu,
Sichuan University, China

*CORRESPONDENCE
Qiangmao Wan,
wanqiangmao@qq.com

RECEIVED 28 May 2024
ACCEPTED 24 June 2024
PUBLISHED 22 July 2024

CITATION
Wan Q, Shu G, Tang J, Pang J, Chen L, Wang D, Lin H and Ding H (2024), Cluster dynamics study on nano damage of RPV steels under proton irradiation at 290°C.
Front. Energy Res. 12:1439489.
doi: 10.3389/fenrg.2024.1439489

Cluster dynamics study on nano damage of RPV steels under proton irradiation at 290°C

Qiangmao Wan[1,2,3]*, Guogang Shu[4], Jiaxuan Tang[1], Jianjun Pang[2], Lisha Chen[3], Duan Wang[1], Hui Lin[1] and Hui Ding[5]

[1]Nuclear Industry College, CNNC, Beijing, China, [2]School of Mechanical and Automotive Engineering, Zhejiang University of Water Resources and Electric Power, Hangzhou, Zhejiang, China, [3]School of Modern Information Technology, Zhejiang Institute of Mechanical and Electrical Engineering, Hangzhou, Zhejiang, China, [4]China United Gas Turbine Technology Co., Ltd, Beijing, China, [5]School of Materials Science and Engineering, Southeast University, Suzhou, China

Irradiation-induced defects such as dislocation loops, cavities or solute clusters and chemical composition segregation of reactor pressure vessel (RPV) steel are the root causes of irradiation embrittlement. Combining two nucleation mechanisms, namely, the uniform nucleation and non-uniform nucleation of solute clusters (such as Cu-rich phase), a cluster kinetic simulation was established based on the reaction rate theory, and the co-evolution of matrix damage and Cu-rich phase in low-copper RPV steel was simulated under irradiation. And the average size and number density of defective clusters and solute clusters were established with irradiation dose. Compared with the average size and number density of dislocation loops observed by transmission electron microscopy (TEM) of proton irradiated RPV steel at 290°C, the verification results show that the cluster dynamics model considering both the nucleation mechanism of interstitial dislocation loops and vacancy clusters can well simulate the irradiation damage behavior of materials.

KEYWORDS

reactor pressure vessels, cluster dynamics, proton irradiation, dislocation loops, solute clusters

Introduction

Nuclear power is an important part of China's modern energy system to achieve cleanliness, efficiency, safety, and sustainability. The reactor pressure vessel (RPV) is a primary safety component of a pressurized water reactor (PWR) nuclear power plant, which loads the core and supports all components inside the reactor. It serves as a safety boundary for primary coolant pressure and radioactive material shielding. RPV is the only non replaceable component. Neutron irradiation can reduce the toughness of RPV materials and increase the risk of brittle failure. The lifespan of nuclear power plants is determined by the operation life of RPV.

The neutron irradiation damage problem of RPV steel is a key issue for the long-term and safe operation of nuclear power plants. Neutron irradiation of RPV steel involves two principal effects. Firstly, nuclear transmutation reaction, and the deexcitation process may also trigger γ, β radiation. Secondly, The collision of neutrons with lattice atoms could form primary collision atoms (PKA), which triggers a cascade of collision processes, including displacement damage and ionization damage. Displacement damage is the most important role, which induce excess interstitial atoms and vacancies. The migration, aggregation, and annihilation of interstitial atoms and vacancies, as well as their interactions with solute atoms and existing defects such as defects of line, surface, and body, or irradiation products such as H and He, ultimately form nanoscale point defect clusters (such as dislocation loops and voids), complexes of point defects and solute yards, solute atom clusters (such as Cu rich clusters or Ni-Mn-Si rich clusters), or interface weakening element segregation (such as P). These nano-structure features hinder dislocation movement or weaken the interface, which cause hardening and embrittlement of RPV materials. Under high dose irradiation conditions, the embrittlement process of RPV steel may be accelerated beyond expectations, ultimately leading to a reduction in the safety window of RPV operation parameters, endangering its structural integrity and restricting its long-term economic and safe operation (Qingmao Wan, 2013; Wang et al., 2020; Ke and Spencer, 2022).

The performance data of RPV materials under high dose irradiation is scarce or scattered in various countries. So it is not possible to reliably extrapolate the prediction model of RPV performance in regulations to new service conditions (Wan et al., 2010). Conducting high dose irradiation testing and evaluating RPV materials directly in experimental or commercial reactors is costly, time-consuming, difficult to control parameters. And neutron irradiation materials and specimens are radioactive and must be operated in hot rooms. Therefore, only a few key parameters can be selectively implemented, so it difficult to conduct comprehensive and systematic neutron irradiation experimental research. Ion irradiation of RPV materials causes displacement damage, ionization damage, and minimal doping. When selecting the appropriate ion energy for irradiation, the collision between the incident ion and the lattice atoms generates cascade collisions induced by PKA, resulting in displacement damage, which plays a major role. Because of the similar mass between protons and neutrons, proton irradiation is commonly used to simulate neutron irradiation to study radiation damage issues.

The experimental method of high flux proton irradiation is used to simulate the irradiation process of materials in nuclear reactors. Combined with theoretical analysis, the performance and related laws of nuclear power materials can be studied (Chitra and and Kotliar, 2000; Huibin et al., 2017; Cui et al., 2020). However, there are also drawbacks such as time consumption and harsh environment for experiment. In contrast, computer simulation methods (He et al., 2012; Mathew et al., 2018; Shimodaira et al., 2018) can not only save a lot of manpower and material resources, reduce development costs, but also provide “experimental data” under extreme conditions (ultra-high radiation, ultra-high pressure, and ultra-high temperature), so as to overcome experimental difficulties. They can also obtain microscopic details of material changes under irradiation conditions and obtain information that cannot be obtained in macroscopic experiments. It has very important theoretical significance for the prediction and evaluation of high dose radiation damage in RPV steel.

The cluster dynamics model based on mean field approximation has high computational efficiency and can quickly describe defect reaction events that occur at different time scales within the same framework. It simulates the diffusion reaction process of defects (clusters) to study the changes of single or small defects with time, space, and size (Wan et al., 2011; Wan Q. M et al., 2012; Yoshiie et al., 2015). It can achieve the same spatial resolution as transmission electron microscopy (TEM). Therefore, cluster dynamics can simulate the kinetic evolution process of defects under reactor irradiation dose across time scales (ps to year) and spatial scales (nm to m).

This study focuses on low copper RPV steel as the research object, establishes a model based on the average rate field theory, and develops a cluster dynamics program for radiation damage. It simulates the micro evolution process of various defects such as migration, aggregation, and nucleation during the radiation damage process, studies the generation and evolution of dislocation loops, voids, and solute clusters, the results of which were compared and verified by the experimental results. The study will provide reference for the prediction and evaluation radiation embrittlement of RPV.

2 Cluster dynamics model and method

2.1 Assumption

Radiation generates displacement cascades and isolated point defects between cascades, which include endogenous vacancy clusters, endogenous interstitial clusters, and endogenous isolated point defects. Most vacancy and interstitial atoms recombine and annihilate. The ratio of endogenous vacancy clusters and interstitial atomic clusters in displacement cascades to the total number of surviving point defects will decay with increasing irradiation dose. The three-dimensional cavity changes include (1) endogenous vacancy clusters of displacement cascades; (2) Two vacancies aggregate to form nuclei; (3) Vacancy clusters capture Cu atoms and transform into Cu rich clusters. The variation of two-dimensional planar interstitial clusters (or dislocation loops) includes (1) endogenous interstitial clusters of displacement cascades; (2) Two interstitial atoms aggregate to form nuclei; (3) Interstitial clusters capture Cu atoms and transform into Cu rich clusters. Three dimensional Cu rich clusters can also nucleate through the aggregation of two Cu atoms, which belongs to uniform nucleation, namely, homogeneous nucleation. Vacancy clusters or interstitial clusters capture Cu atoms and transform into Cu rich clusters, which belongs to heterogeneous nucleation.

2.2 Basic equations

2.2.1 Changes in monomer concentration

Isolated vacancies, interstitial atoms, and Cu atoms can be collectively referred to as monomers. During the irradiation process, the concentrations of vacancies, interstitial atoms, and Cu atoms will evolve over time, and their evolution equations can be expressed as Eqs 1–3:

$$dC_i/dt = P(1-\varepsilon_r)(1-k\varepsilon_{ic,dc}) - Z_{i,v}(D_i+D_v)C_iC_v - Z_{i,i}D_iC_iC_i - Z_{i,d}D_iC_i\rho - Z_{i,ic}D_iC_iS_{ic} - Z_{i,vc}D_iC_iS_{vc} \tag{1}$$

$$dC_v/dt = P(1-\varepsilon_r)(1-k\varepsilon_{vc,dc}) - Z_{v,i}(D_i+D_v)C_iC_v - Z_{v,v}D_vC_vC_v - Z_{v,d}D_vC_v\rho - Z_{v,ic}D_vC_vS_{ic} - Z_{v,vc}D_v(C_v - C_{v,emit})S_{vc} \tag{2}$$

$$
\begin{aligned}
dC_{Cu}/dt = &-Z_{Cu,Cu}D_{Cu}C_{Cu} - Z_{Cu,vc}D_{Cu}S_{vc} \\
&-Z_{Cu,ic}D_{Cu}S_{ic} - Z_{Cu,crp}D_{Cu}\left(C_{Cu} - C_{Cu,emit}\right)S_{crp}
\end{aligned}
\tag{3}
$$

In the formula: C_{i}, C_{v} and C_{Cu} represents the concentrations of interstitial atoms, vacancies, and Cu atoms, respectively; $C_{\mathrm{v,emit}}$ and $C_{Cu,emit}$ represents the concentration of vacancies on the surface of voids and the concentration of Cu atoms at the interface of Cu rich phases, respectively; P is the damage rate, i.e., the injection rate, in units of dpa/s; The recombination probability ε_{r} of Frenkel point defects during the displacement cascade cooling process and $1 - \varepsilon_{\mathrm{r}}$ is represented by the damage efficiency. $\varepsilon_{\mathrm{ic,dc}}$ is the percentage of interstitial atoms in the endogenous interstitial clusters of the displacement cascades; While $\varepsilon_{\mathrm{vc,dc}}$ is the percentage of vacancies in the endogenous vacancy clusters of the displacement cascades; Z is the combination constants or capture reaction constants, the lower corners of i, v, Cu, ic, vc, CRP andρ respectively represent interstitial atoms, vacancies, Cu atoms, dislocation loops, voids, Cu rich phases, and dislocation lines density in the matrix; And $\mathrm{D_i}$, D_v andD_{Cu} is the diffusion coefficients of interstitial atoms, vacancies and Cu atoms, respectively; And S_{ic}, S_{vc} and S_{crp} represents the sink strength of dislocation loops, voids and Cu rich phase for absorption point defects, respectively.

2.2.2 Concentration evolution of clusters

Dislocation loops, vacancies, and Cu rich phases can be collectively referred to as clusters. During the irradiation process, the concentration and size of dislocation loops, vacancies, and Cu rich phases will evolve over time, and their evolution equation can be expressed as Eqs 4–6:

$$
dC_{\mathrm{loop}}/dt = \frac{1}{2}Z_{\mathrm{ii}}D_iC_iC_i + C_{ic,dc} - Z_{Cu,ic}D_{Cu}C_{Cu}S_{ic} \tag{4}
$$

$$
dC_{void}/dt = \frac{1}{2}Z_{vv}D_vC_vC_v + C_{vc,dc} - Z_{Cu,vc}D_{Cu}S_{vc} \tag{5}
$$

$$
\begin{aligned}
dC_{crp}/dt = &\frac{1}{2}Z_{Cu,Cu}D_{Cu}C_{Cu}C_{Cu} + Z_{Cu,ic}D_{Cu}C_{Cu}S_{ic} \\
&+ Z_{Cu,vc}D_{Cu}C_{Cu}S_{vc}
\end{aligned}
\tag{6}
$$

In the formula: C_{loop}、 C_{void} and C_{crp} represents the concentration of dislocation loops, voids, and Cu rich phases, respectively; $C_{ic,dc}$ and $C_{vc,dc}$ represents the concentrations of endogenous interstitial clusters and endogenous vacancy clusters in the displacement cascades, respectively.

2.2.3 Cluster size evolution

During the irradiation process, the size of dislocation loops, voids, and Cu rich phases will evolve over time, and their evolution equation can be expressed as Eqs 7–9:

$$
\begin{aligned}
dN_{loop}/dt = &\left(Z_{i,ic}D_iC_i - Z_{v,ic}D_vC_v\right)S_{ic}/C_{loop} \\
&+N_{ic,dc}C_{ic,dc}/C_{loop} - Z_{Cu,ic}D_{Cu}C_{Cu}S_{ic}/C_{loop}
\end{aligned}
\tag{7}
$$

$$
\begin{aligned}
dN_{void}/dt = &\left[Z_{v,vc}D_v\left(C_v - C_{v,emit}\right) - Z_{i,vc}D_iC_i\right]S_{vc}/C_{void} \\
&+N_{vc,dc}C_{vc,dc}/C_{void} - Z_{Cu,vc}D_{Cu}C_{Cu}S_{vc}/C_{void} \\
&+4\pi R_{void}\left[Z_{v,vc}D_v\left(C_v - C_{v,emit}\right) - Z_{i,vc}D_iC_i\right]
\end{aligned}
\tag{8}
$$

$$
\begin{aligned}
dN_{crp}/dt = &\left[Z_{Cu,crp}D_{Cu}\left(C_{Cu} - C_{Cu,emit}\right)\right]S_{crp}/C_{crp} \\
&+Z_{Cu,vc}D_{Cu}C_{Cu}S_{vc}/C_{crp} + Z_{Cu,ic}D_{Cu}C_{Cu}S_{ic}/C_{crp} \\
&+4\pi R_{crp}\left[Z_{Cu,crp}D_{Cu}\left(C_{Cu} - C_{Cu,emit}\right)\right]
\end{aligned}
\tag{9}
$$

In the formula, N_{loop}, N_{void} andN_{crp} represents the number of monomers contained in each dislocation loop, void, and Cu rich phase, respectively; And $N_{ic,dc}$ and $N_{vc,dc}$ is the number of interstitial atoms contained in each endogenous interstitial atomic cluster and the number of vacancies contained in the endogenous vacancy cluster of displace cascades, respectively; And R_{loop}, R_{void} andR_{crp} is the radii of each dislocation loop, void, and Cu rich phase, in units of the number of monomers.

The radius of dislocation loops, vacancies, and Cu rich phases can be expressed as Eqs 10–12:

$$
R_{loop} = \left(\frac{N_{loop}}{\pi}\right)^{\frac{1}{2}} \tag{10}
$$

$$
R_{void} = \left(\frac{3N_{void}}{4\pi}\right)^{\frac{1}{3}} \tag{11}
$$

$$
R_{crp} = \left(\frac{3N_{crp}}{4\pi}\right)^{\frac{1}{3}} \tag{12}
$$

2.2.4 Cluster hardening

The increase in yield strength caused by irradiation-induced dislocation loops, voids, and Cu rich phases can be expressed as Eq. 13:

$$
\Delta\sigma = \alpha MGb\begin{cases} \sqrt{\rho} - \sqrt{\rho_0}\,, \ \text{for dislocation line} \\ \sqrt{2RN}\,, \text{for disloation loops, voids or Cu} - \text{rich phase} \end{cases} \tag{13}
$$

In the formula: α is the strengthening factor, with a value of 0.1 for dislocation lines; For dislocation loops, the value is 0.267; For voids, the value is 0.05; For the rich Cu phase, the value is 0.15. And ρ are ρ_0 the dislocation line density after irradiation and the initial dislocation line surface density, respectively.

Based on the research results of Garner and Wolfer, the following equation for the evolution of dislocation lines can be proposed (Eq. 14):

$$
d\rho/dt = B\rho^{\frac{1}{2}} - A\rho^{\frac{3}{2}} \tag{14}
$$

The superposition method of various cluster hardening contributions adopts the sum of squares square root method. It can be expressed as Eq. 15.

$$
\sigma_{tot} = \sqrt{\sum \sigma_i^2} \tag{15}
$$

2.3 Main parameters

When solving the partial differential equation of the average rate field, it is important to choose material parameters as accurately as possible, which is beneficial for obtaining reliable prediction results. Table 1 lists the main input parameters for proton irradiated RPV steel at 290°C. Most of the parameters come from literature data (Gan et al., 1999; Kwon et al., 2003; Dubinko et al., 2009; Qingmao Wan, 2013).

2.4 Algorithm for multi-dimensional pathological differential equations

This model belongs to multidimensional ill conditioned rigid differential equations. If we consider the size distribution of various

TABLE 1 Main input parameters of proton-irradiated RPV steel at 290°C.

Parameter name	Parametric symbol	unit	Proton irradiation
Flux	P	dpa/s	1×10^{-5}
Combination probability	ε_r	—	0.98
Point defect percentage in cascaded endogenous clusters	$\varepsilon_{ic,dc}$, $\varepsilon_{vc,dc}$	—	2.5×10^{-4}
Point defect percentage attenuation factor in cascaded endogenous clusters	K	—	0.7
Endogenous interstitial clusters of cascades	$N_{ic,dc}$	atoms	3
Endogenous vacancy clusters of cascades	$N_{vc,dc}$		6
Reaction constant	$Z_{i,v}$, $Z_{v,i}$	—	50
	$Z_{i,i}$, $Z_{v,v}$, $Z_{i,vc}$, $Z_{v,d}$		1
	$Z_{i,d}$, $Z_{i,ic}$		1.25
	$Z_{v,ic}$, $Z_{v,vc}$		1
	$Z_{Cu,Cu}$; $Z_{Cu,vc}$; $Z_{Cu,ic}$		1×10^{-5}; 1.5×10^{-5}; 0.5×10^{-5}
	$Z_{Cu,Crp}$		1
Vacancy formation energy	E_{vf}	ev	1.55
Migration energy	$E_{i,m}$; $E_{v,m}$; $E_{Cu,m}$;		0.25; 1.25; 2.70;
Surface energy; Interface energy	$E_{void,surf}$; $E_{crp,surf}$		0.13; 0.25
Pre coefficient refers to diffusion coefficient	D_{i0}; D_{v0}; D_{Cu0}	cm^2/s	0.05; 0.5; 300
Initial dislocation density	ρ_0	cm^{-2}	1×10^{10}
Lattice constant	a	nm	0.29064

clusters, the number of equations will reach approximately 10^9. This study does not currently consider the size distribution of clusters and only calculates the average size of clusters. The algorithm used is the Runge Kutta method, and a simulation program for nano-structure damage has been developed.

3 Calculation results

3.1 Cluster evolution

Figure 1 shows the dynamic simulation results of A508-3 steel under proton irradiation at 290°C, including a 3 × 5 array diagram. The first line shows the interstitial defects and the hardening components of dislocation loops with the variation of irradiation dose. While the second line shows the vacancy type defects and the hardening components of voids with the variation of irradiation dose. The third line shows the Cu atomic related cluster and the hardening component of Cu rich phases with the variation of irradiation dose. The columns a-e represents monomer concentration, number of monomers contained in the cluster, cluster concentration, cluster size, and cluster hardening component, respectively.

Within the irradiation dose range of 0.01–0.4 dpa, (a) the concentration range of interstitial atoms is 3.4×10^{-16}–1.3×10^{-15}, which gradually decreases with increasing irradiation dose and tends towards equilibrium concentration, with an order of magnitude of 10^{-16}; (b) The number of interstitial atoms contained in every dislocation loop is approximately 100–500; (c) The density range of dislocation loops is 1.3×10^{21}–1.3×10^{22} m^{-3}, which gradually increases with the increase of irradiation dose, fast firstly and then slow, with an order of magnitude of 10^{22} m^{-3}; (d) The diameter is about 2–8 nm, and the diameter shows an increasing trend with increasing dose, and the growth rate shares the same "fast followed by slow" type; (e) The hardening component of dislocation loops shows a similar increasing trend with the irradiation dose, first fast and then slow, increasing from less than 50–160 MPa up to 0.4 dpa.

Within the irradiation dose range of 0.01 to 0.4 dpa, (a) the vacancy concentration range is 4×10^{-8}–1.6×10^{-7}, which gradually decreases with increasing irradiation dose and tends towards equilibrium concentration, with an order of magnitude of 10^{-8}; (b) The number of vacancies contained in a void is approximately 50–150; (c) The density range of voids is 6.0×10^{21}–1.3×10^{23} m^{-3}, which gradually increases with the increase of irradiation dose, fast firstly and then slow, with an order of $10^{23} m^{-3}$; (d) The diameter is about 1–1.5 nm, and the diameter shows an increasing trend with increasing dose, and the growth rate shares the same "fast followed by slow" type; (e) The hardening component of voids shows a similar increasing trend with the irradiation dose, first fast and then slow, increasing from less than 25–50 MPa up to 0.4 dpa.

Within the irradiation dose range of 0.01 to 0.4 dpa, (a) the concentration range of Cu atoms is 9.6×10^{-6}–5.9×10^{-4}, which decreases continuously with increasing irradiation dose; (b) The number of Cu atoms in the Cu-rich phase is approximately 100–800; (c) The density range of Cu rich phases is 4.0×10^{20}–3.1×10^{22} m^{-3},

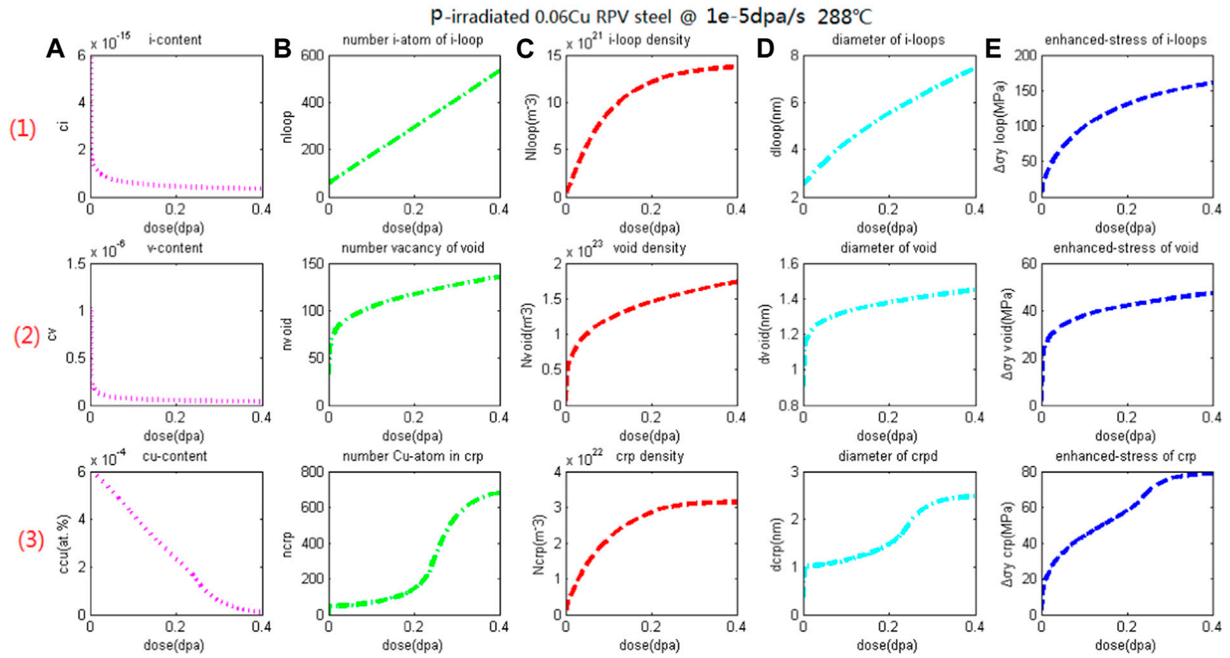

FIGURE 1
Dynamic simulation results of A508-3 steel irradiation at 290°C, the variation of clusters, i.e., (1) interstitial dislocation loops, (2) microvoids, and (3) Cu-rich phases with irradiation flux, including **(A)** monomer concentration; **(B)** the number of monomers in the cluster, **(C)** the concentration of the cluster; **(D)** cluster diameter; **(E)** The amount of hardening caused by clusters.

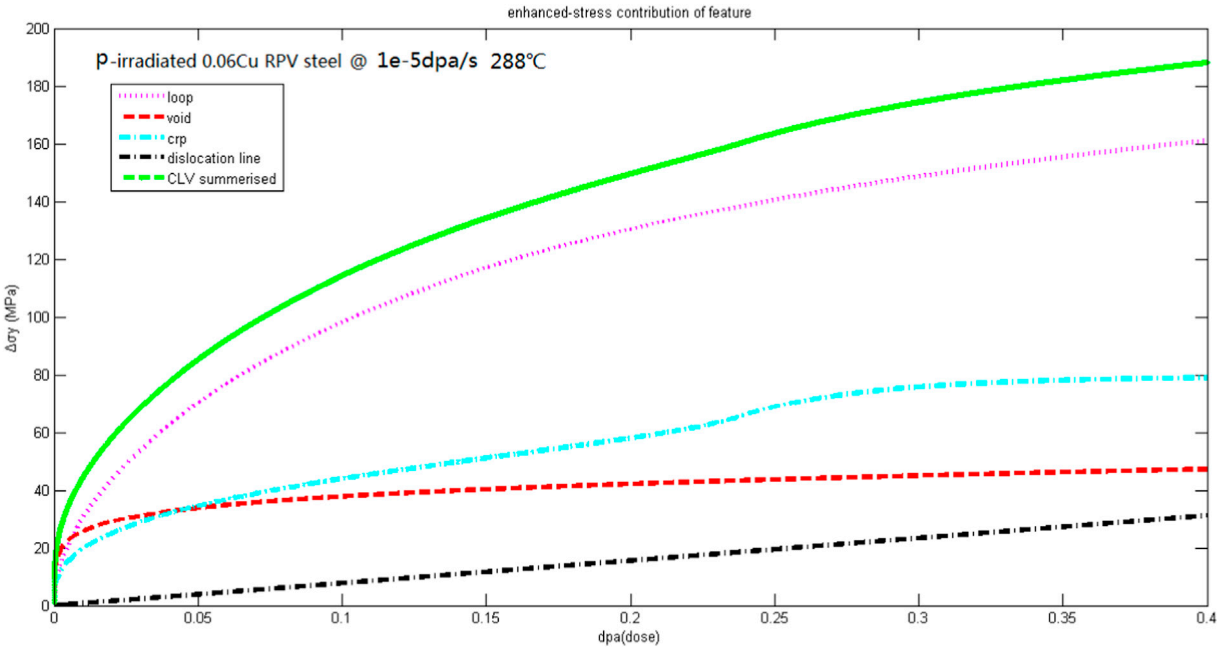

FIGURE 2
Dynamic simulation results of A508-3 steel irradiated by protons at 290°C, the contribution of clusters, i.e., (1) interstitial dislocation loops, (2) microvoids, (3) Cu-rich phases, and (4) dislocation lines, to irradiation hardening.

which gradually increases with the increase of irradiation dose, fast firstly and then slow, with an order of magnitude of 10^{22} m^{-3}; (d) The diameter is about 1–2.5 nm, and the diameter shows an increasing trend with increasing dose, and the growth rate shares the same "fast followed by slow" type; (d) The hardening component of the Cu-rich phases shows a similar increasing trend with the irradiation dose,

TABLE 2 Experimental measurements and simulated values of cluster dynamics of dislocation loops in proton-irradiated Chinese A508-3 RPV steel at 290°C.

	T_i °C	Dose dpa	d nm	N $\times 10^{22} m^{-3}$	$\Delta\sigma_{loop}$ MPa
Measured values of TEM	290	0.163	10.1	0.88	150
Calculated values of DC	290	0.163	~5	0.8	~120
Relative deviation, %	—	—	50%	10%	20%

first fast and then slow, increasing from less than 20–80 MPa up to 0.4 dpa, which is close to the saturation hardening amount of Cu rich phase. The supersaturated solid solution Cu atoms basically precipitate.

3.2 Relationship between cluster hardening component and total hardening amount

Figure 2 shows the variation of various hardening amounts of A508-3 steel under proton irradiation at 290°C with the irradiation dose. Below 0.05 dpa, the hardening components of dislocation loops, voids, and Cu rich phases are comparable for the contribution of the total hardening amount; After 0.05 dpa, the hardening components of dislocation loops, Cu rich phases, voids, and dislocation line networks are ranked in descending order, with hardening component of dislocation loops dominating the total hardening amount. This indicates that the evolution of dislocation loops is the dominant factor for the irradiation embrittlement of A508-3 steel under high dose proton irradiation conditions at 290°C.

4 Experimental verification

The high-temperature proton irradiation test utilizes the 320 kV high charge ion experimental research platform of the National Laboratory of Heavy Ion Accelerator at Lanzhou Institute of Modern Physics. Using an incident beam perpendicular to the surface of the sample, with a scanning area of approximately 1.5 cm^2 × 1.5 cm^2, the total current intensity of the proton beam reaching the sample stage is approximately 25 μ A. The vacuum degree is better than 1×10^{-4} Pa, and the temperature control accuracy is ±5°C. Under the proton irradiation at 290°C, the proton beam density is approximately 6.8×10^{13} ion/cm^2-s, equivalent to 11 μ A/cm^2. This irradiation was conducted to 5.57 ion/cm^2 × 10^{17} ion/cm^2, equivalent to 0.163 dpa. The measured size and number density values were obtained by quantifying the dislocation loops of proton irradiated Chinese A508-3 RPV steel using TEM (Wan Q et al., 2012; Lei et al., 2014). The comparison between the experimental measured values of dislocation loops and the simulated values of cluster dynamics is shown in Table 2. The verification results show that for the dislocation loops in RPV steel irradiated with 290°C proton, the calculated values of cluster dynamics are on the same order of magnitude as the TEM measured values in proton irradiation experiments, with a size deviation of 50%, a number density of 10%, and a hardening deviation of 20%. This indicates that cluster dynamics can effectively simulate the proton irradiation of RPV steel at 290°C.

5 Conclusion

Considered both the homogeneous nucleation mechanisms and the heterogeneous nucleation mechanisms of solute clusters, the study developed a simulation program based on cluster dynamics model for the nano-structure evolution of RPV steel during irradiation. The average size and number density evolution of interstitial dislocation loops, voids, and solute clusters generated by proton irradiation at 290°C were calculated, which were compared and verified with TEM measurements of specific proton irradiation experiment for Chinese A508-3 RPV steels at 0.163 dpa. The research results indicate that the simulation results are roughly consistent with the experimental results. Subsequent research can consider developing more universal cluster dynamics simulation methods with much more defects, conducting parameter sensitivity analysis and comprehensive experimental data validation.

Data availability statement

The datasets presented in this article are not readily available due to some procedural restrictions. Requests to access the datasets should be directed to wanqiangmao@qq.com.

Author contributions

QW: Conceptualization, Data curation, Writing–original draft, Writing–review and editing. GS: Formal Analysis, Writing–original draft, Writing–review and editing, Conceptualization. JT: Methodology, Supervision, Writing–review and editing. JP: Validation, Writing–review and editing. LC: Software, Writing–review and editing, Writing–original draft. DW: Supervision, Writing–review and editing. HL: Project administration, Writing–review and editing. HD: Investigation, Writing–review and editing.

Funding

The author(s) declare that financial support was received for the research, authorship, and/or publication of this article. This work was financially supported by the Zhejiang Provincial Natural Science Foundation of China under Grant No. LGG20E010005, No. LY21E010001, Dean's Fund of nuclear industry college under Grant No. YZJJ-2023-05.

Conflict of interest

Author GS was employed by China United Gas Turbine Technology Co., Ltd.

The remaining authors declare that the research was conducted in the absence of any commercial or financial relationships that could be construed as a potential conflict of interest.

Publisher's note

References

Chitra, G., and Kotliar, R. (2000). Dynamical mean-field theory and electronic structure calculations. *Phys. Rev. B* 62 (19), 12715–12723. doi:10.1103/physrevb.62.12715

Cui, S., Mamivand, M., and Morgan, D. (2020). Simulation of Cu precipitation in Fe-Cu dilute alloys with cluster mobility. *Mater. Des.* 191, 108574. doi:10.1016/j.matdes.2020.108574

Dubinko, V. I., Kotrechko, S. A., and Klepikov, V. F. (2009). Irradiation hardening of reactor pressure vessel steels due to the dislocation loop evolution. *Radiat. Eff. Defects Solids* 164 (10), 647–655. doi:10.1080/10420150903115743

Gan, J., Was, G. S., and Stoller, R. E. (1999). Modeling of microstructure evolution in austenitic stainless steels irradiated under light water reactor condition. *J. Nucl. Mater* 299 (1), 53–67. doi:10.1016/s0022-3115(01)00673-0

He, X., Guo, L., Wu, S., Yang, P., and Wen, Y. (2012). Multiscale modeling and experiment validation of microstructure evolution induced by Ar+ irradiation in Hastlloy C276. *Atomic Energy Sci. Technol.* 46 (2), 130–132. doi:10.7538/yzk.2012.46.02.0129

Huibin, Ke, Peter, W., Edmondson, P. D., Almirall, N., Barnard, L., Robert Odette, G., et al. (2017). Thermodynamic and kinetic modeling of Mn-Ni-Si precipitates in low-Cu reactor pressure vessel steels. *Acta Mater* 138, 10–26. doi:10.1016/j.actamat.2017.07.021

Ke, J. H., and Spencer, B. W. (2022). Mn-Ni-Si precipitates coupled with radiation-induced segregation in low-Cu reactor pressure vessel steels. *J. Nucl. Mater.* 569, 153–163. doi:10.1016/j.jnucmat.2022.153910

Kwon, J., Kwon, S. C., and Hong, J. H. (2003). Prediction of radiation hardening in reactor pressure vessel steel based on a theoretical model. *Ann. Nucl. Energy* 30 (15), 1549–1559. doi:10.1016/s0306-4549(03)00102-6

Lei, J., Ding, H., Shu, G. G, and Wan, Q. M. (2014). Study on the mechanical properties evolution of A508-3 steel under proton irradiation. *Nucl. Instrum. Methods Phys. Res. Sect. B* 338, 13–18. doi:10.1016/j.nimb.2014.07.030

Mathew, J., Parfitt, D., Wilford, K., Riddle, N., Alamaniotis, M., Chroneos, A., et al. (2018). Reactor pressure vessel embrittlement: Insights from neural network modelling. *J. Nucl. Mater* 502, 311–322. doi:10.1016/j.jnucmat.2018.02.027

Qingmao Wan (2013). "Microstructure evolution law and brittlement Prediction model of reactor pressure vessel steels under the irradiation condition,". [dissertation] (Wuhan: Wuhan University), 1–209.

Shimodaira, M., Toyama, T., Yoshida, K., Inoue, K., Ebisawa, N., Tomura, K., et al. (2018). Contribution of irradiation-induced defects to hardening of a low copper reactor pressure vessel steel. *Acta Mater* 155, 402–409. doi:10.1016/j.actamat.2018.06.015

Wan, Q., Shu, G., Ding, H., and Wang, R. (2010). Anyalysis on life extension of PWR-RPV in USA and key isssues on life extension of RPV in China. *Press. Vessel* 27 (6), 105–109. doi:10.3969/j.issn.1001-4837.2010.06.010

Wan, Q., Shu, G., Wang, R., Ding, H., Xiao, P., Qi, Z., et al. (2012b). Study on the microstructure evolution of A508-3 Steel under proton irradiaiton. *Acta metall. Sin* 48 (8), 929–934. doi:10.3724/sp.j.1037.2012.00060

Wan, Q. M., Shu, G. G., Wang, R. S., Ding, H., Peng, X., Zhang, Q., et al. (2012a). Characterization of proton irradiation-induced defect in the 508-3 steel by slowpositron beam. *Nucl. Instrum. Methods Phys. Res. Sect. B Beam Interact. Mater. Atoms* 287 (0), 48–152. doi:10.1016/j.nimb.2012.04.013

Wan, Q. M., Wang, R. S., Shu, G. G., Ding, H., Huang, P., Feng, L., et al. (2011). Analysis method of Charpy V-notch impact data before and after electron beam welding reconstitution. *Nucl. Eng. Des* 241, 459–463. doi:10.1016/j.nucengdes.2010.11.005

Wang, X., Yao, W., Ying, L., and Dong, Y. (2020). Numerical simulation of irradiation induced precipitates in low copper RPV steels based on cluster dynamics. *Nucl. Power Eng.* 41 (S1), 188–193. doi:10.13832/j.jnpe.2020.S1.0188

Yoshiie, T., Sato, K., Xu, Q., and Naga, Y. (2015). Reaction kinetic analysis of reactor surveillance data. *Nucl. Instrum. Methods Phys. Res. B* 352, 125–129. doi:10.1016/j.nimb.2015.01.028

frontiers | Frontiers in Energy Research

TYPE Original Research
PUBLISHED 30 July 2024
DOI 10.3389/fenrg.2024.1436245

Coupling of the best-estimate system code and containment analysis code and its application to TMLB' accident

Xiaoli Wu*, Zhifeng Zheng, Jian Deng, Yu Liu, Qi Lu, Qingan Xiang, Chong Chen, Hongping Sun, Yazhe Lu, Danhong Shen and Wei Li

Science and Technology on Reactor System Design Technology Laboratory, Nuclear Power Institute of China, Chengdu, China

OPEN ACCESS

EDITED BY
Jiankai Yu,
Massachusetts Institute of Technology,
United States

REVIEWED BY
Ivo Kljenak,
Institut Jožef Stefan (IJS), Slovenia
Fulong Zhao,
Harbin Engineering University, China

*CORRESPONDENCE
Xiaoli Wu,
✉ wuxiaollidongli@gmail.com

RECEIVED 21 May 2024
ACCEPTED 08 July 2024
PUBLISHED 30 July 2024

CITATION
Wu X, Zheng Z, Deng J, Liu Y, Lu Q, Xiang Q, Chen C, Sun H, Lu Y, Shen D and Li W (2024), Coupling of the best-estimate system code and containment analysis code and its application to TMLB' accident.
Front. Energy Res. 12:1436245.
doi: 10.3389/fenrg.2024.1436245

With the development of advanced pressurized water reactor technology, the thermal-hydraulic coupling effect between the containment and the primary system becomes increasingly tight. In order to meet the demand for integrated safety analysis between the containment and the primary system, this paper investigates a direct coupling method between the best-estimate system code Advanced Reactor Safety Analysis Code and the containment analysis program ATHROC (Analysis of Thermal Hydraulic Response Of Containment). The feasibility of this direct coupling method and the applicability of the coupled program for overall safety analysis are demonstrated using Marviken two-phase flow release experiments. The ATHROC/ARSAC coupled program is employed to analyze the impact of the pressure relief function of the CPR1000 nuclear power plant pressurizer on the behavior of the primary system and containment during the TMLB' accident. The calculation results indicate that these measures can reduce the pressure of the primary system to the level acceptable by the low-pressure injection system, but at the same time, they cause the pressure in the containment to rise to nearly 0.4 MPa. Therefore, to ensure the structural integrity of the containment, it is necessary for the non-passive hydrogen recombiner to effectively reduce the hydrogen concentration, thereby avoiding additional pressure increase in the containment due to hydrogen deflagration, which could lead to overpressure failure. The findings of this study are of significant reference value for improving the safety performance of thermal-hydraulic systems in operational Gen-II and advanced Gen-III pressurized water reactor nuclear power plants.

KEYWORDS

best-estimate code, containment, code coupling, active depressurization measure4, TMLB' accident

1 Introduction

As nuclear technology advances, the thermal-hydraulic coupling between the containment and the primary system becomes even tighter. As large pressurized water reactors, both the Hualong One (Xing et al., 2016) and AP1000 (Schulz, 2006) incorporate the In-Containment Refueling Water Storage Tank (IRWST) as a crucial heat trap. During the prolonged recirculation cooling phase following a loss-of-coolant accident, there's no need for switching water withdrawal points as required in Generation II PWRs, thus reducing the number of penetrations through the containment. The Automatic Depressurization System (ADS) of the AP1000 directly connects the primary system to the IRWST. In accident conditions, high-temperature, high-pressure steam from the primary system is discharged to both the IRWST and the containment compartment via the ADS Sparger and the fourth-stage sparger, respectively, reducing the pressure in the primary system while causing an increase in the pressure within the containment. The water level in the IRWST is influenced by the flow rate driven by the gravity head pressure. The water level and temperature in the IRWST also affect the natural circulation capability of the Passive Residual Heat Removal System (PRHRS). In Small Modular Reactors (SMRs), such as the structure is highly compact, the mutual influence between the containment and the primary system is even more evident. For Generation II nuclear power plant technology, such as the CPR1000, the containment cavity is crucial, as the water level in the sump determines whether long-term safety injection to reactor core and containment spray cooling functions can be achieved during accidents. The pressure relief tank of the CPR1000 primarily receives steam discharged from safety valves and, when the pressure in the relief tank is too high, discharges coolant to the containment. In summary, coupling safety analyses of the primary system and the containment play a crucial role in enhancing the safety of advanced reactors.

In order to analyze the complex physical phenomena within the containment during accident conditions, specialized containment analysis programs such as CONTEMPT (Wheat et al., 1975), GOTHIC (Gavrilas et al., 1996), CONTAIN (Murata et al., 1989), ATHROC (Chen et al., 2018) etc., as well as integrated programs with full-scope accident analysis capabilities such as MAAP (Williams et al., 2008), MELCOR (Gauntt et al., 2000) etc., are available in the literature, capable of simultaneously analyzing both the primary system and the containment. Currently, integrated programs are predominantly utilized in understanding containment behavior. Taking the MAAP program as an example, it encompasses models for both the reactor coolant system and the containment, with the containment model capable of describing most physical phenomena, including mass and energy exchange between containment compartments, condensation and evaporation, containment spray, molten material-concrete interaction, gas combustion, steam explosions, and direct containment heating, among others. For the primary system model, MAAP employs thermal-hydraulic governing equations based on quasi-equilibrium assumptions, yielding conservative results. Due to computational efficiency considerations, the nodalization schemes of these integrated programs are fixed and rather coarse within the code, resulting in much less refined calculation results. In contrast, system codes typically solve more mechanistically based two-phase flow thermal-hydraulic governing equation sets (such as the commonly used one-dimensional two-fluid model), which also include neutron kinetics models, widely used for best-estimate safety analysis of PWRs. However, these best-estimate system codes solve one-dimensional Euler equations and are not suitable for describing natural circulation phenomena within the large spaces of the containment. Moreover, when simulating dedicated safety features, best-estimate system codes such as RELAP5 (Fletcher and Schultz, 1992) and ASRAC (Deng et al., 2021) can only use simple time-dependent volumes and time-dependent junctions to represent injection water sources and injection rates, respectively, unable to quantitatively analyze changes in IRWST water level, injection flow rates, and pressure head variations. Therefore, applying best-estimate system codes and containment analysis programs separately for primary system and containment analysis, considering their coupling, is more advantageous compared to using integrated analysis programs alone, providing important guidance for conducting comprehensive safety analyses of nuclear power plants.

Smith (Smith, 1993; Smith et al., 1994; Smith et al., 1995) developed a coupling program for RELAP5/MOD3 and CONTAIN 1.12 using PVM technology on workstations. RELAP5 models the primary system, analyzing its thermal-hydraulic behavior, while CONTAIN models the containment, analyzing thermal-hydraulic phenomena within it. Calculations for ATWS accidents caused by the closure of the main steam isolation valve in pressurized water reactors showed that the results obtained from the coupled program were more accurate. Similarly, Martin et al. (Martin, 1995) developed a coupling program for RELAP5/MOD3 and CONTAIN based on PVM technology. By modifying RELAP5 and inputting coupling information into RELAP5’s input cards to initiate the calculation of the coupling program, they demonstrated the feasibility of the coupling method through calculations of pressurized water reactor pressure vessel discharge problems and main steam pipe rupture accidents, showing that the results obtained were more accurate than those from independent CONTAIN calculations. Park et al. (Park and Lee, 1994) developed a coupling program for RELAP5/MOD3 and CONTEMPT 4 based on UNIX process control technology. CONTEMPT is primarily used for calculating thermal-hydraulic phenomena within the containment and limited severe accident phenomena such as gas combustion. Calculations on a simplified nuclear power plant model using the coupling program demonstrated the feasibility of the coupling technique. The coupling program, utilizing specialized safety feature models within the containment and best-estimate models of the primary system, helped provide a realistic assessment model of the Emergency Core Cooling System (ECCS) in LOCA scenarios. Kwon et al. (Kwon et al., 1998) conducted realistic estimation analyses of large-break LOCA scenarios for Units 3 and 4 of the Yonggwang nuclear power plant using the coupling program and compared the results with conservative design analysis. The coupling program demonstrated that peak containment pressure occurred during the discharge phase, while the conservative design analysis showed peak containment pressure occurring later in the discharge phase. Based on the analysis, the authors concluded that the results from the coupling program were more reasonable. Chung et al. (Chung et al., 1998) studied the coupling of the system code MARS 1.3 with CONTEMPT using DLL technology and the coupling of RELAP5/MOD3 with CONTAIN 2 (Chung et al., 2001). The authors suggested that DLL technology could be more convenient than UNIX process control technology for coupling multiple programs. Rodríguez et al. (Rodriguez, 2002) coupled MELCOR with RELAP5 using PVM technology, demonstrating the feasibility of coupling technology. MELCOR is used to calculate severe accident phenomena within the containment, while RELAP5 calculates the thermal-hydraulic behavior of the

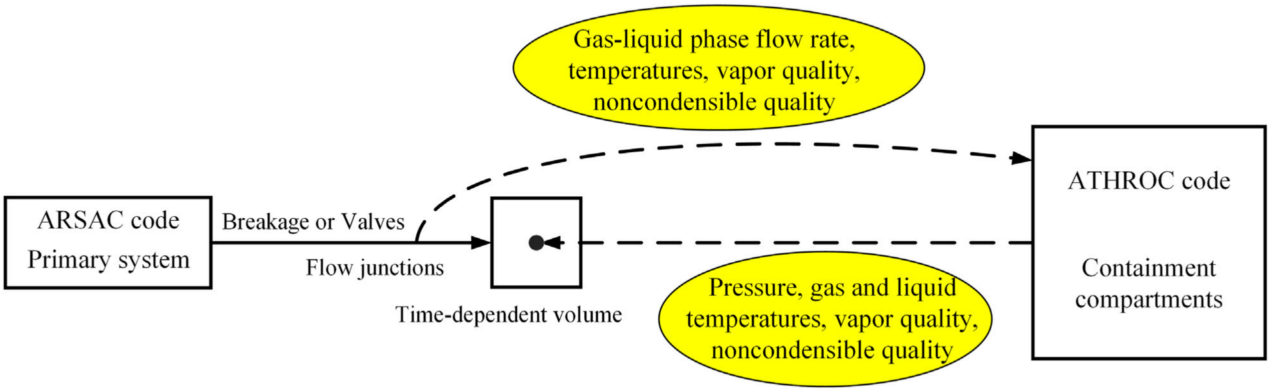

FIGURE 1
Schematic Diagram of the Coupling Interface between ATHROC and ARSAC when the Breach is on the Primary System Pressure Boundary.

primary system. If SCDAP/RELAP5 is used, it can also simulate severe accident phenomena within the primary system. The authors argued that multi-physics coupling programs can handle complex system analyses and achieve best-estimate capabilities for each system.

Based on the thermal-hydraulic system interface between the primary system and the containment, this study investigates a direct coupling method between the containment analysis program ATHROC and the system code ARSAC. ATHROC is a lumped parameter code developed for the analysis of flow and heat transfer phenomena under accident conditions in a PWR containment which is nodalized into a network of interconnected compartments (Chen et al., 2018). Critical models include buoyant plume, spray heat removal, flow between compartments etc. ARSAC is a system safety analysis code based on the well-known one-dimensional two-fluid two-phase model, and particularly designed for PWRs (Deng et al., 2021). ARSAC and ATHROC are respectively utilized to analyze the complex thermal-hydraulic phenomena in the primary system and containment. Data exchange between the two programs is conducted to account for the mutual influence between the primary system and containment through breach or valve flow rates, as well as specialized safety features. Finally, based on this coupling program, focusing on the CPR1000, the impact of active depressurization via the pressurizer safety valves during a TMLB’ accident on the thermal-hydraulic response of the primary system and containment is analyzed. This has important reference value for re-evaluating the pressurizer’s depressurization function as a severe accident mitigation measure.

2 Description of the coupling method

In accident conditions, the containment receives high-temperature and high-pressure gas-liquid mixtures from the primary system, thus the coupling interface between the two programs is the breach or valve of the primary system pressure boundary. When the emergency core cooling system (ECCS) in the specialized safety features is activated, the primary system receives fluid from the containment (e.g., IRWST, containment sump), and the coupling interface between the two programs is the interface of the ECCS within the primary system. In coupling ARSAC with ATHROC, for both best-estimate and realistic analyses, the situations of both coupling interfaces must be considered simultaneously. Below, we’ll introduce the coupling of the programs under each interface separately.

2.1 The breakage or valve in the primary system pressure boundary as the coupling interface

The breaches in the primary system pressure boundary mainly include large, medium, and small breaches in the cold and hot legs, leakage through the pressurizer relief valves, leakage in the main pump shaft seals, failed rupture disks on the pressure relief tank, failed pressure vessel lower head during severe accidents, breaches of the secondary side main steam pipes inside the containment, and so on. As shown in Figure 1, after ARSAC successfully completes a time step, it transfers breach flow rates, temperatures, and other parameters to ATHROC. Upon receiving this information, ATHROC calculates the containment pressure and gas temperature for the same time step and transfers them back to ARSAC, completing one computational cycle.

2.2 The interface between the safety injection system and the primary system as the coupling interface

The water sources for the Emergency Core Cooling System (ECCS) include the Reactor Water Storage Tank (RWST) or IRWST, containment sump, and non-passive injection tank. Taking the CPR1000 as an example, in the event of a loss-of-coolant accident causing depressurization of the primary system, the high-pressure injection pump is first activated to inject water from the RWST into the main pipeline. If necessary, water is injected into the main pipeline from the non-passive medium-pressure injection tank. Finally, the low-pressure injection pump is activated to inject water from the RWST into the main pipeline. When the water level in the RWST is too low, the low-pressure

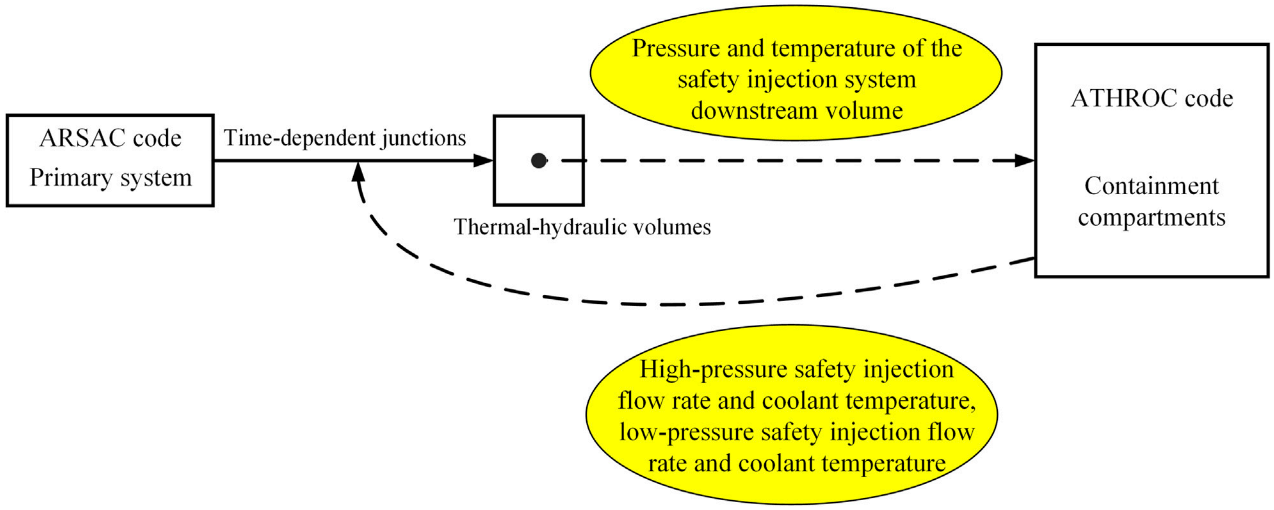

FIGURE 2
Schematic Diagram of the Coupling Interface between ATHROC and ARSAC when the Interface is between the ECCS and the Primary System.

injection pump switches to draw water from the containment sump for long-term recirculation cooling. When coupling ARSAC with ATHROC, ATHROC is responsible for modeling the ECCS, and the coupling approach is illustrated in Figure 2. After ARSAC successfully completes a time step, when the ECCS subsystem reaches activation conditions, ARSAC transfers the thermal-hydraulic information of the primary system required by the ECCS (such as pressure and temperature) to ATHROC. ATHROC then performs calculations for the same time step, updating the thermal-hydraulic information of the RWST, containment sump, and injection tank, and transfers the injection flow rate to ARSAC, thus completing one computational cycle. It is worth noting that the non-passive injection tank model still utilizes ARSAC's built-in ACCUM component for detailed simulation because ATHROC's injection tank model injects flow directly into the pressure vessel downcomer rather than the main pipeline, and ARSAC's injection tank model is more mechanistic.

To couple ATHROC with ARSAC, ATHROC was modified into a subroutine and called within the control loop of ARSAC's computational subroutine. Data exchange between the programs was achieved through global variables.

3 Demonstration of the coupling method

Based on ARSAC modeling of the Marviken CFT 24 experiment (USNRC, 1982) and utilizing the containment calculation model commonly used for testing in the ATHROC series programs at the Zion Nuclear Power Plant, the coupling of the ARSAC code and ATHROC code was setup for validation and demonstration. The Marviken CFT experiment was conducted at Marviken Power Station which employs a boiling heavy water reactor, while the Zion Nuclear Power plant adopted PWR. The critical flow data of water and steam water mixtures collected in the Marviken CFT experiment can be readily used to assess the two-phase critical flow model of a system code like ARSAC during LOCA analysis, because the input model of the experiment was simple to build (mainly consisting of a large vessel and a pipe) and the experimental data is publicly available (Kim and Kim, 1992). On the other side, the containment model of Zion Nuclear Power Plant was also a frequently used example to demonstrate the modeling capability of integrated safety analysis codes for PWR large dry containment under accident conditions (Brunett, 2014). Therefore, the two models are combined in this paper for validation and demonstration of analyzing highly transient discharge of water-steam mixture into the containment compartments, although it is noted that they were physically unrelated.

3.1 Description of the Marviken experiment

The ARSAC calculation model for the Marviken CFT 24 experiment is shown in Figure 3. The ATHROC calculation model for the large dry containment (with a free volume of 78,927 m^3) includes containment compartments and atmospheric surroundings: the cavity, lower compartment, upper compartment, annular compartment, and environment. The Zion Nuclear Power Plant is a Generation II four-loop pressurized water reactor designed by Westinghouse. When the containment pressure exceeds 0.25 MPa, the containment spray pump begins operation 30 s after receiving a high-pressure signal, drawing water from the external Reactor Water Storage Tank (RWST) to spray onto the containment dome. In this test scenario, a significant amount of gas-liquid two-phase mixture released vertically downward from the Marviken CFT 24 pressure vessel located in the upper compartment is discharged into the cavity of the containment (with a free volume of 217 m^3). As the Marviken CFT 24 experiment lasts less than 80 s and there is a 30-s delay in the operation of the containment spray pump, the calculation time is extended to 200 s to facilitate a clearer analysis of the containment spray effect and RWST water level changes.

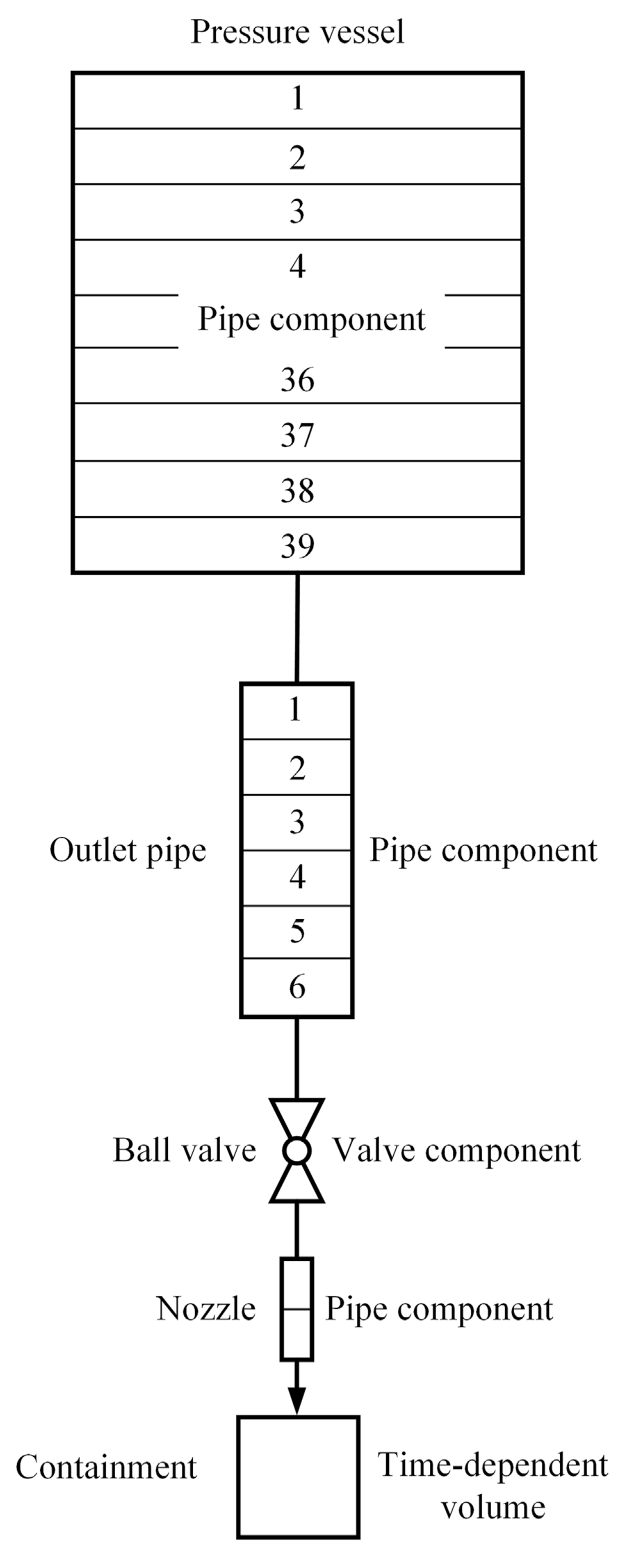

FIGURE 3
Nodalization of the Marviken CFT 24 experiment in ARSAC.

3.2 Demonstration results

As shown in Figure 4, the release immediately caused pressure to rise in the cavity, reaching a maximum of 0.31 MPa. Due to its large free volume, pressure in the upper compartment increased slowly. As the pressure in the upper compartment of the containment exceeded 0.25 MPa, the containment spray system would be initiated. Figure 5 indicates a rapid increase in gas temperature within the containment, with steam temperature reaching 418 K in the upper compartment by the end of the release. Figure 6 illustrates the cavity rapidly reaching its full water level. Figure 7 compares the integrated flow rate through the breach with the increase in containment fluid mass. Before the containment spray system was activated, the integrated flow rate through the breach matched the increase in containment fluid mass perfectly, indicating reasonable data transfer during the coupled calculations, i.e., the fluid mass from the breach matched the increase in fluid mass within the containment. After the containment spray system was activated, it caused continued increase in fluid mass within the containment, exceeding the integrated flow rate through the breach. This case study demonstrates the successful and reasonable coupling between ATHROC and ARSAC, laying the foundation for comprehensive analysis of both the containment and the primary system.

4 Analysis of the active depressurization measure for CPR1000 in TMLB’

Under accident conditions, maintaining a high-pressure level in the primary system can adversely affect the successful implementation of accident mitigation measures, even leading to severe accidents such as High Pressure Melt Ejection (HPME), threatening the structural integrity of the containment. In situations where the Emergency Core Cooling System (ECCS) is available, prompt depressurization of the primary system allows for effective core cooling to be restored by external cooling water. In scenarios where the ECCS is unavailable, even if core melting is inevitable, depressurization of the primary system can prevent a large amount of molten core material from entering the containment in a jet-like manner, thereby avoiding severe issues such as Direct Containment Heating (DCH) and preserving the structural integrity of the containment. Manual opening of the relief valves of the pressurizer to directly depressurize the primary system when the core outlet temperature exceeds 650°C is a severe accident mitigation measure implemented in CPR1000 nuclear power plants, known as “pressurizer relief extension function”. Primary system fluid is directed through the relief valves of the pressurizer into the relief tank and eventually enters the containment due to the limited capacity of the relief tank. This measure carries some risks in situations where the active low-pressure injection system fails to restore promptly, as it leads to rapid pressurization of the containment alongside depressurization of the primary system. Under such circumstances, it is essential to avoid introducing additional uncertain factors into the containment that could cause further pressure increase, such as hydrogen combustion.

The TMLB’ accident is a type of Station Blackout (SBO) accident sequence in pressurized water reactors, where the auxiliary feedwater pumps also fail. In this accident scenario, the secondary side quickly boils dry after losing auxiliary feedwater. When the core outlet temperature exceeds 650°C, it is assumed that the operators manually open the relief valves of the three

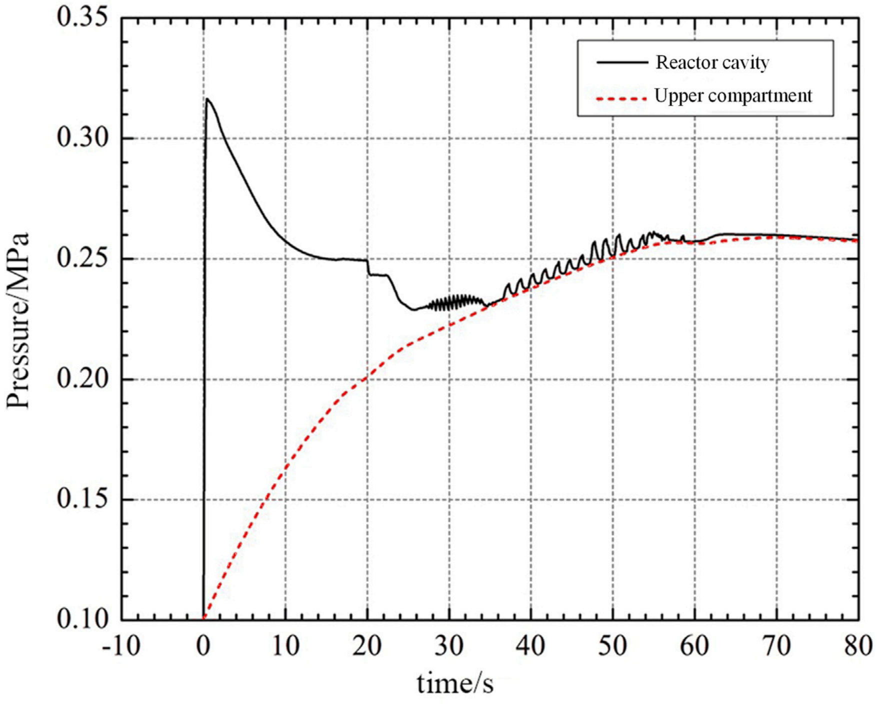

FIGURE 4
Variation of pressure in the upper compartment and cavity of the containment over time.

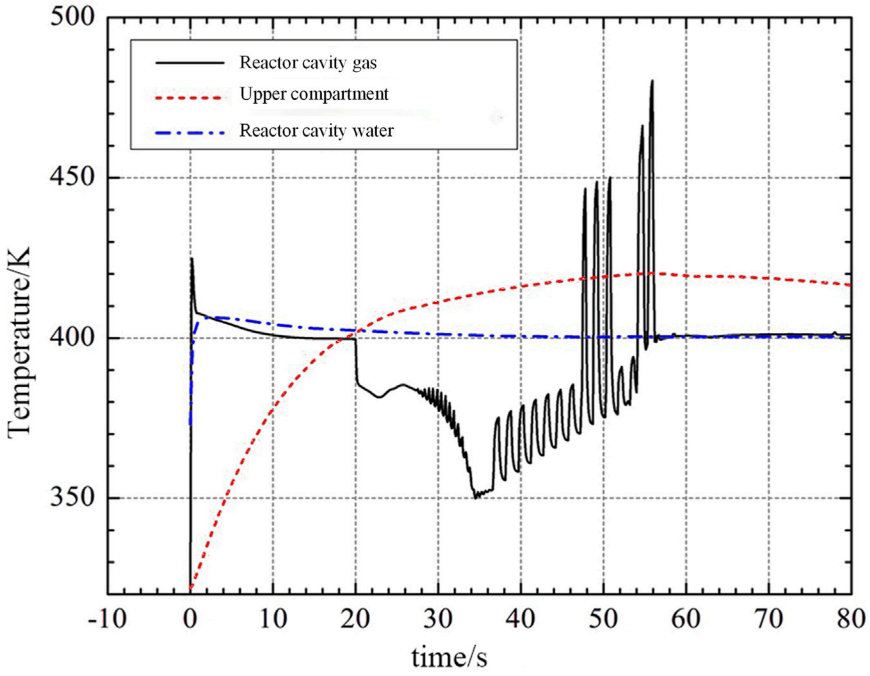

FIGURE 5
Variation of fluid temperature in the upper compartment and cavity of the containment over time.

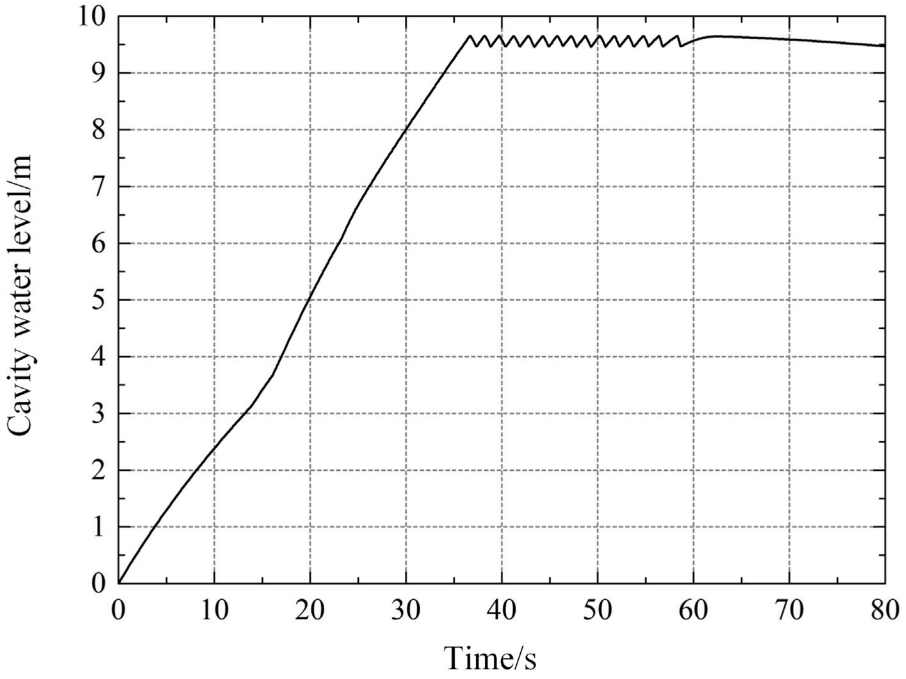

FIGURE 6
Variation of water level in the containment cavity the over time.

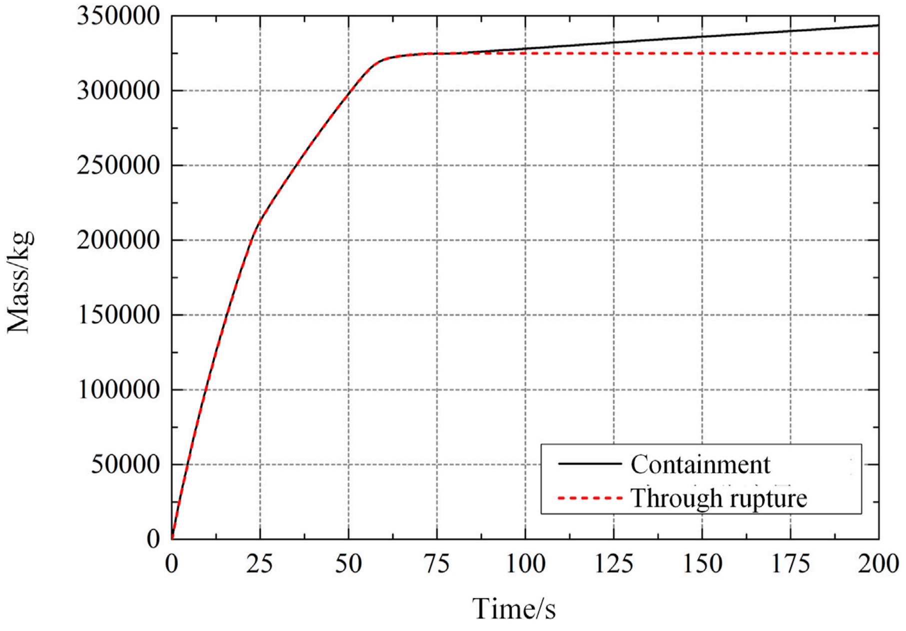

FIGURE 7
Comparison of the increase in fluid mass within the containment with the integrated flow rate through the rupture.

pressurizers for active depressurization. The failure of the main pump shaft seals, the creep failure of the heat pipe sections and the pressurizer surge line, as well as the rupture of the steam generator heat transfer tubes, are not considered. The computational model is illustrated in Figure 8, where the blue portion is modeled using ARSAC and the gray portion is modeled using ATHROC.

4.1 The effect of active depressurization on the primary system

The variation of pressurizer pressure is shown in Figure 9. Due to the unavailability of the auxiliary feedwater system, the water level on the secondary side of the steam generators continues to decrease,

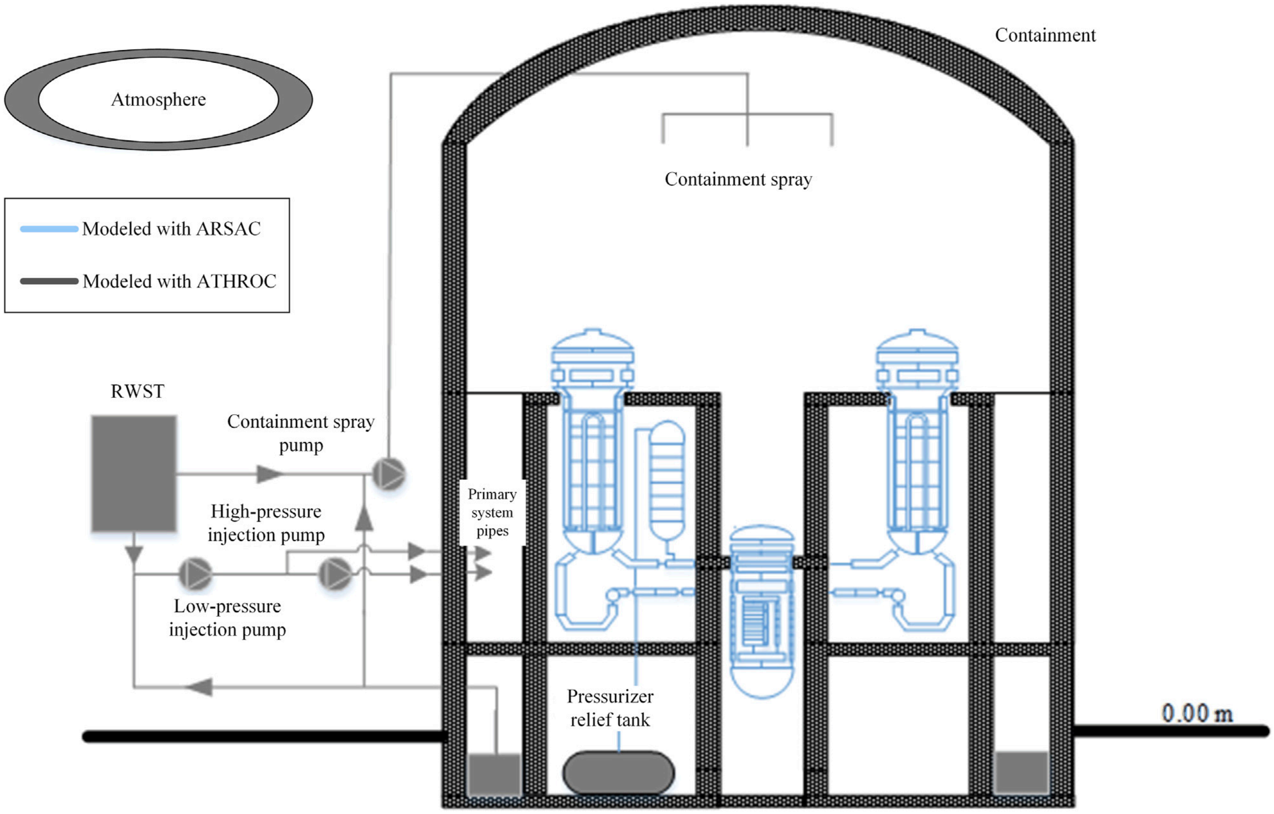

FIGURE 8
Input model of ATHROC/ARSAC coupled analysis for CPR1000 primary system/containment.

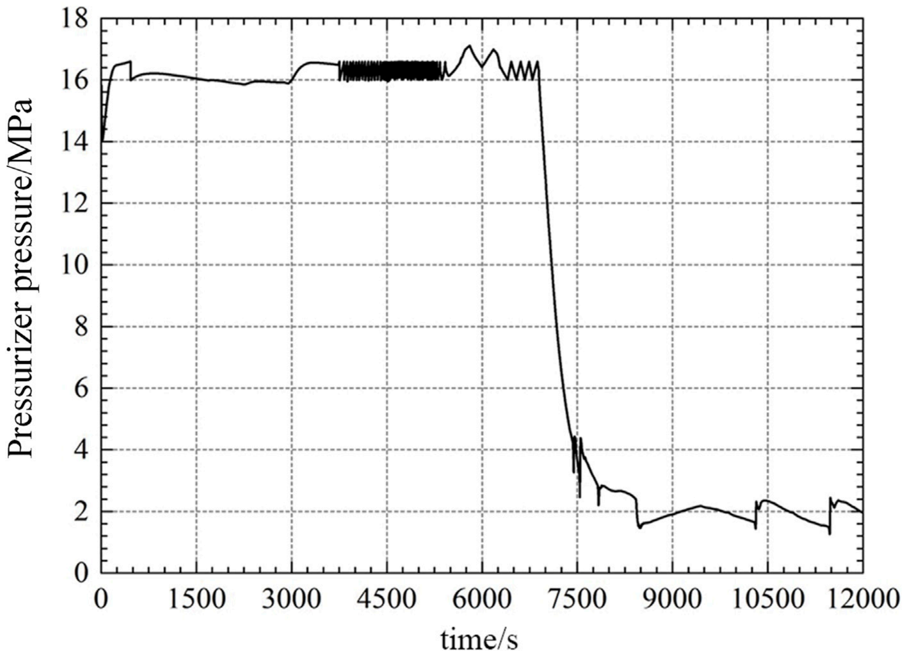

FIGURE 9
Variation of pressurizer pressure over time.

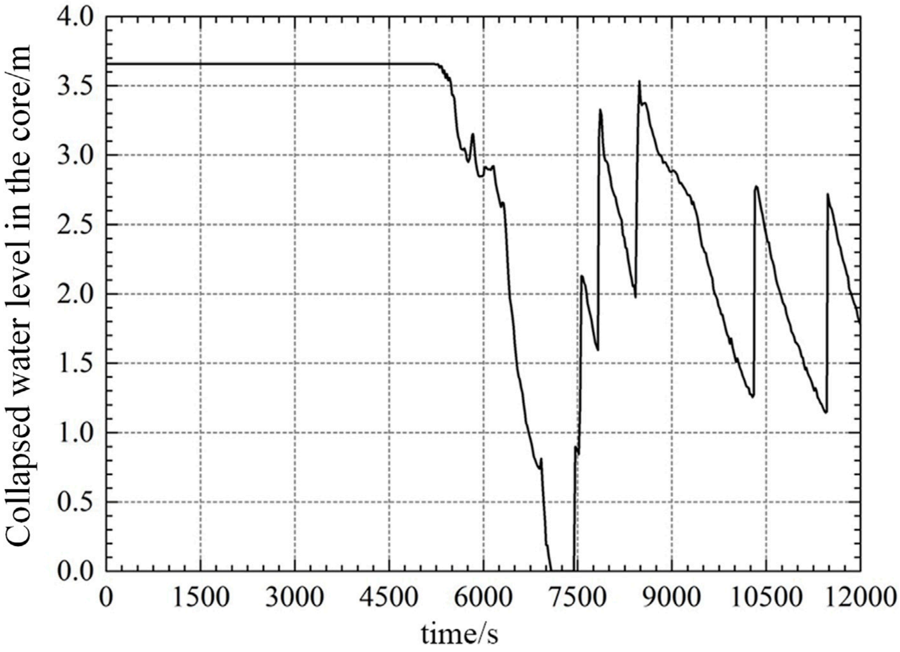

FIGURE 10
Variation of collapsed water level in the core over time.

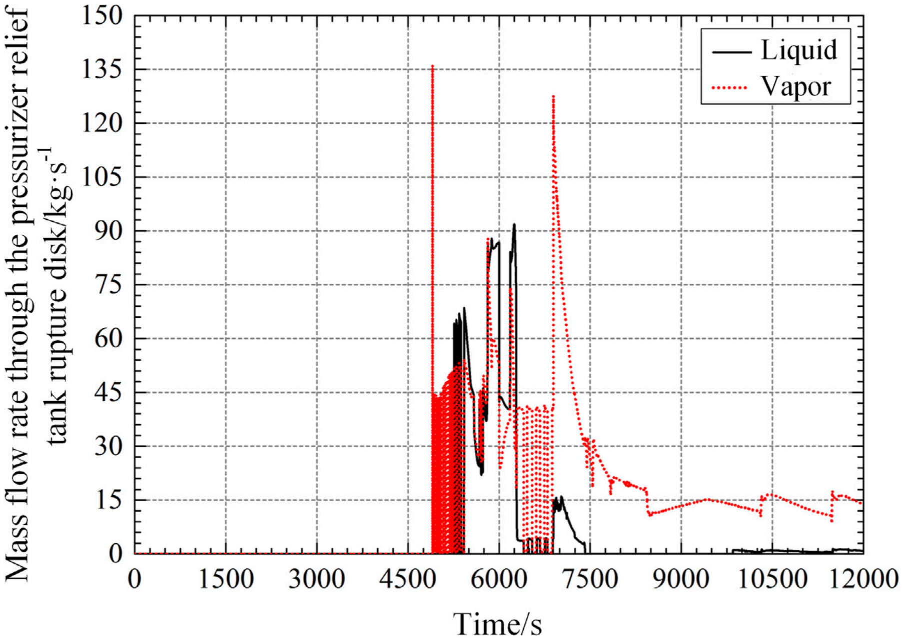

FIGURE 11
Variation of mass flow rate through the pressurizer relief tank rupture disk over time.

causing the pressure in the primary system to start rising. As the pressure increases, the pressurizer relief valves perform overpressure protection, automatically cycling open and closed to maintain the pressurizer pressure between 16.0 and 17.2 MPa. Subsequently, the operators manually open the relief valves of the three pressurizers, releasing a large amount of steam from the safety valves. As a result, the pressurizer pressure rapidly decreases, and the passive containment cooling system automatically injects water into the primary system.

As shown in Figure 10, the collapsed water level in the core experienced four decreases before complete uncovering.

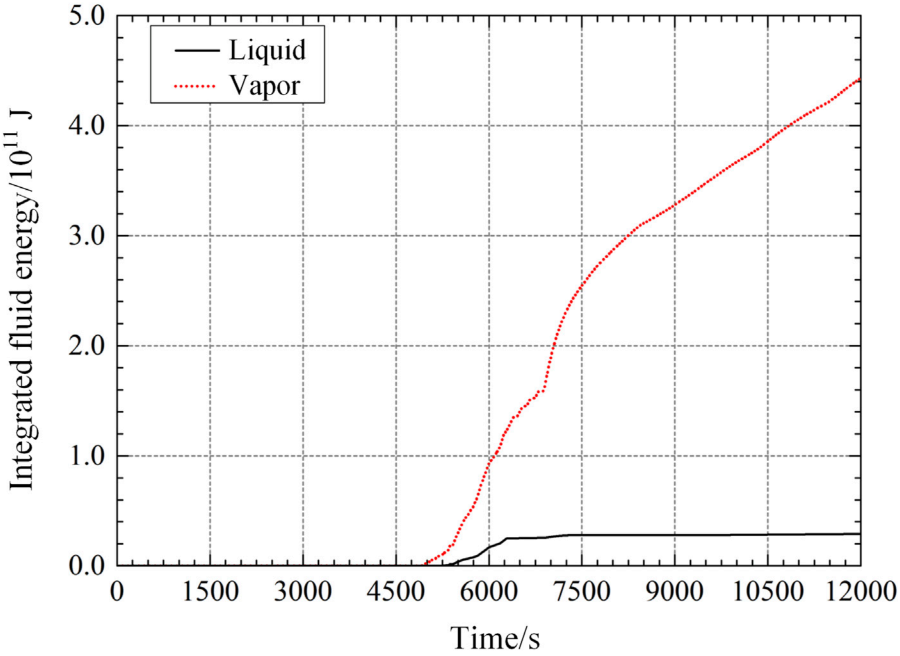

FIGURE 12
Variation of integrated fluid energy into the containment over time.

Approximately 820 s after the secondary side of the steam generators dried up, significant boiling occurred in the core region, marking the first decrease. The pressurizer overflowed during the automatic opening of all relief valves for overpressure protection, causing partial high-temperature single-phase water to discharge from the safety valves and resulting in the second decrease in core collapse water level. Subsequently, steam became the predominant fluid discharged from the safety valves, leading to the third decrease in core collapse water level. When all relief valves of the pressurizer were manually opened, the core collapse water level rapidly decreased for the fourth time until complete exposure. By the time the proactive depressurization measures were taken, the core was nearly completely exposed. About 500 s later, with the injection from the passive containment cooling system, the core water level rapidly increased. Under the influence of injection from the containment cooling system, the core water level exhibited significant fluctuations but did not reach complete exposure. Nonetheless, the possibility of a zirconium-water reaction releasing hydrogen during the accident process is still high.

4.2 The effect of active depressurization on the containment

After active depressurization, the pressurizer safety valves forcibly open, leading to the rupture of the depressurization tank due to its limited volume, and the flow discharged through the rupture disk into the containment is shown in Figure 11. The variation of fluid energy entering the containment over time is depicted in Figure 12, which is beneficial for the active depressurization of the primary system but leads to an increase in pressure and temperature within the containment. The variation of pressure at the containment dome after the accident is shown in Figure 13. Prior to the implementation of active depressurization measures, the pressure at the containment dome increases due to the automatic opening of safety valves, reaching a maximum pressure of 0.216 MPa. The active depressurization measures result in a significant amount of high-temperature steam entering the containment through the rupture disk of the depressurization tank, causing a rapid increase in pressure at the containment dome. After 12,000 s post-accident, the pressure in the containment rises to 0.39 MPa, with only 0.12 MPa margin from the containment's design pressure of 0.52 MPa, and it continues to rise. Lacking the containment spray, the containment is filled with steam with temperatures as high as 130°C, as seen in Figure 14. Due to the inability of the containment spray system to operate, as shown in Figure 15, the water level in the sump is low, and the water temperature exceeds 100°C.

5 Conclusion

The study investigated the direct coupling method between ATHROC and ARSAC. Apart from the common data transfer of containment pressure and break flow rates, it also enables the transfer of injection flow rates to facilitate the use of ATHROC's realistic dedicated models of safety systems. By modeling Marviken CFT 24 with ARSAC and simulating the containment compartments with ATHROC, this case was utilized to validate and test the ATHROC/ARSAC coupling program, demonstrating its rationality and showcasing its comprehensive analysis capabilities.

Using the ATHROC/ARSAC coupling program, the impact of extending the function of the pressurizer safety valve on mitigating

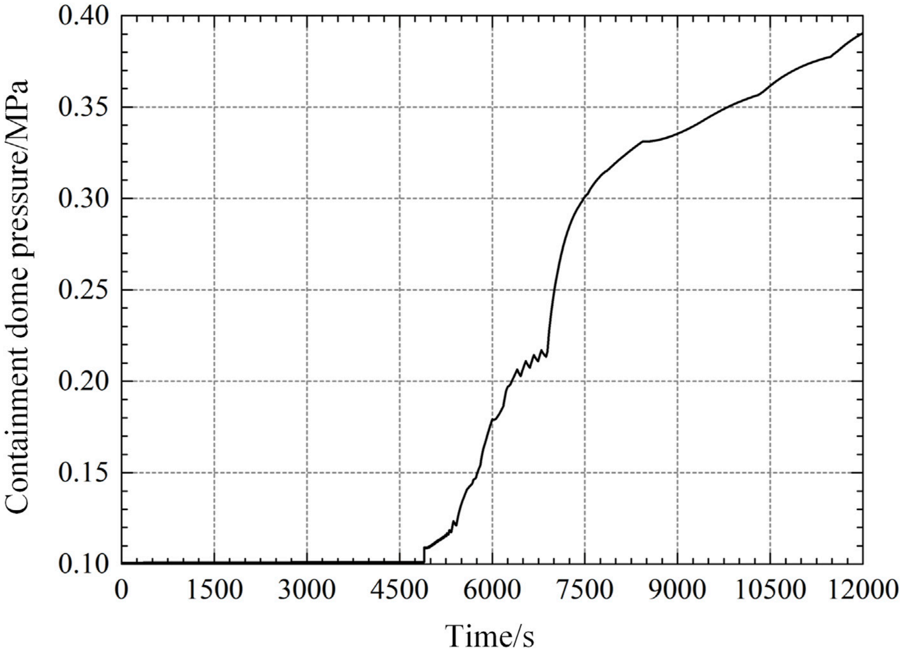

FIGURE 13
Variation of containment dome pressure over time.

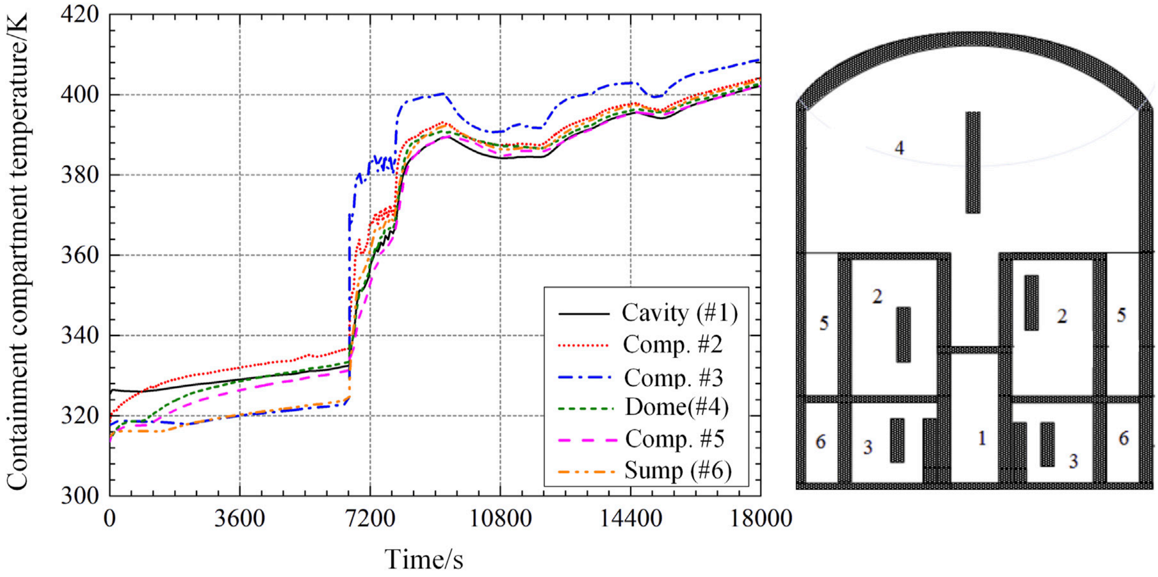

FIGURE 14
Variation of gas temperature in the containment compartments.

TMLB' high-pressure accidents was analyzed. The purpose of this measure is to actively release the heat from the primary system through the pressure safety valves, triggering injection from the accumulator, but the fluid goes directly into the containment compartments. While the proactive opening of the pressurizer safety valve played a positive role in delaying core meltdown, the pressure in the primary system remains relatively high, around 1.8 MPa, making it unfavorable for sustained stable injection from the low-pressure safety injection pump. Hence, it is essential to promptly restore the auxiliary injection system (electric or pneumatic) to further relieve pressure from the primary system.

The extension of the pressurizer's pressure relief function had adverse effects on the containment, as a large quantity of high-temperature fluid entered the containment compartment through the pressure relief tank. Assuming no hydrogen combustion occurred, the containment pressure had risen to nearly 0.4 MPa.

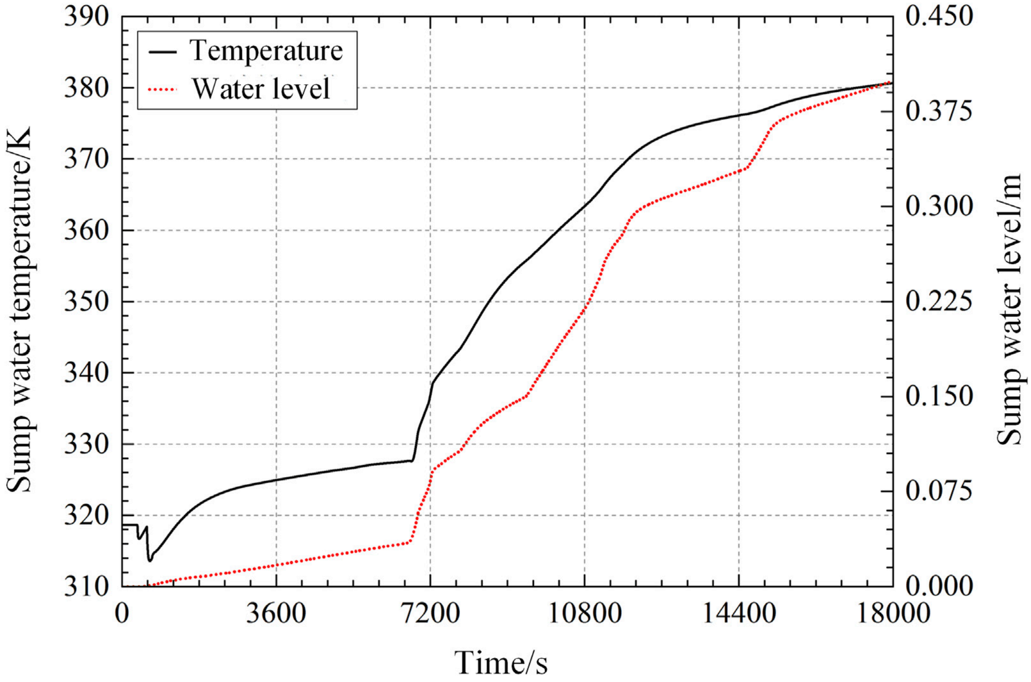

FIGURE 15
Variation of water temperature and water level in the containment sump.

Therefore, to prevent containment overpressure, it is crucial to ensure the proper functioning of the passive hydrogen recombiner.

Data availability statement

The raw data supporting the conclusions of this article will be made available by the authors, without undue reservation.

Author contributions

XW: Writing–original draft, Writing–review and editing. ZZ: Investigation, Software, Writing–original draft. JD: Supervision, Writing–review and editing. YL: Data curation, Writing–review and editing. QL: Methodology, Writing–review and editing. QX: Writing–review and editing. CC: Writing–review and editing. HS: Writing–original draft. YL: Writing–original draft. DS: Writing–original draft. WL: Writing–review and editing.

Funding

The author(s) declare financial support was received for the research, authorship, and/or publication of this article. This work was supported by the Joint Funds of the National Natural Science Foundation of China (U2067210), and the Innovative Scientific Program of China National Nuclear Corporation (2022). The authors declare that this study received funding from China National Nuclear Corporation. The funder was not involved in the study design, collection, analysis, interpretation of data, the writing of this article, or the decision to submit it for publication.

Conflict of interest

The authors declare that the research was conducted in the absence of any commercial or financial relationships that could be construed as a potential conflict of interest.

Publisher's note

References

Brunett, A., Denning, R., and Aldemir, T. (2014). A Reassessment of low Probability containment failure Modes and phenomena in a long-term Station Blackout. *Nucl. Technol.* 186 (2), 198–215. doi:10.13182/nt13-40

Chen, Y., Wu, Y. W., Wang, M. J., Zhang, Y. P., Tan, B., Zhang, D. L., et al. (2018). Development of a multi-compartment containment code for advanced PWR plant. *Nucl. Eng. Des.* 334, 75–89. doi:10.1016/j.nucengdes.2018.05.001

Chung, B. D., Jeong, J. J., and Lee, W. J. (1998) “MARS 1.3 system analysis code coupling with CONTEMPT4/MOD5/PCCS containment analysis code using dynamic link library,” in *Proceedings of the Korean nuclear Society autumn meeting*, 29–30.

Chung, B. D., Jo, J. J., and Rohatgi, U. S. (2001). *RELAP5/MOD3.2.2 coupling with CONTAIN 2.0 containment analysis code using Dynamic Link Library*. Washington, DC: CAMP Meeting.

Deng, J., Ding, S., Li, Z., Huang, T., Wu, D., Wang, J., et al. (2021). The development of ARSAC for modeling nuclear power plant system. *Prog. Nucl. Energy* 140, 103880. doi:10.1016/j.pnucene.2021.103880

Fletcher, C. D., and Schultz, R. R. (1992). *RELAP5/MOD3 code manual (No. NUREG/CR-5535-Vol. 5; EGG-2596-Vol. 5). Nuclear Regulatory Commission, Washington, DC (United States). Div. Of systems research; EG and G Idaho*. Idaho Falls, ID (United States): Inc.

Gauntt, R. O., Cole, R. K., Erickson, C. M., Gido, R. G., Gasser, R. D., Rodriguez, S. B., et al. (2000). MELCOR computer code manuals. *Sandia Natl. Lab. NUREG/CR* 6119, 785.

Gavrilas, M., Hejzlar, P., Todreas, N. E., and Driscoll, M. J. (1996). Gothic code evaluation of alternative passive containment cooling features. *Nucl. Eng. Des.* 166 (3), 427–442. doi:10.1016/s0029-5493(96)01259-9

Kim, K., and Kim, H. J. (1992). *Assessment of RELAP5/MOD2 critical flow model using Marviken Test Data 15 and 24. NUREG/IA-0086*. Washington, DC: Nuclear Regulatory Commission. Office of Nuclear Regulatory Research

Kwon, Y. M., Park, C. E., and Song, J. H. (1998). Comparative mass and energy release and containment analyses for a large-break loss-of-coolant accident using RELAP5/CONTEMPT4 and design computer codes. *Nucl. Technol.* 122 (3), 295–305. doi:10.13182/NT98-A2871

Martin, R. (1995). RELAP5/MOD3 code coupling model. *Nucl. Saf.* 36 (2), 290–298. doi:10.2172/238548

Murata, K. K., Carroll, D. E., Washington, K. E., Gelbard, F., Valdez, G. D., Williams, D. C., et al. (1989). *User’s manual for CONTAIN 1.1: a computer code for severe nuclear reactor accident containment analysis No. NUREG/CR-5026; SAND-87-2309*. Albuquerque, NM (United States): Sandia National Lab SNL-NM.

Park, C. E., Lee, G. H., Lee, W. J., Chung, B. D., and Lee, S. Y. (1994). “Development of a merged version of RELAP5/MOD3 and CONTEMPT4/MOD5,” in *Proceedings of the KNS spring meeting*.

Rodriguez, S. (2002). *Using the coupled MELCOR-RELAP5 codes for simulation of the Edward’s pipe*. Albuquerque, NM, USA: Sandia National Laboratories.

Schulz, T. L. (2006). Westinghouse AP1000 advanced passive plant. *Nucl. Eng. Des.* 236 (14-16), 1547–1557. doi:10.1016/j.nucengdes.2006.03.049

Smith, K., Baratta, A. J., and Miller, J. (1994) “Simulation of coupled primary system and containment response using RELAP5 and CONTAIN on a Multiprocessor computer,” in *International Conference on New Trends in nuclear system Thermohydraulics*.

Smith, K., Baratta, A. J., and Robinson, G. E. (1995). Coupled relap5 and contain accident analysis using PVM. *Nucl. Saf.* 36 (1), 94–108.

Smith, K. A. (1993) “Multi-processor based accident using PVM,” in *SIAM Conference on Parallel processing for Scientific computing*.

USNRC (1982). *The Marviken full-Scale critical flow tests, summary Report*. NUREG/CR-2671, MXC-301.

Wheat, L. L., Wagner, R. J., Niederauer, G. F., and Obenchain, C. F. (1975). *Contempt-LT: a computer program for predicting containment pressure-temperature response to a loss-of-coolant accident (No. ANCR-1219)*. Idaho Falls, ID (United States): Aerojet Nuclear Co.

Williams, E. S., Martin, R., Gandrille, P., Meireles, R., Prior, R., Henry, C., et al. (2008). “Recent revisions to MAAP4 for US EPR severe accident applications,” in *Proceedings of the ICAPP 2008 Conference* (CA: Anaheim).

Xing, J., Song, D., and Wu, Y. (2016). HPR1000: advanced pressurized water reactor with active and passive safety. *Engineering* 2 (1), 79–87. doi:10.1016/j.eng.2016.01.017

Frontiers in Energy Research

TYPE Original Research
PUBLISHED 13 August 2024
DOI 10.3389/fenrg.2024.1417594

EDITED BY
Yang Zou,
Chinese Academy of Sciences (CAS), China

REVIEWED BY
Jian Guo,
Chinese Academy of Sciences (CAS), China
Shichang Liu,
North China Electric Power University, China

*CORRESPONDENCE
Dan Gabriel Cacuci,
cacuci@cec.sc.edu

RECEIVED 15 April 2024
ACCEPTED 26 June 2024
PUBLISHED 13 August 2024

CITATION
Cacuci DG (2024), The nth-order features adjoint sensitivity analysis methodology for response-coupled forward/adjoint linear systems (nth-FASAM-L): I. mathematical framework.
Front. Energy Res. 12:1417594.
doi: 10.3389/fenrg.2024.1417594

The nth-order features adjoint sensitivity analysis methodology for response-coupled forward/adjoint linear systems (nth-FASAM-L): I. mathematical framework

Dan Gabriel Cacuci*

Department of Mechanical Engineering, University of South Carolina, Columbia, SC, United States

This work presents the mathematical/theoretical framework of the "nth-Order Feature Adjoint Sensitivity Analysis Methodology for Response-Coupled Forward/Adjoint Linear Systems" (abbreviated as "nth-FASAM-L"), which enables the most efficient computation of exactly obtained mathematical expressions of arbitrarily-high-order (nth-order) sensitivities of a generic system response with respect to all of the parameters (including boundary and initial conditions) underlying the respective forward/adjoint systems. Responses of linear models can depend simultaneously on both the forward and the adjoint state functions. This is in contradistinction to responses for nonlinear systems, which can depend only on the forward state functions since nonlinear operators do not admit bona-fide adjoint operators. Among the best-known model responses that depend simultaneously on both the forward and adjoint state functions are Lagrangians used for system optimization, the Schwinger and Roussopoulos functionals for analyzing reaction rates and ratios thereof, and the Rayleigh quotient for analyzing eigenvalues and/or separation constants. The sensitivity analysis of such responses makes it necessary to treat linear models/systems in their own right, rather than treating them just as particular cases of nonlinear systems. The unparalleled efficiency and accuracy of the nth-FASAM-L methodology stems from the maximal reduction of the number of adjoint computations (which are "large-scale" computations) for computing high-order sensitivities, since the number of large-scale computations when applying the nth-FASAM-N methodology is proportional to the number of model features as opposed to the number of model parameters (which are considerably more than the number of features). The mathematical framework underlying the nth-FASAM-L is developed in linearly increasing higher-dimensional Hilbert spaces, as opposed to the exponentially increasing "parameter-dimensional" spaces in which response sensitivities are computed by other methods (statistical, finite differences, etc.), thus providing the basis for overcoming the curse of dimensionality in sensitivity analysis and all other fields (uncertainty quantification, predictive modeling, etc.) which need such sensitivities.

KEYWORDS

response-coupled forward/adjoint model, features of model parameters, adjoint operators in Hilbert spaces, exact sensitivities of arbitrarily high order, most efficient computation of high order response sensitivities

1 Introduction

The analysis of computational models fundamentally relies on the use of functional derivatives (called "sensitivities") of the results (called "model responses") with respect to the imprecisely known parameters underlying the computational model. Sensitivities are used for many purposes, including: (a) ranking the importance of the various parameters and performing "reduced-order modeling" by eliminating unimportant parameters and/or processes; (b) quantifying the uncertainties induced in a model response due to uncertainties in the model's parameters; (c) performing "model validation" by comparing computational and experimental results to address the question "does the model represent reality?"; (d) performing data assimilation and model calibration as part of forward and inverse "predictive modeling" to obtain best-estimate predicted results with reduced predicted uncertainties; (e) prioritizing improvements while optimizing the model.

Response sensitivities are computed by using either deterministic or statistical methods. The simplest deterministic method for computing response sensitivities is to use finite-difference schemes in conjunction with re-computations using the model with "judiciously chosen" altered parameter values. Evidently, such methods can at best compute approximate values of a very limited number of sensitivities. Deterministic methods that can compute more exactly the values of first-order sensitivities include the "Green's function method" (Kramer et al., 1981), the "forward sensitivity analysis methodology" (Cacuci, 1981), and the "direct method" (Dunker, 1984), which rely on analytical or numerical differentiation of the computational model under investigation to compute local response sensitivities exactly. On the other hand, "statistical methods" construct an approximate response distribution (often called "response surface") in the parameters space, and subsequently use scatter plots, regression, rank transformation, correlations, and so-called "partial correlation analysis," in order to identify approximate expectation values, variances and covariances for the responses. These statistical quantities are subsequently used to construct quantities that play the role of approximate first-order response sensitivities. Thus, statistical methods commence with "uncertainty analysis" and subsequently attempt an approximate "sensitivity analysis" of the approximately computed model response (called a "response surface") in the phase-space of the parameters under consideration. The currently popular statistical methods for uncertainty and sensitivity analysis are broadly categorized as sampling-based methods (Iman et al., 1981a; Iman et al., 1981b), variance-based methods (Cukier et al., 1978; Hora and Iman, 1986), and Bayesian methods (Rios Insua, 1990). Various variants of the statistical methods for uncertainty and sensitivity analysis are reviewed in the book edited by Saltarelli et al. (2000).

For a computational model comprising many parameters, the conventional deterministic and statistical methods become impractical for computing sensitivities higher than first-order because they are subject to the "curse of dimensionality," a term coined by Bellman (1957) to describe phenomena in which the number of computations increases exponentially in the respective phase-space. It is known that the "adjoint method of sensitivity analysis" has been the most efficient method for computing exactly first-order sensitivities, since it requires a single large-scale (adjoint) computation for computing all of the first-order sensitivities, regardless of the number of model parameters. The idea underlying the computation of response sensitivities with respect to model parameters using adjoint operators was first used by Wigner (1945) to analyze first-order perturbations in nuclear reactor physics and shielding models based on the *linear* neutron transport (or diffusion) equation, as subsequently described in textbooks on these subjects (Weiberg and Wigner, 1958; Weisbin et al., 1978; Williams, 1986; Shultis and Faw, 2000; Stacey, 2001). Cacuci (1981) is credited (see, e.g., Práger and Kelemen, 2014; Luo et al., 2020) for having conceived the rigorous "1st-order adjoint sensitivity analysis methodology" for generic large-scale *nonlinear* (as opposed to linearized) systems involving generic operator responses and having introduced these principles to the earth, atmospheric and other sciences.

Cacuci (2015), Cacuci (2016) has extended his 1st-order adjoint sensitivity analysis methodology to enable the comprehensive and exact computation of 2nd-order sensitivities of model responses to model parameters (including imprecisely known domain boundaries and interfaces) for large-scale linear and nonlinear systems. The unparalleled efficiency of the 2nd-order adjoint sensitivity analysis methodology for linear systems (Cacuci, 2015) was demonstrated (see Cacuci and Fang, 2023, and references therein) by applying this methodology to compute exactly the 21,976 first-order sensitivities and 482,944,576 second-order sensitivities (of which 241,483,276 are distinct from each other) for an OECD/NEA reactor physics benchmark (Valentine, 2006). This benchmark is modeled by the neutron transport equation involving 21,976 uncertain parameters, the solving of which is representative of "large-scale computations." The neutron transport equation was solved using the software package PARTISN (Alcouffe et al., 2008) in conjunction with the MENDF71X cross section library (Conlin et al., 2013), which comprises 618-group cross sections based on ENDF/B-VII.1 nuclear data (Chadwick et al., 2011). The spontaneous fission source was computed using the code SOURCES4C (Wilson et al., 2002). Contrary to the widely held belief that second- and higher-order sensitivities are negligeable for reactor physics systems, it was found (see Cacuci and Fang, 2023, and references therein) that many 2nd-order sensitivities of this OECD/

NEA benchmark's leakage response to the benchmark's uncertain parameters were much larger than the largest 1st-order ones, which motivated the investigation of the largest 3rd-order sensitivities, many of which were found to be even larger than the 2nd-order ones. This finding has motivated the development of the mathematical framework for determining and computing the 4th-order sensitivities, many of which were found to be larger than the 3rd-order ones. This sequence of findings has motivated the development by Cacuci (2022) of the "nth-Order Comprehensive Adjoint Sensitivity Analysis Methodology for Response-Coupled Forward/Adjoint Linear Systems" (which is abbreviated as "nth-CASAM-L"). The "nth-CASAM-L" mathematical framework was developed specifically for linear systems because the most important model responses produced by such systems can depend *simultaneously* on both the forward and adjoint state functions governing the respective linear system. Among the most important responses of linear systems that involve both the forward and adjoint functions are various Lagrangian functionals, the Raleigh quotient for computing eigenvalues and/or separation constants when solving partial differential equations, and the Schwinger functional for first-order "normalization-free" solutions (see, e.g., Lewins, 1965; Williams and Engle, 1977; Stacey, 2001). These functionals play fundamental roles in optimization and control procedures, derivation of numerical methods for solving equations (differential, integral, integro-differential), etc. Nonlinear operators do not admit adjoint operators, so responses in nonlinear systems can only depend on the system's forward state functions. Therefore, the sensitivity analysis of responses that simultaneously involve both forward and adjoint state functions makes it necessary to treat linear models/systems in their own right, rather than treating them as particular cases of nonlinear systems.

The traditional methods of sensitivity analysis aim at computing sensitivities of responses directly to the *primary* parameters (i.e., microscopic cross sections, isotopic number densities, etc.) involved in the computational model of the physical system under consideration. Although the sensitivities to the primary model parameters are ultimately of interest for subsequent use in predictive modeling activities (which includes the quantification of the uncertainties induced in responses by uncertainties in the primary model parameters, assimilation of experimental data for calibrating the model's parameters and improving the model's predictions), the primary parameters seldom appear explicitly in the equations underlying the model. For example, the primary model parameters (e.g., microscopic cross sections, atomic number densities) do not appear explicitly in the forward and adjoint transport equations modeling (Cacuci and Fang, 2023) the above-mentioned OECD/NEA reactor physics benchmark. What appear explicitly in these equations are the macroscopic cross sections, which are functions of the primary model parameters, and which can be considered to be *features* of the transport equation. This fact has motivated the development by Cacuci (2024a), Cacuci (2024b) of the "nth-Order Features Adjoint Sensitivity Analysis Methodology for Nonlinear Systems (nth-FASAM-N)," which significantly reduces the computational effort computing efficiently and exactly *sensitivities of model responses to model features* (i.e., functions of the primary model responses), and subsequently compute the sensitivities to responses to the primary model parameters by using the sensitivities to the model features.

Paralleling the mathematical framework of the nth-FASAM-N, it is the purpose of this work to develop a methodology which will enable the efficient and exact computation of *sensitivities of model responses to model features for response-coupled forward and adjoint linear systems*; this new methodology will be abbreviated as the "nth-FASAM-L" methodology. The mathematical framework of this methodology is established in Section 2 of this work by using the proof by "mathematical induction" as follows: (i) establish the mathematical framework underlying the nth-CASAM-L for $n = 1$; (ii) assume that the mathematical framework is valid for an arbitrarily high-order, n; (iii) prove that the mathematical framework proposed for n is also valid for $n+1$. Section 3 presents a concluding discussion that prepares the ground for an illustrative application of the nth-FASAM-L methodology to a representative energy-dependent neutron slowing down model of fundamental importance to reactor physics, which will be presented in an accompanying manuscript (because of word limitations per article), designated as "Part II (Cacuci, 2024c)."

2 The Nth-order function/feature adjoint sensitivity analysis methodology for response-coupled forward and adjoint linear systems (Nth-FASAM-L)

The mathematical framework of the nth-FASAM-L methodology, to be presented in this Section, was established while striving to maximize the computational efficiency of the mathematical framework of the "nth-Order Comprehensive Adjoint Sensitivity Analysis Methodology for Coupled Forward/Adjoint Linear Systems" (abbreviated as: nth-CASAM-L)" conceived by Cacuci (2022). The starting point for both the nth-CASAM-L and the nth-FASAM-L is the *generic* mathematical modeling of a response-coupled forward/adjoint linear system, which is presented in Section 2.1, for convenient referencing.

The validity of mathematical framework underlying the nth-FASAM-L methodology will be established in this Section by using the "proof by mathematical induction" comprising the usual steps, as follows:

1. Conjecture the pattern underlying the nth-FASAM-L, for arbitrary n, based on prior experience.
2. Prove that the conjectured pattern for arbitrary n, is valid for the lowest value of n, i.e., for $n = 1$.
3. Assuming that that the pattern underlying the nth-FASAM-L is valid for an arbitrarily high-order n, prove that this pattern is also valid for $n \to n + 1$, i.e., for the $(n + 1)^{th}$-FASAM-L.

2.1 Mathematical modeling of response-coupled linear forward and adjoint systems establishing the mathematical framework of the nth-FASAM-L methodology

The mathematical model of a process and/or state of a physical system comprises equations that relate the system's independent variables and parameters to the system's state/dependent variables. A *linear* physical system can generally be modeled by a system of coupled equations written generically in operator form as follows:

$$\mathbf{L}[\mathbf{x};\mathbf{g}(\boldsymbol{\alpha})]\boldsymbol{\varphi}(\mathbf{x}) = \mathbf{Q}[\mathbf{x};\mathbf{g}(\boldsymbol{\alpha})], \mathbf{x} \in \Omega(\boldsymbol{\alpha}). \tag{1}$$

The quantities that appear in Eq. 1 are defined as follows:

1. The vector $\boldsymbol{\varphi}(\mathbf{x}) \triangleq [\varphi_1(\mathbf{x}), \ldots, \varphi_{TD}(\mathbf{x})]^\dagger$ is a TD-dimensional column vector of dependent variables and where the sub/superscript "TD" denotes the "*Total* (number of) *Dependent* variables." The functions $\varphi_i(\mathbf{x}), i = 1, ..., TD$, denote the system's "dependent variables" (also called "state functions"). The symbol "$\triangleq$" denotes "is defined as" or "is by definition equal to." Transposition is indicated by a dagger $(\dagger)$ superscript.
2. The components of the vector $\boldsymbol{\alpha} \triangleq (\alpha_1, \ldots, \alpha_{TP})^\dagger \in \mathbb{R}^{TP}$ denote the *primary* model parameters, where the subscript/superscript "*TP*" indicates "*Total* number of *Primary Parameters*" and where $\mathbb{R}^{TP}$ denotes the TP-dimensional subset of the set of real scalars. Without loss of generality, the model parameters can be considered to be real scalar quantities, having known nominal (or mean) values and, possibly, known higher-order moments or cumulants (i.e., variance/covariances, skewness, kurtosis), which are usually determined from experimental data and/or processes external to the physical system under consideration. These imprecisely known model parameters are considered to include imprecisely known geometrical parameters that characterize the physical system's boundaries in the phase-space of the model's independent variables. The nominal parameter values will be denoted as $\boldsymbol{\alpha}^0 \triangleq [\alpha_1^0, ..., \alpha_i^0, .., \alpha_{TP}^0]^\dagger$; the superscript "0" will be used throughout this work to denote "nominal" or "mean" values.
3. The components of the TI-dimensional column vector $\mathbf{x} \triangleq (x_1, \ldots, x_{TI})^\dagger \in \mathbb{R}^{TI}$ denote the model's independent variables $x_i, i = 1, ..., TI$, where the sub/superscript "TI" denotes the "*Total* number of *Independent* variables." The vector $\mathbf{x} \in \mathbb{R}^{TI}$ of independent variables is considered to be defined on a phase-space domain $\Omega(\boldsymbol{\alpha}) \triangleq \{-\infty \le \lambda_i(\boldsymbol{\alpha}) \le x_i \le \omega_i(\boldsymbol{\alpha}) \le \infty\ ;\ i = 1, ..., TI\}$, the boundaries of which may depend on some of the model parameters $\boldsymbol{\alpha}$. The lower boundary-point of an independent variable is denoted as $\lambda_i(\boldsymbol{\alpha})$, while the corresponding upper boundary-point is denoted as $\omega_i(\boldsymbol{\alpha})$. The boundary of $\Omega(\boldsymbol{\alpha})$, which will be denoted as $\partial\Omega[\boldsymbol{\lambda}(\boldsymbol{\alpha}); \boldsymbol{\omega}(\boldsymbol{\alpha})]$, comprises the set of all of the endpoints $\lambda_i(\boldsymbol{\alpha}), \omega_i(\boldsymbol{\alpha}), i = 1, ..., TI$, of the respective intervals on which the components of $\mathbf{x}$ are defined, i.e., $\partial\Omega[\boldsymbol{\lambda}(\boldsymbol{\alpha}); \boldsymbol{\omega}(\boldsymbol{\alpha})] \triangleq \{\lambda_i(\boldsymbol{\alpha}) \cup \omega_i(\boldsymbol{\alpha}), i = 1, ..., TI\}$.
4. The components $\mathbf{L}_{ij}(\mathbf{x};\boldsymbol{\alpha})$ of the $TD \times TD$-dimensional matrix $\mathbf{L}(\mathbf{x};\boldsymbol{\alpha}) \triangleq [L_{ij}(\mathbf{x};\boldsymbol{\alpha})\ ]$, $i, j = 1, ..., TD$, are operators that act linearly on the dependent variables $\varphi_j(\mathbf{x})$ and also depend on the uncertain model parameters $\boldsymbol{\alpha}$.
5. The vector $\mathbf{g}(\boldsymbol{\alpha}) \triangleq [g_1(\boldsymbol{\alpha}), \ldots, g_{TG}(\boldsymbol{\alpha})]$ is a TG-dimensional vector having components $g_i(\boldsymbol{\alpha}), i = 1, ..., TG$, which are real-valued functions of (some of) the primary model parameters $\boldsymbol{\alpha} \in \mathbb{R}^{TP}$. The quantity TG denotes the total number of such functions which appear exclusively in the definition of the model's underlying equations. Such functions customarily appear in models in the form of correlations that describe "features" of the system under consideration, such as material properties, flow regimes. etc. Usually, the number of functions $g_i(\boldsymbol{\alpha})$ is considerably smaller than the total number of model parameters, i.e., $TG \ll TP$. For example, the numerical model (Cacuci and Fang, 2023) of the OECD/NEA "Polyethylene-Reflected Plutonium" reactor physics benchmark (Valentine, 2006) comprises 21,976 uncertain primary model parameters (including microscopic cross sections and isotopic number densities) but the neutron transport equation, which is solved numerically to determine the neutron flux distribution within the benchmark, does not use these primary parameters directly but instead uses just several hundreds of "group-averaged macroscopic cross sections" which are functions/features of the microscopic cross sections and isotopic number densities (which in turn are uncertain quantities that would be components of the vector of primary model parameters). In particular, a component $g_j(\boldsymbol{\alpha})$ may simply be one of the primary model parameters α_j, i.e., $g_j(\boldsymbol{\alpha}) \equiv \alpha_j$.
6. The TD-dimensional column vector $\mathbf{Q}[\mathbf{x};\mathbf{g}(\boldsymbol{\alpha})] \triangleq (q_1, ..., q_{TD})^\dagger$, having components $q_i[\mathbf{x};\mathbf{g}(\boldsymbol{\alpha})], i = 1, ..., TD$, denotes inhomogeneous source terms, which usually depend nonlinearly on the uncertain parameters $\boldsymbol{\alpha}$. Since the right-side of Eq. 1 may contain distributions, the equality in this equation is considered to hold in the weak (i.e., "distributional") sense. Similarly, all of the equalities that involve differential equations in this work will be considered to hold in the distributional sense.
7. When $\mathbf{L}[\mathbf{x};\mathbf{g}(\boldsymbol{\alpha})]$ contains differential operators, corresponding boundary and initial conditions which define the domain of $\mathbf{L}[\mathbf{x};\mathbf{g}(\boldsymbol{\alpha})]$ must also be given. Since the complete mathematical model is considered to be linear in $\boldsymbol{\varphi}(\mathbf{x})$, the boundary and/or initial conditions needed to define the domain of $\mathbf{L}[\mathbf{x};\mathbf{g}(\boldsymbol{\alpha})]$ must also be linear in $\boldsymbol{\varphi}(\mathbf{x})$. Such linear boundary and initial conditions are represented in the following operator form:

$$\mathbf{B}[\mathbf{x};\mathbf{g}(\boldsymbol{\alpha});\ \boldsymbol{\lambda}(\boldsymbol{\alpha});\boldsymbol{\omega}(\boldsymbol{\alpha})]\ \boldsymbol{\varphi}(\mathbf{x}) = \mathbf{C}[\mathbf{x};\mathbf{g}(\boldsymbol{\alpha});\ \boldsymbol{\lambda}(\boldsymbol{\alpha});\boldsymbol{\omega}(\boldsymbol{\alpha})],\quad \mathbf{x} \in \partial\Omega[\boldsymbol{\lambda}(\boldsymbol{\alpha});\boldsymbol{\omega}(\boldsymbol{\alpha})] \tag{2}$$

In Eq. 2, the quantity $\mathbf{B}[\mathbf{x};\mathbf{g}(\boldsymbol{\alpha});\ \boldsymbol{\lambda}(\boldsymbol{\alpha});\boldsymbol{\omega}(\boldsymbol{\alpha})]$ denotes a matrix of dimensions $N_B \times TD$ having components denoted as $B_{ij}(\mathbf{x};\boldsymbol{\alpha});\ i = 1, ..., N_B;\ j = 1, ..., TD$, which are operators that act linearly on $\boldsymbol{\varphi}(\mathbf{x})$ and nonlinearly on the components of $\mathbf{g}(\boldsymbol{\alpha})$; the quantity N_B denotes the total number of boundary and initial conditions. The N_B-dimensional column vector $\mathbf{C}[\mathbf{x};\mathbf{g}(\boldsymbol{\alpha});\ \boldsymbol{\lambda}(\boldsymbol{\alpha});\boldsymbol{\omega}(\boldsymbol{\alpha})]$ comprises components that are operators which, in general, act nonlinearly on the components of $\mathbf{g}(\boldsymbol{\alpha})$.

Physical problems modeled by linear systems and/or operators are naturally defined in Hilbert spaces. The dependent variables $\varphi_i(\mathbf{x}), i = 1, ..., TD$, for the physical system represented by Eqs 1, 2 are considered to be square-integrable functions of the independent variables and are considered to belong to a Hilbert space which will be denoted as $\mathrm{H}_0(\Omega)$, where the subscript "zero" denotes "zeroth-level" or "original." Higher-level Hilbert spaces, which will be denoted as $\mathrm{H}_1(\Omega), \mathrm{H}_2(\Omega)$, etc., will also be introduced and used in this work. The Hilbert space $\mathrm{H}_0(\Omega)$ is considered to be endowed with the following inner product, denoted as $\langle \boldsymbol{\varphi}(\mathbf{x}), \boldsymbol{\psi}(\mathbf{x})\rangle_0$, between two elements $\boldsymbol{\varphi}(\mathbf{x}) \in \mathrm{H}_0(\Omega)$ and $\boldsymbol{\psi}(\mathbf{x}) \in \mathrm{H}_0(\Omega)$:

$$\langle \boldsymbol{\varphi}(\mathbf{x}), \boldsymbol{\psi}(\mathbf{x}) \rangle_0 \triangleq \prod_{i=1}^{TI} \int\limits_{\lambda_i(\boldsymbol{\alpha})}^{\omega_i(\boldsymbol{\alpha})} \boldsymbol{\varphi}(\mathbf{x}) \cdot \boldsymbol{\psi}(\mathbf{x})\, d\mathbf{x}$$
$$= \sum_{j=1}^{TD} \int\limits_{\lambda_1(\boldsymbol{\alpha})}^{\omega_1(\boldsymbol{\alpha})} \dots \int\limits_{\lambda_i(\boldsymbol{\alpha})}^{\omega_i(\boldsymbol{\alpha})} \dots \int\limits_{\lambda_{TI}(\boldsymbol{\alpha})}^{\omega_{TI}(\boldsymbol{\alpha})} \varphi_j(\mathbf{x})\psi_j(\mathbf{x})\, dx_1 \dots dx_i \dots dx_{TI}. \tag{3}$$

The "dot" in Eq. 3 indicates the "scalar product of two vectors," which is defined in Eq. 4, below, as follows:

$$\boldsymbol{\varphi}(\mathbf{x}) \cdot \boldsymbol{\psi}(\mathbf{x}) \triangleq \sum_{i=1}^{TD} \varphi_i(\mathbf{x})\psi_i(\mathbf{x}). \tag{4}$$

The product-notation $\prod_{i=1}^{TI} \int_{\lambda_i(\boldsymbol{\alpha})}^{\omega_i(\boldsymbol{\alpha})} [\,]\, dx_i$ in Eq. 3 denotes the respective multiple integrals.

The linear operator $\mathbf{L}[\mathbf{x}; \mathbf{g}(\boldsymbol{\alpha})]$ admits an adjoint operator, which will be denoted as $\mathbf{L}^*[\mathbf{x}; \mathbf{g}(\boldsymbol{\alpha})]$ and which is defined through the following relation for a vector $\boldsymbol{\psi}(\mathbf{x}) \in \mathrm{H}_0$:

$$\langle \boldsymbol{\psi}(\mathbf{x}), \mathbf{L}[\mathbf{x}; \mathbf{g}(\boldsymbol{\alpha})]\, \boldsymbol{\varphi}(\mathbf{x}) \rangle_0 = \langle \mathbf{L}^*[\mathbf{x}; \mathbf{g}(\boldsymbol{\alpha})]\, \boldsymbol{\psi}(\mathbf{x}), \boldsymbol{\varphi}(\mathbf{x}) \rangle_0$$
$$= \langle \boldsymbol{\psi}(\mathbf{x}), \mathbf{Q}[\mathbf{x}; \mathbf{g}(\boldsymbol{\alpha})] \rangle_0$$
$$= \langle \mathbf{Q}^*[\mathbf{x}; \mathbf{g}(\boldsymbol{\alpha})], \boldsymbol{\varphi}(\mathbf{x}) \rangle_0. \tag{5}$$

In Eq. 5, the formal adjoint operator $\mathbf{L}^*[\mathbf{x}; \mathbf{g}(\boldsymbol{\alpha})]$ is the $TD \times TD$ matrix comprising elements $L^*_{ji}[\mathbf{x}; \mathbf{g}(\boldsymbol{\alpha})]$ which are obtained by transposing the formal adjoints of the forward operators $L_{ij}[\mathbf{x}; \mathbf{g}(\boldsymbol{\alpha})]$. Hence, the system adjoint to the linear system represented by Eqs 1, 2 can generally be represented as follows:

$$\mathbf{L}^*[\mathbf{x}; \mathbf{g}(\boldsymbol{\alpha})]\, \boldsymbol{\psi}(\mathbf{x}) = \mathbf{Q}^*[\mathbf{x}; \mathbf{g}(\boldsymbol{\alpha})], \mathbf{x} \in \Omega(\boldsymbol{\alpha}), \tag{6}$$

$$\mathbf{B}^*[\mathbf{x}; \mathbf{g}(\boldsymbol{\alpha});\ \boldsymbol{\lambda}(\boldsymbol{\alpha}); \boldsymbol{\omega}(\boldsymbol{\alpha})]\, \boldsymbol{\psi}(\mathbf{x}) = \mathbf{C}^*[\mathbf{x}; \mathbf{g}(\boldsymbol{\alpha});\ \boldsymbol{\lambda}(\boldsymbol{\alpha}); \boldsymbol{\omega}(\boldsymbol{\alpha})],$$
$$\mathbf{x} \in \partial\Omega[\boldsymbol{\lambda}(\boldsymbol{\alpha}); \boldsymbol{\omega}(\boldsymbol{\alpha})]. \tag{7}$$

When the forward operator $\mathbf{L}[\mathbf{x}; \mathbf{g}(\boldsymbol{\alpha})]$ comprises differential operators, the operations (e.g., integration by parts) that implement the transition from the left-side to the right side of Eq. 5 give rise to boundary terms which are collectively called the "bilinear concomitant." The domain of $\mathbf{L}^*[\mathbf{x}; \mathbf{g}(\boldsymbol{\alpha})]$ is determined by selecting adjoint boundary and/or initial conditions so as to ensure that the bilinear concomitant vanishes when the selected adjoint boundary conditions are implemented together with the forward boundary conditions given in Eq. 2. The adjoint boundary conditions thus selected are represented in operator form by Eq. 7.

The results computed using a mathematical model are customarily called "model responses" (or "system responses" or "objective functions" or "indices of performance"). For linear physical systems, the system's response may depend not only on the model's state-functions and on the system parameters but may simultaneously also depend on the adjoint state function. As has been discussed by Cacuci (2022, 2023a), Cacuci D. G. (2023), any response of a linear system can be formally represented (using expansions or interpolation, if necessary) and fundamentally analyzed in terms of the following generic integral representation:

$$R[\boldsymbol{\varphi}(\mathbf{x}), \boldsymbol{\psi}(\mathbf{x}); \mathbf{f}(\boldsymbol{\alpha})] \triangleq \int\limits_{\lambda_1(\boldsymbol{\alpha})}^{\omega_1(\boldsymbol{\alpha})} \dots \int\limits_{\lambda_{TI}(\boldsymbol{\alpha})}^{\omega_{TI}(\boldsymbol{\alpha})} S[\boldsymbol{\varphi}(\mathbf{x}), \boldsymbol{\psi}(\mathbf{x}); \mathbf{g}(\boldsymbol{\alpha}); \mathbf{h}(\boldsymbol{\alpha}); \mathbf{x}]\, dx_1 \dots dx_{TI}, \tag{8}$$

where $S[\boldsymbol{\varphi}(\mathbf{x}), \boldsymbol{\psi}(\mathbf{x}); \mathbf{g}(\boldsymbol{\alpha}); \mathbf{h}(\boldsymbol{\alpha}); \mathbf{x}]$ is a suitably differentiable nonlinear function of $\boldsymbol{\varphi}(\mathbf{x}), \boldsymbol{\psi}(\mathbf{x})$, and $\boldsymbol{\alpha}$. The integral representation of the response provided in Eq. 8 can represent "averaged" and/or "point-valued" quantities in the phase-space of independent variables. For example, if $R[\boldsymbol{\varphi}(\mathbf{x}), \boldsymbol{\psi}(\mathbf{x}); \mathbf{f}(\boldsymbol{\alpha})]$ represents the computation or the measurement (which would be a "detector-response") of a quantity of interest at a point $\mathbf{x}_d$ in the phase-space of independent variables, then $S[\boldsymbol{\varphi}(\mathbf{x}), \boldsymbol{\psi}(\mathbf{x}); \mathbf{g}(\boldsymbol{\alpha}); \mathbf{h}(\boldsymbol{\alpha}); \mathbf{x}]$ would contain a Dirac-delta functional of the form $\delta(\mathbf{x} - \mathbf{x}_d)$. Responses that represent "differentials/derivatives of quantities" would contain derivatives of Dirac-delta functionals in the definition of $S[\boldsymbol{\varphi}(\mathbf{x}), \boldsymbol{\psi}(\mathbf{x}); \mathbf{g}(\boldsymbol{\alpha}); \mathbf{h}(\boldsymbol{\alpha}); \mathbf{x}]$. The vector $\mathbf{h}(\boldsymbol{\alpha}) \triangleq [h_1(\boldsymbol{\alpha}), \dots, h_{TH}(\boldsymbol{\alpha})]$, having components $h_i(\boldsymbol{\alpha}), i = 1, \dots, TH$, which appears among the arguments of the function $S[\boldsymbol{\varphi}(\mathbf{x}), \boldsymbol{\psi}(\mathbf{x}); \mathbf{g}(\boldsymbol{\alpha}); \mathbf{h}(\boldsymbol{\alpha}); \mathbf{x}]$, represents functions of primary parameters that often appear solely in the definition of the response but do not appear in the mathematical definition of the model, i.e., in Eqs 1, 2, 6, 7. The quantity TH denotes the total number of such functions which appear exclusively in the definition of the model's response. Evidently, the response will depend directly and/or indirectly (through the "feature"-functions) on all of the primary model parameters. This fact has been indicated in Eq. 8 by using the vector-valued function $\mathbf{f}(\boldsymbol{\alpha})$ as an argument in the definition of the response $R[\boldsymbol{\varphi}(\mathbf{x}), \boldsymbol{\psi}(\mathbf{x}); \mathbf{f}(\boldsymbol{\alpha})]$ to represent the concatenation of all of the "features" of the model and response under consideration. The vector $\mathbf{f}(\boldsymbol{\alpha})$ of "model features" is thus defined as follows:

$$\mathbf{f}(\boldsymbol{\alpha}) \triangleq [\mathbf{g}(\boldsymbol{\alpha}); \mathbf{h}(\boldsymbol{\alpha}); \boldsymbol{\lambda}(\boldsymbol{\alpha}); \boldsymbol{\omega}(\boldsymbol{\alpha})]^\dagger \triangleq [f_1(\boldsymbol{\alpha}), \dots, f_{TF}(\boldsymbol{\alpha})]^\dagger;\ TF \triangleq TG + TH + 2TI. \tag{9}$$

As defined in Eq. 9, the quantity TF denotes the total number of "feature functions of the model's parameters" which appear in the definition of the nonlinear model's underlying equations and response.

Solving Eqs 1, 2, at the nominal (or mean) values, denoted as $\boldsymbol{\alpha}^0 \triangleq [\alpha_1^0, \dots, \alpha_i^0, \dots, \alpha_{TP}^0]^\dagger$, of the model parameters, yields the nominal forward solution, which will be denoted as $\boldsymbol{\varphi}^0(\mathbf{x})$. Solving Eqs 6, 7 at the nominal values, $\boldsymbol{\alpha}^0$, of the model parameters yields the nominal adjoint solution, which will be denoted as $\boldsymbol{\psi}^0(\mathbf{x})$. The nominal value of the response, $R[\boldsymbol{\varphi}^0(\mathbf{x}), \boldsymbol{\psi}^0(\mathbf{x}); \mathbf{f}(\boldsymbol{\alpha}^0)]$, is determined by using the nominal parameter values $\boldsymbol{\alpha}^0$, the nominal value $\boldsymbol{\varphi}^0(\mathbf{x})$ of the forward state function, and the nominal value $\boldsymbol{\psi}^0(\mathbf{x})$ of the adjoint state function.

The definition provided by Eq. 8 implies that the model response $R[\boldsymbol{\varphi}(\mathbf{x}), \boldsymbol{\psi}(\mathbf{x}); \mathbf{f}(\boldsymbol{\alpha})]$ depends on the components of the feature function $\mathbf{f}(\boldsymbol{\alpha})$, and would therefore admit a Taylor-series expansion around the nominal value $\mathbf{f}^0 \triangleq \mathbf{f}(\boldsymbol{\alpha}^0)$, having the following form:

$$R[\mathbf{f}(\boldsymbol{\alpha})] = R(\mathbf{f}^0) + \sum_{j_1=1}^{TF} \left\{ \frac{\partial R(\mathbf{f})}{\partial f_{j_1}} \right\}_{\mathbf{f}^0} \delta f_{j_1} + \frac{1}{2} \sum_{j_1=1}^{TF}$$
$$\times \sum_{j_2=1}^{TF} \left\{ \frac{\partial^2 R(\mathbf{f})}{\partial f_{j_1} \partial f_{j_2}} \right\}_{\mathbf{f}^0} \delta f_{j_1} \delta f_{j_2} + \cdots \tag{10}$$

where $\delta f_j \triangleq [f_j(\boldsymbol{\alpha}) - f_j^0];\ f_j^0 \triangleq f_j(\boldsymbol{\alpha}^0);\quad j = 1, \dots, TF.$ The "sensitivities of the model response with respect to the (feature) functions” are naturally defined as being the functional derivatives of $R[\mathbf{f}(\boldsymbol{\alpha})]$ with respect to the components (“features”) $f_j(\boldsymbol{\alpha})$ of $\mathbf{f}(\boldsymbol{\alpha})$. The notation $\{\cdot\}_{\mathbf{f}^0}$ indicates that the quantity enclosed within the braces is to be evaluated at the nominal values $\mathbf{f}^0 \triangleq \mathbf{f}(\boldsymbol{\alpha}^0)$. Since $TF \ll TP$, there will be fewer derivatives of the response with respect to the feature functions than there are response derivatives with respect to the primary model parameters. Hence, the computations of the functional derivatives of $R[\mathbf{f}(\boldsymbol{\alpha})]$ with respect to the functions $f_j(\boldsymbol{\alpha})$, which appear in Eq. 10, will be considerably less expensive computationally than the computation of the functional derivatives involved in the Taylor-series of the response with respect to the model parameters. The functional derivatives of the response with respect to the primary parameters can be obtained from the functional derivatives of the response with respect to the “feature” functions $f_j(\boldsymbol{\alpha})$ by simply using the chain rule, i.e.,:

$$\begin{aligned}\left\{\frac{\partial R(\boldsymbol{\alpha})}{\partial \alpha_{j_1}}\right\}_{\boldsymbol{\alpha}^0} &= \sum_{i_1=1}^{TF}\left\{\frac{\partial R(\mathbf{f})}{\partial f_{i_1}}\frac{\partial f_{i_1}(\boldsymbol{\alpha})}{\partial \alpha_{j_1}}\right\}_{\boldsymbol{\alpha}^0};\ \left\{\frac{\partial^2 R(\boldsymbol{\alpha})}{\partial \alpha_{j_1}\partial \alpha_{j_2}}\right\}_{\boldsymbol{\alpha}^0}\\ &= \frac{\partial}{\partial \alpha_{j_2}}\sum_{i_1=1}^{TF}\left\{\frac{\partial R(\mathbf{f})}{\partial f_{i_1}}\frac{\partial f_{i_1}(\boldsymbol{\alpha})}{\partial \alpha_{j_1}}\right\}_{\boldsymbol{\alpha}^0}; \qquad (11)\end{aligned}$$

and so on. The evaluation/computation of the functional derivatives $\partial f_{i_1}(\boldsymbol{\alpha})/\partial\alpha_{j_1}$, $\partial^2 f_{i_1}(\boldsymbol{\alpha})/\partial\alpha_{j_1}\partial\alpha_{j_2}$, etc., does not require computations involving the model, and is therefore trivial (computationally) by comparison to the evaluation of the functional derivatives (“sensitivities”) of the response with respect to either the functions (“features”) $f_j(\boldsymbol{\alpha})$ or the model parameters $\alpha_i, i = 1, ..., TP$.

The range of validity of the Taylor-series shown in Eq. 10 is defined by its radius of convergence. The accuracy –as opposed to the “validity”– of the Taylor-series in predicting the value of the response at an arbitrary point in the phase-space of model parameters depends on the order of sensitivities retained in the Taylor-expansion: the higher the respective order, the more accurate the respective response value predicted by the Taylor-series. In the particular cases when the response happens to be a polynomial function of the “feature” functions $f_j(\boldsymbol{\alpha})$, the Taylor series is actually exact.

In turn, the functions $f_i(\boldsymbol{\alpha})$ can also be formally expanded in a multivariate Taylor-series around the nominal (mean) parameter values $\boldsymbol{\alpha}^0$, namely,:

$$\begin{aligned}f_i(\boldsymbol{\alpha}) = f_i(\boldsymbol{\alpha}^0) &+ \sum_{j_1=1}^{TP}\left\{\frac{\partial f_i(\boldsymbol{\alpha})}{\partial \alpha_{j_1}}\right\}_{\boldsymbol{\alpha}^0}\delta\alpha_{j_1} + \frac{1}{2}\sum_{j_1=1}^{TP}\\ &\times\sum_{j_2=1}^{TP}\left\{\frac{\partial^2 f_i(\boldsymbol{\alpha})}{\partial \alpha_{j_1}\partial \alpha_{j_2}}\right\}_{\boldsymbol{\alpha}^0}\delta\alpha_{j_1}\delta\alpha_{j_2} + \frac{1}{3!}\sum_{j_1=1}^{TP}\sum_{j_2=1}^{TP}\\ &\times\sum_{j_3=1}^{TP}\left\{\frac{\partial^3 f_i(\boldsymbol{\alpha})}{\partial \alpha_{j_1}\partial \alpha_{j_2}\partial \alpha_{j_3}}\right\}_{\boldsymbol{\alpha}^0}\delta\alpha_{j_1}\delta\alpha_{j_2}\delta\alpha_{j_3} + ..., \qquad (12)\end{aligned}$$

The domain of validity of the Taylor-series in Eq. 12 is defined by its own radius of convergence.

The choice of feature functions $f_i(\boldsymbol{\alpha})$ is not unique but can be tailored by the user to the problem at hand. The two most important guiding principles for constructing the feature functions $f_i(\boldsymbol{\alpha})$ based on the primary parameters are as follows:

(i) As shown in Section 2.2 while establishing the mathematical framework underlying the nth-FASAM-L, the number of large-scale computations needed to determine the numerical value of the second- and higher-order sensitivities is proportional to the number of first-order sensitivities of the model’s response with respect to the feature functions $f_i(\boldsymbol{\alpha})$. Consequently, it is important to minimize the number of feature functions $f_i(\boldsymbol{\alpha})$, while ensuring that all of the primary model parameters are encompassed within the expressions constructed for the feature functions $f_i(\boldsymbol{\alpha})$. In the extreme case when some primary parameters, α_j, cannot be grouped into the expressions of the feature functions $f_i(\boldsymbol{\alpha})$, then each of the respective primary model parameters α_j becomes a feature function $f_j(\boldsymbol{\alpha})$.

(ii) The expressions of the features functions $f_i(\boldsymbol{\alpha})$ must be independent of the model’s state functions; they must be exact, closed-form, scalar-valued functions of the primary model parameters α_j, so the exact expressions of the derivatives of $f_i(\boldsymbol{\alpha})$ with respect to the primary model parameters α_j can be obtained analytically (with “pencil and paper”). The motivation for this requirement is to ensure that the numerical determination of the subsequent derivatives of the features functions $f_i(\boldsymbol{\alpha})$ with respect to the primary model parameters α_j becomes trivial computationally. In the extreme case when no feature function can be constructed, the feature functions are the primary parameters themselves, in which case the nth-FASAM-L methodology becomes identical to the previously established nth-CASAM-L methodology (Cacuci, 2022)

2.2 Establishing the mathematical framework of the nth-FASAM-L methodology

Cacuci D. G. (2023), Cacuci (2024a), Cacuci (2024b) has recently developed the “nth-Order Features Adjoint Sensitivity Analysis Methodology for Nonlinear Systems (nth-FASAM-N)” which enables the computation of arbitrarily-high-order sensitivities of responses to features/functions of parameters for *nonlinear* models/systems. Together, the nth-CASAM-L and the nth-FASAM-N provide the basis for the development of the “nth-Order Features Adjoint Sensitivity Analysis Methodology for Response-Coupled Forward and Adjoint Linear Systems (Nth-FASAM-L)” to be presented in this Section. In particular, comparing the mathematical framework of the 1st-FASAM-L to the framework of the 1st-CASAM-L (Cacuci and Fang, 2023) suggests that the components $f_i(\boldsymbol{\alpha}), i = 1, ..., TF$, of the “feature function” $\mathbf{f}(\boldsymbol{\alpha}) \triangleq [f_1(\boldsymbol{\alpha}), ..., f_{TF}(\boldsymbol{\alpha})]^\dagger$ will play within the 1st-FASAM-L the same role as played by the components $\alpha_j, j = 1, ..., TP$, of the “vector of primary model parameters” $\boldsymbol{\alpha} \triangleq (\alpha_1, \dots, \alpha_{TP})^\dagger$ within the framework of the 1st-CASAM-L. It can therefore be conjectured that the same correspondence would be expected to hold in general, between the general frameworks of the nth-FASAM-L and the nth-CASAM-L methodologies. As will be demonstrated in this Section, this conjecture is indeed correct.

Considering the analogy to the framework of the nth-CASAM-L methodology (Cacuci, 2022), *it is conjectured that that the*

G-differential of the (n-1)th-order sensitivity of the model's response $R[\mathbf{u}(\mathbf{x}); \mathbf{f}(\boldsymbol{\alpha})]$ *with respect to the components* $f_1, ..., f_{TF}$ *of the "feature" function* $\mathbf{f}(\boldsymbol{\alpha}) \triangleq [f_1(\boldsymbol{\alpha}), ..., f_{TF}(\boldsymbol{\alpha})]^\dagger$ will have the following form:

$$\begin{aligned}&\left\{\delta R^{(n-1)}\left[j_{n-1}; ...; j_1; \mathbf{u}^{(n)}; \mathbf{f}\right]\right\}_{\boldsymbol{\alpha}^0} \\ &= \sum_{j_n=1}^{TF}\left\{\frac{\partial}{\partial f_{j_n}}\int_{\lambda_1(\boldsymbol{\alpha})}^{\omega_1(\boldsymbol{\alpha})} dx_1 ... \int_{\lambda_{TI}(\boldsymbol{\alpha})}^{\omega_{TI}(\boldsymbol{\alpha})} dx_{TI} S^{(n-1)}\left(j_{n-1}, ..., j_1; \mathbf{u}^{(n)}; \boldsymbol{\alpha}\right)\delta f_{j_n}\right\}_{\boldsymbol{\alpha}^0} \\ &\quad + \left\{\left\langle \mathbf{a}^{(n)}\left(j_{n-1}, ..., j_1; \mathbf{x}\right), \mathbf{q}_V^{(n)}\left[2^n; \mathbf{u}^{(n)}\left(2^n; \mathbf{x}\right); \mathbf{f}; \delta\mathbf{f}\right]\right\rangle_n\right\}_{\boldsymbol{\alpha}^0} \\ &\quad - \left\{\hat{P}^{(n)}\left(\mathbf{a}^{(n)}; \mathbf{u}^{(n)}; \mathbf{f}; \delta\mathbf{f}\right)\right\}_{\boldsymbol{\alpha}^0} \equiv \sum_{j_n=1}^{TF}\left\{R^{(n)}\left(j_n, ..., j_1; \mathbf{u}^{(n)}; \mathbf{a}^{(n)}; \mathbf{f}\right)\right\}_{(\boldsymbol{\alpha}^0)}\delta f_{j_n},\end{aligned} \tag{13}$$

such that the nth-*order sensitivity* of the model's response $R[\mathbf{u}(\mathbf{x}); \mathbf{f}(\boldsymbol{\alpha})]$ with respect to the components $f_{j_1}, ..., f_{j_n}$ of the "feature" function $\mathbf{f}(\boldsymbol{\alpha}) \triangleq [f_{j_1}(\boldsymbol{\alpha}), ..., f_{j_n}(\boldsymbol{\alpha})]^\dagger$ is expected to have the following functional form:

$$\begin{aligned}&R^{(n)}\left[j_n; ...; j_1; \mathbf{u}^{(n)}\left(2^n; j_{n-2}, ..., j_1; \mathbf{x}\right); \mathbf{a}^{(n)}\left(2^n; j_{n-1}, ..., j_1; \mathbf{x}\right); \mathbf{f}(\boldsymbol{\alpha})\right] \\ &\triangleq \int_{\lambda_1(\boldsymbol{\alpha})}^{\omega_1(\boldsymbol{\alpha})} dx_1 ... \int_{\lambda_{TI}(\boldsymbol{\alpha})}^{\omega_{TI}(\boldsymbol{\alpha})} dx_{TI} S^{(n)}\left[j_n; ...; j_1; \mathbf{u}^{(n)}; \mathbf{a}^{(n)}; \mathbf{f}(\boldsymbol{\alpha})\right] \\ &\triangleq \partial^n R[\mathbf{u}(\mathbf{x}); \mathbf{f}(\boldsymbol{\alpha})] \big/ \partial f_{j_n} ... \partial f_{j_1};\ \ j_1 = 1, ..., TF;\ \ j_n = 1, ..., j_{n-1};\ \ n = 2, 3, ...\end{aligned} \tag{14}$$

where TF denotes the "total number of features," i.e., functions of the primary model parameters.

It is also conjectured that the nth-level adjoint functions $\mathbf{u}^{(n)}(2^n; j_{n-2}, ..., j_1; \mathbf{x})$ and $\mathbf{a}^{(n)}(j_{n-1}, ..., j_1; 2^n; \mathbf{x})$, which are needed to compute the nth-order sensitivities shown in Eq. 14, are obtained as follows:

(i) $\mathbf{u}^{(n)}(2^n; j_{n-2}, ..., j_1; \mathbf{x}) \triangleq [\mathbf{u}^{(n-1)}(2^{n-1}; j_{n-3}, ..., j_1; \mathbf{x}), \mathbf{a}^{(n-1)}(2^{n-1}; j_{n-2}, ..., j_1; \mathbf{x})]^\dagger$ are the solutions of the following nth-*Level Forward/Adjoint System (*n*th-LFAS)* for $j_n = 1, ..., j_{n-1};\ \ n \geq 3$:

$$\begin{aligned}\mathbf{F}^{(n)}\left[2^n \times 2^n; \mathbf{f}(\boldsymbol{\alpha})\right]\mathbf{u}^{(n)}\left(2^n; j_{n-2}, ..., j_1; \mathbf{x}\right) \\ = \mathbf{q}_F^{(n)}\left[2^n; \mathbf{u}^{(n-1)}; \mathbf{f}(\boldsymbol{\alpha})\right];\ \ \mathbf{x} \in \Omega;\end{aligned} \tag{15}$$

$$\mathbf{b}_F^{(n)}\left(2^n; \mathbf{u}^{(n)}; \mathbf{f}\right) = \mathbf{0};\quad \mathbf{x} \in \partial\Omega; \tag{16}$$

(ii) $\mathbf{a}^{(n)}(j_{n-1}, ..., j_1; 2^n; \mathbf{x})$ are the solutions of the following nth-*Level Adjoint Sensitivity System (*n*th-LASS)* for $j_n = 1, ..., j_{n-1};\ \ n \geq 3$:

$$\mathbf{A}^{(n)}\left[2^n \times 2^n; \mathbf{f}(\boldsymbol{\alpha})\right]\mathbf{a}^{(n)}\left(2^n; j_{n-1}, ..., j_1; \mathbf{x}\right) = \mathbf{s}^{(n)}\left(2^n; \mathbf{u}^{(n)}; \mathbf{f}\right);\quad \mathbf{x} \in \Omega; \tag{17}$$

$$\left\{\mathbf{b}_A^{(n)}\left[\mathbf{u}^{(n)}\left(2^n; j_{n-1}, ..., j_1; \mathbf{x}\right); \mathbf{a}^{(n)}\left(2^n; j_{n-1}, ..., j_1; \mathbf{x}\right); \mathbf{f}\right]\right\}_{\boldsymbol{\alpha}^0} = \mathbf{0}, \mathbf{x} \in \partial\Omega. \tag{18}$$

Through their implicit dependence on lower-level forward and adjoint functions, the block-matrix valued operators $\mathbf{F}^{(n)}[2^n \times 2^n; \mathbf{f}(\boldsymbol{\alpha})]$ and $\mathbf{A}^{(n)}[2^n \times 2^n; \mathbf{f}(\boldsymbol{\alpha})]$, as well as the source terms $\mathbf{q}_F^{(n)}[2^n; \mathbf{u}^{(n-1)}; \mathbf{f}(\boldsymbol{\alpha})]$ and $\mathbf{s}^{(n)}(2^n; \mathbf{u}^{(n)}; \mathbf{f})$, also depend on lower-level indices $j_k, k < n$, but this dependence is not material to establishing the general framework of the nth-FASAM-L and has therefore been omitted, to keep the notation as simple as possible.

2.3 Proving that the conjectured mathematical framework of the nth-FASAM-L methodology is correct for $n = 1$

The proof that the framework conjectured in Section 2.2 for the nth-FASAM-L methodology is indeed correct/valid when $n = 1$ (for the 1st-FASAM-L methodology) parallels the proof used in (Cacuci, 2022) to show that the framework of the nth-CASAM-L methodology reduces to the corresponding 1st-CASAM-L methodology when $n = 1$. In preparation for subsequent generalizations towards establishing the generic pattern for computing sensitivities of arbitrarily high-order, the function $\mathbf{u}^{(1)}(2; \mathbf{x}) \triangleq [\boldsymbol{\varphi}(\mathbf{x}), \boldsymbol{\psi}(\mathbf{x})]^\dagger$ will be called the "*1st-level forward/adjoint function*" and the system of equations satisfied by this function (which is obtained by concatenating the original forward and adjoint equations together with their respective boundary/initial conditions) will be called "*the 1st-Level Forward/Adjoint System (1st-LFAS)*" and will be re-written in the following concatenated matrix-form:

$$\mathbf{F}^{(1)}[2 \times 2; \mathbf{x}; \mathbf{f}]\mathbf{u}^{(1)}(2; \mathbf{x}) = \mathbf{q}_F^{(1)}(2; \mathbf{x}; \mathbf{f});\quad \mathbf{x} \in \Omega(\boldsymbol{\alpha}); \tag{19}$$

$$\mathbf{b}_F^{(1)}\left[\mathbf{u}^{(1)}(2; \mathbf{x});\ \mathbf{f}\right] = \mathbf{0};\quad \mathbf{x} \in \partial\Omega[\boldsymbol{\lambda}(\boldsymbol{\alpha}); \boldsymbol{\omega}(\boldsymbol{\alpha})]; \tag{20}$$

where the following definitions were used:

$$\begin{aligned}\mathbf{F}^{(1)}[2 \times 2; \mathbf{x}; \mathbf{f}] &\triangleq \begin{pmatrix}\mathbf{L}(\mathbf{x}; \mathbf{f}) & \mathbf{0} \\ \mathbf{0} & \mathbf{L}^*(\mathbf{x}; \mathbf{f})\end{pmatrix}; \\ \mathbf{u}^{(1)}(2; \mathbf{x}) &\triangleq [\boldsymbol{\varphi}(\mathbf{x}), \boldsymbol{\psi}(\mathbf{x})]^\dagger;\end{aligned} \tag{21}$$

$$\begin{aligned}\mathbf{q}_F^{(1)}(2; \mathbf{x}; \mathbf{f}) &\triangleq \begin{pmatrix}\mathbf{Q}(\mathbf{x}; \mathbf{g}) \\ \mathbf{Q}^*(\mathbf{x}; \mathbf{g})\end{pmatrix}; \\ \mathbf{b}_F^{(1)}\left[2; \mathbf{u}^{(1)}(2; \mathbf{x});\ \mathbf{f}\right] &\triangleq \begin{pmatrix}\mathbf{B}(\mathbf{x}; \mathbf{f})\boldsymbol{\varphi}(\mathbf{x}) - \mathbf{C}(\mathbf{f}) \\ \mathbf{B}^*(\mathbf{x}; \mathbf{f})\boldsymbol{\psi}(\mathbf{x}) - \mathbf{C}^*(\mathbf{f})\end{pmatrix}.\end{aligned} \tag{22}$$

In the list of arguments of the matrix $\mathbf{F}^{(1)}[2 \times 2; \mathbf{x}; \mathbf{f}]$, the argument "$2 \times 2$" indicates that this square matrix comprises four component sub-matrices, as indicated in Eq. 21. Similarly, the argument "2" that appears in the block-vectors $\mathbf{u}^{(1)}(2; \mathbf{x})$, $\mathbf{q}_F^{(1)}(2; \mathbf{x}; \mathbf{f})$, and $\mathbf{b}_F^{(1)}[2; \mathbf{u}^{(1)}(2; \mathbf{x});\ \mathbf{f}]$ defined in Eq. 22 indicates that each of these column block-vectors comprises two sub-vectors as components. Also, throughout this work, the quantity "$\mathbf{0}$" will be used to denote either as a vector with zero-valued components or a matrix zero-valued components, depending on the context. For example, the vector "$\mathbf{0}$" in Eq. 20 is considered to have as many components as the vector $\mathbf{b}_F^{(1)}[\mathbf{u}^{(1)}(2; \mathbf{x});\ \mathbf{f}]$. On the other hand, the quantity "$\mathbf{0}$" which appears in Eq. 21 may represent either a (sub) matrix or a vector of the requisite dimensions.

The primary parameters $\boldsymbol{\alpha}$ are subject to uncertainties; their nominal (or mean) values, denoted as $\boldsymbol{\alpha}^0$, are considered to be known, but these values will differ from the true values $\boldsymbol{\alpha}$, which are unknown, by variations $\delta\boldsymbol{\alpha} \triangleq (\delta\alpha_1, \ldots, \delta\alpha_{TP})^\dagger$, where $\delta\alpha_i \triangleq \alpha_i - \alpha_i^0$. The parameter variations $\delta\boldsymbol{\alpha}$ will induce variations $\delta\mathbf{f}(\boldsymbol{\alpha}) \triangleq [\delta f_1(\boldsymbol{\alpha}), \ldots, \delta f_{TF}(\boldsymbol{\alpha})]^\dagger$ in the vector-valued "feature" function $\mathbf{f}(\boldsymbol{\alpha})$, around the nominal value $\mathbf{f}^0 \triangleq \mathbf{f}(\boldsymbol{\alpha}^0)$, and will also induce variations $\delta\boldsymbol{\varphi}(\mathbf{x})$ and $\delta\boldsymbol{\psi}(\mathbf{x})$, respectively, around the nominal solutions $\boldsymbol{\varphi}^0, \boldsymbol{\psi}^0$, through the equations underlying the model. All of these variations will induce variations in the model response $R[\mathbf{u}^{(1)}(2; \mathbf{x}); \mathbf{f}] \equiv R[\boldsymbol{\varphi}(\mathbf{x}), \boldsymbol{\psi}(\mathbf{x}); \mathbf{f}(\boldsymbol{\alpha})]$.

Formally, the first-order sensitivities of the response $R[\mathbf{u}^{(1)}(2;\mathbf{x});\mathbf{f}]$ with respect to the components of the feature function $\mathbf{f}(\boldsymbol{\alpha})$ are provided by the first-order Gateaux (G-)variation of $R(\boldsymbol{\varphi},\boldsymbol{\psi},\mathbf{f})$ at the phase-space point $(\boldsymbol{\varphi}^0,\boldsymbol{\psi}^0,\mathbf{f}^0)$, which is defined as follows:

$$\begin{aligned}\delta R(\boldsymbol{\varphi}^0,\boldsymbol{\psi}^0,\mathbf{f}^0;\delta\boldsymbol{\varphi},\delta\boldsymbol{\psi},\delta\mathbf{f}) &\triangleq \left\{\frac{d}{d\varepsilon}R[\boldsymbol{\varphi}^0(\mathbf{x})+\varepsilon\delta\boldsymbol{\varphi}(\mathbf{x}),\boldsymbol{\psi}^0(\mathbf{x})+\varepsilon\delta\boldsymbol{\psi}(\mathbf{x});\mathbf{f}^0+\varepsilon\delta\mathbf{f}]\right\}_{\varepsilon=0}\\ &\equiv \left\{\frac{d}{d\varepsilon}R\left[\mathbf{u}^{(1,0)}(2;\mathbf{x})+\varepsilon\mathbf{v}^{(1)}(2;\mathbf{x});\mathbf{f}^0+\varepsilon\delta\mathbf{f}\right]\right\}_{\varepsilon=0}\\ &\equiv \delta R\left[\mathbf{u}^{(1,0)}(2;\mathbf{x});\mathbf{f}^0;\mathbf{v}^{(1)}(2;\mathbf{x}),\delta\mathbf{f}\right].\end{aligned}\tag{23}$$

The definitions provided in Eq. 24, below, were used in Eq. 23:

$$\mathbf{u}^{(1,0)}(2;\mathbf{x}) \triangleq \left[\boldsymbol{\varphi}^0(\mathbf{x}),\boldsymbol{\psi}^0(\mathbf{x})\right]^{\dagger};\quad \mathbf{v}^{(1)}(2;\mathbf{x}) \triangleq \left[\delta\boldsymbol{\varphi}(\mathbf{x}),\delta\boldsymbol{\psi}\right]^{\dagger}.\tag{24}$$

The numerical methods (e.g., Newton's method and variants thereof) for solving large-scale systems require the existence of the first-order G-derivatives of the original model equations and of the model's response; these will be assumed to exist. When the 1st-order G-derivatives exists, the variation $\delta R[\mathbf{u}^{(1,0)}(2;\mathbf{x});\mathbf{f}^0;\mathbf{v}^{(1)}(2;\mathbf{x}),\delta\mathbf{f}]$ can be written as follows:

$$\begin{aligned}\delta R\left[\mathbf{u}^{(1,0)}(2;\mathbf{x});\mathbf{f}^0;\mathbf{v}^{(1)}(2;\mathbf{x}),\delta\mathbf{f}\right] = &\left\{\delta R\left[\mathbf{u}^{(1)}(2;\mathbf{x});\mathbf{f};\delta\mathbf{f}\right]\right\}_{dir}\\ &+\left\{\delta R\left[\mathbf{u}^{(1)}(2;\mathbf{x});\mathbf{f};\mathbf{v}^{(1)}(2;\mathbf{x})\right]\right\}_{ind}.\end{aligned}\tag{25}$$

In Eq. 25, the "direct-effect" term $\{\delta R[\mathbf{u}^{(1)}(2;\mathbf{x});\mathbf{f};\delta\mathbf{f}]\}_{dir}$ comprises only dependencies on $\delta\mathbf{f}(\boldsymbol{\alpha})$ and is defined as follows:

$$\left\{\delta R\left[\mathbf{u}^{(1)}(2;\mathbf{x});\mathbf{f};\delta\mathbf{f}\right]\right\}_{dir} \triangleq \left\{\frac{\partial R(\mathbf{u}^{(1)};\mathbf{f})}{\partial\mathbf{f}}\delta\mathbf{f}\right\}_{\boldsymbol{\alpha}^0}.\tag{26}$$

The following convention/definition was used in Eq. 26:

$$\begin{aligned}\frac{\partial[\,]}{\partial\mathbf{f}}\delta\mathbf{f} \triangleq \sum_{i=1}^{TF}\frac{\partial[\,]}{\partial f_i}\delta f_i = \sum_{i=1}^{TG}\frac{\partial[\,]}{\partial g_i}\delta g_i + \sum_{i=1}^{TH}\frac{\partial[\,]}{\partial h_i}\delta h_i + \sum_{i=1}^{TI}\frac{\partial[\,]}{\partial\omega_i}\delta\omega_i\\ +\sum_{i=1}^{TI}\frac{\partial[\,]}{\partial\lambda_i}\delta\lambda_i.\end{aligned}\tag{27}$$

The notation on the left-side of Eq. 27 represents the inner product between two vectors, but the "dagger" symbol "(†)" which indicates "transposition" has been omitted in order to keep the notation as simple as possible. "Daggers" indicating transposition will also be omitted in other inner products, whenever possible, while avoiding ambiguities.

In Eq. 25, the "indirect-effect" term $\{\delta R[\mathbf{u}^{(1)}(2;\mathbf{x});\mathbf{f};\mathbf{v}^{(1)}(2;\mathbf{x})]\}_{ind}$ depends only on the variations $\mathbf{v}^{(1)}(2;\mathbf{x}) \triangleq [\delta\boldsymbol{\varphi}(\mathbf{x}),\delta\boldsymbol{\psi}]^{\dagger}$ in the state functions, and is defined as follows:

$$\begin{aligned}&\left\{\delta R\left[\mathbf{u}^{(1)}(2;\mathbf{x});\mathbf{f};\mathbf{v}^{(1)}(2;\mathbf{x})\right]\right\}_{ind}\\ &\triangleq \left\{\int_{\lambda_1(\boldsymbol{\alpha})}^{\omega_1(\boldsymbol{\alpha})}dx_1\ldots\int_{\lambda_{TI}(\boldsymbol{\alpha})}^{\omega_{TI}(\boldsymbol{\alpha})}dx_{TI}\frac{\partial S(\boldsymbol{\varphi},\boldsymbol{\psi};\mathbf{g};\mathbf{h})}{\partial\mathbf{u}^{(1)}(2;\mathbf{x})}\mathbf{v}^{(1)}(2;\mathbf{x})\right\}_{\boldsymbol{\alpha}^0}\\ &\triangleq \left\{\int_{\lambda_1(\boldsymbol{\alpha})}^{\omega_1(\boldsymbol{\alpha})}dx_1\ldots\int_{\lambda_{TI}(\boldsymbol{\alpha})}^{\omega_{TI}(\boldsymbol{\alpha})}dx_{TI}\frac{\partial S(\boldsymbol{\varphi},\boldsymbol{\psi};\mathbf{g};\mathbf{h})}{\partial\boldsymbol{\varphi}}\delta\boldsymbol{\varphi}\right\}_{\boldsymbol{\alpha}^0}\\ &+\left\{\int_{\lambda_1(\boldsymbol{\alpha})}^{\omega_1(\boldsymbol{\alpha})}dx_1\ldots\int_{\lambda_{TI}(\boldsymbol{\alpha})}^{\omega_{TI}(\boldsymbol{\alpha})}dx_{TI}\frac{\partial S(\boldsymbol{\varphi},\boldsymbol{\psi};\mathbf{g};\mathbf{h})}{\partial\boldsymbol{\psi}}\delta\boldsymbol{\psi}\right\}_{\boldsymbol{\alpha}^0}.\end{aligned}\tag{28}$$

In Eqs 26, 28, the notation $\{\quad\}_{\boldsymbol{\alpha}^0}$ has been used to indicate that the quantity within the brackets is to be evaluated at the nominal values of the parameters *and* state functions. This simplified notation is justified by the fact that when the parameters take on their nominal values, it implicitly means that the corresponding state functions also take on their corresponding nominal values. This simplified notation will be used throughout this work.

The direct-effect term can be computed after having solved the forward system modeled by Eqs 1, 2, as well as the adjoint system modeled by Eqs 6, 7, using the nominal parameter values to obtain the nominal values $\boldsymbol{\varphi}^0,\boldsymbol{\psi}^0$ of the forward and adjoint dependent variables.

On the other hand, the indirect-effect term $\{\delta R[\mathbf{u}^{(1)}(2;\mathbf{x});\mathbf{f};\mathbf{v}^{(1)}(2;\mathbf{x})]\}_{ind}$ defined in Eq. 28 can be quantified only after having determined the variations $\mathbf{v}^{(1)}(2;\mathbf{x}) \triangleq [\delta\boldsymbol{\varphi}(\mathbf{x}),\delta\boldsymbol{\psi}]^{\dagger}$ in the state functions of the 1st-Level Forward/Adjoint System (1st-LFAS). The variations $\mathbf{v}^{(1)}(2;\mathbf{x})$ are obtained as the solutions of the system of equations obtained by taking the first-order G-differentials of the 1st-LFAS defined by Eqs 19, 20, which are obtained by definition as follows:

$$\begin{aligned}&\left\{\frac{d}{d\varepsilon}\mathbf{F}^{(1)}[2\times 2;\mathbf{x};\mathbf{f}^0+\varepsilon\delta\mathbf{f}]\left[\mathbf{u}^{(1,0)}(2;\mathbf{x})+\varepsilon\mathbf{v}^{(1)}(2;\mathbf{x})\right]\right\}_{\varepsilon=0}\\ &\quad=\left\{\frac{d}{d\varepsilon}\mathbf{q}_F^{(1)}[2;\mathbf{x};\mathbf{f}^0+\varepsilon\delta\mathbf{f}]\right\}_{\varepsilon=0},\end{aligned}\tag{29}$$

$$\left\{\frac{d}{d\varepsilon}\mathbf{b}_F^{(1)}\left[2;\mathbf{u}^{(1,0)}(2;\mathbf{x})+\varepsilon\mathbf{v}^{(1)}(2;\mathbf{x});\ \mathbf{f}^0+\varepsilon\delta\mathbf{f}\right]\right\}_{\varepsilon=0}=\mathbf{0}[2].\tag{30}$$

Carrying out the differentiations with respect to ε in Eqs 29, 30 and setting $\varepsilon = 0$ in the resulting expressions yields the following matrix-vector equations:

$$\begin{aligned}&\left\{\mathbf{V}^{(1)}[2\times 2;\mathbf{x};\mathbf{f}]\mathbf{v}^{(1)}(2;\mathbf{x})\right\}_{\boldsymbol{\alpha}^0}=\left\{\mathbf{q}_V^{(1)}\left[2;\mathbf{u}^{(1)}(2;\mathbf{x});\mathbf{f};\delta\mathbf{f}\right]\right\}_{\boldsymbol{\alpha}^0};\\ &\mathbf{x}\in\Omega(\boldsymbol{\alpha}^0);\end{aligned}\tag{31}$$

$$\left\{\mathbf{b}_v^{(1)}(\mathbf{u}^{(1)};\mathbf{v}^{(1)};\mathbf{f};\delta\mathbf{f})\right\}_{\boldsymbol{\alpha}^0}=\mathbf{0};\quad \mathbf{x}\in\partial\Omega[\boldsymbol{\lambda}(\boldsymbol{\alpha}^0);\boldsymbol{\omega}(\boldsymbol{\alpha}^0)];\tag{32}$$

where:

$$\mathbf{V}^{(1)}[2\times 2;\mathbf{x};\mathbf{f}] \triangleq \begin{pmatrix}\mathbf{L}(\mathbf{x};\mathbf{f}) & \mathbf{0}\\ \mathbf{0} & \mathbf{L}^{*}(\mathbf{x};\mathbf{f})\end{pmatrix}=\mathbf{F}^{(1)}[2\times 2;\mathbf{x};\mathbf{f}];\tag{33}$$

$$\begin{aligned}\mathbf{q}_V^{(1)}\left[2;\mathbf{u}^{(1)};\mathbf{f};\delta\mathbf{f}\right] &\triangleq \begin{pmatrix}\mathbf{q}_1^{(1)}(\boldsymbol{\varphi};\mathbf{f};\delta\mathbf{f})\\ \mathbf{q}_2^{(1)}(\boldsymbol{\psi};\mathbf{f};\delta\mathbf{f})\end{pmatrix};\\ \mathbf{b}_v^{(1)}(\mathbf{u}^{(1)};\ \mathbf{v}^{(1)};\mathbf{f};\delta\mathbf{f}) &\triangleq \begin{pmatrix}\mathbf{b}_1^{(1)}(\boldsymbol{\varphi};\delta\boldsymbol{\varphi};\mathbf{f};\delta\mathbf{f})\\ \mathbf{b}_2^{(1)}(\boldsymbol{\psi};\delta\boldsymbol{\psi};\mathbf{f};\delta\mathbf{f})\end{pmatrix};\end{aligned}\tag{34}$$

$$\mathbf{q}_1^{(1)}(\boldsymbol{\varphi};\mathbf{f};\delta\mathbf{f}) \triangleq \frac{\partial[\mathbf{Q}-\mathbf{L}\boldsymbol{\varphi}(\mathbf{x})]}{\partial\mathbf{f}}\delta\mathbf{f} \triangleq \sum_{j_1=1}^{TF}\mathbf{s}_1^{(1)}(j_1;\boldsymbol{\varphi};\mathbf{f})\delta f_{j_1}\tag{35}$$

$$\mathbf{q}_2^{(1)}(\boldsymbol{\psi},\mathbf{f};\delta\mathbf{f}) \triangleq \frac{\partial[\mathbf{Q}^{*}-\mathbf{L}^{*}\boldsymbol{\psi}(\mathbf{x})]}{\partial\mathbf{f}}\delta\mathbf{f} \triangleq \sum_{j_1=1}^{TF}\mathbf{s}_2^{(1)}(j_1;\boldsymbol{\psi};\mathbf{f})\delta f_{j_1}\tag{36}$$

$$\mathbf{b}_1^{(1)}(\boldsymbol{\varphi};\delta\boldsymbol{\varphi};\mathbf{f};\delta\mathbf{f}) \triangleq \mathbf{B}\delta\boldsymbol{\varphi}+\frac{\partial(\mathbf{B}\boldsymbol{\varphi}-\mathbf{C})}{\partial\mathbf{f}}\delta\mathbf{f};\tag{37}$$

$$\mathbf{b}_2^{(1)}(\boldsymbol{\psi};\delta\boldsymbol{\psi};\mathbf{f};\delta\mathbf{f}) \triangleq \mathbf{B}^{*}\delta\boldsymbol{\psi}+\frac{\partial(\mathbf{B}^{*}\boldsymbol{\psi}-\mathbf{C}^{*})}{\partial\mathbf{f}}\delta\mathbf{f}.\tag{38}$$

In order to keep the notation as simple as possible in Eqs 31–38, the differentials with respect to the various components of the feature function $\mathbf{f}(\boldsymbol{\alpha})$ have all been written in the form

$(\partial[]/\partial\mathbf{f})\delta\mathbf{f}$, keeping in mind the convention/notation introduced in Eq. 27. The system of equations comprising Eqs 31, 32 will be called the "*1st-Level Variational Sensitivity System* (1st-LVSS)" and its solution, $\mathbf{v}^{(1)}(2;\mathbf{x})$, will be called the "*1st-level variational sensitivity function*," which is indicated by the superscript "(1)". The solution, $\mathbf{v}^{(1)}(2;\mathbf{x})$, of the 1st-LVSS will be a function of the components of the vector of variations $\delta\mathbf{f}$. In principle, therefore, if the response sensitivities with respect to the components of the feature function $\mathbf{f}(\boldsymbol{\alpha})$ are of interest, then the 1st-LVSS would need to be solved as many times as there are components in the variational features-function $\delta\mathbf{f}$. On the other hand, if the response sensitivities with respect to the primary parameters are of interest, then the 1st-LVSS would need to be solved as many times as there are primary parameters. Solving the 1st-LVSS involves "large-scale computations."

Solving the 1st-LVSS can be avoided altogether by using the ideas underlying the "adjoint sensitivity analysis methodology" originally conceived by Cacuci (1981), and subsequently generalized by Cacuci (2022), Cacuci D. G. (2023) to enable the computation of arbitrarily high-order response sensitivities to primary model parameters for both linear and nonlinear models. Thus, the need for solving repeatedly the 1st-LVSS for every variation in the components of the feature function (or for every variation in the model's parameters) is eliminated by expressing the indirect-effect term $\{\delta R[\mathbf{u}^{(1)}(2;\mathbf{x});\mathbf{f};\mathbf{v}^{(1)}(2;\mathbf{x})]\}_{ind}$ defined in Eq. 28 in terms of the solutions of the "*1st-Level Adjoint Sensitivity System*" (1st-LASS), which will be constructed by implementing the following sequence of steps:

1. Introduce a Hilbert space, denoted as H_1, comprising vector-valued elements of the form $\boldsymbol{\chi}^{(1)}(2;\mathbf{x}) \triangleq [\boldsymbol{\chi}_1^{(1)}(\mathbf{x}),\boldsymbol{\chi}_2^{(1)}(\mathbf{x})]^\dagger$, where the components $\boldsymbol{\chi}_i^{(1)}(\mathbf{x}) \triangleq [\chi_{i,1}^{(1)}(\mathbf{x}),...,\chi_{i,j}^{(1)}(\mathbf{x}),...,\chi_{i,TD}^{(1)}(\mathbf{x})]^\dagger$, $i=1,2$, are square-integrable functions. Consider further that this Hilbert space is endowed with an inner product denoted as $\langle\boldsymbol{\chi}^{(1)}(2;\mathbf{x}),\boldsymbol{\theta}^{(1)}(2;\mathbf{x})\rangle_1$ between two elements, $\boldsymbol{\chi}^{(1)}(2;\mathbf{x})\in\mathrm{H}_1$, $\boldsymbol{\theta}^{(1)}(2;\mathbf{x})\in\mathrm{H}_1$, which is defined as follows:
$$\langle\boldsymbol{\chi}^{(1)}(2;\mathbf{x}),\boldsymbol{\theta}^{(1)}(2;\mathbf{x})\rangle_1 \triangleq \sum_{i=1}^{2}\langle\boldsymbol{\chi}_i^{(1)}(\mathbf{x}),\boldsymbol{\theta}_i^{(1)}(\mathbf{x})\rangle_0. \tag{39}$$
2. In the Hilbert H_1, use Eq. 39 to form the inner product of Eq. 31 with a yet undefined vector-valued function $\mathbf{a}^{(1)}(2;\mathbf{x}) \triangleq [\mathbf{a}_1^{(1)}(\mathbf{x}),\ \mathbf{a}_2^{(1)}(\mathbf{x})]^\dagger \in \mathrm{H}_1$ to obtain the following relation:
$$\begin{aligned}&\{\langle\mathbf{a}^{(1)}(2;\mathbf{x}),\mathbf{V}^{(1)}[2\times2;\mathbf{x};\mathbf{f}^0]\mathbf{v}^{(1)}(2;\mathbf{x})\rangle_1\}_{\boldsymbol{\alpha}^0}\\&\quad=\left\{\langle\mathbf{a}^{(1)}(2;\mathbf{x}),\mathbf{q}_V^{(1)}\left[2;\mathbf{u}^{(1)}(2;\mathbf{x});\mathbf{f};\delta\mathbf{f}\right]\rangle_1\right\}_{\boldsymbol{\alpha}^0}.\end{aligned} \tag{40}$$
3. Using the definition of the adjoint operator in the Hilbert space H_1, recast the left-side of Eq. 40 as follows:
$$\begin{aligned}&\{\langle\mathbf{a}^{(1)}(2;\mathbf{x}),\mathbf{V}^{(1)}[2\times2;\mathbf{x};\mathbf{f}]\mathbf{v}^{(1)}(2;\mathbf{x})\rangle_1\}_{\boldsymbol{\alpha}^0}\\&\quad=\{\langle\mathbf{v}^{(1)}(2;\mathbf{x}),\mathbf{A}^{(1)}[2\times2;\mathbf{x};\mathbf{f}]\mathbf{a}^{(1)}(2;\mathbf{x})\rangle_1\}_{\boldsymbol{\alpha}^0}\\&\qquad+\left\{P^{(1)}\left[\mathbf{v}^{(1)}(2;\mathbf{x});\mathbf{a}^{(1)}(2;\mathbf{x});\mathbf{f};\delta\mathbf{f}\right]\right\}_{\boldsymbol{\alpha}^0},\end{aligned} \tag{41}$$

where $\{P^{(1)}[\mathbf{v}^{(1)}(2;\mathbf{x});\mathbf{a}^{(1)}(2;\mathbf{x});\mathbf{f};\delta\mathbf{f}]\}_{\boldsymbol{\alpha}^0}$ denotes the bilinear concomitant defined on the phase-space boundary $\mathbf{x}\in\partial\Omega(\boldsymbol{\alpha}^0)$, and where $\mathbf{A}^{(1)}[2\times2;\mathbf{x};\mathbf{f}]$ is the operator formally adjoint to $\mathbf{V}^{(1)}[2\times2;\mathbf{x};\mathbf{f}]$, as defined in Eq. 42 below:

$$\mathbf{A}^{(1)}[2\times2;\mathbf{x};\mathbf{f}] \triangleq \{\mathbf{V}^{(1)}[2\times2;\mathbf{x};\mathbf{f}]\}^* = \begin{pmatrix}\mathbf{L}^*(\mathbf{x};\mathbf{f}) & \mathbf{0}\\ \mathbf{0} & \mathbf{L}(\mathbf{x};\mathbf{f})\end{pmatrix}. \tag{42}$$

4. Require the first term on right-side of Eq. 41 to represent the indirect-effect term defined in Eq. 28, to obtain the following relation:

$$\mathbf{A}^{(1)}[2\times2;\mathbf{x};\mathbf{f}]\mathbf{a}^{(1)}(2;\mathbf{x}) = \mathbf{q}_A^{(1)}\left[2;\mathbf{u}^{(1)}(2;\mathbf{x});\mathbf{f}\right],\mathbf{x}\in\Omega\left(\boldsymbol{\alpha}^0\right); \tag{43}$$

where the source term on the right-side of Eq. 43 is defined in Eq. 44, below:

$$\mathbf{q}_A^{(1)}\left[2;\mathbf{u}^{(1)}(2;\mathbf{x});\mathbf{f}\right] \triangleq \left[\frac{\partial S(\mathbf{u}^{(1)};\mathbf{f})}{\partial\mathbf{u}^{(1)}(2;\mathbf{x})}\right]^\dagger \triangleq \begin{pmatrix}\left[\partial S\left(\mathbf{u}^{(1)};\mathbf{f}\right)/\partial\boldsymbol{\varphi}\right]^\dagger\\ \left[\partial S\left(\mathbf{u}^{(1)};\mathbf{f}\right)/\partial\boldsymbol{\psi}\right]^\dagger\end{pmatrix}. \tag{44}$$

5. Implement the boundary conditions represented by Eq. 32 into Eq. 41 and eliminate the remaining unknown boundary-values of the function $\mathbf{v}^{(1)}(2;\mathbf{x})$ from the expression of the bilinear concomitant $\{P^{(1)}[\mathbf{v}^{(1)}(2;\mathbf{x});\mathbf{a}^{(1)}(2;\mathbf{x});\mathbf{f};\delta\mathbf{f}]\}_{\boldsymbol{\alpha}^0}$ by selecting appropriate boundary conditions for the function $\mathbf{a}^{(1)}(2;\mathbf{x}) \triangleq [\mathbf{a}_1^{(1)}(\mathbf{x}),\mathbf{a}_2^{(1)}(\mathbf{x})]^\dagger$, to ensure that Eq. 43 is well-posed while being independent of *unknown* values of $\mathbf{v}^{(1)}(2;\mathbf{x})$ and of $\delta\mathbf{f}$. The boundary conditions thus chosen for the function $\mathbf{a}^{(1)}(2;\mathbf{x}) \triangleq [\mathbf{a}_1^{(1)}(\mathbf{x}),\mathbf{a}_2^{(1)}(\mathbf{x})]^\dagger$ can be represented in operator form as follows:

$$\left\{\mathbf{b}_A^{(1)}\left[\mathbf{u}^{(1)}(2;\mathbf{x});\mathbf{a}^{(1)}(2;\mathbf{x});\mathbf{f}\right]\right\}_{\boldsymbol{\alpha}^0} = \mathbf{0},\mathbf{x}\in\partial\Omega[\boldsymbol{\lambda}(\boldsymbol{\alpha}^0);\boldsymbol{\omega}(\boldsymbol{\alpha}^0)]. \tag{45}$$

The selection of the boundary conditions for $\mathbf{a}^{(1)}(2;\mathbf{x}) \triangleq [\mathbf{a}_1^{(1)}(\mathbf{x}),\mathbf{a}_2^{(1)}(\mathbf{x})]^\dagger$ represented by Eq. 45 eliminates the appearance of the *unknown* values of $\mathbf{v}^{(1)}(2;\mathbf{x})$ in $\{P^{(1)}[\mathbf{v}^{(1)}(2;\mathbf{x});\mathbf{a}^{(1)}(2;\mathbf{x});\mathbf{f};\delta\mathbf{f}]\}_{\boldsymbol{\alpha}^0}$ and reduces this bilinear concomitant to a residual quantity containing boundary terms which involve only known values of $\mathbf{u}^{(1)}(2;\mathbf{x})$, $\mathbf{a}^{(1)}(2;\mathbf{x})$, $\mathbf{f}$, and $\delta\mathbf{f}$. This residual quantity will be denoted as $\left\{\hat{P}^{(1)}\left[\mathbf{u}^{(1)}(2;\mathbf{x});\mathbf{a}^{(1)}(2;\mathbf{x});\mathbf{f};\delta\mathbf{f}\right]\right\}_{\boldsymbol{\alpha}^0}$. In general, this residual quantity does not automatically vanish, although it may do so occasionally.

6. The system of equations comprising Eq. 43 together with the boundary conditions represented Eq. 45 will be called the *1st-Level Adjoint Sensitivity System* (1st-LASS). The solution $\mathbf{a}^{(1)}(2;\mathbf{x}) \triangleq [\mathbf{a}_1^{(1)}(\mathbf{x}),\mathbf{a}_2^{(1)}(\mathbf{x})]^\dagger$ of the 1st-LASS will be called the *1st-level adjoint sensitivity function*. The 1st-LASS is called "first-level" (as opposed to "first-order") because it does not contain any differential or functional-derivatives, but its solution, $\mathbf{a}^{(1)}(2;\mathbf{x})$, will be used below to compute the first-order sensitivities of the response with respect to the components of the feature function $\mathbf{f}(\boldsymbol{\alpha})$.
7. Using Eq. 40 together with the forward and adjoint boundary conditions represented by Eqs 32, 45 in Eq. 41 reduces the latter to the following relation:

$$\left\{\langle \mathbf{a}^{(1)}(2;\mathbf{x}), \mathbf{q}_V^{(1)}\left[2;\mathbf{u}^{(1)}(2;\mathbf{x});\mathbf{f};\delta\mathbf{f}\right]\rangle_1\right\}_{\boldsymbol{\alpha}^0} = \left\{\langle \mathbf{v}^{(1)}(2;\mathbf{x}), \mathbf{A}^{(1)}[2\times 2;\mathbf{x};\mathbf{f}]\mathbf{a}^{(1)}(2;\mathbf{x})\rangle_1\right\}_{\boldsymbol{\alpha}^0} + \left\{\hat{P}^{(1)}\left[\mathbf{u}^{(1)}(2;\mathbf{x});\mathbf{a}^{(1)}(2;\mathbf{x});\mathbf{f};\delta\mathbf{f}\right]\right\}_{\boldsymbol{\alpha}^0}. \tag{46}$$

8. In view of Eqs 28, 43, the first term on the right-side of Eq. 46 represents the indirect-effect term $\{\delta R[\mathbf{u}^{(1)}(2;\mathbf{x});\mathbf{f};\mathbf{v}^{(1)}]\}_{ind}$. It therefore follows from Eq. 46 that the indirect-effect term can be expressed in terms of the 1st-level adjoint sensitivity function $\mathbf{a}^{(1)}(2;\mathbf{x}) \triangleq [\mathbf{a}_1^{(1)}(\mathbf{x}), \mathbf{a}_2^{(1)}(\mathbf{x})]^\dagger$ as follows:

$$\left\{\delta R\left[\mathbf{u}^{(1)}(2;\mathbf{x});\mathbf{f};\mathbf{v}^{(1)}(2;\mathbf{x})\right]\right\}_{ind} = \left\{\langle \mathbf{a}^{(1)}(2;\mathbf{x}), \mathbf{q}_V^{(1)}\left[2;\mathbf{u}^{(1)}(2;\mathbf{x});\mathbf{f};\delta\mathbf{f}\right]\rangle_1\right\}_{\boldsymbol{\alpha}^0} - \left\{\hat{P}^{(1)}\left[\mathbf{u}^{(1)}(2;\mathbf{x});\mathbf{a}^{(1)}(2;\mathbf{x});\mathbf{f};\delta\mathbf{f}\right]\right\}_{\boldsymbol{\alpha}^0} \equiv \left\{\delta R\left[\mathbf{u}^{(1)}(2;\mathbf{x});\mathbf{a}^{(1)}(2;\mathbf{x});\mathbf{f};\delta\mathbf{f}\right]\right\}_{ind}. \tag{47}$$

As indicated by the identity shown in Eq. 47, the variations $\delta\boldsymbol{\varphi}$ and $\delta\boldsymbol{\psi}$ have been eliminated from the original expression of the indirect-effect term, which now depends on the 1st-level adjoint sensitivity function $\mathbf{a}^{(1)}(2;\mathbf{x}) \triangleq [\mathbf{a}_1^{(1)}(\mathbf{x}), \mathbf{a}_2^{(1)}(\mathbf{x})]^\dagger$. Adding the expression obtained in Eq. 47 with the expression for the direct-effect term defined in Eq. 26 yields, according to Eq. 25 the following expression for the total 1st-order sensitivity $\{\delta R(\boldsymbol{\varphi},\boldsymbol{\psi},\mathbf{f};\delta\boldsymbol{\varphi},\delta\boldsymbol{\psi},\delta\mathbf{f})\}_{\boldsymbol{\alpha}^0}$ of the response $R[\boldsymbol{\varphi}(\mathbf{x}),\boldsymbol{\psi}(\mathbf{x});\mathbf{f}]$ with respect to the components of the feature function $\mathbf{f}(\boldsymbol{\alpha})$:

$$\{\delta R(\boldsymbol{\varphi},\boldsymbol{\psi},\mathbf{f};\delta\boldsymbol{\varphi},\delta\boldsymbol{\psi},\delta\mathbf{f})\}_{\boldsymbol{\alpha}^0} = \left\{\frac{\partial \mathbf{R}(\mathbf{u}^{(1)};\mathbf{f})}{\partial \mathbf{f}}\delta\mathbf{f}\right\}_{\boldsymbol{\alpha}^0} + \left\{\langle \mathbf{a}^{(1)}(2;\mathbf{x}), \mathbf{q}_V^{(1)}\left[2;\mathbf{u}^{(1)}(2;\mathbf{x});\mathbf{f};\delta\mathbf{f}\right]\rangle_1\right\}_{\boldsymbol{\alpha}^0} - \left\{\hat{P}^{(1)}\left[\mathbf{u}^{(1)}(2;\mathbf{x});\mathbf{a}^{(1)}(2;\mathbf{x});\mathbf{f};\delta\mathbf{f}\right]\right\}_{\boldsymbol{\alpha}^0} \equiv \sum_{j_1=1}^{TF}\left\{R^{(1)}\left[j_1;\mathbf{u}^{(1)}(2;\mathbf{x});\mathbf{a}^{(1)}(2;\mathbf{x});\mathbf{f}(\boldsymbol{\alpha})\right]\delta f_{j_1}\right\}_{\boldsymbol{\alpha}^0}. \tag{48}$$

The identity which appears in Eq. 48 emphasizes the fact that the variations $\delta\boldsymbol{\varphi}$ and $\delta\boldsymbol{\psi}$, which are expensive to compute, have been eliminated from the final expressions of the 1st-order sensitivities $R^{(1)}[j_1;\mathbf{u}^{(1)}(2;\mathbf{x});\mathbf{a}^{(1)}(2;\mathbf{x});\mathbf{f}(\boldsymbol{\alpha})]$ of the response with respect to the components $f_{j_1}(\boldsymbol{\alpha}), j_1 = 1,...,TF$, of the "features function" $\mathbf{f}(\boldsymbol{\alpha})$. The dependence on the variations $\delta\boldsymbol{\varphi}$ and $\delta\boldsymbol{\psi}$ has been replaced in the expression of $R^{(1)}[j_1;\mathbf{u}^{(1)}(2;\mathbf{x});\mathbf{a}^{(1)}(2;\mathbf{x});\mathbf{f}(\boldsymbol{\alpha})]$ by the dependence on the 1st-level adjoint sensitivity function $\mathbf{a}^{(1)}(2;\mathbf{x}) \triangleq [\mathbf{a}_1^{(1)}(\mathbf{x}), \mathbf{a}_2^{(1)}(\mathbf{x})]^\dagger$. It is very important to note that the *1st-LASS* is independent of variations $\delta\mathbf{f}(\boldsymbol{\alpha})$ in the components of the feature function and is consequently also independent of any variations $\delta\boldsymbol{\alpha}$ in the primary model parameters. Hence, the 1st-LASS needs to be solved only once to obtain the 1st-level adjoint sensitivity function $\mathbf{a}^{(1)}(2;\mathbf{x}) \triangleq [\mathbf{a}_1^{(1)}(\mathbf{x}), \mathbf{a}_2^{(1)}(\mathbf{x})]^\dagger$. Subsequently, the "indirect-effect term" is computed efficiently and exactly by simply performing the integrations required to compute the inner product over the adjoint function $\mathbf{a}^{(1)}(2;\mathbf{x}) \triangleq [\mathbf{a}_1^{(1)}(\mathbf{x}), \mathbf{a}_2^{(1)}(\mathbf{x})]^\dagger$, as indicated on the right-side of Eq. 48. Solving the *1st-Level Adjoint Sensitivity System* (1st-LASS) requires the same computational effort as solving the original coupled linear system, entailing the following operations: (i) inverting (i.e., solving): the left-side of the original adjoint equation with the source $[\partial S(\mathbf{u}^{(1)};\boldsymbol{\alpha})/\partial\boldsymbol{\varphi}]^\dagger$ to obtain the 1st-level adjoint sensitivity function $\mathbf{a}_1^{(1)}(\mathbf{x})$; and (ii) inverting the left-side of the original forward equation with the source $[\partial S(\mathbf{u}^{(1)};\boldsymbol{\alpha})/\partial\boldsymbol{\psi}]^\dagger$ to obtain the 1st-level adjoint sensitivity function $\mathbf{a}_2^{(1)}(\mathbf{x})$.

The 1st-order sensitivities $R^{(1)}[j_1;\mathbf{u}^{(1)}(2;\mathbf{x});\mathbf{a}^{(1)}(2;\mathbf{x});\mathbf{f}(\boldsymbol{\alpha})]$, $j_1 = 1,...,TF$, can be expressed as an integral over the independent variables as follows:

$$R^{(1)}\left[j_1;\mathbf{u}^{(1)}(2;\mathbf{x});\mathbf{a}^{(1)}(2;\mathbf{x});\mathbf{f}(\boldsymbol{\alpha})\right] \triangleq \int_{\lambda_1(\boldsymbol{\alpha})}^{\omega_1(\boldsymbol{\alpha})} dx_1 ... \int_{\lambda_{TI}(\boldsymbol{\alpha})}^{\omega_{TI}(\boldsymbol{\alpha})} dx_{TI} S^{(1)}\left[j_1;\mathbf{u}^{(1)}(2;\mathbf{x});\mathbf{a}^{(1)}(2;\mathbf{x});\mathbf{f}(\boldsymbol{\alpha})\right]. \tag{49}$$

In particular, if the residual bilinear concomitant is non-zero, the functions $S^{(1)}[j_1;\mathbf{u}^{(1)}(2;\mathbf{x});\mathbf{a}^{(1)}(2;\mathbf{x});\mathbf{f}(\boldsymbol{\alpha})]$ would contain suitably defined Dirac delta-functionals for expressing the respective non-zero boundary terms as volume-integrals over the phase-space of the independent variables. Dirac-delta functionals would also be used in the expression of $S^{(1)}[j_1;\mathbf{u}^{(1)}(2;\mathbf{x});\mathbf{a}^{(1)}(2;\mathbf{x});\mathbf{f}(\boldsymbol{\alpha})]$ to represent terms containing the derivatives of the boundary end-points with respect to the model and/or response parameters.

The response sensitivities with respect to the primary model parameters would be obtained by using the expression obtained in Eq. 49 in conjunction with the "chain rule" of differentiation provided in Eq. 11.

It is important to compare the results produced by the 1st-FASAM-L (for obtaining the sensitivities of the model response with respect to the model's features) with the results produced by the 1st-CASAM methodology (the *1st-Order Comprehensive Adjoint Sensitivity Analysis Methodology for Response-Coupled Forward/Adjoint Linear Systems*), which provides the expressions of the responses sensitivities directly with respect to the model's primary parameters. Recall that the 1st-CASAM-L (Cacuci, 2022) yields the following expression for the 1st-order sensitivities of the response with respect to the primary model parameters:

$$\left\{\frac{\partial R[j_1;\mathbf{u}^{(1)}(2;\mathbf{x});\mathbf{a}^{(1)}(2;\mathbf{x});\boldsymbol{\alpha}]}{\partial \alpha_{j_1}}\right\}_{\boldsymbol{\alpha}^0} = \left\{\int_{\lambda_1(\boldsymbol{\alpha})}^{\omega_1(\boldsymbol{\alpha})} dx_1 ... \int_{\lambda_{TI}(\boldsymbol{\alpha})}^{\omega_{TI}(\boldsymbol{\alpha})} dx_{TI} \frac{\partial S[\mathbf{u}^{(1)}(2;\mathbf{x});\boldsymbol{\alpha}]}{\partial \alpha_{j_1}}\right\}_{\boldsymbol{\alpha}^0} + \sum_{k=1}^{TI} \times \prod_{m=1,k\neq j}^{TI}\left\{\int_{\lambda_m(\boldsymbol{\alpha})}^{\omega_m(\boldsymbol{\alpha})} dx_m S\left[\mathbf{u}^{(1)}(2;...,\omega_k,...);\boldsymbol{\alpha}\right]\frac{\partial \omega_k(\boldsymbol{\alpha})}{\partial \alpha_{j_1}} - S\left[\mathbf{u}^{(1)}(2;...,\lambda_k,...);\boldsymbol{\alpha}\right]\frac{\partial \lambda_k(\boldsymbol{\alpha})}{\partial \alpha_{j_1}}\right\}_{\boldsymbol{\alpha}^0} + \left\{\langle \mathbf{a}^{(1)}(2;\mathbf{x}), \frac{\partial}{\partial \alpha_{j_1}}\mathbf{q}^{(1)}\left[\mathbf{u}^{(1)}(2;\mathbf{x});\boldsymbol{\alpha}\right]\rangle_1\right\}_{\boldsymbol{\alpha}^0} - \left\{\frac{\partial}{\partial \alpha_{j_1}}\hat{P}^{(1)}\left[\mathbf{u}^{(1)};\mathbf{a}^{(1)};\boldsymbol{\alpha}\right]\right\}_{\boldsymbol{\alpha}^0};\ j_1 = 1,...,TP. \tag{50}$$

The same 1st-level adjoint function $\mathbf{a}^{(1)}(2;\mathbf{x})$ appears in Eq. 50 as well as in Eq. 49. Therefore, a single "large-scale computation" (needed to solve the 1st-LASS to determine the 1st-level adjoint function) is required for obtaining either the response sensitivities with respect to the components, $f_j(\boldsymbol{\alpha})$, $j = 1, ..., TF$, of the feature function $\mathbf{f}(\boldsymbol{\alpha})$ using the 1st-FASAM-L, or for obtaining the response sensitivities directly with respect to the primary model parameters α_j, $j = 1, ..., TP$, using the 1st-CASAM-L. On the other hand, the use of the 1st-CASAM-L would require performing a number of TP integrations to compute all of the response sensitivities with respect to the primary parameters, but the 1st-FASAM-L would require only TF integrations ($TF \ll TP$) to compute all of the response sensitivities with respect to the components $f_j(\boldsymbol{\alpha})$ of the feature function. Hence, the 1st-FASAM-L is more efficient than the 1st-CASAM-L, so the 1st-FASAM-L is the most efficient method for computing the exact expressions of the first-order sensitivities of a generic model response of the form $R[\boldsymbol{\varphi}(\mathbf{x}), \boldsymbol{\psi}(\mathbf{x}); \boldsymbol{\alpha}]$ with respect to the components of the "features" function $\mathbf{f}(\boldsymbol{\alpha})$, and subsequently with respect to the primary model parameters. As will be shown in the sequel, the computational savings provided by the nth-FASAM-L increase massively by comparison to the nth-CASAM-L (or any other method) as the order "n" of the computed sensitivities increases.

The expression obtained in Eq. 48 is the same as the particular form taken on by general expression provided in Eq. 13 for $n = 1$, where:

(i) the 1st-level forward/adjoint function $\mathbf{u}^{(1)}(2; \mathbf{x}) \triangleq [\boldsymbol{\varphi}(\mathbf{x}), \boldsymbol{\psi}(\mathbf{x})]^\dagger$ is the solution of the 1st-LFAS defined by Eqs 19, 20, which has the same expression as the particular form taken on by the nth-LFAS, cf. Eqs 15, 16, for $n = 1$;

(ii) the 1st-level adjoint sensitivity function $\mathbf{a}^{(1)}(2; \mathbf{x}) \triangleq [\mathbf{a}_1^{(1)}(\mathbf{x}), \mathbf{a}_2^{(1)}(\mathbf{x})]^\dagger$ is the solution of the 1st-LASS defined by Eqs 43, 45, which has the same expression as the particular form taken on by the nth-LFAS, cf. Eqs 17, 18, for $n = 1$.

Thus, the first step in the "proof by mathematical induction" of the pattern underlying the nth-FASAM-L has been completed, having shown that this pattern holds for $n = 1$.

2.4 Proving that the conjectured mathematical framework of the nth-FASAM-L methodology also holds for $n \rightarrow n+1$, i.e., for the (n + 1)$^{\text{th}}$-FASAM-L framework

The last step of the "proof by mathematical induction" to establish the validity the nth-FASAM-L framework is to show that the formalism assumed to be correct for the computation of the nth-order sensitivities also holds true for the computation of the (n + 1)$^{\text{th}}$-order sensitivities. This proof entails showing that the formulas obtained by computing the (n + 1)$^{\text{th}}$-order sensitivities using Eqs 14–18 as the starting point will be the same as would be obtained by replacing "n" with "(n + 1)" in Eqs 14–18.

The nth-order response sensitivity defined in Eq. 14 can be considered to be a function of the *(n + 1)th-level function* $\mathbf{u}^{(n+1)}(2^{(n+1)}; \mathbf{x}) \triangleq [\mathbf{u}^{(n)}(2^n; \mathbf{x}), \mathbf{a}^{(n)}(2^n; \mathbf{x})]^\dagger$, which is the solution of the *(n + 1)th-Level Forward/Adjoint System,* abbreviated as "*(n + 1)th-LFAS*", which is obtained by concatenating Eqs 15–18 and is written in the following form:

$$\mathbf{F}^{(n+1)}[2^{n+1} \times 2^{n+1}; \mathbf{f}(\boldsymbol{\alpha})]\mathbf{u}^{(n+1)}(2^{n+1}; \mathbf{x}) \\ = \mathbf{q}_F^{(n+1)}\left[2^{n+1}; \mathbf{u}^{(n)}(2^n; \mathbf{x}); \mathbf{f}(\boldsymbol{\alpha})\right]; \quad \mathbf{x} \in \Omega; \tag{51}$$

$$\mathbf{b}_F^{(n+1)}(2^{(n+1)}; \mathbf{u}^{(n+1)};\ \mathbf{f}) \triangleq \left(\mathbf{b}_F^{(n)}, \mathbf{b}_A^{(n)}\right)^\dagger = \mathbf{0}; \quad \mathbf{x} \in \partial\Omega. \tag{52}$$

The following definitions were used in Eqs 51, 52, where the explicit dependence on the indices $j_k, k = 1, ..., n$, has been omitted, for simplicity:

$$\mathbf{F}^{(n+1)}[2^{n+1} \times 2^{n+1}; \mathbf{f}(\boldsymbol{\alpha})] \triangleq diag\left(\mathbf{F}^{(n)}, \mathbf{A}^{(n)}\right); \\ \mathbf{u}^{(n+1)}(2^{n+1}; \mathbf{x}) \triangleq \left[\mathbf{u}^{(n)}(2^n; \mathbf{x}), \mathbf{a}^{(n)}(2^n; \mathbf{x})\right]^\dagger; \tag{53}$$

$$\mathbf{q}_F^{(n+1)}\left[2^{n+1}; \mathbf{u}^{(n+1)}(2^{n+1}; \mathbf{x}); \mathbf{f}(\boldsymbol{\alpha})\right] \triangleq \left[\mathbf{q}_F^{(n)}(2^n; \mathbf{x}; \mathbf{f}), \mathbf{q}_A^{(n)}(2^n; \mathbf{u}^{(n)}; \mathbf{f})\right]^\dagger. \tag{54}$$

Next, it will be assumed that, for each index $j_1, ..., j_n$, the 1st-order total G-differential of the nth-order sensitivities $R^{(n)}[j_n; ...; j_1; \mathbf{u}^{(n+1)}(2^{n+1}; \mathbf{x}); \mathbf{f}(\boldsymbol{\alpha})]$ exists and is linear in the variational functions $\mathbf{v}^{(n+1)}(2^{n+1}; j_{n-1}, ..., j_1; \mathbf{x}) \triangleq [\mathbf{v}^{(n)}(2^n; \mathbf{x}), \delta\mathbf{a}^{(n)}(2^n; \mathbf{x})]^\dagger$ and $\delta\mathbf{f}$ in a neighborhood around the nominal values of the respective state functions and components of the feature function. In this case, the 1st-order total G-differential of $R^{(n)}[j_n; ...; j_1; \mathbf{u}^{(n+1)}; \mathbf{f}]$ is by definition obtained as follows:

$$\left\{\delta R^{(n)}\left[j_n; ...; j_1; \mathbf{u}^{(n+1)}; \mathbf{f}\right]\right\}_{\boldsymbol{\alpha}^0} \triangleq \left\{\frac{d}{d\varepsilon} R^{(n)}\left[j_n; ...; j_1; \mathbf{u}^{(n+1)} + \varepsilon\mathbf{v}^{(n+1)}; \mathbf{f} + \varepsilon\delta\mathbf{f}\right]\right\}_{\varepsilon=0} \\ \triangleq \sum_{j_{n+1}=1}^{TF} \left\{\frac{\partial R^{(n)}[...; \mathbf{u}^{(n+1)}; \mathbf{f}]}{\partial f_{j_{n+1}}}\right\}_{\boldsymbol{\alpha}^0} \delta f_{j_{n+1}} \\ + \left\{\delta R^{(n)}\left[j_n; ...; j_1; \mathbf{u}^{(n+1)}; \mathbf{v}^{(n+1)}; \mathbf{f}\right]\right\}_{ind}, \tag{55}$$

where the quantity $\{\delta R^{(n)}[j_n; ...; j_1; \mathbf{u}^{(n+1)}; \mathbf{v}^{(n+1)}; \mathbf{f}]\}_{ind}$ denotes the "indirect-effect term" and is defined as follows:

$$\left\{\delta R^{(n)}\left[j_n; ...; j_1; \mathbf{u}^{(n+1)}; \mathbf{v}^{(n+1)}; \mathbf{f}\right]\right\}_{ind} \\ \triangleq \int_{\lambda_1(\boldsymbol{\alpha})}^{\omega_1(\boldsymbol{\alpha})} dx_1 ... \int_{\lambda_{TI}(\boldsymbol{\alpha})}^{\omega_{TI}(\boldsymbol{\alpha})} dx_{TI} \left\{\frac{\partial S^{(n)}}{\partial \mathbf{u}^{(n+1)}(\mathbf{x})} \mathbf{v}^{(n+1)}(\mathbf{x})\right\}_{\boldsymbol{\alpha}^0}. \tag{56}$$

The vector $\mathbf{v}^{(n+1)}(2^{n+1}; j_{n-1}, ..., j_1; \mathbf{x})$, which is needed to evaluate the indirect-effect term $\{\delta R^{(n)}[j_n; ...; j_1; \mathbf{u}^{(n+1)}; \mathbf{v}^{(n+1)}; \mathbf{f}]\}_{ind}$, is the solution of the *(n + 1)th-Level Variational Sensitivity System*, abbreviated as *(n + 1)th-LVSS*, which is obtained by taking the (first-order) G-differential of the *(n + 1)th-LFAS* defined by Eqs 53, 54. Performing this G-differentiation yields the following relations which define the (n + 1)$^{\text{th}}$-LVSS:

$$\left\{\frac{d}{d\varepsilon}\mathbf{F}^{(n+1)}[2^{n+1} \times 2^{n+1}; \mathbf{f}^0 + \varepsilon\delta\mathbf{f}]\left[\mathbf{u}^{(n+1,0)}(2^{n+1}; \mathbf{x}) + \varepsilon\mathbf{v}^{(n+1)}(2^{n+1}; \mathbf{x})\right]\right\}_{\varepsilon=0} \\ = \left\{\frac{d}{d\varepsilon}\mathbf{q}_F^{(n+1)}\left[2^{n+1}; \mathbf{u}^{(n,0)}(2^n; \mathbf{x}) + \varepsilon\mathbf{v}^{(n)}(2^n; \mathbf{x}); \mathbf{f}^0 + \varepsilon\delta\mathbf{f}\right]\right\}_{\varepsilon=0}; \quad \mathbf{x} \in \Omega; \tag{57}$$

$$\left\{\frac{d}{d\varepsilon}\mathbf{b}_F^{(n+1)}\left[2^{n+1}; \mathbf{u}^{(n+1,0)}(2^{n+1}; \mathbf{x}) + \varepsilon\mathbf{v}^{(n+1)}(2^{n+1}; \mathbf{x}); \mathbf{f}^0 + \varepsilon\delta\mathbf{f}\right]\right\}_{\varepsilon=0} \\ = \mathbf{0};\ \ \mathbf{x} \in \partial\Omega; \tag{58}$$

Carrying out the differentiation with respect to ε in Eqs 57, 58, and setting $\varepsilon = 0$ in the resulting expressions yields the following *(n+1)th-LVSS* for the *(n + 1)th-level variational function* $\mathbf{v}^{(n+1)}(2^{n+1}; j_{n-1}, ..., j_1; \mathbf{x})$:

$$\{\mathbf{V}^{(n+1)}[2^{n+1} \times 2^{n+1}; \mathbf{x}; \mathbf{f}]\mathbf{v}^{(n+1)}(2^{n+1}; \mathbf{x})\}_{\boldsymbol{\alpha}^0}$$

$$= \left\{\mathbf{q}_V^{(n+1)}\left[2^{n+1}; \mathbf{u}^{(n+1)}(2^{n+1}; \mathbf{x}); \mathbf{f}; \delta\mathbf{f}\right]\right\}_{\boldsymbol{\alpha}^0}; \ \mathbf{x} \in \Omega; \tag{59}$$

$$\left\{\mathbf{b}_v^{(n+1)}(\mathbf{u}^{(n+1)}; \mathbf{v}^{(n+1)}; \mathbf{f}; \delta\mathbf{f})\right\}_{\boldsymbol{\alpha}^0} = \mathbf{0}; \quad \mathbf{x} \in \partial\Omega. \tag{60}$$

Solving the *(n + 1)th-LVSS* is prohibitive computationally. Therefore, the need for solving the *(n + 1)th-LVSS* will be avoided by expressing the indirect-effect term $\{\delta R^{(n)}[j_n; ...; j_1; \mathbf{u}^{(n+1)}; \mathbf{v}^{(n+1)}; \mathbf{f}]\}_{ind}$ in an alternative way, which eliminates the appearance of the variational function $\mathbf{v}^{(n+1)}(2^{n+1}; j_{n-1}, ..., j_1; \mathbf{x})$ by replacing it with the solution of the "*(n + 1)th-Level Adjoint Sensitivity System,*" abbreviated as *(n + 1)th-LASS*). This *(n + 1)th-LASS* will be constructed below by implementing the same sequence of logical steps as were followed when constructing the first- (and lower-) level adjoint sensitivity systems, namely,:

(i) The *(n + 1)th-LASS* is constructed in a Hilbert space, denoted as H_{n+1}, comprising block-vectors of the form $\boldsymbol{\chi}^{(n+1)}(2^{n+1}; \mathbf{x}) \in \mathrm{H}_{n+1}$, $\boldsymbol{\chi}^{(n+1)}(\mathbf{x}) \triangleq [..., \boldsymbol{\chi}_k^{(n+1)}(\mathbf{x}), ...]^\dagger$, for $k = 1, ..., 2^{n+1}$, each of these comprising elements having the following structure: $\boldsymbol{\chi}_k^{(n+1)}(\mathbf{x}) \triangleq [\chi_{k,1}^{(n+1)}(\mathbf{x}), ..., \chi_{k,TD}^{(n+1)}(\mathbf{x})]^\dagger$. The inner product between two elements, $\boldsymbol{\chi}^{(n+1)}(\mathbf{x}) \in \mathrm{H}_{n+1}$ and $\boldsymbol{\theta}^{(n+1)}(\mathbf{x}) \in \mathrm{H}_{n+1}$, of the Hilbert space H_{n+1}, will be denoted as $\langle\boldsymbol{\chi}^{(n+1)}(\mathbf{x}), \boldsymbol{\theta}^{(n+1)}(\mathbf{x})\rangle_{n+1}$ and is defined as follows:

$$\langle\boldsymbol{\chi}^{(n+1)}(2^{n+1}; \mathbf{x}), \boldsymbol{\theta}^{(n+1)}(2^{n+1}; \mathbf{x})\rangle_{(n+1)} \triangleq \sum_{i=1}^{2^{n+1}} \langle\boldsymbol{\chi}_i^{(n+1)}(2^{n+1}; \mathbf{x}), \boldsymbol{\theta}_i^{(n+1)}(2^{n+1}; \mathbf{x})\rangle_0. \tag{61}$$

(ii) Using the definition provided in Eq. 61, form the inner product in H_{n+1} of Eq. 59 with a yet undefined vector-valued function $\mathbf{a}^{(n+1)}(j_n, ..., j_1; \mathbf{x}) \triangleq [..., \mathbf{a}_k^{(n+1)}(j_n, ..., j_1; \mathbf{x}), ...]^\dagger \in \mathrm{H}_{n+1}; k = 1, ..., 2^{n+1}$, $j_1 = 1, ..., TF$, $j_2 = 1, ..., j_1$; $j_{n+1} = 1, ..., j_n$, to obtain the following relation:

$$\begin{aligned}&\{\langle\mathbf{a}^{(n+1)}(j_n, ..., j_1; \mathbf{x}), \mathbf{V}^{(n+1)}[2^{n+1} \times 2^{n+1}; \mathbf{x}; \mathbf{f}]\mathbf{v}^{(n+1)}(2^{n+1}; \mathbf{x})\rangle_{n+1}\}_{\boldsymbol{\alpha}^0}\\ &\quad = \left\{\langle\mathbf{a}^{(n+1)}(j_n, ..., j_1; \mathbf{x}), \mathbf{q}_V^{(n+1)}\left[2^{n+1}; \mathbf{u}^{(n+1)}(2^{n+1}; \mathbf{x}); \mathbf{f}; \delta\mathbf{f}\right]\rangle_{n+1}\right\}_{\boldsymbol{\alpha}^0}\\ &\quad = \{\langle\mathbf{v}^{(n+1)}(2^{n+1}; \mathbf{x}), \mathbf{A}^{(n+1)}[2^{n+1} \times 2^{n+1}; \mathbf{x}; \mathbf{f}]\mathbf{a}^{(n+1)}(j_n, ..., j_1; \mathbf{x})\rangle_{n+1}\}_{\boldsymbol{\alpha}^0}\\ &\quad\quad + \left\{P^{(n+1)}\left[\mathbf{v}^{(n+1)}; \mathbf{a}^{(n+1)}; \mathbf{f}; \delta\mathbf{f}\right]\right\}_{\boldsymbol{\alpha}^0},\end{aligned} \tag{62}$$

where $\{P^{(n+1)}[\mathbf{v}^{(n+1)}; \mathbf{a}^{(n+1)}; \mathbf{f}; \delta\mathbf{f}]\}_{\boldsymbol{\alpha}^0}$ denotes the bilinear concomitant defined on the phase-space boundary $\mathbf{x} \in \partial\Omega$, evaluated at the nominal values of the model parameter and respective functions, and where $\mathbf{A}^{(n+1)}[2^{n+1} \times 2^{n+1}; \mathbf{x}; \mathbf{f}]$ is the formal adjoint of the matrix-valued operator $\mathbf{V}^{(n+1)}[2^{n+1} \times 2^{n+1}; \mathbf{x}; \mathbf{f}]$ as defined in Eq. 63, below:

$$\mathbf{A}^{(n+1)}[2^{n+1} \times 2^{n+1}; \mathbf{x}; \mathbf{f}] \triangleq \{\mathbf{V}^{(n+1)}[2^{n+1} \times 2^{n+1}; \mathbf{x}; \mathbf{f}]\}^*. \tag{63}$$

(iii) The first term on right-side of the second equality in Eq. 62 is now required to represent the indirect-effect term $\{\delta R^{(n)}[j_n; ...; j_1; \mathbf{u}^{(n+1)}; \mathbf{v}^{(n+1)}; \mathbf{f}]\}_{ind}$. This is achieved by requiring that the (n+1)th-level adjoint sensitivity function $\mathbf{a}^{(n)}(j_n, ..., j_1; \mathbf{x}) \triangleq [..., \mathbf{a}_k^{(n+1)}(j_n, ..., j_1; \mathbf{x}), ...]^\dagger \in \mathrm{H}_{n+1}$; $k = 1, ..., 2^{n+1}$, be the solution of the following (n+1)th-LASS defined in Eqs. 64, 65, below, for $j_1 = 1, ..., TP$; $j_2 = 1, ..., j_1; . . . \ j_n = 1, ..., j_{n-1}$:

$$\mathbf{A}^{(n+1)}[2^{n+1} \times 2^{n+1}; \mathbf{x}; \mathbf{f}]\mathbf{a}^{(n+1)}(j_n, ..., j_1; \mathbf{x}) = \mathbf{s}_A^{(n+1)}(j_n, ..., j_1; \mathbf{f}), \tag{64}$$

$$\left\{\mathbf{b}_A^{(n+1)}\left[\mathbf{a}^{(n+1)}(j_n, ..., j_1; \mathbf{x}); \mathbf{u}^{(n+1)}(j_{n-1}, ..., j_1; \mathbf{x}); \mathbf{f}\right]\right\}_{\boldsymbol{\alpha}^0} = \mathbf{0}, \mathbf{x} \in \partial\Omega, \tag{65}$$

where the vector $\mathbf{s}_A^{(n+1)}(j_n, ..., j_1; \mathbf{f}) \triangleq [..., \mathbf{s}_k^{(n+1)}(j_n, ..., j_1; \mathbf{f}), ...]^\dagger$, $k = 1, ..., 2^{n+1}$, comprises 2^{n+1} components defined in Eq. 66, below, for each $j_1 = 1, ..., TP$; $j_2 = 1, ..., j_1; . . .; j_n = 1, ..., j_{n-1}$:

$$\mathbf{s}_A^{(n+1)}(j_n, ..., j_1; \mathbf{f}) \triangleq \partial S^{(n)} \big/ \partial\mathbf{u}^{(n+1)}(\mathbf{x}). \tag{66}$$

(iv) The (n + 1)th-level adjoint boundary conditions represented by Eq. 65 are selected so as to eliminate, in conjunction with the boundary conditions represented by Eq. 60, all of the unknown values of the functions $\mathbf{v}^{(n+1)}(2^{n+1}; j_{n-1}, ..., j_1; \mathbf{x})$ in the expression of the bilinear concomitant $\{P^{(n+1)}[\mathbf{v}^{(n+1)}; \mathbf{a}^{(n+1)}; \mathbf{f}; \delta\mathbf{f}]\}_{\boldsymbol{\alpha}^0}$. This bilinear concomitant may vanish after implementing the boundary conditions represented by Eqs 60, 65. However, if it does not vanish, this bilinear concomitant will be reduced to a residual quantity which will comprise only known values of $\mathbf{a}^{(n+1)}(j_n, ..., j_1; \mathbf{x})$, $\mathbf{u}^{(n+1)}(j_{n-1}...j_1; \mathbf{x})$, $\mathbf{f}(\boldsymbol{\alpha})$ and $\delta\mathbf{f}(\boldsymbol{\alpha})$, and which will be denoted as $\left\{\hat{P}^{(n+1)}(\mathbf{a}^{(n+1)}; \mathbf{u}^{(n+1)}; \mathbf{f}; \delta\mathbf{f})\right\}_{\boldsymbol{\alpha}^0}$.

(v) Using in Eq. 56 the equations underlying the (n + 1)th-LASS together with the relation provided in Eq. 62 yields the following expression for the indirect-effect term $\{\delta R^{(n)}[j_n; ...; j_1; \mathbf{u}^{(n+1)}; \mathbf{v}^{(n+1)}; \mathbf{f}]\}_{ind}$ in terms of the *(n + 1)th-level adjoint sensitivity functions* $\mathbf{a}^{(n+1)}(j_n, ..., j_1; \mathbf{x})$, for each $j_1 = 1, ..., TP$; $j_2 = 1, ..., j_1; . . .; j_n = 1, ..., j_{n-1}$:

$$\begin{aligned}&\left\{\delta R^{(n)}\left[j_n; ...; j_1; \mathbf{u}^{(n+1)}; \mathbf{v}^{(n+1)}; \mathbf{f}\right]\right\}_{ind}\\ &\quad = -\left\{\hat{P}^{(n+1)}(\mathbf{a}^{(n+1)}; \mathbf{u}^{(n+1)}; \mathbf{f}; \delta\mathbf{f})\right\}_{\boldsymbol{\alpha}^0} + \{\langle\mathbf{a}^{(n+1)}(j_n, ..., j_1; \mathbf{x}),\\ &\quad\quad \times \mathbf{q}_V^{(n+1)}\left[2^{n+1}; \mathbf{u}^{(n+1)}(2^{n+1}; \mathbf{x}); \mathbf{f}; \delta\mathbf{f}\right]\rangle_{n+1}\}_{\boldsymbol{\alpha}^0}.\end{aligned} \tag{67}$$

Adding the result obtained in Eq. 67 for the indirect effect term to the result provided in Eq. 55 for the direct effect term yields the following expression for the total nth-order G-variation of the response:

$$\begin{aligned}&\left\{\delta R^{(n)}\left[j_n; ...; j_1; \mathbf{u}^{(n+1)}; \mathbf{f}\right]\right\}_{\boldsymbol{\alpha}^0}\\ &\quad = \sum_{j_{n+1}=1}^{TF} \left\{\frac{\partial}{\partial f_{j_{n+1}}} \int_{\lambda_1(\boldsymbol{\alpha})}^{\omega_1(\boldsymbol{\alpha})} dx_1 ... \int_{\lambda_{TI}(\boldsymbol{\alpha})}^{\omega_{TI}(\boldsymbol{\alpha})} dx_{TI} S^{(n)}(j_n, ..., j_1; \mathbf{u}^{(n+1)}; \boldsymbol{\alpha})\delta f_{j_{n+1}}\right\}_{\boldsymbol{\alpha}^0}\\ &\quad\quad + \left\{\langle\mathbf{a}^{(n+1)}(j_n, ..., j_1; \mathbf{x}), \mathbf{q}_V^{(n+1)}\left[2^{n+1}; \mathbf{u}^{(n+1)}(2^{n+1}; \mathbf{x}); \mathbf{f}; \delta\mathbf{f}\right]\rangle_{n+1}\right\}_{\boldsymbol{\alpha}^0}\\ &\quad\quad - \left\{\hat{P}^{(n+1)}(\mathbf{a}^{(n+1)}; \mathbf{u}^{(n+1)}; \mathbf{f}; \delta\mathbf{f})\right\}_{\boldsymbol{\alpha}^0}\\ &\quad \equiv \sum_{j_{n+1}=1}^{TF} \{R^{(n+1)}(j_{n+1}, ..., j_1; \mathbf{u}^{(n+1)}; \mathbf{a}^{(n+1)}; \mathbf{f})\}_{(\boldsymbol{\alpha}^0)} \delta f_{j_{n+1}},\end{aligned} \tag{68}$$

where $R^{(n+1)}(j_{n+1}, ..., j_1; \mathbf{u}^{(n+1)}; \mathbf{a}^{(n+1)}; \mathbf{f})$ denotes the *(n + 1)th-order partial sensitivity of the response* $R[\mathbf{u}^{(1)}(\mathbf{x}); \boldsymbol{\alpha}]$ *with respect to the components of the feature function* $\mathbf{f}(\boldsymbol{\alpha})$, evaluated at the nominal parameter values $\boldsymbol{\alpha}^0$.

TABLE 1 1st-FASAM-L: 1st-order (n = 1) sensitivities of response to model features.

1st-LFAS	$\mathbf{F}^{(1)}[2\times 2;\mathbf{x};\mathbf{f}]\mathbf{u}^{(1)}(2;\mathbf{x}) = \mathbf{q}_F^{(1)}(2;\ \mathbf{x};\mathbf{f});\quad \mathbf{x}\in\Omega;\mathbf{b}_F^{(2)}(2^2;\mathbf{u}^{(2)};\ \mathbf{f}) \triangleq (\ \mathbf{b}_F^{(1)},\mathbf{b}_A^{(1)})^\dagger = \mathbf{0};\quad \mathbf{x}\in\partial\Omega;\ \ \mathbf{u}^{(1)}(2;\mathbf{x}) \triangleq [\boldsymbol{\varphi}(\mathbf{x}),\boldsymbol{\psi}(\mathbf{x})]^\dagger$
1st-LVSS	$\mathbf{V}^{(1)}[2\times 2;\mathbf{x};\mathbf{f}]\mathbf{v}^{(1)}(2;\mathbf{x}) = \mathbf{q}_V^{(1)}[2;\mathbf{u}^{(1)}(2;\mathbf{x});$ $\mathbf{f};\delta\mathbf{f}];\ \ \mathbf{x}\in\Omega\mathbf{b}_F^{(2)}(2^2;\mathbf{u}^{(2)};\ \mathbf{f}) \triangleq (\ \mathbf{b}_F^{(1)},\mathbf{b}_A^{(1)})^\dagger = \mathbf{0};\quad \mathbf{x}\in\partial\Omega;\mathbf{v}^{(1)}(2;\mathbf{x}) \triangleq [\delta\boldsymbol{\varphi}(\mathbf{x}),\delta\boldsymbol{\psi}]^\dagger$
1st-Level Hilbert Space	$\mathrm{H}_1\colon \langle\boldsymbol{\chi}^{(1)}(2;\mathbf{x}),\boldsymbol{\theta}^{(1)}(2;\mathbf{x})\rangle_1 \triangleq \sum_{i=1}^{2}\langle\boldsymbol{\chi}_i^{(1)}(\mathbf{x}),\boldsymbol{\theta}_i^{(1)}(\mathbf{x})\rangle_0\langle\boldsymbol{\varphi}(\mathbf{x}),\boldsymbol{\psi}(\mathbf{x})\rangle_0 \triangleq \sum_{j=1}^{TD}\int_{\lambda_1(\boldsymbol{\alpha})}^{\omega_1(\boldsymbol{\alpha})}\dots\int_{\lambda_i(\boldsymbol{\alpha})}^{\omega_i(\boldsymbol{\alpha})}\dots\int_{\lambda_{TI}(\boldsymbol{\alpha})}^{\omega_{TI}(\boldsymbol{\alpha})}\varphi_j(\mathbf{x})\psi_j(\mathbf{x})\,dx_1\dots dx_i\dots dx_{TI}.$
1st-LASS	$\mathbf{A}^{(1)}[2\times 2;\mathbf{x};\mathbf{f}]\mathbf{a}^{(1)}(2;\mathbf{x}) = \mathbf{q}_A^{(1)}[2;\mathbf{u}^{(1)}(2;\mathbf{x});\mathbf{f}],\mathbf{x}\in\Omega;\ \mathbf{b}_A^{(1)}[\ \mathbf{u}^{(1)}(2;\mathbf{x});\mathbf{a}^{(1)}(2;\mathbf{x});\mathbf{f}] = \mathbf{0},\mathbf{x}\in\partial\Omega;\ \mathbf{a}^{(1)}(2;\mathbf{x}) \triangleq [\mathbf{a}_1^{(1)}(\mathbf{x}),\mathbf{a}_2^{(1)}(\mathbf{x})]^\dagger$
1st-Order Resp. Sensitivities to Model Features	$R^{(1)}[j_1;\mathbf{u}^{(1)}(2;\mathbf{x});\mathbf{a}^{(1)}(2;\mathbf{x});\mathbf{f}(\boldsymbol{\alpha})];\ \ j_1 = 1,\dots,TF$

TABLE 2 2nd-FASAM-L: 2nd-order (n = 2) sensitivities of response to model features.

2nd-LFAS = 1st-LFAS +1st-LASS	$\mathbf{F}^{(2)}[2^2\times 2^2;\mathbf{f}(\boldsymbol{\alpha})]\mathbf{u}^{(2)}(2^2;\mathbf{x}) = \mathbf{q}_F^{(2)}[2^2;\mathbf{u}^{(1)}(2;\mathbf{x});\mathbf{f}(\boldsymbol{\alpha})];\ \ \mathbf{x}\in\Omega\mathbf{b}_F^{(2)}(2^2;\mathbf{u}^{(2)};\ \mathbf{f}) \triangleq (\ \mathbf{b}_F^{(1)},\mathbf{b}_A^{(1)})^\dagger = \mathbf{0};$ $\mathbf{x}\in\partial\Omega;\ \mathbf{u}^{(2)}(2^2;\ \mathbf{x}) \triangleq [\mathbf{u}^{(1)}(2;\mathbf{x}),\mathbf{a}^{(1)}(2;\mathbf{x})]^\dagger$
2nd-LVSS	$\mathbf{V}^{(2)}[2^2\times 2^2;\mathbf{x};\mathbf{f}]\mathbf{v}^{(2)}(2^2;\mathbf{x}) = \mathbf{q}_V^{(2)}[2^2;\mathbf{u}^{(2)}(2^2;\mathbf{x});\mathbf{f};\delta\mathbf{f}];\ \mathbf{x}\in\Omega;\ \mathbf{b}_v^{(2)}(\mathbf{u}^{(2)};\mathbf{v}^{(2)};\mathbf{f};\delta\mathbf{f}) = \mathbf{0};\quad \mathbf{x}\in\partial\Omega;\mathbf{v}^{(2)}(2^2;\mathbf{x}) \triangleq [\mathbf{v}^{(1)}(2;\mathbf{x}),\delta\mathbf{a}^{(1)}(2;\mathbf{x})]$
2nd-Level Hilbert space	$\mathrm{H}_2\colon \langle\boldsymbol{\chi}^{(2)}(2^2;\mathbf{x}),\boldsymbol{\theta}^{(2)}(2^2;\mathbf{x})\rangle_2 \triangleq \sum_{i=1}^{2^2}\langle\boldsymbol{\chi}_i^{(2)}(2^2;\mathbf{x}),\boldsymbol{\theta}_i^{(2)}(2^2;\mathbf{x})\rangle_0$
2nd-LASS	$\mathbf{A}^{(2)}[2^2\times 2^2;\mathbf{x};\mathbf{f}]\mathbf{a}^{(2)}(2^2;j_1;\mathbf{x}) = \mathbf{s}^{(2)}(2^2;j_1;\mathbf{u}^{(2)};\mathbf{f});\quad \mathbf{x}\in\Omega;\ \ j_1 = 1,\dots,TF;$ $\left\{\mathbf{b}_A^{(2)}[\mathbf{u}^{(2)}(2^2;\mathbf{x});\mathbf{a}^{(2)}(2^2;j_1;\mathbf{x});\mathbf{f}]\right\}_{\boldsymbol{\alpha}^0} = \mathbf{0},\mathbf{x}\in\partial\Omega,\ j_1 = 1,\dots,TF.\ \ \mathbf{a}^{(2)}(2^2;j_1;\mathbf{x}) \triangleq \left[\mathbf{a}_1^{(2)}(j_1;\mathbf{x}),\mathbf{a}_2^{(2)}(j_1;\mathbf{x}),\mathbf{a}_3^{(2)}(j_1;\mathbf{x}),\mathbf{a}_4^{(2)}(j_1;\mathbf{x})\right]^\dagger = \left[..,\mathbf{a}_k^{(2)}(j_1;\mathbf{x}),..\right]^\dagger;\quad k = 1,\dots,2^2.$
2nd-order Resp. Sensitivities to Model Features	$R^{(2)}[j_2;j_1;\mathbf{u}^{(2)}(\mathbf{x});\mathbf{a}^{(2)}(j_1;\mathbf{x});\mathbf{f}(\boldsymbol{\alpha})];\ \ j_1 = 1,\dots,TF;\ \ j_2 = 1,\dots,j_1.$ Distinct Sensitivities: $TF(TF+1)/2!$

The result obtained in Eq. 68 for the expression of the $(\mathrm{n}+1)^{\mathrm{th}}$-order sensitivity, which was obtained by determining the first-order differential of the nth-order sensitivity, is identical to the expression that would be obtained by advancing the index, from n to $(n+1)$, in the expression of the nth-order sensitivity that was conjectured in Eq. 13. Thus, the proof by mathematical induction of the general mathematical framework underlying the nth-CASAM-L is thereby completed.

The essential characteristics of the nth-FASAM-L methodology are tabularized in Tables 1–4, below, to underscore the conceptual parallelism between the nth-FASAM-L and the nth-CASAM-L (Cacuci, 2022) methodologies.

An overview, in tabular form, of the computational frameworks of the nth-CASAM-L, nth-CASAM-N, nth-FASAM-L, and nth-FASAM-N methodologies, highlighting their objectives, characteristics, and interrelationships is presented in Table 5, below.

Formally, the results produced by the nth-FASAM-L can be written in the same mathematical forms as those produced by the nth-CASAM-L, with the fundamental difference that the number of large-scale computations needed within the nth-FASAM-L is dictated by the number TF of "feature function components" whereas the number of large-scale computations needed within the nth-CASAM-L is dictated by the number TP of primary model parameters. In particular, a single large-scale adjoint computation is needed to solve the 1st-LASS (which is the same for both the 1st-FASAM-L and the 1st-CASAM-L) to obtain the first-order sensitivities with respect to the model parameters. Obtaining the second-order sensitivities of the response with respect to the primary model parameters requires at most $TP(TP+1)/2$ large-scale computations (to solve the 2nd-LASS) within the 2nd-CASAM-L. Obtaining the same second-order sensitivities using the 2nd-FASAM-L requires at most $TF(TF+1)/2$ large-scale computations (to solve the 2nd-LASS) followed by analytical derivations to obtain the second-order sensitivities with respect to the model parameters from the second-order sensitivities with respect to the components of the feature function produced by the 2nd-FASAM-L. The same parallel holds for the computation of all of the higher-order sensitivities: the computation of the 3rd-order sensitivities with respect to the primary model parameters requires at most $TP(TP+1)(TP+2)/3!$ computations if using the 3rd-CASAM-L, as opposed to at most $TF(TF+1)(TF+2)/3!$ large-scale computations plus analytical derivations if using the 3rd-CASAM-L. The computation of the 4th-order sensitivities with respect to the primary model parameters requires at most $TP(TP+1)(TP+2)(TP+3)/4!$ computations if using the 4th-CASAM-L, as opposed to at most $TF(TF+1)(TF+2)(TF+3)/4!$ large-scale computations plus analytical derivations if using the 4th-CASAM-L; and so on. Since $TF \ll TP$, it is evident that the nth-FASAM-L methodology becomes increasingly more efficient than the nth-CASAM-L as the order of computed sensitivities increases.

3 Concluding discussion

This work has presented the "nth-Order Feature Adjoint Sensitivity Analysis Methodology for Response-Coupled Forward/

TABLE 3 nth-FASAM-L: nth-order sensitivities of response to model features.

nth-LFAS =(n-1)th-LFAS +(n-1)th-LASS	$\mathbf{F}^{(n)}[2^n \times 2^n;\ \mathbf{f}(\boldsymbol{\alpha})]\mathbf{u}^{(n)}(2^n;\ \mathbf{x}) = \mathbf{q}_F^{(n)}[2^n;\ \mathbf{u}^{(n-1)}(2^{n-1};\mathbf{x});\mathbf{f}(\boldsymbol{\alpha})];\mathbf{b}_F^{(n)}(2^{(n)};\mathbf{u}^{(n)};\ \mathbf{f}) \triangleq (\mathbf{b}_F^{(n-1)},\ \mathbf{b}_A^{(n-1)})^\dagger = \mathbf{0};\ \mathbf{x} \in \partial\Omega;$ $\mathbf{F}^{(n)}[2^n \times 2^n;\mathbf{f}] \triangleq diag(\mathbf{F}^{(n-1)},\mathbf{A}^{(n-1)});\mathbf{u}^{(n)}(2^n;j_{n-2},...,j_1;\mathbf{x}) = [\mathbf{u}^{(n-1)}(2^{n-1};j_{n-3},...,j_1;\mathbf{x}),\mathbf{a}^{(n-1)}(2^{n-1};$ $j_{n-2},...,j_1;\mathbf{x})]^\dagger;\mathbf{q}_F^{(n)}[2^n;\mathbf{u}^{(n)}(2^n;\mathbf{x});\mathbf{f}(\boldsymbol{\alpha})] \triangleq [\mathbf{q}_F^{(n-1)}(2^{n-1};\mathbf{x};\mathbf{f}),\mathbf{q}_A^{(n-1)}(2^{n-1};\mathbf{x};\mathbf{f})]^\dagger;$
nth-LVSS	$\mathbf{V}^{(n)}[2^n \times 2^n;\mathbf{x};\mathbf{f}]\mathbf{v}^{(n)}(2^n;\mathbf{x}) = \mathbf{q}_V^{(n)}[2^n;\mathbf{u}^{(n)}(2^n;\mathbf{x});\mathbf{f};\delta\mathbf{f}];\ \mathbf{x} \in \Omega;$ $\mathbf{v}^{(n)}(2^n;j_{n-2},...,j_1;\mathbf{x}) \triangleq [\mathbf{v}^{(n-1)}(2^{n-1};\mathbf{x}),\delta\mathbf{a}^{(n-1)}(2^{n-1};\mathbf{x})]^\dagger\mathbf{b}_v^{(n)}(\mathbf{u}^{(n)};\mathbf{v}^{(n)};\mathbf{f};\delta\mathbf{f}) \triangleq [\mathbf{b}_V^{(n-1)},\delta\mathbf{b}_A^{(n-1)}]^\dagger = \mathbf{0};\quad \mathbf{x} \in \partial\Omega.$
nth-Level Hilbert space	$\mathrm{H}_n\colon \langle\boldsymbol{\chi}^{(n)}(2^n;\mathbf{x}),\boldsymbol{\theta}^{(n)}(2^n;\mathbf{x})\rangle_n \triangleq \sum_{i=1}^{2^n}\langle\boldsymbol{\chi}_i^{(n)}(2^n;\mathbf{x}),\boldsymbol{\theta}_i^{(n)}(2^n;\mathbf{x})\rangle_0$
nth-LASS	$\mathbf{A}^{(n)}[2^n \times 2^n;\mathbf{x};\mathbf{f}]\mathbf{a}^{(n)}(2^n;j_{n-1},...,j_1;\mathbf{x}) = \mathbf{s}_A^{(n)}(2^n;j_{n-1},...,j_1;\mathbf{f});$ $\mathbf{b}_A^{(n)}[\mathbf{a}^{(n)}(j_{n-1},...,j_1;\mathbf{x});\mathbf{u}^{(n)}(j_{n-2},...,j_1;\mathbf{x});\mathbf{f}] = \mathbf{0},\mathbf{x} \in \partial\Omega;\mathbf{A}^{(n)}[2^n \times 2^n;\mathbf{x};\mathbf{f}] \triangleq \left\{\mathbf{V}^{(n)}[2^n \times 2^n;\mathbf{x};\mathbf{f}]\right\}^*$
nth-order Resp. Sensitivities to Model Features	$R^{(n)}\left[j_n;...;j_1;\mathbf{u}^{(n)}(2^n;j_{n-2},...,j_1;\mathbf{x});\mathbf{a}^{(n)}(2^n;j_{n-1},...,j_1;\mathbf{x});\mathbf{f}(\boldsymbol{\alpha})\right]$ $\triangleq \partial^n R[\boldsymbol{\varphi}(\mathbf{x}),\boldsymbol{\psi}(\mathbf{x});\boldsymbol{\alpha}]/\partial f_{j_1}...\partial f_{j_n};\ j_1 = 1,...,TF;\ j_2 = 1,...,j_1;\ .....j_n = 1,...,j_{n-1};$ Distinct Sensitivities: $TF(TF+1)(TF+2)...(TF+n-1)/n!$

TABLE 4 (n + 1)th-FASAM-L: (n + 1)th-order sensitivities of response to model features.

(n + 1)th-LASS = nth-LFAS + nth-LASS	$\mathbf{F}^{(n+1)}[2^{n+1} \times 2^{n+1};\ \mathbf{f}(\boldsymbol{\alpha})]\mathbf{u}^{(n+1)}(2^{n+1};\mathbf{x}) = \mathbf{q}_F^{(n+1)}[2^{n+1};\ \mathbf{u}^{(n)}(2^n;\mathbf{x});\mathbf{f}(\boldsymbol{\alpha})];\ \mathbf{F}^{(n+1)}[2^{n+1} \times 2^{n+1};\ \mathbf{f}(\boldsymbol{\alpha})] \triangleq diag(\mathbf{F}^{(n)},\mathbf{A}^{(n)});\mathbf{u}^{(n+1)}$ $(2^{n+1};j_{n-1},...,j_1;\mathbf{x}) = [\mathbf{u}^{(n)}(2^n;j_{n-2},...,j_1;\ \mathbf{x}),\mathbf{a}^{(n)}(2^n;j_{n-1},...,j_1;\mathbf{x})]^\dagger\mathbf{q}_F^{(n+1)}[2^{n+1};\mathbf{u}^{(n+1)}(2^{n+1};\mathbf{x});$ $\mathbf{f}(\boldsymbol{\alpha})] \triangleq [\mathbf{q}_F^{(n)}(2^n;\mathbf{x};\mathbf{f}),\mathbf{q}_A^{(n)}(2^n;\mathbf{u}^{(n)};\ \mathbf{f})]^\dagger\mathbf{b}_F^{(n+1)}(2^{(n+1)};\mathbf{u}^{(n+1)};\ \mathbf{f}) \triangleq (\mathbf{b}_F^{(n)},\mathbf{b}_A^{(n)})^\dagger = \mathbf{0};\quad \mathbf{x} \in \partial\Omega.$
(n + 1)th-LVSS	$\mathbf{V}^{(n+1)}[2^{n+1} \times 2^{n+1};\mathbf{x};\mathbf{f}]\mathbf{v}^{(n+1)}(2^{n+1};\mathbf{x}) = \mathbf{q}_V^{(n+1)}[2^{n+1};\mathbf{u}^{(n+1)}(2^{n+1};\mathbf{x});\mathbf{f};\delta\mathbf{f}];\ \mathbf{x} \in \Omega;$ $\mathbf{v}^{(n+1)}(2^{n+1};j_{n-1},...,j_1;\mathbf{x}) \triangleq [\mathbf{v}^{(n)}(2^n;\mathbf{x}),\delta\mathbf{a}^{(n)}(2^n;\mathbf{x})]^\dagger\mathbf{b}_v^{(n+1)}(\mathbf{u}^{(n+1)};\mathbf{v}^{(n+1)};\mathbf{f};\delta\mathbf{f}) \triangleq [\mathbf{b}_V^{(n)},\delta\mathbf{b}_A^{(n)}]^\dagger = \mathbf{0};\quad \mathbf{x} \in \partial\Omega.$
(n + 1)th-Level Hilbert space	$\mathrm{H}_{n+1}\colon \langle\boldsymbol{\chi}^{(n+1)}(2^{n+1};\mathbf{x}),\boldsymbol{\theta}^{(n+1)}(2^{n+1};\mathbf{x})\rangle_{(n+1)} \triangleq \sum_{i=1}^{2^{n+1}}\langle\boldsymbol{\chi}_i^{(n+1)}(2^{n+1};\mathbf{x}),\boldsymbol{\theta}_i^{(n+1)}(2^{n+1};\mathbf{x})\rangle_0$
(n + 1)th-LASS	$\mathbf{A}^{(n+1)}[2^{n+1} \times 2^{n+1};\mathbf{x};\mathbf{f}]\mathbf{a}^{(n+1)}(2^{n+1};j_n,...,j_1;\mathbf{x}) = \mathbf{s}_A^{(n+1)}(2^{n+1};j_n,...,j_1;\mathbf{f}),\mathbf{A}^{(n+1)}[2^{n+1} \times 2^{n+1};\mathbf{x};\mathbf{f}] \triangleq \left\{\mathbf{V}^{(n+1)}[2^{n+1} \times 2^{n+1};\mathbf{x};\mathbf{f}]\right\}^*;$ $\mathbf{b}_A^{(n+1)}[\mathbf{a}^{(n+1)}(j_n,...,j_1;\mathbf{x});\mathbf{u}^{(n+1)}(j_{n-1},...,j_1;\mathbf{x});\mathbf{f}] = \mathbf{0},\mathbf{x} \in \partial\Omega;$
(n + 1)th- Resp. Sensitivities to Model Features	$R^{(n+1)}\left(j_{n+1},...,j_1;\mathbf{u}^{(n+1)};\mathbf{a}^{(n+1)};\mathbf{f}\right) \triangleq \partial^{n+1}R[\boldsymbol{\varphi}(\mathbf{x}),\boldsymbol{\psi}(\mathbf{x});\boldsymbol{\alpha}]/\partial f_{j_1}...\partial f_{j_{n+1}};$ $j_1 = 1,...,TF;\ ...j_{n+1} = 1,...,j_n;$ Distinct Sensitivities: $TF(TF+1)(TF+2)...(TF+n)/(n+1)!$

Adjoint Linear Systems” (abbreviated as “nth-FASAM-L”), which is the most efficient methodology for computing exact expressions of sensitivities of model responses to features of model parameters and, subsequently, to the model parameters themselves for such linear systems. This efficiency stems from the maximal reduction of the number of adjoint computations (which are “large-scale” computations), by comparison to the extant high-order adjoint sensitivity analysis methodology nth-CASAM-N (the “nth-Order Comprehensive Adjoint Sensitivity Analysis Methodology for Nonlinear Systems”). Specific details are as follows:

(i) Comparing the mathematical framework of the nth-FASAM-N methodology to the framework of the nth-CASAM-N methodology indicates that the components $f_i(\boldsymbol{\alpha}), i = 1,...,TF$, of the “feature function” $\mathbf{f}(\boldsymbol{\alpha}) \triangleq [f_1(\boldsymbol{\alpha}),...,f_{TF}(\boldsymbol{\alpha})]^\dagger$ play within the nth-FASAM-N the same role as played by the components $\alpha_j, j = 1,...,TP$, of the “vector of primary model parameters” $\boldsymbol{\alpha} \triangleq (\alpha_1,\ldots,\alpha_{TP})^\dagger$ within the framework of the nth-CASAM-N. It is important to note that the total number of model parameters is always larger (usually by wide margin) than the total number of components of the feature function $\mathbf{f}(\boldsymbol{\alpha})$, i.e., $TP \gg TF$.

(ii) The 1st-FASAM-N and the 1st-CASAM-N methodologies require a *single* large-scale “adjoint” computations for solving the 1st-LASS (1st-Level Adjoint Sensitivity System), so they are comparably efficient for computing the exact expressions of the *first-order* sensitivities of a model response to the model’s uncertain parameters, boundaries, and internal interfaces.

(iii) For computing the exact expressions of the second-order response sensitivities with respect to the primary model’s parameters, the 2nd-FASAM-N methodology requires, at most, as many large-scale “adjoint” computations as there are “feature functions of parameters” $f_i(\boldsymbol{\alpha}), i = 1,...,TF$ (where TF denotes the total number of feature functions) for solving the left-side of the 2nd-LASS with TF distinct sources on its right-side. By comparison, the 2nd-CASAM-N methodology requires at most TP (where TP denotes the total number of model parameters) large-scale computations for solving the same left-side of the 2nd-LASS but with TP distinct sources. Since $TF \ll TP$, the 2nd-FASAM-N methodology is considerably more efficient than the 2nd-CASAM-N methodology for computing the exact expressions of the second-order sensitivities of a model response to the model’s uncertain parameters, boundaries, and internal interfaces.

(iv) For computing the exact expressions of the third-order response sensitivities with respect to the primary model’s parameters, the 3rd-FASAM-N requires at most $TF(TF+1)/2$ large-scale “adjoint” computations for solving the 3rd-LASS with $TF(TF+1)/2$ distinct sources, while the 3rd-CASAM-N methodology requires at most

TABLE 5 The nth-CASAM-L, nth-CASAM-N, nth-FASAM-L, nth-FASAM-N methodologies: main features.

Methodology	Objective	Characteristics	Inter-relationships
nth-FASAM-L	Develop forward and adjoint operators in linearly increasing Hilbert spaces to enable the most efficient computation of exact expressions of any-order sensitivities of responses to features/functions of primary model parameters	Especially applicable to response-coupled forward/adjoint linear models. Also applicable to responses that depend just on the forward or just the adjoint state functions in linear systems	Reduces to the nth-CASAM-L in the absence of "feature functions," i.e., when the feature functions coincide with the primary parameters
nth-CASAM-L	Develop forward and adjoint operators in linearly increasing Hilbert spaces to enable the most efficient computation of exact expressions of any-order sensitivities of responses to primary model parameters	Same characteristics as nth-FASAM-L, but directly considering the primary model parameters	Becomes identical to the nth-FASAM-L in the absence of "feature functions" of parameters
nth-FASAM-N	Same objective as the nth-FASAM-L, but for nonlinear models	Subsumes the nth-FASAM-L if the responses depend just on the forward state functions	Reduces to the nth-CASAM-N in the absence of "feature functions," i.e., when the feature functions coincide with the primary parameters
nth-CASAM-N	Same objective as the nth-CASAM-L, but for nonlinear models	Subsumes the nth-CASAM-L if the responses depend just on the forward state functions	Becomes identical to the nth-FASAM-N in the absence of "feature functions" of parameters

$TP(TP+1)/2$ large-scale computations for solving the 3rd-LASS with $TP(TP+1)/2$ distinct sources. The same computational-count of "large-scale computations" caries over when computing the higher-order sensitivities, i.e., the formula for calculating the "number of large-scale adjoint computations" is formally the same for both the nth-FASAM-N and the nth-CASAM-N methodologies, but the "variable" in the formula for determining the number of adjoint computations for the nth-FASAM-N methodology is TF (i.e., total number of feature functions) while the counterpart for the formula for determining the number of adjoint computations for the nth-CASAM-N is methodology is TP (i.e., total number of model parameters). Since $TF \ll TP$, it follows that the higher the order of computed sensitivities, the mode efficient the nth-FASAM-N methodology becomes by comparison to the nth-CASAM-N methodology.

(v) When a model has no "feature" functions of parameters, but only comprises primary parameters, the nth-FASAM-N methodology becomes identical to the nth-CASAM-N methodology.

(vi) Both the nth-FASAM-N and the nth-CASAM-N methodologies are formulated in linearly increasing higher-dimensional Hilbert spaces –as opposed to exponentially increasing parameter-dimensional spaces– thus overcoming the curse of dimensionality in sensitivity analysis of nonlinear systems. Both the nth-FASAM-N and the nth-CASAM-N methodologies are incomparably more efficient and more accurate than any other methods (statistical, finite differences, etc.) for computing exact expressions of response sensitivities (of any order) with respect to the model's uncertain parameters, boundaries, and internal interfaces.

The question of "when to stop computing progressively higher-order sensitivities ?" has been addressed by Cacuci (2022), Cacuci D. G. (2023) in conjunction with the question of convergence of the Taylor-series expansion of the response in terms of the uncertain model parameters, cf; Eqs 10, 12. These Taylor-series expansions provide the fundamental premise, even if not explicitly recognized, for obtaining the expressions provided by the "propagation of errors" methodology (as originally proposed by Tukey, 1957; and generalized by Cacuci, 2022) for the cumulants of the model response distribution in the phase-space of model parameters. The convergence of these Taylor-series, which depend on both the response sensitivities with respect to parameters and the uncertainties associated with the parameter distribution, must be ensured. This can be done by ensuring that the combination of parameter uncertainties and response sensitivities are sufficiently small to fall inside the respective radius of convergence of each of these Taylor-series expansions. The application of the nth-FASAM-N to a representative response-coupled forward/adjoint linear model stemming from the field of energy-dependent particle transport in a mixture of materials will be presented in the accompanying work designated as "Part II" (Cacuci, 2024c).

Data availability statement

The original contributions presented in the study are included in the article/supplementary material, further inquiries can be directed to the corresponding author.

Author contributions

DC: Conceptualization, Methodology, Project administration, Validation, Writing–original draft, Writing–review and editing.

Funding

The author(s) declare that no financial support was received for the research, authorship, and/or publication of this article.

Conflict of interest

The author declares that the research was conducted in the absence of any commercial or financial relationships that could be construed as a potential conflict of interest.

Publisher's note

References

Alcouffe, R. E., Baker, R. S., Dahl, J. A., Turner, S. A., and Ward, R. (2008). *PARTISN: a time-dependent, parallel neutral particle transport code system*. Los Alamos, NM, USA: Los Alamos National Laboratory. LA-UR-08-07258.

Bellman, R. E. (1957). *Dynamic programming*. USA: Rand Corporation, Princeton University Press. Republished: Bellman, RE (2003) Dynamic Programming. Courier Dover Publications, ISBN 978-0-486-42809-3, USA.

Cacuci, D. G. (1981). Sensitivity theory for nonlinear systems: I. Nonlinear functional analysis approach. *J. Math. Phys.* 22, 2794–2802. doi:10.1063/1.525186

Cacuci, D. G. (2015). Second-order adjoint sensitivity analysis methodology (2nd-ASAM) for computing exactly and efficiently first- and second-order sensitivities in large-scale linear systems: I. Computational methodology. *J. Comp. Phys.* 284, 687–699. doi:10.1016/j.jcp.2014.12.042

Cacuci, D. G. (2016). The second-order adjoint sensitivity analysis methodology for nonlinear systems—I: theory. *Nucl. Sci. Eng.* 184, 16–30. doi:10.13182/nse16-16

Cacuci, D. G. (2022). *The nth-order comprehensive adjoint sensitivity analysis methodology (nth-CASAM): overcoming the curse of dimensionality in sensitivity and uncertainty analysis, Volume I: linear systems*. Cham, Switzerland: Springer Nature, 362. doi:10.1007/978-3-030-96364-4

Cacuci, D. G. (2023a). *The nth-order comprehensive adjoint sensitivity analysis methodology (nth-CASAM): overcoming the curse of dimensionality in sensitivity and uncertainty analysis, volume III: nonlinear systems*. Cham, Switzerland: Springer Nature, 369. doi:10.1007/978-3-031-22757-8

Cacuci, D. G. (2023b). Computation of high-order sensitivities of model responses to model parameters. II: introducing the second-order adjoint sensitivity analysis methodology for computing response sensitivities to functions/features of parameters. *Energies* 16, 6356. doi:10.3390/en16176356

Cacuci, D. G. (2024a). Introducing the nth-order features adjoint sensitivity analysis methodology for nonlinear systems (nth-FASAM-N): I. Mathematical framework. *Am. J. Comput. Math.* 14, 11–42. doi:10.4236/ajcm.2024.141002

Cacuci, D. G. (2024b). Introducing the nth-order features adjoint sensitivity analysis methodology for nonlinear systems (nth-FASAM-N): II. Illustrative example. *Am. J. Comput. Math.* 14, 43–95. doi:10.4236/ajcm.2024.141003

Cacuci, D. G. (2024c). The nth-order features adjoint sensitivity analysis methodology for response-coupled forward/adjoint linear systems (nth-FASAM-L): I. mathematical framework. *Front. Energy Res* 12, 1417594. doi:10.3389/fenrg.2024.1417594

Cacuci, D. G., and Fang, R. (2023). *The nth-order comprehensive adjoint sensitivity analysis methodology (nth-CASAM): overcoming the curse of dimensionality in sensitivity and uncertainty analysis, volume II: application to a large-scale system*. Nature Switzerland, Cham: Springer, 463. doi:10.1007/978-3-031-19635-5

Chadwick, M. B., Herman, M., Obložinský, P., Dunn, M. E., Danon, Y., Kahler, A. C., et al. (2011). ENDF/B-VII.1: nuclear data for science and technology: cross sections, covariances, fission product yields and decay data. *Nucl. Data Sheets* 112, 2887–2996. doi:10.1016/j.nds.2011.11.002

Conlin, J. L., Parsons, D. K., Gardiner, S. J., Gray, M., Lee, M. B., and White, M. C. (2013). *MENDF71X: multigroup neutron cross-section data tables based upon ENDF/B-VII.1X; los alamos national laboratory report LA-UR-15-29571*. Los Alamos, NM, USA: Los Alamos National Laboratory, 2013.

Cukier, R. I., Levine, H. B., and Shuler, K. E. (1978). Nonlinear sensitivity analysis of multiparameter model systems. *J. Comput. Phys.* 26, 1–42. doi:10.1016/0021-9991(78)90097-9

Dunker, A. M. (1984). The decoupled direct method for calculating sensitivity coefficients in chemical kinetics. *J. Chem. Phys.* 81, 2385–2393. doi:10.1063/1.447938

Hora, S. C., and Iman, R. L. (1986). *A Comparison of maximum/bounding and Bayesian/Monte Carlo for fault tree uncertainty analysis*. Albuquerque, NM, USA: Sandia National Laboratories. Technical Report SAND85-2839.

Iman, R. L., Helton, J. C., and Campbell, J. E. (1981a). An approach to sensitivity analysis of computer models: Part I—introduction, input variable selection and preliminary variable assessment. *J. Qual. Technol.* 13, 174–183. doi:10.1080/00224065.1981.11978748

Iman, R. L., Helton, J. C., and Campbell, J. E. (1981b). An approach to sensitivity analysis of computer models: Part II—ranking of input variables, response surface validation, distribution effect and technique synopsis. *J. Qual. Technol.* 13, 232–240. doi:10.1080/00224065.1981.11978763

Kramer, M. A., Calo, J. M., and Rabitz, H. (1981). An improved computational method for sensitivity analysis: green's Function Method with "AIM". *Appl. Math. Model.* 5, 432–441. doi:10.1016/s0307-904x(81)80027-3

Lewins, J. (1965). *IMPORTANCE: the adjoint function*. Oxford, UK: Pergamon Press Ltd.

Luo, Z., Wang, X., and Liu, D. (2020). Prediction on the static response of structures with large-scale uncertain-but-bounded parameters based on the adjoint sensitivity analysis. *Struct. Multidiscip. Optim.* 61, 123–139. doi:10.1007/s00158-019-02349-w

Práger, T., and Kelemen, F. D. (2014). "Adjoint methods and their application in earth sciences," in *Advanced numerical methods for complex environmental models: needs and availability*. Editors I. Faragó, Á. Havasi, and Z. Zlatev (Oak Park, IL, USA: Bentham Science Publishers), 203–275. Chapter 4A.

Rios Insua, D. (1990). *Sensitivity analysis in multiobjective decision making*. New York, USA: Springer Verlag.

Saltarelli, A., Chan, K., and Scott, E. M. (2000). *Sensitivity analysis* (Chichester, UK: J. Wiley and Sons Ltd).

Shultis, J. K., and Faw, R. E. (2000). *Radiation shielding*. La Grange Park, Illinois, USA: American Nuclear Society.

Stacey, W. M. (2001). *Nuclear reactor physics*. New York. USA: John Wiley and Sons.

Tukey, J. W. (1957). *The propagation of errors, fluctuations and tolerances*. Princeton, NJ, USA: Princeton University. Technical Reports No. 10-12.

Valentine, T. E. (2006). *Polyethylene-reflected plutonium metal sphere subcritical noise measurements, SUB-PU-METMIXED-001. International handbook of evaluated criticality safety benchmark experiments, NEA/NSC/DOC(95)03/I-IX, organization for economic Co-operation and development (OECD)*. Paris, France: Nuclear Energy Agency.

Weiberg, A. M., and Wigner, E. P. (1958). *The physical theory of neutron chain reactors*. Chicago, Illinois, USA: University of Chicago Press.

Weisbin, C. R., Oblow, E. M., Marable, J. H., Peelle, R. W., and Lucius, J. L. (1978). Application of sensitivity and uncertainty methodology to fast reactor integral experiment analysis. *Nucl. Sci. Eng.* 66, 307–333. doi:10.13182/nse78-3

Wigner, E. P. (1945). *Effect of small perturbations on pile period*. Chicago, IL, USA: Scientific Research Publishing. Chicago Report CP-G-3048.

Williams, M. L. (1986). "Perturbation theory for nuclear reactor analysis," in *Handbook of nuclear reactor calculations*. Editor Y. Ronen (Boca Raton, Florida, USA: CRC Press), 63–188. Volume 3.

Williams, M. L., and Engle, W. W. (1977). The concept of spatial channel theory applied to reactor shielding analysis. *Nucl. Sci. Eng.* 62, 92–104. doi:10.13182/nse77-a26941

Wilson, W. B., Perry, R. T., Shores, E. F., Charlton, W. S., Parish, T. A., Estes, G. P., et al. (2002). "SOURCES4C: a code for calculating (α,n), spontaneous fission, and delayed neutron sources and spectra," in Proceedings of the American Nuclear Society/Radiation Protection and Shielding Division 12th Biennial Topical Meeting, Santa Fe, NM, USA, 14–18 April 2002.

frontiers | Frontiers in Energy Research

TYPE Original Research
PUBLISHED 05 September 2024
DOI 10.3389/fenrg.2024.1421519

OPEN ACCESS

EDITED BY
Shripad T. Revankar,
Purdue University, United States

REVIEWED BY
Shichang Liu,
North China Electric Power University, China
Jian Guo,
Chinese Academy of Sciences (CAS), China

*CORRESPONDENCE
Dan Gabriel Cacuci,
✉ cacuci@cec.sc.edu

RECEIVED 22 April 2024
ACCEPTED 14 August 2024
PUBLISHED 05 September 2024

CITATION
Cacuci DG (2024) n^{th}-order feature adjoint sensitivity analysis methodology for response-coupled forward/adjoint linear systems: II. Illustrative application to a paradigm energy system.
Front. Energy Res. 12:1421519.
doi: 10.3389/fenrg.2024.1421519

n^{th}-order feature adjoint sensitivity analysis methodology for response-coupled forward/adjoint linear systems: II. Illustrative application to a paradigm energy system

Dan Gabriel Cacuci*

Department of Mechanical Engineering, University of South Carolina, Columbia, SC, United States

This work presents a representative application of the newly developed "n^{th}-order feature adjoint sensitivity analysis methodology for response-coupled forward/adjoint linear systems" (abbreviated as "n^{th}-FASAM-L"), which enables the most efficient computation of exactly obtained mathematical expressions of arbitrarily high-order (n^{th}-order) sensitivities of a generic system response with respect to all of the parameters (including boundary and initial conditions) underlying the respective forward/adjoint systems. The n^{th}-FASAM-L has been developed to treat responses of linear systems that simultaneously depend on both the forward and adjoint state functions. Such systems cannot be considered particular cases of nonlinear systems, as illustrated in this work by analyzing an analytically solvable model of the energy distribution of the "contributon flux" of neutrons in a mixture of materials. The unparalleled efficiency and accuracy of the n^{th}-FASAM-L stem from the maximal reduction in the number of adjoint computations (which are "large-scale" computations) for determining the exact expressions of arbitrarily high-order sensitivities since the number of large-scale computations when applying the n^{th}-FASAM-N is proportional to the number of model features as opposed to the number of model parameters (which are considerably more than the number of features). Hence, the higher the order of computed sensitivities, the more efficient the n^{th}-FASAM-N becomes compared to any other methodology. Furthermore, as illustrated in this work, the probability of encountering identically vanishing sensitivities is much higher when using the n^{th}-FASAM-L than other methods.

KEYWORDS

arbitrarily high-order adjoint sensitivity analysis, n^{th}-order feature adjoint sensitivity analysis methodology for response-coupled forward/adjoint linear systems, response-coupled forward/adjoint systems, neutron-slowing down, sensitivity of responses to model features

1 Introduction

The accompanying work ("part I") has presented the newly developed mathematical framework, the "n^{th}-order feature adjoint sensitivity analysis methodology for response-coupled forward/adjoint linear systems" (abbreviated as "n^{th}-FASAM-L"), conceived by Cacuci (2024c). This work illustrates the application of the n^{th}-FASAM-L to a representative energy-dependent neutron-slowing down model of fundamental importance to reactor physics. The physical considerations underlying this model are presented in Section 2, which briefly reviews the concept of "contributon-flux density response" and particularizes this concept within the modeling of neutron slowing down in a mixture of materials. This physical model is of fundamental importance in nuclear reactor physics and enables the derivation of exact closed-form results for the application of the nth-FASAM-L. Section 2 also defines the "features" inherent to this model, which enable the advantageous application of the nth-FASAM-L. By definition, there are considerably fewer "feature functions" of the primary model parameters than there are primary model parameters.

Section 3 presents the first-order adjoint sensitivity analysis of the contributon flux with respect to the features and primary model parameters of the slowing-down model, comparing the application of the 1st-FASAM-L *versus* the first-order comprehensive adjoint sensitivity analysis methodology for response-coupled forward/adjoint linear systems (1st-CASAM-L). Using either the 1st-FASAM-L or 1st-CASAM-L involves solving the same operator equations and boundary conditions within the respective 1st-LASS but with differing source terms. For the computation of the first-order sensitivities, the 1st-FASAM-L enjoys only a slight computational advantage since it requires only one quadrature per component of the feature function, whereas the 1st-CASAM-L requires one quadrature per primary model parameter.

Section 4 presents the second-order adjoint sensitivity analysis of the contributon flux with respect to the features and primary model parameters of the slowing-down model, comparing the application of the 2nd-FASAM-L *versus* the 2nd-CASAM-L. It is shown that the 2nd-FASAM-L requires as many large-scale "adjoint" computations as there are non-vanishing first-order response sensitivities with respect to the components of the feature functions, whereas the 2nd-CASAM-L requires as many large-scale computations as there are non-vanishing first-order response sensitivities with respect to the primary model parameters. Hence, the 2nd-FASAM-L is inherently more efficient than the 2nd-CASAM-L. In particular, one of the three distinct second-order sensitivities with respect to the model's features vanishes identically within the 2nd-FASAM-L but none of the ca. 100 second-order sensitivities with respect to the primary model parameters vanish within the 2nd-CASAM-L.

Section 5 presents the third-order adjoint sensitivity analysis of the contributon flux with respect to the features and primary model parameters of the slowing-down model, comparing the application of the 3rd-FASAM-L *versus* the 3rd-CASAM-L. For computing the exact expressions of the *third-order* contributon-response sensitivities, the 3rd-FASAM-L requires only *two* large-scale computations, whereas the 3rd-CASAM-L would require hundreds of large-scale computations.

The concluding discussion presented in Section 6 emphasizes the fact that the unparalleled efficiency of the nth-FASAM-N increases as the order of computed sensitivities increases, and the probability of encountering vanishing sensitivities is much higher when using the nth-FASAM-L rather than any other methodology. Both the nth-FASAM-L and nth-CASAM-L overcome the limitation of dimensionality in the sensitivity analysis of linear systems, being incomparably more efficient and more accurate than any other method (statistical, finite differences, etc.) for computing exact expressions of response sensitivities (of any order) with respect to the uncertain parameters, boundaries, and internal interfaces of the model.

2 Modeling the contributon flux in a paradigm neutron slowing-down model

Fundamentally important responses of linear models depend *simultaneously* on both the forward and adjoint state functions governing the respective linear model, which makes it necessary to treat linear models/systems in their own right since such responses cannot be treated as particular cases of responses of nonlinear models. Typical examples of such responses arise in the modeling of self-diffusion processes in which the interaction mean free path is independent of the phase-space density. Such processes are modeled by linear equations of the Lorentz–Boltzmann type, and they occur in neutron, electron, and photon transport through media, as well as in certain types of transport processes in gas or plasma dynamics. Numerically solving such time-dependent integro-differential equations, albeit linear, is representative of "large-scale" computations and will be used in the sequel for illustrating the application of the nth-FASAM-L. In particular, the distribution of neutrons in a medium is modeled by the following standard form of the linear Boltzmann equation:

$$L(\mathbf{r},E,\mathbf{\Omega},t)\varphi(\mathbf{r},E,\mathbf{\Omega},t)=Q(\mathbf{r},E,\mathbf{\Omega},t), \tag{1}$$

where the linear integro-differential operator $L(\mathbf{r},E,\mathbf{\Omega},t)$ is defined below:

$$\begin{aligned} L(\mathbf{r},E,\mathbf{\Omega},t)\varphi(\mathbf{r},E,\mathbf{\Omega},t) \triangleq {} & \frac{1}{v}\frac{\partial\varphi(\mathbf{r},E,\mathbf{\Omega},t)}{\partial t}+\ \mathbf{\Omega}\cdot\nabla\varphi(\mathbf{r},E,\mathbf{\Omega},t) \\ & +\Sigma_t(\mathbf{r},E)\,\varphi(\mathbf{r},E,\mathbf{\Omega},t) \\ & -\int_0^{E_f}dE'\int_{4\pi}d\mathbf{\Omega}'\Sigma_s(\mathbf{r},E'\to E,\mathbf{\Omega}'\to\mathbf{\Omega})\,\varphi(\mathbf{r},E',\mathbf{\Omega}',t) \\ & -\int_0^{E_f}dE'\int_{4\pi}\chi(\mathbf{r},E'\to E)\nu\Sigma(\mathbf{r},E')\,\varphi(\mathbf{r},E',\mathbf{\Omega}',t)d\mathbf{\Omega}'. \end{aligned} \tag{2}$$

The quantities that appear in the standard notation used in Equation 2 are defined as follows:

(i) $\mathbf{r}$ denotes the three-dimensional position vector in space; E denotes the energy-independent variable; the directional vector $\mathbf{\Omega}$ denotes the scattering solid angle; t denotes the time-independent variable; and v denotes the neutron particle speed.
(ii) $\varphi(\mathbf{r},E,\mathbf{\Omega},t)$ denotes the flux of particles (i.e., particle number density multiplied by the particle speed) in the energy range dE about E and volume element $d\mathbf{r}$ about $\mathbf{r}$, with directions of motion in the solid angle element $d\mathbf{\Omega}$ about $\mathbf{\Omega}$.
(iii) $Q(\mathbf{r},E,\mathbf{\Omega},t)$ denotes the rate at which particles are produced in the same element of phase space from sources that are independent of the flux.
(iv) $\Sigma_t(\mathbf{r},E)$ denotes the macroscopic total cross section.

(v) $\Sigma_s(\mathbf{r}, E' \to E, \mathbf{\Omega}' \to \mathbf{\Omega})$ denotes the macroscopic scattering transfer cross section from energy E' to energy E and from a scattering angle through angle $\mathbf{\Omega}' \cdot \mathbf{\Omega}$.
(vi) ν denotes the number of particles emitted isotropically $(1/4\pi)$ per fission.
(vii) $\Sigma_f(\mathbf{r}, E)$ denotes the macroscopic fission cross section.
(viii) $\chi(\mathbf{r}, E' \to E)$ denotes the fraction of fission particles appearing in energy dE about E from fissions in dE' about E'.

The adjoint Boltzmann transport equation is formulated in the Hilbert space denoted as $\mathcal{H}_B$ and is endowed with the following inner product, denoted as $\langle \varphi(\mathbf{r}, E, \mathbf{\Omega}, t), \psi(\mathbf{r}, E, \mathbf{\Omega}, t) \rangle_B$, between two elements $\varphi(\mathbf{r}, E, \mathbf{\Omega}, t) \in \mathcal{H}_B$ and $\psi(\mathbf{r}, E, \mathbf{\Omega}, t) \in \mathcal{H}_B$:

$$\langle \varphi, \psi \rangle_B \triangleq \int_0^{t_f} dt \int_0^{\infty} dE \int_{4\pi} d\mathbf{\Omega} \int_V dV \varphi(\mathbf{r}, E, \mathbf{\Omega}, t) \psi(\mathbf{r}, E, \mathbf{\Omega}, t) \,. \tag{3}$$

In the Hilbert space $\mathcal{H}_B$, the generic adjoint Boltzmann transport equation is as follows:

$$L^*(\mathbf{r}, E, \mathbf{\Omega}, t) \psi(\mathbf{r}, E, \mathbf{\Omega}, t) = Q^*(\mathbf{r}, E, \mathbf{\Omega}, t), \tag{4}$$

where the (adjoint) linear integro-differential operator $L^*(\mathbf{r}, E, \mathbf{\Omega}, t)$ is defined below:

$$\begin{aligned} L^*(\mathbf{r}, E, \mathbf{\Omega}, t)\psi(\mathbf{r}, E, \mathbf{\Omega}, t) \triangleq & -\frac{1}{v}\frac{\partial \psi(\mathbf{r}, E, \mathbf{\Omega}, t)}{\partial t} - \mathbf{\Omega} \cdot \nabla \psi(\mathbf{r}, E, \mathbf{\Omega}, t) \\ & + \Sigma_t(\mathbf{r}, E)\, \psi(\mathbf{r}, E, \mathbf{\Omega}, t) \\ & - \int_0^{E_f} dE' \int_{4\pi} d\mathbf{\Omega}' \Sigma_s(\mathbf{r}, E \to E', \mathbf{\Omega} \to \mathbf{\Omega}')\, \psi(\mathbf{r}, E', \mathbf{\Omega}', t) \\ & - \nu \Sigma(\mathbf{r}, E) \int_0^{E_f} dE' \int_{4\pi} \chi(\mathbf{r}, E \to E')\, \psi(\mathbf{r}, E', \mathbf{\Omega}', t) d\mathbf{\Omega}'. \end{aligned} \tag{5}$$

By construction, the forward and adjoint transport equations satisfy the following relation:

$$\langle \varphi, L^* \psi \rangle_B - \langle \psi, L \varphi \rangle_B = P[\varphi, \psi] = \langle \varphi, Q^* \rangle_B - \langle \psi, Q \rangle_B, \tag{6}$$

where $P[\varphi, \psi]$ denotes the bilinear concomitant evaluated on the boundary of the phase-space domain under consideration. The "generalized reciprocity relation" expressed by Equation 6 relates the bilinear concomitant, which is a functional of the forward and adjoint fluxes at the initial and final times along the incoming and outgoing directions at the surface of the medium, to the fluxes in the interior of the medium comprising fixed sources. This reciprocity relation provides a physical interpretation of the adjoint flux as an "importance function," which quantifies the contribution of a source to a detector and enables transport problems to be posed either in the forward or adjoint descriptions. These reciprocity relations also restrict the combination of forward and adjoint boundary conditions to those that ensure both the forward and adjoint formulations are mathematically "well posed." The reciprocity relation expressed by Equation 6 is extensively used in the so-called "source-detector" problems in steady-state subcritical systems, where $Q^*(\mathbf{r}, E, \mathbf{\Omega})$ models the detector properties (cross section) in the sub-region occupied by the respective detector.

When the boundary conditions for Equation 1 are homogeneous and there is no external source, i.e., when $Q(r, E, \mathbf{\Omega}, t) = 0$, the stationary neutron transport problem becomes an eigenvalue problem. The largest (i.e., fundamental) eigenvalue in such a case is called the "effective multiplication factor" and, depending on its value, corresponds to a critical, subcritical, or supercritical physical system (e.g., nuclear reactor). This eigenvalue (multiplication factor) is an important system (model) response, and its mathematical expression is a functional ("Raleigh quotient") of the forward and the adjoint fluxes. Additional important model responses that are functionals of both the forward and adjoint fluxes include the reactivity, generation time, and lifetime of the system, along with several other Lagrangian functionals used in variational principles for developing efficient Raleigh–Ritz type numerical methods (see, e.g., Lewins, 1965; Stacey, 1974; Stacey, 2001). Perhaps the simplest quantity that depends on both the forward and adjoint fluxes—and has important applications in particle transport (particularly in particle shielding)—is the so-called "*contributon flux*" (Williams and Engle, 1977), which arises as follows:

(i) Multiplying the stationary form of Equation 1 by $\psi(r, E, \mathbf{\Omega})$, multiplying the stationary form of Equation 4 by $\varphi(r, E, \mathbf{\Omega})$, subtracting the resulting equations from each other, and integrating the resulting equation over only the energy- and solid angle-independent variables yield the following relation:

$$\nabla \cdot \mathbf{v}_c R(\mathbf{r}) = S(\mathbf{r}) - S^*(\mathbf{r}), \tag{7}$$

where

$$R_c(\mathbf{r}) \triangleq \frac{1}{v} \int_0^{E_f} dE \int_{4\pi} d\mathbf{\Omega}\, \varphi(r, E, \mathbf{\Omega}) \psi(r, E, \mathbf{\Omega}), \tag{8}$$

$$\mathbf{v}_c \triangleq \frac{\int_0^{E_f} dE \int_{4\pi} d\mathbf{\Omega}\, [\mathbf{\Omega} \varphi(r, E, \mathbf{\Omega}) \psi(r, E, \mathbf{\Omega})]}{\frac{1}{v} \int_0^{E_f} dE \int_{4\pi} d\mathbf{\Omega}\, \varphi(r, E, \mathbf{\Omega}) \psi(r, E, \mathbf{\Omega})}, \tag{9}$$

$$S_c(\mathbf{r}) \triangleq \int_0^{E_f} dE \int_{4\pi} d\mathbf{\Omega} [Q(r, E, \mathbf{\Omega}) \psi(r, E, \mathbf{\Omega})], \tag{10}$$

$$S_c^*(\mathbf{r}) \triangleq \int_0^{E_f} dE \int_{4\pi} d\mathbf{\Omega} [Q^*(r, E, \mathbf{\Omega}) \varphi(r, E, \mathbf{\Omega})]. \tag{11}$$

(ii) The form of Equation 7 is the same as the mass continuity balance/equation for compressible flow, indicating that the "contributon response density" $R_c(\mathbf{r})$ is conserved as it flows from the "contributon response source" $S_c(\mathbf{r})$ toward the "contributon response sink" $S_c^*(\mathbf{r})$, with a "contributon response mean velocity" $\mathbf{v}_c$ corresponding to the neutron speed v.

The application of the n$^{\text{th}}$-FASAM-L is illustrated in this section by considering the simplified model of the distribution in the asymptotic energy range of neutrons produced by a source of neutrons placed in an isotropic medium comprising a homogeneous mixture of "M" non-fissionable materials having constant (i.e., energy-independent) properties. For simplicity, but without diminishing the applicability of the n$^{\text{th}}$-FASAM-L, this medium is considered to be infinitely large. The simplified form of the Boltzmann neutron transport equation, as shown in Equation 1, that models the energy distributions of neutrons within a mixture of materials is called the "neutron slowing-down equation." This equation is written using neutron *lethargy* (rather than the neutron energy) as the independent variable. Neutron lethargy is customarily denoted using the variable/letter "u" and is defined as $u \triangleq \ln(E_0/E)$, where E denotes the energy variable and E_0 denotes the highest energy in the system. Thus, the neutron slowing-down model (see, e.g., Meghreblian and Holmes, 1960; Lamarsh, 1966) for the energy distribution of the neutron flux in a homogeneous mixture of non-fissionable materials of infinite extent takes the following simplified form of Equation 1:

$$\frac{d\varphi(u)}{du} + \frac{\Sigma_a}{\bar{\xi}\,\Sigma_t}\varphi(u) = \frac{S(u)}{\bar{\xi}\,\Sigma_t}; \quad 0 < u \le u_{th}; \tag{12}$$

$$\varphi(0) = 0; \; at \; u = 0. \tag{13}$$

The quantities that appear in Equation 12 are defined as follows.

(i) The lethargy-dependent neutron flux is denoted as $\varphi(u)$; u_{th} denotes a cut-off lethargy, usually corresponding to the thermal neutron energy (ca. 0.0024 electron volts).

(ii) The macroscopic elastic scattering cross section for the homogeneous mixture of "M" materials is denoted as Σ_s and is defined as follows:

$$\Sigma_s \triangleq \sum_{i=1}^{M} N_m^{(i)}\sigma_s^{(i)}, \tag{14}$$

where $\sigma_s^{(i)}, i = 1, ..., M$ denotes the elastic scattering cross section of material "i," and the atomic or molecular number density of material "i" is denoted as $N_m^{(i)}, i = 1, ..., M$ and is defined as $N_m^{(i)} \triangleq \rho_i N_A / A_i$, where N_A is Avogadro's number $(0.602 \times 10^{24}\, nuclei/mole)$, while A_i and ρ_i denote the mass number and density of the material, respectively.

(iii) The average gain in lethargy of a neutron per collision is denoted as $\bar{\xi}$ and is defined as follows for the homogeneous mixture:

$$\bar{\xi} \triangleq \frac{1}{\Sigma_s}\sum_{i=1}^{M}\xi_i N_m^{(i)}\sigma_s^{(i)}; \quad \xi_i \triangleq 1 + \frac{a_i \ln a_i}{1 - a_i}; \quad a_i \triangleq \left(\frac{A_i - 1}{A_i + 1}\right)^2. \tag{15}$$

(iv) The macroscopic absorption cross section is denoted as Σ_a and is defined as follows for the homogeneous mixture:

$$\Sigma_a \triangleq \sum_{i=1}^{M} N_m^{(i)}\sigma_\gamma^{(i)}, \tag{16}$$

where $\sigma_\gamma^{(i)}, i = 1, ..., M$ denotes the microscopic radiative-capture cross section of material "i."

(v) The macroscopic total cross section is denoted as Σ_t and is defined as follows for the homogeneous mixture:

$$\Sigma_t \triangleq \Sigma_a + \Sigma_s. \tag{17}$$

(vi) The source $S(u)$ is considered to be a simplified "spontaneous fission" source stemming from fissionable actinides, such as ^{239}Pu and ^{240}Pu, emitting monoenergetic neutrons at the highest energy (i.e., zero lethargy). Such a source is comprised within the OECD/NEA polyethylene-reflected plutonium (PERP) OECD/NEA reactor physics benchmark (Valentine, 2006; Cacuci and Fang, 2023), which can be modeled using the following simplified expression:

$$S(u) = S_0\delta(u); \quad S_0 \triangleq \sum_{k=1}^{2}\lambda_k^S N_k^S F_k^S \nu_k^S W_k^S, \tag{18}$$

where the superscript "S" indicates the "source; " the subscript index $k = 1$ indicates material properties pertaining to the isotope ^{239}Pu; the subscript index $k = 2$ indicates material properties pertaining to the isotope ^{240}Pu; λ_k^S denotes the decay constant; N_k^S denotes the atomic density of the respective actinide; F_k^S denotes the spontaneous fission branching ratio; ν_k^S denotes the average number of neutrons per spontaneous fission; and W_k^S denotes a function of parameters used in Watt's fission spectrum to approximate the spontaneous fission neutron spectrum of the respective actinide. The detailed forms of the parameters W_k^S are unimportant for illustrating the application of the n^th^-FASAM-L. The nominal values for these imprecisely known parameters are available from a library file contained in SOURCES 4C (Wilson et al., 2002).

Mirroring the considerations for the Boltzmann transport equation presented in Equations 1–6, the "adjoint slowing-down model" is constructed in the Hilbert space $\mathcal{H}_B$ of square-integrable functions $\varphi(u) \in \mathcal{H}_B$ and $\psi(u) \in \mathcal{H}_B$ endowed with the following inner product, denoted as $\langle\varphi(u), \psi(u)\rangle_B$:

$$\langle\varphi(u), \psi(u)\rangle_B \triangleq \int_0^{u_{th}} \varphi(u)\psi(u)du. \tag{19}$$

Using the inner product $\langle\varphi(u), \psi(u)\rangle_B$ defined in Equation 19, the adjoint slowing-down model is constructed by the usual procedure, i.e., by (i) constructing the inner product of Equation 12 with a function $\psi(u) \in \mathcal{H}_B$; (ii) integrating by parts the resulting relation so as to transfer the differential operation from the forward function $\varphi(u)$ onto the adjoint function $\psi(u)$; (iii) using the initial condition provided in Equation 13 and eliminating the unknown function $\varphi(u_{th})$ by choosing the final-value condition $\psi(u_{th}) = 0$; and (iv) choosing the source for the resulting adjoint slowing-down model so as to satisfy the generalized reciprocity relation shown in Equation 6. The result of these operations is the following adjoint slowing-down model for the adjoint slowing-down function $\psi(u)$:

$$-\frac{d\psi(u)}{du} + f_1(\boldsymbol{\alpha})\psi(u) = \delta(u - u_d), \tag{20}$$

$$\psi(u_{th}) = 0, at \; u = u_{th}. \tag{21}$$

The "contributon-flux response density" $R_c(\varphi, \psi)$, as generally defined in Equation 8, specialized for the neutron slowing-down model, coincides with the inner product used in this context, i.e.,

$$R_c(\varphi, \psi) \triangleq \int_0^{u_{th}} \varphi(u)\psi(u)\,du \equiv \langle\varphi(u), \psi(u)\rangle_B. \tag{22}$$

It is important to note that $R_c(\varphi, \psi)$ does *not* depend *explicitly* on either the feature function $\mathbf{f}(\boldsymbol{\alpha})$ or any primary model parameter. Therefore, the G-differential of $R_c(\varphi, \psi)$ will not comprise a direct-effect term but will consist entirely of the indirect-effect term.

For this "contributon-flux response density" model, the following *primary model parameters* are subject to experimental uncertainties.

(i) For each material "*i*," $i = 1, ..., M$, included in the homogeneous mixture, the following are primary model parameters: the atomic number densities $N_m^{(i)}$; the microscopic radiative-capture cross section $\sigma_\gamma^{(i)}$; and the scattering cross section $\sigma_s^{(i)}$;
(ii) The source parameters λ_k^S, N_k^S, F_k^S, ν_k^S, and W_k^S, for $k = 1,2$.

The above primary parameters are considered to constitute the components of a "vector of primary model parameters" defined as follows:

$$\boldsymbol{\alpha} \triangleq \left(N_m^{(1)}, \sigma_\gamma^{(1)}, \sigma_s^{(1)}, ..., N_m^{(M)}, \sigma_\gamma^{(M)}, \sigma_s^{(M)}, \lambda_1^S, \lambda_2^S, N_1^S, N_2^S, F_1^S, F_2^S, \nu_1^S, \nu_2^S, W_1^S, W_2^S\right)^\dagger \triangleq (\alpha_1, \ldots, \alpha_{TP})^\dagger; \quad TP \triangleq 3M + 10. \tag{23}$$

The first-level forward/adjoint system (1st-LFAS) for the "first-level forward/adjoint function" $\mathbf{u}^{(1)}(2;u) \triangleq [\varphi(u), \psi(u)]^\dagger$ comprises Equations 12, 13, 20, and 21. The structure of the 1st-LFAS suggests that the components $f_i(\boldsymbol{\alpha})$ of the feature function $\mathbf{f}(\boldsymbol{\alpha})$ can be defined as follows:

$$\mathbf{f}(\boldsymbol{\alpha}) \triangleq [f_1(\boldsymbol{\alpha}), f_2(\boldsymbol{\alpha})]^\dagger; \quad f_1(\boldsymbol{\alpha}) \triangleq \frac{\Sigma_a(\boldsymbol{\alpha})}{\bar{\xi}(\boldsymbol{\alpha})\Sigma_t(\boldsymbol{\alpha})}; \quad f_2(\boldsymbol{\alpha}) \triangleq \frac{S_0(\boldsymbol{\alpha})}{\bar{\xi}(\boldsymbol{\alpha})\Sigma_t(\boldsymbol{\alpha})}. \tag{24}$$

Solving Equations 12, 13 while using the definitions introduced in Equation 24 yields the following expression for the flux $\varphi(u)$ in terms of the components $f_i(\boldsymbol{\alpha})$ of the feature function $\mathbf{f}(\boldsymbol{\alpha})$:

$$\varphi(u) = H(u) f_2(\boldsymbol{\alpha}) \exp[-u f_1(\boldsymbol{\alpha})]; \quad H(0) = 0; \quad H(u) = 1, if\ u > 0. \tag{25}$$

Solving the above adjoint slowing-down model yields the following closed-form expression for the adjoint slowing-down function $\psi(u)$:

$$\psi(u) = H(u_d - u) \exp[(u - u_d) f_1(\boldsymbol{\alpha})]. \tag{26}$$

In terms of the components $f_i(\boldsymbol{\alpha})$ of the feature function $\mathbf{f}(\boldsymbol{\alpha})$, the closed-form expression of the "contributon response density" is obtained by substituting the expressions provided in Equations 25, 26 into Equation 22 and performing the integration over lethargy, which yields

$$R_c(\varphi, \psi) = \int_0^{u_{th}} H(u) f_2(\boldsymbol{\alpha}) \exp[-u f_1(\boldsymbol{\alpha})] H(u_d - u) \exp[(u - u_d) f_1(\boldsymbol{\alpha})]\, du = u_d f_2(\boldsymbol{\alpha}) \exp[-u_d f_1(\boldsymbol{\alpha})]. \tag{27}$$

In terms of the primary model parameters, the closed-form expression of the "contributon response density" is

$$R_c(\varphi, \psi) = u_d \frac{S_0(\boldsymbol{\alpha})}{\bar{\xi}(\boldsymbol{\alpha})\Sigma_t(\boldsymbol{\alpha})} \exp\left[-u_d \frac{\Sigma_a(\boldsymbol{\alpha})}{\bar{\xi}(\boldsymbol{\alpha})\Sigma_t(\boldsymbol{\alpha})}\right]. \tag{28}$$

As Equation 28 indicates, the model response can be considered to depend directly on $TP \triangleq 3M + 10$ primary model parameters. In view of Equation 27, however, the model response can alternatively be considered to depend directly on two feature functions and only indirectly (through the two feature functions) on the primary model parameters. In the former consideration/interpretation, the response sensitivities to the primary model parameters will be obtained by applying the nth-CASAM-L. In the later consideration/interpretation, the response sensitivities to the primary model parameters will be obtained by applying the nth-FASAM-L, which will involve two stages: (a) the response sensitivities with respect to the feature functions will be obtained in the first stage; (b) the subsequent computation of the response sensitivities to the primary model parameters will be performed in the second stage by using the response sensitivities with respect to the feature functions obtained in the first stage. The computational distinctions that stem from these differing considerations/interpretations underlying the nth-CASAM-L *versus* the nth-FASAM-L will become evident in the next section by using a paradigm neutron slowing-down model, which is representative of the general situation for any linear system.

3 First-order adjoint sensitivity analysis of the contributon flux to the slowing-down model's features and parameters

The first-order sensitivities of the response $R_c[\mathbf{u}^{(1)}(2;u)]$, where $\mathbf{u}^{(1)}(2;u) \triangleq [\varphi(u), \psi(u)]^\dagger$, are obtained by determining the first-order Gateaux (G-)- differential, denoted as $\{\delta R_c[\mathbf{u}^{(1)}(2;u), \mathbf{v}^{(1)}(2;u)]\}_{\boldsymbol{\alpha}^0}$, of this response for variations $\mathbf{v}^{(1)}(2;u) \triangleq [\delta\varphi(u), \delta\psi(u)]^\dagger$ around the phase-space point (φ^0, ψ^0). By definition, the first-order G-differential $\{\delta R_c[\mathbf{u}^{(1)}(2;u), \mathbf{v}^{(1)}(2;u)]\}_{\boldsymbol{\alpha}^0}$ is obtained as follows:

$$\begin{aligned}\{\delta R_c[\mathbf{u}^{(1)}(2;u), \mathbf{v}^{(1)}(2;u)]\}_{\boldsymbol{\alpha}^0} &\triangleq \left\{\frac{d}{d\varepsilon}\int_0^{u_{th}} \left[\varphi^0(u) + \varepsilon v^{(1)}(u)\right]\left[\psi^0(u) + \varepsilon\delta\psi(u)\right] du\right\}_{\varepsilon=0} \\ &= \left\{\int_0^{u_{th}} \left[v^{(1)}(u)\psi(u) + \varphi(u)\delta\psi(u)\right] du\right\}_{\boldsymbol{\alpha}^0}.\end{aligned} \tag{29}$$

The sensitivities of $R_c[\mathbf{u}^{(1)}(2;u)]$ with respect to the feature functions (and subsequently to the primary model parameters) will be determined in Section 3.1 by applying the 1st-FASAM-L. Alternatively, the sensitivities of $R_c[\mathbf{u}^{(1)}(2;u)]$ directly with respect to the primary model parameters will be determined in Section 3.2 by applying the 1st-CASAM-L.

3.1 Application of the 1st-FASAM-L

The first-level variational sensitivity function $\mathbf{v}^{(1)}(2;u) \triangleq [v^{(1)}(u), \delta\psi(u)]^\dagger$ is the solution of the first-level variational sensitivity system (1st-LVSS) obtained by differentiating the 1st-LFAS. The function $v^{(1)}(u)$ is obtained by taking the first-order G-differentials of Equations 12, 13 to obtain

$$\left\{\frac{d}{d\varepsilon}\left[\frac{d(\varphi^0 + \varepsilon v^{(1)})}{du} + (f_1^0 + \varepsilon\delta f_1)(\varphi^0 + \varepsilon v^{(1)})\right]\right\}_{\varepsilon=0} = \delta(u)\left\{\frac{d}{d\varepsilon}(f_2^0 + \varepsilon\delta f_2)\right\}_{\varepsilon=0}, \tag{30}$$

$$\left\{ \frac{d}{d\varepsilon} \left[\varphi^0(u) + \varepsilon v^{(1)}(u) \right] \right\}_{\varepsilon=0} = 0; \quad at\ u = 0. \tag{31}$$

Carrying out the differentiations with respect to ε in the above equations and setting $\varepsilon = 0$ in the resulting expressions yields the following relations:

$$\frac{dv^{(1)}(u)}{du} + f_1(\boldsymbol{\alpha}^0) v^{(1)}(u) = (\delta f_2)\delta(u) - (\delta f_1)\varphi^0(u), \tag{32}$$

$$v^{(1)}(u) = 0; \quad at\ u = 0. \tag{33}$$

The equations satisfied by the variational function $\delta\psi(u)$ are obtained by G-differentiating Equations 20, 21 to obtain the equations below:

$$-\frac{d}{du}[\delta\psi(u)] + f_1(\boldsymbol{\alpha}^0)[\delta\psi(u)] = -(\delta f_1)\psi(u), \tag{34}$$

$$\delta\psi(u_{th}) = 0, at\ u = u_{th}. \tag{35}$$

Concatenating Equations 32–35 yields the following 1st-LVSS for the first-level variational sensitivity function $\mathbf{v}^{(1)}(2;u) \triangleq [\delta\varphi(u), \delta\psi(u)]^\dagger$:

$$\left\{ \mathbf{V}^{(1)}[2 \times 2; u; \mathbf{f}] \mathbf{v}^{(1)}(2;u) \right\}_{\boldsymbol{\alpha}^0} = \left\{ \mathbf{q}_V^{(1)}\left[2; \mathbf{u}^{(1)}(2;u); \mathbf{f}; \delta\mathbf{f}\right] \right\}_{\boldsymbol{\alpha}^0}, \tag{36}$$

$$\left\{ \mathbf{b}_v^{(1)}(\mathbf{v}^{(1)}; \mathbf{f}; \delta\mathbf{f}) \right\}_{\boldsymbol{\alpha}^0} = \mathbf{0}, \tag{37}$$

where

$$\mathbf{V}^{(1)}[2 \times 2; u; \mathbf{f}] \triangleq \begin{pmatrix} d/du + f_1 & 0 \\ 0 & -d/du + f_1 \end{pmatrix}, \mathbf{b}_v^{(1)}(\mathbf{v}^{(1)}; \mathbf{f}; \delta\mathbf{f}) \triangleq \begin{pmatrix} v^{(1)}(0) \\ \delta\psi(u_{th}) \end{pmatrix}, \tag{38}$$

$$\mathbf{q}_V^{(1)}\left[2; \mathbf{u}^{(1)}; \mathbf{f}; \delta\mathbf{f}\right] \triangleq \begin{pmatrix} (\delta f_2)\delta(u) - (\delta f_1)\varphi(u) \\ -(\delta f_1)\psi(u) \end{pmatrix}. \tag{39}$$

Rather than repeatedly solving the 1st-LVSS for every possible variations δf_i, $i = 1, 2$, the appearance of the first-level variational sensitivity function $\mathbf{v}^{(1)}(2;u) \triangleq [\delta\varphi(u), \delta\psi(u)]^\dagger$ will be eliminated from the expression of the G-differential of the response $\{\delta R_c[\mathbf{u}^{(1)}(2;u), \mathbf{v}^{(1)}(2;u)]\}_{\boldsymbol{\alpha}^0}$, defined in Equation 29), by applying the principles of the 1st-FASAM-L outlined in the accompanying "Part I" by Cacuci (2024c). The specific steps are as follows:

1. A Hilbert space, denoted as H_1, is introduced endowed with the following inner product denoted as $\langle \boldsymbol{\chi}^{(1)}(2;u), \boldsymbol{\theta}^{(1)}(2;u) \rangle_1$, between two elements, $\boldsymbol{\chi}^{(1)}(2;u) \triangleq [\chi_1^{(1)}(u), \chi_2^{(1)}(u)]^\dagger \in \mathcal{H}_1$ and $\boldsymbol{\theta}^{(1)}(2;u) \triangleq [\theta_1^{(1)}(u), \theta_2^{(1)}(u)]^\dagger \in \mathcal{H}_1$:

$$\langle \boldsymbol{\chi}^{(1)}(2;u), \boldsymbol{\theta}^{(1)}(2;u) \rangle_1 \triangleq \sum_{i=1}^{2} \int_0^{u_{th}} \chi_i^{(1)}(u) \theta_i^{(1)}(u)\, du. \tag{40}$$

2. In the Hilbert $\mathcal{H}_1$, the inner product of Equation 36 is formed with a yet undefined vector-valued function $\mathbf{a}^{(1)}(2;u) \triangleq [a_1^{(1)}(u), a_2^{(1)}(u)]^\dagger \in \mathcal{H}_1$ to obtain the following relation:

$$\begin{aligned} &\{\langle \mathbf{a}^{(1)}(2;u), \mathbf{V}^{(1)}[2 \times 2; u; \mathbf{f}^0] \mathbf{v}^{(1)}(2;u) \rangle_1\}_{\boldsymbol{\alpha}^0} \\ &= \left\{ \langle \mathbf{a}^{(1)}(2;u), \mathbf{q}_V^{(1)}\left[2; \mathbf{u}^{(1)}(2;u); \mathbf{f}; \delta\mathbf{f}\right] \rangle_1 \right\}_{\boldsymbol{\alpha}^0}. \end{aligned} \tag{41}$$

3. The left-side of Equation 41 is integrated by parts to obtain the following relation, where the specification $\{\}_{\boldsymbol{\alpha}^0}$ is omitted to simplify the notation:

$$\begin{aligned} &\int_0^{u_{th}} a_1^{(1)}(u) \left[\frac{dv^{(1)}}{du} + f_1 v^{(1)} \right] du + \int_0^{u_{th}} a_2^{(1)}(u) \left[-\frac{d}{du}\delta\psi + f_1 \delta\psi \right] du \\ &= \int_0^{u_{th}} v^{(1)} \left[-\frac{d}{du} a_1^{(1)}(u) + f_1 a_1^{(1)}(u) \right] du \\ &\quad + \int_0^{u_{th}} \delta\psi(u) \left[\frac{d}{du} a_2^{(1)}(u) + f_1 a_2^{(1)}(u) \right] du + a_1^{(1)}(u_{th}) v^{(1)}(u_{th}) \\ &\quad - a_1^{(1)}(0) v^{(1)}(0) - a_2^{(1)}(u_{th}) \delta\psi(u_{th}) + a_2^{(1)}(0) \delta\psi(0). \end{aligned} \tag{42}$$

4. The first two terms on the right side of Equation 42 are required to represent the G-differentiated response defined in Equation 29, and the unknown boundary values of the function $\mathbf{v}^{(1)}(2;u)$ are eliminated from the bilinear concomitant on the right side of Equation 42 to obtain the following 1st-LASS for the first-level adjoint sensitivity function $\mathbf{a}^{(1)}(2;u) \triangleq [a_1^{(1)}(u), a_2^{(1)}(u)]^\dagger$:

$$\mathbf{A}^{(1)}[2 \times 2; \mathbf{x}; \mathbf{f}] \mathbf{a}^{(1)}(2;\mathbf{x}) = \mathbf{q}_A^{(1)}\left[2; \mathbf{u}^{(1)}(2;\mathbf{x}); \mathbf{f}\right], \tag{43}$$

$$\left\{ \mathbf{b}_A^{(1)}\left[\mathbf{u}^{(1)}(2;u); \mathbf{a}^{(1)}(2;u); \mathbf{f} \right] \right\}_{\boldsymbol{\alpha}^0} \triangleq \begin{pmatrix} a_1^{(1)}(u_{th}) \\ a_2^{(1)}(0) \end{pmatrix} = \mathbf{0}, \tag{44}$$

where

$$\mathbf{A}^{(1)}[2 \times 2; u; \mathbf{f}] \triangleq \begin{pmatrix} -d/du + f_1 & 0 \\ 0 & d/du + f_1 \end{pmatrix} = \{\mathbf{V}^{(1)}[2 \times 2; u; \mathbf{f}]\}^*, \tag{45}$$

$$\mathbf{q}_A^{(1)}\left[2; \mathbf{u}^{(1)}(2;\mathbf{x}); \mathbf{f}\right] \triangleq \begin{pmatrix} \psi(u) \\ \varphi(u) \end{pmatrix}. \tag{46}$$

5. It follows from Equations 29, 41–44 that G-differentiated response defined in Equation 29 takes the following expression in terms of the first-level adjoint sensitivity function $\mathbf{a}^{(1)}(2;u) \triangleq [a_1^{(1)}(u), a_2^{(1)}(u)]^\dagger$:

$$\begin{aligned} &\left\{ \delta R_c\left[\mathbf{u}^{(1)}(2;u), \mathbf{a}^{(1)}(2;u) \right] \right\}_{\boldsymbol{\alpha}^0} \\ &= \left\{ \int_0^{u_{th}} a_1^{(1)}(u) \left[(\delta f_2)\delta(u) - (\delta f_1)\varphi(u) \right] du \right\}_{\boldsymbol{\alpha}^0} \\ &+ \left\{ \int_0^{u_{th}} a_2^{(1)}(u) \left[-(\delta f_1)\psi(u) \right] du \right\}_{\boldsymbol{\alpha}^0}, \end{aligned} \tag{47}$$

The expressions of the sensitivities of the response $R_c(\varphi, \psi)$ with respect to the components of the feature function $\mathbf{f}(\boldsymbol{\alpha})$ are given by the expressions that multiply the respective components of $\mathbf{f}(\boldsymbol{\alpha})$ in Equation 47, i.e.,

$$\frac{\partial R_c(\varphi, \psi)}{\partial f_1} = -\int_0^{u_{th}} \left[a_1^{(1)}(u)\varphi(u) + a_2^{(1)}(u)\psi(u) \right] du, \tag{48}$$

$$\frac{\partial R_c(\varphi, \psi)}{\partial f_2} = \int_0^{u_{th}} a_1^{(1)}(u)\, \delta(u)\, du. \tag{49}$$

The above expressions are to be evaluated at the nominal parameter values $\boldsymbol{\alpha}^0$, but the indication $\{\}_{\boldsymbol{\alpha}^0}$ has been omitted for simplicity.

The first-order sensitivities of the response $R_c(\varphi, \psi)$ with respect to the primary model parameters are obtained by using the results obtained in Equations 48, 49, respectively, in conjunction with the "chain rule" of differentiating the components of the feature function $\mathbf{f}(\boldsymbol{\alpha})$ with respect to the primary model parameters defined in Equation 29 to obtain the following expressions:

$$\frac{\partial R_c(\varphi,\psi)}{\partial \alpha_i} = \frac{\partial R_c(\varphi,\psi)}{\partial f_1}\frac{\partial f_1}{\partial \alpha_i} + \frac{\partial R_c(\varphi,\psi)}{\partial f_2}\frac{\partial f_2}{\partial \alpha_i}$$

$$= -\left(\frac{\partial f_1}{\partial \alpha_i}\right)\int_0^{u_{th}}\left[a_1^{(1)}(u)\varphi(u) + a_2^{(1)}(u)\psi(u)\right]du$$

$$+\left(\frac{\partial f_2}{\partial \alpha_i}\right)\int_0^{u_{th}} a_1^{(1)}(u)\,\delta(u)\,du\,. \tag{50}$$

Solving the 1st-LASS defined by Equations 43, 44 yields the following closed-form expressions for the components of the first-level adjoint sensitivity function $\mathbf{a}^{(1)}(2;u) \triangleq [a_1^{(1)}(u), a_2^{(1)}(u)]^\dagger$:

$$a_1^{(1)}(u) = (u_d - u)H(u_d - u)\exp\left[(u - u_d)f_1(\boldsymbol{\alpha})\right], \tag{51}$$

$$a_2^{(1)}(u) = u f_2(\boldsymbol{\alpha})\exp\left[-u f_1(\boldsymbol{\alpha})\right]. \tag{52}$$

Using the above expressions in Equations 48, 49 yields the following closed-form expressions for the respective sensitivities:

$$\frac{\partial R_c(\varphi,\psi)}{\partial f_1} = -(u_d)^2 f_2(\boldsymbol{\alpha})\exp\left[-u_d f_1(\boldsymbol{\alpha})\right], \tag{53}$$

$$\frac{\partial R_c(\varphi,\psi)}{\partial f_2} = u_d\exp\left[-u_d f_1(\boldsymbol{\alpha})\right]. \tag{54}$$

The correctness of the expressions obtained in Equations 53, 54 can be verified by differentiating accordingly the closed-form expression given in Equation 27.

3.2 Application of the 1st-CASAM-L

The 1st-CASAM-L delivers the first-order sensitivities of the response directly with respect to the primary model parameters. The expression of the G-differentiated response is as shown in Equation 29, but the source term on the right side of the 1st-LVSS takes the following form:

$$\mathbf{q}_V^{(1)}\left[2;\mathbf{u}^{(1)};\mathbf{f};\delta\mathbf{f}\right] \triangleq \begin{pmatrix} \delta(u)\sum_{i=1}^{TP}\frac{\partial f_2}{\partial \alpha_i}\delta\alpha_i - \varphi(u)\sum_{i=1}^{TP}\frac{\partial f_1}{\partial \alpha_i}\delta\alpha_i \\ -\psi(u)\sum_{i=1}^{TP}\frac{\partial f_1}{\partial \alpha_i}\delta\alpha_i \end{pmatrix}. \tag{55}$$

If one were to actually solve the 1st-LVSS to obtain the first-level variational function and subsequently use the respective variational function to compute each sensitivity, one would need to solve the 1st-LVSS *TP-times*, using each time a source that would correspond to the *i*th-primary parameter, of the form $\mathbf{q}_V^{(1)}[i;2;\mathbf{u}^{(1)};\mathbf{f};\delta\mathbf{f}]\mathbf{q} \triangleq [\delta(u)\partial f_2/\partial\alpha_i - \varphi(u)\,\partial f_1/\partial\alpha_i, -\,\psi(u)\partial f_1/\partial\alpha_i]^\dagger$, for each primary parameter $i = 1,\ldots,TP$.

Since the left side of the 1st-LVSS remains the same as in Equation 36 and the boundary conditions also remain the same as obtained in Equation 37, it follows that the 1st-LASS and its solution $\mathbf{a}^{(1)}(2;u) \triangleq [a_1^{(1)}(u), a_2^{(1)}(u)]^\dagger$ remain unchanged. It therefore follows that the counterpart of the expression of the G-differential obtained in Equation 47 takes the following form:

$$\left\{\delta R_c\left[\mathbf{u}^{(1)}(2;u),\mathbf{a}^{(1)}(2;u)\right]\right\}_{\boldsymbol{\alpha}^0} =$$

$$-\left\{\sum_{i=1}^{TP}\frac{\partial f_1}{\partial \alpha_i}\delta\alpha_i\int_0^{u_{th}} a_2^{(1)}(u)\psi(u)\,du\right\}_{\boldsymbol{\alpha}^0}$$

$$+\left\{\int_0^{u_{th}} a_1^{(1)}(u)\left[\delta(u)\sum_{i=1}^{TP}\frac{\partial f_2}{\partial \alpha_i}\delta\alpha_i - \varphi(u)\sum_{i=1}^{TP}\frac{\partial f_1}{\partial \alpha_i}\delta\alpha_i\right]du\right\}_{\boldsymbol{\alpha}^0}. \tag{56}$$

The first-order sensitivities of the response $R_c(\varphi,\psi)$ with respect to the primary model parameters $\alpha_i, i = 1,\ldots,TP$ are obtained by identifying the expressions that multiply the respective variations $\delta\alpha_i$ in Equation 47, which yields the following result:

$$\frac{\partial R_c(\varphi,\psi)}{\partial \alpha_i} = -\left(\frac{\partial f_1}{\partial \alpha_i}\right)\int_0^{u_{th}}\left[a_1^{(1)}(u)\varphi(u) + a_2^{(1)}(u)\psi(u)\right]du$$

$$+\left(\frac{\partial f_2}{\partial \alpha_i}\right)\int_0^{u_{th}} a_1^{(1)}(u)\,\delta(u)\,du\,. \tag{57}$$

As expected, the result obtained from Equation 57 is identical to the result produced from Equation 50 by using the 1st-FASAM-L. Both the 1st-FASAM-L and 1st-CASAM-L require "one large-scale computation" for solving the 1st-LASS represented by Equations 43, 44.

4 Second-order adjoint sensitivity analysis of the contributon flux to the slowing-down model's features and parameters

In practice, closed-form expressions such as those shown in Equations 53, 54 are unavailable. The 1st-FASAM-L yields the expressions provided in Equations 48, 49, while the 1st-CASAM-L yields the expressions provided in Equation 57. Hence, these expressions will provide the starting points for obtaining the second-order sensitivities that stem from the respective first-order sensitivities. As outlined within the general frameworks of both the nth-FASAM-L and nth-CASAM-L methodologies, the second-order sensitivities are obtained by conceptually considering them to arise as the "first-order sensitivities of the first-order sensitivities."

4.1 Application of the 2nd-FASAM-L

The 2nd-FASAM-L uses the first-order sensitivities obtained from the 1st-CASAM-L, as provided in Equations 48, 49, to obtain the respective second-order sensitivities, as presented in Sections 4.1.1 and 4.1.2.

4.1.1 Second-order sensitivities stemming from the first-order sensitivity $\partial R_c/\partial f_1$

The second-order sensitivities that stem from the first-order sensitivity $\partial R_c/\partial f_1$ are obtained by determining the G-differential of $\partial R_c/\partial f_1$. For subsequent "bookkeeping" purposes, this first-order sensitivity will be denoted as $R^{(1)}[1;\mathbf{u}^{(2)}(2^2;u);\mathbf{f}(\boldsymbol{\alpha})] \triangleq \partial R_c/\partial f_1$, where the superscript "(1)" denotes "*first-order*" (sensitivity) and the argument "1" indicates that this sensitivity is with respect to the *first component*, i.e., $f_1(\boldsymbol{\alpha})$, of the feature function $\mathbf{f}(\boldsymbol{\alpha})$. This sensitivity also depends on the function $\mathbf{u}^{(2)}(2^2;u) \triangleq [\mathbf{u}^{(1)}(2;u),\mathbf{a}^{(1)}(2;u)]^{\dagger}$, which is the solution of the "second-level forward/adjoint system (2nd-LFAS)" obtained by concatenating the 1st-LFAS with the 1st-LASS, comprising Equations 12, 13, 20, 21, 43, and 44.

Applying the definition of the G-differential to Equation 48 yields the following expression for the G-differential $\{\delta R^{(1)}[1;\mathbf{u}^{(2)}(2^2;u);\mathbf{v}^{(2)}(2^2;u);\mathbf{f}(\boldsymbol{\alpha})]\}_{\boldsymbol{\alpha}^0}$:

$$\begin{aligned}
&\{\delta R^{(1)}[1;\mathbf{u}^{(2)}(2^2;u);\mathbf{v}^{(2)}(2^2;u);\mathbf{f}(\boldsymbol{\alpha})]\}_{\boldsymbol{\alpha}^0}\\
&\quad\triangleq -\left\{\tfrac{d}{d\varepsilon}\int_0^{u_{th}}\left[a_1^{(1)}(u)+\varepsilon\delta a_1^{(1)}(u)\right]\left[\varphi(u)+\varepsilon v^{(1)}(u)\right]du\right\}_{\boldsymbol{\alpha}^0,\varepsilon=0}\\
&\qquad-\left\{\tfrac{d}{d\varepsilon}\int_0^{u_{th}}\left[a_2^{(1)}(u)+\varepsilon\delta a_2^{(1)}(u)\right]\left[\psi(u)+\varepsilon\delta\psi(u)\right]du\right\}_{\boldsymbol{\alpha}^0,\varepsilon=0}\\
&\quad=-\int_0^{u_{th}}\varphi(u)\left[\delta a_1^{(1)}(u)\right]du-\int_0^{u_{th}}a_1^{(1)}(u)v^{(1)}(u)\,du-\int_0^{u_{th}}\psi(u)\left[\delta a_2^{(1)}(u)\right]du\\
&\qquad-\int_0^{u_{th}}a_2^{(1)}(u)\left[\delta\psi(u)\right]du\equiv\sum_{j=1}^{2}\frac{\partial^2R(\varphi;\mathbf{f})}{\partial f_j\partial f_1}\left(\delta f_j\right).
\end{aligned}\tag{58}$$

The components $v^{(1)}(u)$, $\delta\psi(u)$, $\delta a_1^{(1)}(u)$, and $\delta a_2^{(1)}(u)$ of the second-level variational sensitivity function $\mathbf{v}^{(2)}(2^2;u) \triangleq [v^{(1)}(u),\delta\psi(u),\delta a_1^{(1)}(u),\delta a_2^{(1)}(u)]^{\dagger}$ are the solutions of the 2nd-LVSS, which is obtained by G-differentiating the 2nd-LFAS. Thus, performing the G-differentiation of Equations 12, 13, 20, 21, 43, and 44 yields the following 2nd-LVSS for the second-level variational sensitivity function $\mathbf{v}^{(2)}(2^2;u) \triangleq [v^{(1)}(u),\delta\psi(u),\delta a_1^{(1)}(u),\delta a_2^{(1)}(u)]^{\dagger}$:

$$\left\{\mathbf{V}^{(2)}[2^2\times 2^2;u;\mathbf{f}]\mathbf{v}^{(2)}(2^2;u)\right\}_{\boldsymbol{\alpha}^0}=\left\{\mathbf{q}_V^{(2)}[2^2;u;\mathbf{f};\delta\mathbf{f}]\right\}_{\boldsymbol{\alpha}^0},\tag{59}$$

$$\left\{\mathbf{b}_v^{(2)}(u;\mathbf{f};\delta\mathbf{f})\right\}_{\boldsymbol{\alpha}^0}=\mathbf{0},\tag{60}$$

where

$$\mathbf{V}^{(2)}[2^2\times 2^2;u;\mathbf{f}] \triangleq \begin{pmatrix} d\backslash/du+f_1 & 0 & 0 & 0\\ 0 & -\dfrac{d}{du}+f & 0 & 0\\ 0 & -1 & -\dfrac{d}{du}+f_1 & 0\\ -1 & 0 & 0 & \dfrac{d}{du}+f_1 \end{pmatrix};\tag{61}$$

$$\mathbf{q}_V^{(2)}[2^2;u;\mathbf{f};\delta\mathbf{f}] \triangleq \begin{pmatrix} (\delta f_2)\delta(u)-(\delta f_1)\varphi(u)\\ -(\delta f_1)\psi(u)\\ -(\delta f_1)a_1^{(1)}(u)\\ -(\delta f_1)a_2^{(1)}(u) \end{pmatrix};$$

$$\mathbf{b}_v^{(2)}(u;\mathbf{f};\delta\mathbf{f}) \triangleq \begin{pmatrix} v^{(1)}(0)\\ \delta\psi(u_{th})\\ \delta a_1^{(1)}(u_{th})\\ \delta a_2^{(1)}(0) \end{pmatrix}.\tag{62}$$

The second-level variational sensitivity function $\mathbf{v}^{(2)}(2^2;u)$ will be eliminated from the expression of $\{\delta R^{(1)}[1;\mathbf{u}^{(2)}(2^2;u);\mathbf{v}^{(2)}(2^2;u);\mathbf{f}(\boldsymbol{\alpha})]\}_{\boldsymbol{\alpha}^0}$ by constructing the 2nd-LASS corresponding to the above 2nd-LVSS. The solution of the 2nd-LASS will be used in Equation 58 to construct $\{\delta R^{(1)}[1;\mathbf{u}^{(2)}(2^2;u);\mathbf{v}^{(2)}(2^2;u);\mathbf{f}(\boldsymbol{\alpha})]\}_{\boldsymbol{\alpha}^0}$, an alternative expression that will not depend on $\mathbf{v}^{(2)}(2^2;u)$. This 2nd-LASS will be constructed in a Hilbert space denoted as H_2, comprising four-component vector-valued functions of the form $\boldsymbol{\chi}^{(2)}(2^2;1;u) \triangleq [\chi_1^{(2)}(1;u),\chi_2^{(2)}(1;u),\chi_3^{(2)}(1;u),\chi_4^{(2)}(1;u)]^{\dagger}\in\mathcal{H}_2$ as elements, and is endowed with the following inner product between two vectors $\boldsymbol{\chi}^{(2)}(2^2;1;u)$ and $\boldsymbol{\theta}^{(2)}(2^2;1;u)$:

$$\langle\boldsymbol{\chi}^{(2)}(2^2;u),\boldsymbol{\theta}^{(2)}(2^2;u)\rangle_2 \triangleq \sum_{i=1}^{2^2}\int_0^{u_{th}}\chi_i^{(2)}(1;u)\theta_i^{(2)}(1;u)\,du.\tag{63}$$

The inner product defined in Equation 63 will be used to construct the inner product of Equation 59 with a function denoted as $\mathbf{a}^{(2)}(2^2;1;u) \triangleq [a_1^{(2)}(1;u),a_2^{(2)}(1;u),a_3^{(2)}(1;u),a_4^{(2)}(1;u)]^{\dagger}\in\mathcal{H}_2$, where the argument "1" of the function $\mathbf{a}^{(2)}(2^2;1;u)$ indicates that this (adjoint) function corresponds to the first-order sensitivity of the response with respect to the "*first*" component, $f_1(\boldsymbol{\alpha})$, of the feature function $\mathbf{f}(\boldsymbol{\alpha})$. Constructing this inner product yields the following relation, where the specification $\{\}_{\boldsymbol{\alpha}^0}$ has been omitted to simplify the notation:

$$\begin{aligned}
&\langle\mathbf{a}^{(2)}(2^2;1;\mathbf{x}),\mathbf{V}^{(2)}[2^2\times 2^2;u;\mathbf{f}]\mathbf{v}^{(2)}(2^2;u)\rangle_{2^2}\\
&\quad=\int_0^{u_{th}}a_1^{(2)}(1;u)\left[dv^{(1)}/du+f_1v^{(1)}\right]du\\
&\qquad+\int_0^{u_{th}}a_2^{(2)}(1;u)\left[-d(\delta\psi)/du+f_1(\delta\psi)\right]du\\
&\qquad+\int_0^{u_{th}}a_3^{(2)}(1;u)\left[-\delta\psi-d\left(\delta a_1^{(1)}\right)/du+f_1\left(\delta a_1^{(1)}\right)\right]du\\
&\qquad+\int_0^{u_{th}}a_4^{(2)}(1;u)\left[-v^{(1)}(u)+d\left(\delta a_2^{(1)}\right)/du+f_1\left(\delta a_2^{(1)}\right)\right]du\\
&\quad=\int_0^{u_{th}}a_1^{(2)}(1;u)\left[(\delta f_2)\delta(u)-(\delta f_1)\varphi(u)\right]du\\
&\qquad+\int_0^{u_{th}}a_2^{(2)}(1;u)\left[-(\delta f_1)\psi(u)\right]du\\
&\qquad+\int_0^{u_{th}}a_3^{(2)}(1;u)\left[-(\delta f_1)a_1^{(1)}(u)\right]du\\
&\qquad+\int_0^{u_{th}}a_4^{(2)}(1;u)\left[-(\delta f_1)a_2^{(1)}(u)\right]du.
\end{aligned}\tag{64}$$

Integrating by parts the left side of Equation 64 yields the following relation:

$$\begin{aligned}
&\int_0^{u_{th}} a_1^{(2)}(1;u)\left[dv^{(1)}/du + f_1 v^{(1)}\right] du \\
&\quad + \int_0^{u_{th}} a_2^{(2)}(1;u)\left[-d(\delta\psi)/du + f_1(\delta\psi)\right] du \\
&\quad + \int_0^{u_{th}} a_3^{(2)}(1;u)\left[-\delta\psi - d\left(\delta a_1^{(1)}\right)/du + f_1\left(\delta a_1^{(1)}\right)\right] du \\
&\quad + \int_0^{u_{th}} a_4^{(2)}(1;u)\left[-v^{(1)}(u) + d\left(\delta a_2^{(1)}\right)/du + f_1\left(\delta a_2^{(1)}\right)\right] du \\
&\quad = a_1^{(2)}(1;u_{th})v^{(1)}(u_{th}) - a_1^{(2)}(1;0)v^{(1)}(0) \\
&\qquad + \int_0^{u_{th}} v^{(1)}(u)\left[-da_1^{(2)}(1;u)/du + f_1 a_1^{(2)}(1;u)\right] du \\
&\qquad - a_2^{(2)}(1;u_{th})\delta\psi(u_{th}) + a_2^{(2)}(1;0)\delta\psi(0) + \int_0^{u_{th}} (\delta\psi) \\
&\qquad \times \left[da_2^{(2)}(1;u)/du + f_1 a_2^{(2)}(1;u)\right] du - a_3^{(2)}(1;u_{th})\delta a_1^{(1)}(u_{th}) \\
&\qquad + a_3^{(2)}(1;0)\delta a_1^{(1)}(0) - \int_0^{u_{th}} (\delta\psi) a_3^{(2)}(1;u)\, du \\
&\qquad + \int_0^{u_{th}} \delta a_1^{(1)}(u)\left[da_3^{(2)}(1;u)/du + f_1 a_3^{(2)}(1;u)\right] du \\
&\qquad - \int_0^{u_{th}} v^{(1)}(u) a_4^{(2)}(1;u)\, du + a_4^{(2)}(1;u_{th})\delta a_2^{(1)}(u_{th}) \\
&\qquad - a_4^{(2)}(1;0)\delta a_2^{(1)}(0) \\
&\qquad + \int_0^{u_{th}} \delta a_2^{(1)}(u)\left[-da_4^{(2)}(1;u)/du + f_1 a_4^{(2)}(1;u)\right] du.
\end{aligned} \tag{65}$$

The right side of Equation 65 is now tailored to represent the G-differential $\left\{\delta R^{(1)}\left[1;\mathbf{u}^{(2)}(2^2;u);\mathbf{v}^{(2)}(2^2;u);\mathbf{f}(\boldsymbol{\alpha})\right]\right\}_{\boldsymbol{\alpha}^0}$ expressed by Equation 58 by requiring the second-level adjoint sensitivity function $\mathbf{a}^{(2)}(2^2;1;u)$ to be the solution of the following 2nd-LASS:

$$\text{j}\left\{\mathbf{A}^{(2)}\left[2^2\times 2^2;u;\mathbf{f}\right]\mathbf{a}^{(2)}(2^2;1;u)\right\}_{\boldsymbol{\alpha}^0} = \left\{\mathbf{s}^{(2)}(2^2;1;u;\mathbf{f})\right\}_{\boldsymbol{\alpha}^0}, \tag{66}$$

$$\left\{\mathbf{b}_A^{(2)}(u;\mathbf{f})\right\}_{\boldsymbol{\alpha}^0} = \mathbf{0}, \tag{67}$$

where

$$\mathbf{A}^{(2)}\left[2^2\times 2^2;u;\mathbf{f}\right] \triangleq \begin{pmatrix} -d/du + f_1 & 0 & 0 & -1 \\ 0 & d/du + f_1 & -1 & 0 \\ 0 & 0 & d/du + f_1 & 0 \\ 0 & 0 & 0 & -d/du + f_1 \end{pmatrix}; \tag{68}$$

$$\mathbf{s}^{(2)}(2^2;1;u;\mathbf{f}) \triangleq \begin{pmatrix} -a_1^{(1)}(u) \\ -a_2^{(1)}(u) \\ -\varphi(u) \\ -\psi(u) \end{pmatrix}; \quad \mathbf{b}_A^{(2)}(u;\mathbf{f}) \triangleq \begin{pmatrix} a_1^{(2)}(1;u_{th}) \\ a_2^{(2)}(1;0) \\ a_3^{(2)}(1;0) \\ a_4^{(2)}(1;u_{th}) \end{pmatrix}. \tag{69}$$

Implementing the equations underlying the 2nd-LVSS and the 2nd-LASS and substituting Equation 58 into Equation 64 provide the following alternative expression for the G-differential $\left\{\delta R^{(1)}\left[1;\mathbf{u}^{(2)}(2^2;u);\mathbf{v}^{(2)}(2^2;u);\mathbf{f}(\boldsymbol{\alpha})\right]\right\}_{\boldsymbol{\alpha}^0}$:

$$\begin{aligned}
&\left\{\delta R^{(1)}\left[1;\mathbf{u}^{(2)}(2^2;u);\mathbf{v}^{(2)}(2^2;u);\mathbf{f}(\boldsymbol{\alpha})\right]\right\}_{\boldsymbol{\alpha}^0} \\
&\quad = \left\{\int_0^{u_{th}} a_1^{(2)}(1;u)\left[(\delta f_2)\delta(u) - (\delta f_1)\varphi(u)\right] du\right\}_{\boldsymbol{\alpha}^0} \\
&\qquad + \left\{\int_0^{u_{th}} a_2^{(2)}(1;u)\left[-(\delta f_1)\psi(u)\right] du\right\}_{\boldsymbol{\alpha}^0} \\
&\qquad + \left\{\int_0^{u_{th}} a_3^{(2)}(1;u)\left[-(\delta f_1)a_1^{(1)}(u)\right] du\right\}_{\boldsymbol{\alpha}^0} \\
&\qquad + \left\{\int_0^{u_{th}} a_4^{(2)}(1;u)\left[-(\delta f_1)a_2^{(1)}(u)\right] du\right\}_{\boldsymbol{\alpha}^0}.
\end{aligned} \tag{70}$$

The expressions that multiply the respective components of $\mathbf{f}(\boldsymbol{\alpha})$ in Equation 70 are the expressions of the second-order sensitivities $\partial^2 R_c(\varphi,\psi)/\partial f_1\partial f_j$ (stemming from the first-order sensitivity $\partial R_c/\partial f_1$) of the response $R_c(\varphi,\psi)$, with respect to the components of the feature function $\mathbf{f}(\boldsymbol{\alpha})$. Thus, identifying in Equation 70 the expressions that multiply the respective variations in the components of the feature function $\mathbf{f}(\boldsymbol{\alpha})$ yields the following relations:

$$\begin{aligned}
\frac{\partial^2 R_c(\varphi,\psi)}{\partial f_1\partial f_1} = &-\int_0^{u_{th}} a_1^{(2)}(1;u)\varphi(u)\, du - \int_0^{u_{th}} a_2^{(2)}(1;u)\psi(u)\, du \\
&-\int_0^{u_{th}} a_3^{(2)}(1;u)\, a_1^{(1)}(u)\, du - \int_0^{u_{th}} a_4^{(2)}(1;u)\, a_2^{(1)}(u)\, du\,;
\end{aligned} \tag{71}$$

$$\frac{\partial R_c(\varphi,\psi)}{\partial f_2\partial f_1} = \int_0^{u_{th}} a_1^{(2)}(1;u)\delta(u)\, du\,. \tag{72}$$

Solving the 2nd-LASS represented by Equations 66, 67 yields the following closed-form expressions for the components of the second-level adjoint sensitivity function $\mathbf{a}^{(2)}(2^2;1;u)$:

$$a_1^{(2)}(1;u) = -(u_d-u)^2 H(u_d-u)\exp\left[(u-u_d)f_1(\boldsymbol{\alpha})\right], \tag{73}$$

$$a_2^{(2)}(1;u) = -f_2(\boldsymbol{\alpha})u^2\exp\left[-uf_1(\boldsymbol{\alpha})\right], \tag{74}$$

$$a_3^{(2)}(1;u) = -f_2(\boldsymbol{\alpha})u\exp\left[-uf_1(\boldsymbol{\alpha})\right], \tag{75}$$

$$a_4^{(2)}(1;u) = -(u_d-u)H(u_d-u)\exp\left[(u-u_d)f_1(\boldsymbol{\alpha})\right]. \tag{76}$$

Using the explicit closed-form expressions obtained in Equations 73–76 and substituting them in Equations 71, 72 yield the following closed-form explicit expressions for the respective second-order sensitivities:

$$\frac{\partial^2 R_c(\varphi,\psi)}{\partial f_1\partial f_1} = (u_d)^3 f_2(\boldsymbol{\alpha})\exp\left[-u_d f_1(\boldsymbol{\alpha})\right], \tag{77}$$

$$\frac{\partial R_c(\varphi,\psi)}{\partial f_2\partial f_1} = -(u_d)^2\exp\left[-u_d f_1(\boldsymbol{\alpha})\right]. \tag{78}$$

The correctness of the expressions obtained in Equations 77, 78 can be verified by differentiating accordingly the closed-form expression given in Equation 53.

4.1.2 Second-order sensitivities stemming from the first-order sensitivity $\partial R_c/\partial f_2$

The second-order sensitivities that stem from the first-order sensitivity $\partial R_c/\partial f_2$ are obtained by determining the G-differential of $\partial R_c/\partial f_2$. For subsequent "bookkeeping" purposes, this first-order sensitivity will be denoted as $R^{(1)}[2;\mathbf{u}^{(2)}(2^2;u);\mathbf{f}(\boldsymbol{\alpha})] \triangleq \partial R_c/\partial f_2$, where the superscript "(1)" denotes "*first-order*" (sensitivity) and the argument "2" indicates that this sensitivity is with respect to the *second component*, i.e., $f_2(\boldsymbol{\alpha})$, of the feature function $\mathbf{f}(\boldsymbol{\alpha})$. This sensitivity also depends on the function $\mathbf{u}^{(2)}(2^2;u) \triangleq [\mathbf{u}^{(1)}(2;u),\mathbf{a}^{(1)}(2;u)]^{\dagger}$. Applying the definition of the G-differential to the expression provided in Equation 49 yields the result below for the G-differential $\{\delta R^{(1)}[2;\mathbf{u}^{(2)}(2^2;u);\mathbf{v}^{(2)}(2^2;u);\mathbf{f}(\boldsymbol{\alpha})]\}_{\boldsymbol{\alpha}^0}$:

$$\left\{\delta R^{(1)}\left[2;\mathbf{u}^{(2)}(2^2;u);\mathbf{v}^{(2)}(2^2;u);\mathbf{f}(\boldsymbol{\alpha})\right]\right\}_{\boldsymbol{\alpha}^0} = \int_0^{u_{th}} \delta a_1^{(1)}(u)\delta(u)\,du \equiv \sum_{j=1}^{2}\frac{\partial^2 R(\varphi;\mathbf{f})}{\partial f_j \partial f_2}\left(\delta f_j\right). \tag{79}$$

The function $\delta a_1^{(1)}(u)$, as shown in Equation 79, is the component of the second-level variational sensitivity function $\mathbf{v}^{(2)}(2^2;u) \triangleq [v^{(1)}(u),\delta\psi(u),\delta a_1^{(1)}(u),\delta a_2^{(1)}(u)]^{\dagger}$, which is the solution of the 2nd-LVSS comprising Equations 59, 60. The component $\delta a_1^{(1)}(u)$ will be eliminated from the expression of $\{\delta R^{(1)}[2;\mathbf{u}^{(2)}(2^2;u);\mathbf{v}^{(2)}(2^2;u);\mathbf{f}(\boldsymbol{\alpha})]\}_{\boldsymbol{\alpha}^0}$ by following the same procedure as described in Section 4.1.1 to construct a 2nd-LASS, the solution of which will be denoted as $\mathbf{a}^{(2)}(2^2;2;u) \triangleq [a_1^{(2)}(2;u),a_2^{(2)}(2;u),a_3^{(2)}(2;u),a_4^{(2)}(2;u)]^{\dagger} \in \mathcal{H}_2$ and will be used in Equation 79 to eliminate $\delta a_1^{(1)}(u)$. The argument "2" in $\mathbf{a}^{(2)}(2^2;2;u)$ indicates that this second-level adjoint sensitivity function corresponds to the first-order sensitivity of the response with respect to the "*second*" component, $f_2(\boldsymbol{\alpha})$, of the feature function $\mathbf{f}(\boldsymbol{\alpha})$. The 2nd-LASS for the function $\mathbf{a}^{(2)}(2^2;2;u)$ will have the same left side and boundary conditions as obtained in Equations 66, 67, but the right-side of this 2nd-LASS will correspond to the G-differential obtained in Equation 79, which leads to the following 2nd-LASS:

$$\left\{\mathbf{A}^{(2)}[2^2\times 2^2;u;\mathbf{f}]\mathbf{a}^{(2)}(2^2;2;u)\right\}_{\boldsymbol{\alpha}^0} = \left\{\mathbf{s}^{(2)}(2^2;2;u;\mathbf{f})\right\}_{\boldsymbol{\alpha}^0}, \tag{80}$$

$$\left\{\mathbf{b}_A^{(2)}(u;\mathbf{f})\right\}_{\boldsymbol{\alpha}^0} = \mathbf{0}, \tag{81}$$

where

$$\mathbf{s}^{(2)}(2^2;1;u;\mathbf{f}) \triangleq [0,0,\delta(u),0]^{\dagger}. \tag{82}$$

The alternative expression for the G-differential $\{\delta R^{(1)}[2;\mathbf{u}^{(2)}(2^2;u);\mathbf{v}^{(2)}(2^2;u);\mathbf{f}(\boldsymbol{\alpha})]\}_{\boldsymbol{\alpha}^0}$ in terms of the components of $\mathbf{a}^{(2)}(2^2;2;u)$ has the same formal expression as shown in Equation 70 but with the components of the function $\mathbf{a}^{(2)}(2^2;1;u)$ being replaced by the components of $\mathbf{a}^{(2)}(2^2;2;u)$, i.e.,:

$$\begin{aligned}\delta(\partial R_c/\partial f_2) = &\int_0^{u_{th}} a_1^{(2)}(2;u)\left[(\delta f_2)\delta(u) - (\delta f_1)\varphi(u)\right]du \\ &+ \int_0^{u_{th}} a_2^{(2)}(2;u)\left[-(\delta f_1)\psi(u)\right]du \\ &+ \int_0^{u_{th}} a_3^{(2)}(2;u)\left[-(\delta f_1)a_1^{(1)}(u)\right]du \\ &+ \int_0^{u_{th}} a_4^{(2)}(2;u)\left[-(\delta f_1)a_2^{(1)}(u)\right]du.\end{aligned} \tag{83}$$

Solving the 2nd-LASS represented by Equations 80, 81 yields the following expressions:

$$a_1^{(2)}(2;u) = 0, \tag{84}$$

$$a_2^{(2)}(2;u) = u\exp[-uf_1(\boldsymbol{\alpha})], \tag{85}$$

$$a_3^{(2)}(2;u) = H(u)\exp[-uf_1(\boldsymbol{\alpha})], \tag{86}$$

$$a_4^{(2)}(2;u) = 0\,. \tag{87}$$

Identifying in Equation 83 the expressions that multiply the respective variations δf_i, $i = 1,2$, in the components of the feature function $\mathbf{f}(\boldsymbol{\alpha})$ and using the closed-form expressions obtained in Equations 84–87, 26, 51 yield the following closed-form explicit expressions for the respective second-order sensitivities:

$$\begin{aligned}\frac{\partial^2 R_c(\varphi,\psi)}{\partial f_1 \partial f_2} &= -\int_0^{u_{th}} a_2^{(2)}(2;u)\psi(u)\,du - \int_0^{u_{th}} a_3^{(2)}(2;u)\,a_1^{(1)}(u)\,du \\ &= -(u_d)^2\exp[-u_d f_1(\boldsymbol{\alpha})],\end{aligned} \tag{88}$$

$$\frac{\partial R_c(\varphi,\psi)}{\partial f_2 \partial f_2} = 0\,. \tag{89}$$

The correctness of the expressions obtained in Equations 88, 89 can be verified by differentiating accordingly the closed-form expression given in Equation 54.

Notably, due to the symmetry of the mixed second-order sensitivities, the expressions obtained in Equations 88, 72 provide an intrinsic mutual verification mechanism of the accuracy of the computations of the second-level adjoint sensitivity functions $\mathbf{a}^{(2)}(2^2;1;u)$ and $\mathbf{a}^{(2)}(2^2;2;u)$.

4.2 Application of the 2nd-CASAM-L

The starting point for the application of the 2nd-CASAM-L is to determine the G-differential of the *TP* first-order sensitivities represented by Equation 57. For "bookkeeping" purposes, it is convenient to designate these *TP* first-order sensitivities as follows:

$$\begin{aligned}R_c^{(1)}\left[i;\mathbf{u}^{(2)}(2^2;u);\boldsymbol{\alpha}\right] &\triangleq \partial R_c(\varphi,\psi)\big/\partial\alpha_i \\ &= -g_1(i;\boldsymbol{\alpha})\int_0^{u_{th}}\left[a_1^{(1)}(u)\varphi(u) + a_2^{(1)}(u)\psi(u)\right]du \\ &\quad + g_2(i;\boldsymbol{\alpha})\int_0^{u_{th}} a_1^{(1)}(u)\,\delta(u)\,du,\end{aligned} \tag{90}$$

where

$$g_1(i;\boldsymbol{\alpha}) \triangleq \partial f_1/\partial\alpha_i; \quad g_2(i;\boldsymbol{\alpha}) \triangleq \partial f_2/\partial\alpha_i; \quad i = 1,\ldots,TP. \tag{91}$$

The G-differential of the expression in Equation 90 is obtained, by definition, as follows:

$$\begin{aligned}&\{\delta R_c^{(1)}[i;\mathbf{u}^{(2)}(2^2;u);\mathbf{v}^{(2)}(2^2;u);\boldsymbol{\alpha};\delta\boldsymbol{\alpha}]\}_{\boldsymbol{\alpha}^0} \\ &\triangleq -\left\{\int_0^{u_{th}}\left[a_1^{(1)}(u)\varphi(u) + a_2^{(1)}(u)\psi(u)\right]du\left[\tfrac{d}{d\varepsilon}g_1(i;\boldsymbol{\alpha}+\varepsilon\delta\boldsymbol{\alpha})\right]\right\}_{\boldsymbol{\alpha}^0,\varepsilon=0} \\ &\quad -\left\{g_1(i;\boldsymbol{\alpha})\tfrac{d}{d\varepsilon}\int_0^{u_{th}}\left[\left[a_1^{(1)}(u) + \varepsilon\delta a_1^{(1)}(u)\right]\left[\varphi(u) + \varepsilon v^{(1)}(u)\right]\right]du\right\}_{\boldsymbol{\alpha}^0,\varepsilon=0} \\ &\quad -\left\{g_1(i;\boldsymbol{\alpha})\tfrac{d}{d\varepsilon}\int_0^{u_{th}}\left[a_2^{(1)}(u) + \varepsilon\delta a_2^{(1)}(u)\right]\left[\psi(u) + \varepsilon\delta\psi(u)\right]du\right\}_{\boldsymbol{\alpha}^0,\varepsilon=0} \\ &\quad +\left\{\int_0^{u_{th}} a_1^{(1)}(u)\,\delta(u)\,du\left[\tfrac{d}{d\varepsilon}g_2(i;\boldsymbol{\alpha}+\varepsilon\delta\boldsymbol{\alpha})\right]\right\}_{\boldsymbol{\alpha}^0,\varepsilon=0} \\ &\quad +\left\{g_2(i;\boldsymbol{\alpha})\tfrac{d}{d\varepsilon}\int_0^{u_{th}}\left[a_1^{(1)}(u) + \varepsilon\delta a_1^{(1)}(u)\right]\delta(u)\,du\right\}_{\boldsymbol{\alpha}^0,\varepsilon=0} \\ &\triangleq \{\delta R_c^{(1)}[i;\mathbf{u}^{(2)}(2^2;u);\mathbf{v}^{(2)}(2^2;u);\boldsymbol{\alpha}]\}_{ind} + \{\delta R_c^{(1)}[i;\mathbf{u}^{(2)}(2^2;u);\boldsymbol{\alpha};\delta\boldsymbol{\alpha}]\}_{dir},\end{aligned} \tag{92}$$

where the direct-effect and indirect-effect terms are defined, respectively, as follows:

$$\begin{aligned}&\{\delta R_c^{(1)}[i;\mathbf{u}^{(2)}(2^2;u);\boldsymbol{\alpha};\delta\boldsymbol{\alpha}]\}_{dir}\\&\quad\triangleq\left\{\left[\sum_{j=1}^{TP}\frac{\partial g_2(i;\boldsymbol{\alpha})}{\partial\alpha_j}\delta\alpha_j\right]\int_0^{u_{th}}a_1^{(1)}(u)\,\delta(u)\,du\right\}_{\boldsymbol{\alpha}^0}\\&\quad-\left\{\left[\sum_{j=1}^{TP}\frac{\partial g_1(i;\boldsymbol{\alpha})}{\partial\alpha_j}\delta\alpha_j\right]\int_0^{u_{th}}\left[a_1^{(1)}(u)\varphi(u)+a_2^{(1)}(u)\psi(u)\right]du\right\}_{\boldsymbol{\alpha}^0},\end{aligned}\tag{93}$$

$$\begin{aligned}&\left\{\delta R_c^{(1)}\left[i;\mathbf{u}^{(2)}(2^2;u);\mathbf{v}^{(2)}(2^2;u);\boldsymbol{\alpha}\right]\right\}_{ind}\\&\quad\triangleq\left\{g_2(i;\boldsymbol{\alpha})\int_0^{u_{th}}\delta a_1^{(1)}(u)\,\delta(u)\,du\right\}_{\boldsymbol{\alpha}^0}\\&\qquad-\left\{g_1(i;\boldsymbol{\alpha})\int_0^{u_{th}}\left[a_1^{(1)}(u)v^{(1)}(u)+\varphi(u)\delta a_1^{(1)}(u)\right]du\right\}_{\boldsymbol{\alpha}^0}\\&\qquad-\left\{g_1(i;\boldsymbol{\alpha})\int_0^{u_{th}}\left[a_2^{(1)}(u)\delta\psi(u)+\psi(u)\delta a_2^{(1)}(u)\right]du\right\}_{\boldsymbol{\alpha}^0}.\end{aligned}\tag{94}$$

The direct-effect term can be evaluated/computed already at this stage. On the other hand, the indirect-effect depends on the second-level variational function $\mathbf{v}^{(2)}(2^2;u)\triangleq[v^{(1)}(u),\delta\psi(u),\delta a_1^{(1)}(u),\delta a_2^{(1)}(u)]^{\dagger}$, which is the solution of the counterpart of 2nd-LVSS defined by Equations 59, 60, with the same boundary conditions and right-side but with distinct source terms, each source term involving the quantities $\partial g_1(i;\boldsymbol{\alpha})/\partial\alpha_j$ and $\partial g_2(i;\boldsymbol{\alpha})/\partial\alpha_j$ for $i,j=1,\dots,TP$. If this path were chosen to compute the second-order sensitivities, the 2nd-LVSS would need to be solved TP^2 times, with TP^2 different sources on the respective right sides, albeit with the same left side and boundary conditions.

The components $v^{(1)}(u),\delta\psi(u),\delta a_1^{(1)}(u),\delta a_2^{(1)}(u)$ are eliminated from the expression of the indirect-effect term $\{\delta R_c^{(1)}[i;\mathbf{u}^{(2)}(2^2;u);\mathbf{v}^{(2)}(2^2;u);\boldsymbol{\alpha}]\}_{ind}$ defined in Equation 94 by constructing a corresponding 2nd-LASS in the Hilbert space H_2 by following the same sequence of steps as described in Section 4.1. The formal expression of the 2nd-LASS thus obtained will have the same left side and boundary conditions as those described in Section 4.1, but the right side of this formal 2nd-LASS will have a source term that will correspond to the indirect-effect term defined in Equation 94 and, hence, will be different for each $i=1,\dots,TP$, i.e.,

$$\{\mathbf{A}^{(2)}[2^2\times 2^2;u;\boldsymbol{\alpha}]\mathbf{a}^{(2)}(2^2;i;2;u)\}_{\boldsymbol{\alpha}^0}=\{\mathbf{s}^{(2)}(2^2;i;u;\boldsymbol{\alpha})\}_{\boldsymbol{\alpha}^0},\quad i=1,\dots,TP;\tag{95}$$

$$\left\{\mathbf{b}_A^{(2)}(u;\boldsymbol{\alpha})\right\}_{\boldsymbol{\alpha}^0}=\mathbf{0};\quad i=1,\dots,TP;\tag{96}$$

where

$$\begin{aligned}\mathbf{s}^{(2)}(2^2;i;u;\boldsymbol{\alpha})\triangleq\Big[&-g_1(i;\boldsymbol{\alpha})a_1^{(1)},-g_1(i;\boldsymbol{\alpha})a_2^{(1)},\\&g_2(i;\boldsymbol{\alpha})\delta(u)-g_1(i;\boldsymbol{\alpha})\varphi,-g_1(i;\boldsymbol{\alpha})\psi\Big]^{\dagger}.\end{aligned}\tag{97}$$

In terms of the solution $\mathbf{a}^{(2)}(2^2;i;2;u)$ of the 2nd-LASS represented by Equations 95, 96, the indirect-effect term $\{\delta R_c^{(1)}[i;\mathbf{u}^{(2)}(2^2;u);\mathbf{v}^{(2)}(2^2;u);\boldsymbol{\alpha}]\}_{ind}$ defined in Equation 94 will have a representation that will formally resemble the expressions provided in Section 4.1, e.g., Equation 83, but with the second-level adjoint function(s) from Section 4.1 being replaced by the second-level adjoint sensitivity function $\mathbf{a}^{(2)}(2^2;i;2;u)$. Finally, the total G-differential $\{\delta R_c^{(1)}[i;\mathbf{u}^{(2)}(2^2;u);\mathbf{v}^{(2)}(2^2;u);\boldsymbol{\alpha};\delta\boldsymbol{\alpha}]\}_{\boldsymbol{\alpha}^0}$ will be obtained, as shown in Equation 92, by adding the expression of the indirect-effect term obtained in terms of the second-level adjoint sensitivity function $\mathbf{a}^{(2)}(2^2;i;2;u)$ and the expression of the direct-effect term provided in Equation 93. The expression of the individual second-order sensitivities $\partial^2R_c(\varphi,\psi)/\partial\alpha_i\partial\alpha_j$, $i,j=1,\dots,TP$ will subsequently be obtained by identifying in the final expression of the total G-differential $\{\delta R_c^{(1)}[i;\mathbf{u}^{(2)}(2^2;u);\mathbf{v}^{(2)}(2^2;u);\boldsymbol{\alpha};\delta\boldsymbol{\alpha}]\}_{\boldsymbol{\alpha}^0}$ those terms that multiply the parameter variations $\partial\alpha_j$, $j=1,\dots,TP$.

4.2.1 Comparing the 2nd-FASAM-L *versus* the 2nd-CASAM-L

The computational savings provided by using, whenever possible, the 2nd-FASAM-L rather than the 2nd-CASAM-L are evident by comparing the results obtained in Section 4.1 *versus* the results obtained in Section 4.2. The feature function $\mathbf{f}(\boldsymbol{\alpha})$ comprises two components $f_i(\boldsymbol{\alpha})$, $i=1,2$; consequently, the 2nd-FASAM-L requires two large-scale computations (to solve the corresponding 2nd-LASS) to obtain the second-order response sensitivities with respect to the components of the feature function. Subsequently, the second-order response sensitivities with respect to the primary model parameters are obtained analytically using the chain-rule of differentiation.

In contradistinction, there is $TP\triangleq 3M+10$, where the number (M) of materials in the medium can easily exceed two dozen primary model parameters. Consequently, the 2nd-CASAM-L requires TP large-scale computations (to solve the corresponding 2nd-LASS) to obtain the second-order response sensitivities with respect to the primary model parameters. The boundary conditions and the operators on the left sides for all of the 2nd-LASS, for both the 2nd-FASAM-L and 2nd-CASAM-L, are the same; only the source terms on the left sides of these 2nd-LASS differ from each other. It is therefore computationally advantageous if the inverse operators of the left sides of these 2nd-LASS could be computed just once and stored for subsequent use, in which case the computational advantage of using the 2nd-FASAM-L would not be massive. Such a procedure could be feasible for relatively small models but would be impractical for large-scale problems, for which the advantage of using the 2nd-FASAM-L rather than the 2nd-CASAM-L increases as the number of model parameters increases.

5 Third-order adjoint sensitivity analysis of the contributon flux to the slowing-down model's features and parameters

The 3rd-FASAM-L determines the third-order sensitivities by applying the principles of the 1st-FASAM to the second-order sensitivities, i.e., considering that the third-order sensitivities are "the first-order sensitivities of the second-order sensitivities." The unmixed second-order sensitivity $\partial^2R_c(\varphi,\psi)/\partial f_2\partial f_2$ is identically zero. The two non-zero second-order sensitivities of the model response with respect to the components of the feature function $\mathbf{f}(\boldsymbol{\alpha})$ are as follows: (i) the unmixed second-order sensitivity $\partial^2R_c(\varphi,\psi)/\partial f_1\partial f_1$, expressed in Equation 71, and (ii) the mixed second-order sensitivity $\partial^2 R_c(\varphi,\psi)/\partial f_1\partial f_2 = \partial^2 R_c(\varphi,\psi)/\partial f_2\partial f_1$, expressed in either Equation 72 or Equation 88, which are equivalent, in view of the symmetry property of the mixed second-order sensitivities. Therefore, either the expression obtained in Equation 88 or Equation 72 can be used as the starting point for obtaining the third-order sensitivities stemming from this mixed second-order sensitivity. It appears that the expression provided in Equation 72 is the simpler of the two, so it will be used as the starting point for obtaining the corresponding third-order sensitivities.

The second-order sensitivity $\partial^2 R_c(\varphi,\psi)/\partial f_1\partial f_1$ expressed in Equation 71 depends on the components of the third-level forward/adjoint function, denoted as $\mathbf{u}^{(3)}(2^3;1;1;u) = [\mathbf{u}^{(2)}(2^2;u), \mathbf{a}^{(2)}(2^2;1;u)]^\dagger$, which is the solution of the third-level forward/adjoint system (3rd-LFAS) obtained by concatenating the 2nd-LFAS with the 2nd-LASS, thus comprising Equations 12, 13, 20, 21, 43, 44, 66 and 67. The argument "1;1" of $\mathbf{u}^{(3)}(2^3;1;1;u)$ indicates that this third-level function corresponds to the (unmixed) second-order sensitivity $\partial^2 R_c(\varphi,\psi)/\partial f_1\partial f_1$ of the response with respect to the "first" feature function, f_1. Therefore, the second-order sensitivity $\partial^2 R_c(\varphi,\psi)/\partial f_1\partial f_1$ is denoted as follows: $R^{(2)}[1;1;\mathbf{u}^{(3)};\mathbf{f}(\boldsymbol{\alpha})] \triangleq \partial^2 R_c(\varphi,\psi)/\partial f_1\partial f_1$, where the argument "1;1" indicates that this third-level function corresponds to the (unmixed) second-order sensitivity $\partial^2 R_c(\varphi,\psi)/\partial f_1\partial f_1$ and the arguments of the function $\mathbf{u}^{(3)}(2^3;1;1;u)$ were omitted, for simplicity. Similarly, the mixed second-order sensitivity $\partial^2 R_c(\varphi,\psi)/\partial f_1\partial f_2$ depends on the components of the same function $\mathbf{u}^{(3)}(2^3;1;1;u)$ and will, therefore, be denoted as $R^{(2)}[2;1;\mathbf{u}^{(3)};\mathbf{f}(\boldsymbol{\alpha})] \triangleq \partial^2 R_c(\varphi,\psi)/\partial f_2\partial f_1$, where the argument "2;1" indicates that this second-order sensitivity is with respect to the components (f_2, f_1) of $\mathbf{f}(\boldsymbol{\alpha})$.

5.1 Application of the 3rd-FASAM-L to compute the third-order sensitivities stemming from $\partial^2 R_c(\varphi,\psi)/\partial f_1\partial f_1$

The third-order sensitivities stemming from $R^{(2)}[1;1;\mathbf{u}^{(3)};\mathbf{f}(\boldsymbol{\alpha})] \triangleq \partial^2 R_c(\varphi,\psi)/\partial f_1\partial f_1$ are obtained from the G-differential of Equation 71, which will be denoted as $\{\delta R^{(2)}[1;1;\mathbf{u}^{(3)};\mathbf{v}^{(3)};\mathbf{f}(\boldsymbol{\alpha})]\}_{\boldsymbol{\alpha}^0} \triangleq \left\{\delta[\partial^2 R_c(\varphi,\psi)/\partial f_1\partial f_1]\right\}_{\boldsymbol{\alpha}^0}$, and they are, by definition, determined as follows:

$$
\begin{aligned}
&\{\delta R^{(2)}[1;1;\mathbf{u}^{(3)};\mathbf{v}^{(3)};\mathbf{f}(\boldsymbol{\alpha})]\}_{\boldsymbol{\alpha}^0} \\
&\triangleq -\left\{\frac{d}{d\varepsilon}\int_0^{u_{th}}\left[a_1^{(2)}(1;u)+\varepsilon\delta a_1^{(2)}(1;u)\right]\left[\varphi(u)+\varepsilon v^{(1)}(u)\right]du\right\}_{\boldsymbol{\alpha}^0,\varepsilon=0} \\
&\quad-\left\{\frac{d}{d\varepsilon}\int_0^{u_{th}}\left[a_2^{(2)}(1;u)+\varepsilon\delta a_2^{(2)}(1;u)\right]\left[\psi(u)+\varepsilon\delta\psi(u)\right]du\right\}_{\boldsymbol{\alpha}^0,\varepsilon=0} \\
&\quad-\left\{\frac{d}{d\varepsilon}\int_0^{u_{th}}\left[a_3^{(2)}(1;u)+\varepsilon\delta a_3^{(2)}(1;u)\right]\left[a_1^{(1)}(u)+\varepsilon\delta a_1^{(1)}(u)\right]du\right\}_{\boldsymbol{\alpha}^0,\varepsilon=0} \\
&\quad-\left\{\frac{d}{d\varepsilon}\int_0^{u_{th}}\left[a_4^{(2)}(1;u)+\varepsilon\delta a_4^{(2)}(1;u)\right]\left[a_2^{(1)}(u)+\varepsilon\delta a_2^{(1)}(u)\right]du\right\}_{\boldsymbol{\alpha}^0,\varepsilon=0}.
\end{aligned}
\tag{98}
$$

Performing the differentiation with respect to ε in Equation 98 and setting $\varepsilon = 0$ in the resulting expression yield

$$
\begin{aligned}
&\{\delta R^{(2)}[1;1;\mathbf{u}^{(3)};\mathbf{v}^{(3)};\mathbf{f}(\boldsymbol{\alpha})]\}_{\boldsymbol{\alpha}^0} \\
&= -\left\{\int_0^{u_{th}}\left[a_1^{(2)}(1;u)v^{(1)}(u)+\varphi(u)\delta a_1^{(2)}(1;u)\right]du\right\}_{\boldsymbol{\alpha}^0} \\
&\quad-\left\{\int_0^{u_{th}}\left[a_2^{(2)}(1;u)\delta\psi(u)+\psi(u)\delta a_2^{(2)}(1;u)\right]du\right\}_{\boldsymbol{\alpha}^0} \\
&\quad-\left\{\int_0^{u_{th}}\left[a_3^{(2)}(1;u)\delta a_1^{(1)}(u)+a_1^{(1)}(u)\delta a_3^{(2)}(1;u)\right]du\right\}_{\boldsymbol{\alpha}^0} \\
&\quad-\left\{\int_0^{u_{th}}\left[a_4^{(2)}(1;u)\delta a_2^{(1)}(u)+a_2^{(1)}(u)\delta a_4^{(2)}(1;u)\right]du\right\}_{\boldsymbol{\alpha}^0}.
\end{aligned}
\tag{99}
$$

The third-level variational function $\mathbf{v}^{(3)} \triangleq \mathbf{v}^{(3)}(2^3;1;1;u) \triangleq [\mathbf{v}^{(2)}(2^2;u), \delta\mathbf{a}^{(2)}(2^2;1;u)]^\dagger$, where $\delta\mathbf{a}^{(2)}(2^2;1;u) \triangleq [\delta a_1^{(2)}(1;u), \delta a_2^{(2)}(1;u), \delta a_3^{(2)}(1;u), \delta a_4^{(2)}(1;u)]^\dagger$, is the solution of the 3rd-LVSS obtained by concatenating the 2nd-LVSS (i.e., Equations 59, 60), with the equations obtained by G-differentiating the 2nd-LASS, represented by Equations 66, 67, for the function $\mathbf{a}^{(2)}(2^2;1;u)$. The resulting 3rd-LVSS for the third-level variational function $\mathbf{v}^{(3)}(2^3;1;1;u)$ comprises the following matrix equation, where the dots are used to denote zero-elements for better visibility of the structure:

$$
\begin{pmatrix}
L & \cdot & \cdot & \cdot & \cdot & \cdot & \cdot & \cdot \\
\cdot & M & \cdot & \cdot & \cdot & \cdot & \cdot & \cdot \\
\cdot & -1 & M & \cdot & \cdot & \cdot & \cdot & \cdot \\
-1 & \cdot & \cdot & L & \cdot & \cdot & \cdot & \cdot \\
\cdot & \cdot & 1 & \cdot & M & \cdot & \cdot & -1 \\
\cdot & \cdot & \cdot & 1 & \cdot & L & -1 & \cdot \\
1 & \cdot & \cdot & \cdot & \cdot & \cdot & L & \cdot \\
\cdot & 1 & \cdot & \cdot & \cdot & \cdot & \cdot & M
\end{pmatrix}
\begin{pmatrix}
v^{(1)}(u) \\ \delta\psi(u) \\ \delta a_1^{(1)}(u) \\ \delta a_2^{(1)}(u) \\ \delta a_1^{(2)}(1;u) \\ \delta a_2^{(2)}(1;u) \\ \delta a_3^{(2)}(1;u) \\ \delta a_4^{(2)}(1;u)
\end{pmatrix}
=
\begin{pmatrix}
(\delta f_2)\delta(u)-(\delta f_1)\varphi(u) \\ -(\delta f_1)\psi(u) \\ -(\delta f_1)a_1^{(1)}(u) \\ -(\delta f_1)a_2^{(1)}(u) \\ -(\delta f_1)a_1^{(2)}(1;u) \\ -(\delta f_1)a_2^{(2)}(1;u) \\ -(\delta f_1)a_3^{(2)}(1;u) \\ -(\delta f_1)a_4^{(2)}(1;u)
\end{pmatrix},
$$

$$
\begin{aligned}
&L(u) \triangleq \frac{d}{du}+f_1(\boldsymbol{\alpha});\quad M(u) \triangleq -\frac{d}{du}+f_1(\boldsymbol{\alpha}); \\
&M(u) = L^*(u);
\end{aligned}
\tag{100}
$$

$$
\begin{aligned}
&v^{(1)}(0)=0;\ \delta\psi(u_{th})=0;\ \delta a_1^{(1)}(u_{th})=0; \\
&\delta a_2^{(1)}(0)=0;\delta a_1^{(2)}(1;u_{th})=0;\ \delta a_2^{(2)}(1;0)=0;\ \delta a_3^{(2)}(1;0)=0; \\
&\delta a_4^{(2)}(1;u_{th})=0.
\end{aligned}
\tag{101}
$$

The 3rd-LVSS comprising Equations 100, 101 can be formally expressed in the following $2^3\times 2^3$-matrix form:

$$
\mathbf{V}^{(3)}[2^3\times 2^3;u;\mathbf{f}]\mathbf{v}^{(3)}(2^3;1;1;u) = \mathbf{q}_V^{(3)}\left[2^3;\mathbf{u}^{(3)}(2^3;u);\mathbf{f};\delta\mathbf{f}\right],
\tag{102}
$$

$$
\mathbf{b}_v^{(3)}\left[\mathbf{v}^{(3)}(2^3;1;1;u)\right] = \mathbf{0}.
\tag{103}
$$

The above matrix form of the 3rd-LVSS will be used as a "condensed notation" to construct the 3rd-LASS, the solution of which will be used to derive the alternative expression for the G-differential $\{\delta R^{(2)}[1;1;\mathbf{u}^{(3)}(2^3;1;1;u);\mathbf{v}^{(3)}(2^3;1;1;u);\mathbf{f}(\boldsymbol{\alpha})]\}_{\boldsymbol{\alpha}^0}$. This 3rd-

LASS will be constructed in a Hilbert space denoted as H_3, comprising as elements eight-component vector-valued functions of the form $\boldsymbol{\chi}^{(3)}(2^3;1;1;u) \triangleq [\chi_1^{(2)}(1;1;u),\ldots,\chi_8^{(2)}(1;1;u)]^\dagger \in \mathcal{H}_3$, and endowed with the following inner product between two vectors $\boldsymbol{\chi}^{(3)}(2^3;1;1;u)$ and $\boldsymbol{\theta}^{(3)}(2^3;1;1;u)$:

$$\langle \boldsymbol{\chi}^{(3)}(2^3;1;1;u), \boldsymbol{\theta}^{(3)}(2^3;1;1;u)\rangle_3 \triangleq \sum_{i=1}^{2^3}\int_0^{u_{th}} \chi_i^{(3)}(1;1;u)\theta_i^{(3)}(1;1;u)\,du. \tag{104}$$

The inner product defined in Equation 104 will be used to construct the inner product of Equation 102 with a function denoted as $\mathbf{a}^{(3)}(2^3;1;1;u) \triangleq [a_1^{(3)}(1;1;u),\ldots,a_8^{(3)}(1;1;u)]^\dagger \in \mathcal{H}_3$, where the argument "1,1" of the function indicates that this (third-level adjoint) function corresponds to the unmixed second-order sensitivity of the response with respect to the "*first*" component, $f_1(\boldsymbol{\alpha})$, of the feature function $\mathbf{f}(\boldsymbol{\alpha})$. Constructing this inner product yields the following relation, where the specification $\{\}_{\boldsymbol{\alpha}^0}$ has been omitted to simplify the notation:

$$\begin{aligned}
&\int_0^{u_{th}} a_1^{(3)}(1;1;u)\left[\frac{d}{du}v^{(1)}(u)+f_1v^{(1)}(u)\right]du \\
&\quad+\int_0^{u_{th}} a_2^{(3)}(1;1;u)\left[-\frac{d}{du}\delta\psi(u)+f_1\delta\psi(u)\right]du \\
&\quad+\int_0^{u_{th}} a_3^{(3)}(1;1;u)\left[-\delta\psi(u)-\frac{d}{du}\delta a_1^{(1)}(u)+f_1\delta a_1^{(1)}(u)\right]du \\
&\quad+\int_0^{u_{th}} a_4^{(3)}(1;1;u)\left[-v^{(1)}(u)+\frac{d}{du}\delta a_2^{(1)}(u)+f_1\delta a_2^{(1)}(u)\right]du \\
&\quad+\int_0^{u_{th}} a_5^{(3)}(1;1;u)\left[-\frac{d}{du}\delta a_1^{(2)}(1;u)+f_1\delta a_1^{(2)}(1;u)-\delta a_4^{(2)}(u)+\delta a_1^{(1)}(u)\right]du \\
&\quad+\int_0^{u_{th}} a_6^{(3)}(1;1;u)\left[\frac{d}{du}\delta a_2^{(2)}(1;u)+f_1\delta a_2^{(2)}(1;u)-\delta a_3^{(2)}(u)+\delta a_2^{(1)}(u)\right]du \\
&\quad+\int_0^{u_{th}} a_7^{(3)}(1;1;u)\left[\frac{d}{du}\delta a_3^{(2)}(1;u)+f_1\delta a_3^{(2)}(1;u)+v^{(1)}(u)\right]du \\
&\quad+\int_0^{u_{th}} a_8^{(3)}(1;1;u)\left[-\frac{d}{du}\delta a_4^{(2)}(1;u)+f_1\delta a_4^{(2)}(1;u)+\delta\psi(u)\right]du \\
&=\int_0^{u_{th}} a_1^{(3)}(1;1;u)[(\delta f_2)\delta(u)-(\delta f_1)\varphi(u)]du \\
&\quad+\int_0^{u_{th}} a_2^{(3)}(1;1;u)[-(\delta f_1)\psi(u)]du \\
&\quad+\int_0^{u_{th}} a_3^{(3)}(1;1;u)\left[-(\delta f_1)a_1^{(1)}(u)\right]du \\
&\quad+\int_0^{u_{th}} a_4^{(3)}(1;1;u)\left[-(\delta f_1)a_2^{(1)}(u)\right]du \\
&\quad+\int_0^{u_{th}} a_5^{(3)}(1;1;u)\left[-(\delta f_1)a_1^{(2)}(1;u)\right]du \\
&\quad+\int_0^{u_{th}} a_6^{(3)}(1;1;u)\left[-(\delta f_1)a_2^{(2)}(1;u)\right]du \\
&\quad+\int_0^{u_{th}} a_7^{(3)}(1;1;u)\left[-(\delta f_1)a_3^{(2)}(1;u)\right]du \\
&\quad+\int_0^{u_{th}} a_8^{(3)}(1;1;u)\left[-(\delta f_1)a_4^{(2)}(1;u)\right]du.
\end{aligned} \tag{105}$$

The component for Equation 105 can be written as follows:

$$\begin{aligned}
&\langle \mathbf{a}^{(3)}(2^3;1;1;u), \mathbf{V}^{(3)}[2^3\times 2^3;u;\mathbf{f}]\mathbf{v}^{(3)}(2^3;1;1;u)\rangle_3 \\
&\quad= \langle \mathbf{a}^{(3)}(2^3;1;1;u), \mathbf{q}_V^{(3)}[2^3;\mathbf{u}^{(3)}(2^3;u);\mathbf{f};\delta\mathbf{f}]\rangle_3.
\end{aligned} \tag{106}$$

The left side of Equation 106 is integrated by parts to obtain the relation given below, in which the argument "1;1" has been omitted when writing the components $a_i^{(3)}(1;1;u), i=1,\ldots,8$ to simplify the notation:

$$\begin{aligned}
&\int_0^{u_{th}} a_1^{(3)}(u)\left[\frac{d}{du}v^{(1)}(u)+f_1v^{(1)}(u)\right]du+\int_0^{u_{th}} a_2^{(3)}(u)\left[-\frac{d}{du}\delta\psi(u)+f_1\delta\psi(u)\right]du \\
&\quad+\int_0^{u_{th}} a_3^{(3)}(u)\left[-\delta\psi(u)-\frac{d}{du}\delta a_1^{(1)}(u)+f_1\delta a_1^{(1)}(u)\right]du \\
&\quad+\int_0^{u_{th}} a_4^{(3)}(u)\left[-v^{(1)}(u)+\frac{d}{du}\delta a_2^{(1)}(u)+f_1\delta a_2^{(1)}(u)\right]du \\
&\quad+\int_0^{u_{th}} a_5^{(3)}(u)\left[-\frac{d}{du}\delta a_1^{(2)}(1;u)+f_1\delta a_1^{(2)}(1;u)-\delta a_4^{(2)}(u)+\delta a_1^{(1)}(u)\right]du \\
&\quad+\int_0^{u_{th}} a_6^{(3)}(u)\left[\frac{d}{du}\delta a_2^{(2)}(1;u)+f_1\delta a_2^{(2)}(1;u)-\delta a_3^{(2)}(u)+\delta a_2^{(1)}(u)\right]du \\
&\quad+\int_0^{u_{th}} a_7^{(3)}(u)\left[\frac{d}{du}\delta a_3^{(2)}(1;u)+f_1\delta a_3^{(2)}(1;u)+v^{(1)}(u)\right]du \\
&\quad+\int_0^{u_{th}} a_8^{(3)}(u)\left[-\frac{d}{du}\delta a_4^{(2)}(1;u)+f_1\delta a_4^{(2)}(1;u)+\delta\psi(u)\right]du \\
&=a_1^{(3)}(u_{th})v^{(1)}(u_{th})-\,a_1^{(3)}(0)v^{(1)}(0)+\int_0^{u_{th}} v^{(1)}(u)\left[-\frac{d}{du}a_1^{(3)}(u)+f_1a_1^{(3)}(u)\right]du \\
&\quad-a_2^{(3)}(u_{th})\delta\psi(u_{th})+a_2^{(3)}(0)\delta\psi(0)+\int_0^{u_{th}}\delta\psi(u)\left[\frac{d}{du}a_2^{(3)}(u)+f_1a_2^{(3)}(u)\right]du \\
&\quad-a_3^{(3)}(u_{th})\delta a_1^{(1)}(u_{th})+a_3^{(3)}(0)\delta a_1^{(1)}(0)+\int_0^{u_{th}}\delta a_1^{(1)}(u)\left[\frac{d}{du}a_3^{(3)}(u)+f_1a_3^{(3)}(u)\right]du \\
&\quad-\int_0^{u_{th}} a_3^{(3)}(u)\delta\psi(u)\,du-\int_0^{u_{th}} a_4^{(3)}(u)v^{(1)}(u)\,du \\
&\quad+a_4^{(3)}(u_{th})\delta a_2^{(1)}(u_{th})-a_4^{(3)}(0)\delta a_2^{(1)}(0)+\int_0^{u_{th}}\delta a_2^{(1)}(u)\left[-\frac{d}{du}a_4^{(3)}(u)+f_1a_4^{(3)}(u)\right]du \\
&\quad-a_5^{(3)}(u_{th})\delta a_1^{(2)}(1;u_{th})+a_5^{(3)}(0)\delta a_1^{(2)}(1;0)+\int_0^{u_{th}}\delta a_1^{(2)}(1;u)\left[\frac{d}{du}a_5^{(3)}(u)+f_1a_5^{(3)}(u)\right]du \\
&\quad+\int_0^{u_{th}} a_5^{(3)}(u)\left[-\delta a_4^{(2)}(u)+\delta a_1^{(1)}(u)\right]du+a_6^{(3)}(u_{th})\delta a_2^{(2)}(1;u_{th})-a_6^{(3)}(0)\delta a_2^{(2)}(1;0) \\
&\quad+\int_0^{u_{th}}\delta a_2^{(2)}(1;u)\left[\frac{d}{du}a_6^{(3)}(u)+f_1a_6^{(3)}(u)\right]du+\int_0^{u_{th}} a_6^{(3)}(u)\left[-\delta a_3^{(2)}(u)+\delta a_2^{(1)}(u)\right]du \\
&\quad+a_7^{(3)}(u_{th})\delta a_3^{(2)}(1;u_{th})-a_7^{(3)}(0)\delta a_3^{(2)}(1;0)+\int_0^{u_{th}}\delta a_3^{(2)}(1;u)\left[-\frac{d}{du}a_7^{(3)}(u)+f_1a_7^{(3)}(u)\right]du \\
&\quad+\int_0^{u_{th}} a_7^{(3)}(u)v^{(1)}(u)\,du-a_8^{(3)}(u_{th})\delta a_4^{(2)}(1;u_{th})+a_8^{(3)}(0)\delta a_4^{(2)}(1;0) \\
&\quad+\int_0^{u_{th}}\delta a_4^{(2)}(1;u)\left[\frac{d}{du}a_8^{(3)}(u)+f_1a_8^{(3)}(u)\right]du+\int_0^{u_{th}} a_8^{(3)}(1;1;u)\delta\psi(u)\,du.
\end{aligned} \tag{107}$$

The boundary terms that appear in Equation 107 will vanish by using Equation 101 and imposing the following boundary conditions on the components $a_i^{(3)}(1;1;u), i=1,\ldots,8$ of the third-level adjoint sensitivity function $\mathbf{a}^{(3)}(2^3;1;1;u)$:

$$a_1^{(3)}(1;1;u_{th}) = 0;\ a_2^{(3)}(1;1;0) = 0;\quad a_3^{(3)}(1;1;0) = 0;$$
$$a_4^{(3)}(1;1;u_{th}) = 0; a_5^{(3)}(1;1;0) = 0;\ a_6^{(3)}(1;1;u_{th}) = 0; \tag{108}$$
$$a_7^{(3)}(1;1;u_{th}) = 0;\quad a_8^{(3)}(1;1;0) = 0.$$

Equation 107 can be written in matrix form as follows:

$$\begin{aligned}&\langle \mathbf{a}^{(3)}(2^3;1;1;u), \mathbf{V}^{(3)}[2^3 \times 2^3;u;\mathbf{f}]\mathbf{v}^{(3)}(2^3;1;1;u)\rangle_3 \\ &\quad = \langle \mathbf{v}^{(3)}(2^3;1;1;u), \mathbf{A}^{(3)}[2^3 \times 2^3;u;\mathbf{f}]\mathbf{a}^{(3)}(2^3;1;1;u)\rangle_3,\end{aligned} \tag{109}$$

where $\mathbf{A}^{(3)}[2^3 \times 2^3;u;\mathbf{f}] \triangleq \{\mathbf{V}^{(3)}[2^3 \times 2^3;u;\mathbf{f}]\}^*$ denotes the formal adjoint of $\mathbf{V}^{(3)}[2^3 \times 2^3;u;\mathbf{f}]$. The right side of Equation 109 is now required to represent the G-differential $\{\delta R^{(2)}[1;1;\mathbf{u}^{(3)}(2^3;1;1;u);\mathbf{v}^{(3)}(2^3;1;1;u);\mathbf{f}(\boldsymbol{\alpha})]\}_{\boldsymbol{\alpha}^0}$ by imposing the following relation:

$$\mathbf{A}^{(3)}[2^3 \times 2^3;u;\mathbf{f}]\mathbf{a}^{(3)}(2^3;1;1;u) = \mathbf{s}_A^{(3)}(2^3;1;1;\mathbf{f}), \tag{110}$$

where

$$\begin{aligned}\mathbf{s}_A^{(3)}(2^3;1;1;\mathbf{f}) \triangleq \big[&a_1^{(2)}(1;u), a_2^{(2)}(1;u), a_3^{(2)}(1;u), a_4^{(2)} \\ &(1;u); \varphi(u), \psi(u), a_1^{(1)}(u), a_2^{(1)}(u)\big]^\dagger.\end{aligned} \tag{111}$$

The relations provided in Equations 108, 110 constitute the 3rd-LASS for the third-level adjoint sensitivity function $\mathbf{a}^{(3)}(2^3;1;1;u)$. In component form, Equation 110 has the following expression, where the dots are used to denote zero-elements for better visibility of the structure:

$$\begin{pmatrix} M & \cdot & \cdot & -1 & \cdot & \cdot & 1 & \cdot \\ \cdot & L & -1 & \cdot & \cdot & \cdot & \cdot & 1 \\ \cdot & \cdot & L & \cdot & 1 & \cdot & \cdot & \cdot \\ \cdot & \cdot & \cdot & M & \cdot & 1 & \cdot & \cdot \\ \cdot & \cdot & \cdot & \cdot & L & \cdot & \cdot & \cdot \\ \cdot & \cdot & \cdot & \cdot & \cdot & M & \cdot & \cdot \\ \cdot & \cdot & \cdot & \cdot & \cdot & -1 & M & \cdot \\ \cdot & \cdot & \cdot & \cdot & -1 & \cdot & \cdot & L \end{pmatrix} \begin{pmatrix} a_1^{(3)}(1;1;u) \\ a_2^{(3)}(1;1;u) \\ a_3^{(3)}(1;1;u) \\ a_4^{(3)}(1;1;u) \\ a_5^{(3)}(1;1;u) \\ a_6^{(3)}(1;1;u) \\ a_7^{(3)}(1;1;u) \\ a_8^{(3)}(1;1;u) \end{pmatrix} = \begin{pmatrix} -a_1^{(2)}(1;u) \\ -a_2^{(2)}(1;u) \\ -a_3^{(2)}(1;u) \\ -a_4^{(2)}(1;u) \\ -\varphi(u) \\ -\psi(u) \\ -a_1^{(1)}(u) \\ -a_2^{(1)}(u) \end{pmatrix}. \tag{112}$$

Using the relations in Equations 99, 102, 103, 108, 110 yields the following alternative expression for $\{\delta R^{(2)}[1;1;\mathbf{u}^{(3)}(2^3;1;1;u);\mathbf{v}^{(3)}(2^3;1;1;u);\mathbf{f}(\boldsymbol{\alpha})]\}_{\boldsymbol{\alpha}^0}$:

$$\begin{aligned}&\left\{\delta R^{(2)}\left[1;1;\mathbf{u}^{(3)}(2^3;1;1;u);\mathbf{v}^{(3)}(2^3;1;1;u);\mathbf{f}(\boldsymbol{\alpha})\right]\right\}_{\boldsymbol{\alpha}^0} \\ &= \left\{\int_0^{u_{th}} a_1^{(3)}(1;1;u)\left[(\delta f_2)\delta(u) - (\delta f_1)\varphi(u)\right] du\right\}_{\boldsymbol{\alpha}^0} \\ &\quad - \left\{\int_0^{u_{th}} a_2^{(3)}(1;1;u)(\delta f_1)\psi(u)\, du\right\}_{\boldsymbol{\alpha}^0} \\ &\quad - \left\{\int_0^{u_{th}} a_3^{(3)}(1;1;u)(\delta f_1)a_1^{(1)}(u)\, du\right\}_{\boldsymbol{\alpha}^0} \\ &\quad - \left\{\int_0^{u_{th}} a_4^{(3)}(1;1;u)(\delta f_1)a_2^{(1)}(u)\, du\right\}_{\boldsymbol{\alpha}^0} \\ &\quad - \left\{\int_0^{u_{th}} a_5^{(3)}(1;1;u)(\delta f_1)a_1^{(2)}(1;u)\, du\right\}_{\boldsymbol{\alpha}^0} \\ &\quad - \left\{\int_0^{u_{th}} a_6^{(3)}(1;1;u)(\delta f_1)a_2^{(2)}(1;u)\, du\right\}_{\boldsymbol{\alpha}^0} \\ &\quad - \left\{\int_0^{u_{th}} a_7^{(3)}(1;1;u)(\delta f_1)a_3^{(2)}(1;u)\, du\right\}_{\boldsymbol{\alpha}^0} \\ &\quad - \left\{\int_0^{u_{th}} a_8^{(3)}(1;1;u)(\delta f_1)a_4^{(2)}(1;u)\, du\right\}_{\boldsymbol{\alpha}^0}.\end{aligned} \tag{113}$$

The third-order sensitivities stemming from the relation obtained in Equation 113 are the expressions that multiply the respective variations δf_1 and δf_2 and are as follows:

$$\begin{aligned}\partial^3 R_c(\varphi,\psi)\big/\partial f_1 \partial f_1 \partial f_1 = &-\int_0^{u_{th}} a_1^{(3)}(1;1;u)\varphi(u)\, du \\ &-\int_0^{u_{th}} a_2^{(3)}(1;1;u)\psi(u)\, du \\ &-\int_0^{u_{th}} a_3^{(3)}(1;1;u)a_1^{(1)}(u)\, du \\ &-\int_0^{u_{th}} a_4^{(3)}(1;1;u)a_2^{(1)}(u)\, du \\ &-\int_0^{u_{th}} a_5^{(3)}(1;1;u)a_1^{(2)}(1;u)\, du \\ &-\int_0^{u_{th}} a_6^{(3)}(1;1;u)a_2^{(2)}(1;u)\, du \\ &-\int_0^{u_{th}} a_7^{(3)}(1;1;u)a_3^{(2)}(1;u)\, du \\ &-\int_0^{u_{th}} a_8^{(3)}(1;1;u)a_4^{(2)}(1;u)\, du;\end{aligned} \tag{114}$$

$$\partial^3 R_c(\varphi,\psi)\big/\partial f_1 \partial f_1 \partial f_2 = \int_0^{u_{th}} a_1^{(3)}(1;1;u)\delta(u)\, du. \tag{115}$$

The expressions obtained in Equations 114, 115 are to be evaluated at the nominal values of parameters and state functions, but the notation $\{\}_{\boldsymbol{\alpha}^0}$ has been omitted for simplicity.

Solving Equations 112, 108 yields the following expressions for the components of the third-level adjoint sensitivity function $\mathbf{a}^{(3)}(2^3;1;1;u)$:

$$a_1^{(3)}(1;1;u) = (u_d - u)^3 H(u_d - u)\exp\left[(u - u_d)f_1(\boldsymbol{\alpha})\right], \tag{116}$$
$$a_2^{(3)}(1;1;u) = f_2(\boldsymbol{\alpha})u^3 \exp[-u f_1(\boldsymbol{\alpha})], \tag{117}$$
$$a_3^{(3)}(1;1;u) = f_2(\boldsymbol{\alpha})u^2 \exp[-u f_1(\boldsymbol{\alpha})], \tag{118}$$
$$a_4^{(3)}(1;1;u) = (u_d - u)^2 H(u_d - u)\exp\left[(u - u_d)f_1(\boldsymbol{\alpha})\right], \tag{119}$$
$$a_5^{(3)}(1;1;u) = -f_2(\boldsymbol{\alpha})u \exp[-u f_1(\boldsymbol{\alpha})], \tag{120}$$
$$a_6^{(3)}(1;1;u) = -(u_d - u)H(u_d - u)\exp\left[(u - u_d)f_1(\boldsymbol{\alpha})\right], \tag{121}$$
$$a_7^{(3)}(1;1;u) = -(u_d - u)^2 H(u_d - u)\exp\left[(u - u_d)f_1(\boldsymbol{\alpha})\right], \tag{122}$$
$$a_8^{(3)}(1;1;u) = -f_2(\boldsymbol{\alpha})u^2 \exp[-u f_1(\boldsymbol{\alpha})]. \tag{123}$$

Using the expressions obtained in in Equations 132, 133 and performing the respective operations yield the following results:

$$\partial^3 R_c(\varphi,\psi)\big/\partial f_1 \partial f_1 \partial f_1 = -u_d^4 f_2(\boldsymbol{\alpha})\exp[-u_d f_1(\boldsymbol{\alpha})], \tag{124}$$
$$\partial^3 R_c(\varphi,\psi)\big/\partial f_1 \partial f_1 \partial f_2 = u_d^3 \exp[-u_d f_1(\boldsymbol{\alpha})]. \tag{125}$$

5.2 Application of the 3rd-FASAM-L to compute the 3rd-order sensitivities stemming from $\partial^2 R_c(\varphi,\psi)/\partial f_1 \partial f_2 = \partial^2 R_c(\varphi,\psi)/\partial f_2 \partial f_1$

The third-order sensitivities stemming from $R^{(2)}[2;1;\mathbf{u}^{(3)};\mathbf{f}(\boldsymbol{\alpha})] \triangleq \partial^2 R_c(\varphi,\psi)/\partial f_2 \partial f_1$ will be obtained from the G-differential of (Equation 72), which will be denoted as $\{\delta R^{(2)}[2;1;\mathbf{u}^{(3)};\mathbf{v}^{(3)};\mathbf{f}(\boldsymbol{\alpha})]\}_{\boldsymbol{\alpha}^0} \triangleq \{\delta[\partial^2 R_c(\varphi,\psi)/\partial f_2 \partial f_1]\}_{\boldsymbol{\alpha}^0}$, and which is by definition determined as follows:

$$\begin{aligned}\{\delta R^{(2)}[2;1;\mathbf{u}^{(3)};\mathbf{v}^{(3)};\mathbf{f}(\boldsymbol{\alpha})]\}_{\boldsymbol{\alpha}^0} &\triangleq \left\{\delta\left[\partial^2 R_c(\varphi,\psi)\big/\partial f_2 \partial f_1\right]\right\}_{\boldsymbol{\alpha}^0} \\ &\triangleq \left\{\frac{d}{d\varepsilon}\int_0^{u_{th}}\left[a_1^{(2)}(1;u)+\varepsilon\delta a_1^{(2)}(1;u)\right]\delta(u)\,du\right\}_{\boldsymbol{\alpha}^0,\varepsilon=0} \\ &= \int_0^{u_{th}} \delta a_1^{(2)}(1;u)\delta(u)\,du. \end{aligned} \tag{126}$$

The function $\delta a_1^{(2)}(1;u)$ is one of the components of the third-level variational function $\mathbf{v}^{(3)}(2^3;1;1;u)$, which is the solution of the 3rd-LVSS represented by Equations 101, 102. To avoid the need for solving the 3rd-LVSS, the appearance of this function will be eliminated from Equation 126 by deriving an alternative expression for the G-differential $\{\delta R^{(2)}[2;1;\mathbf{u}^{(3)};\mathbf{v}^{(3)};\mathbf{f}(\boldsymbol{\alpha})]\}_{\boldsymbol{\alpha}^0}$ in terms of a third-level adjoint sensitivity function, denoted as $\mathbf{a}^{(3)}(2^3;2;1;u) \triangleq [a_1^{(3)}(2;1;u),...,a_8^{(3)}(2;1;u)]^\dagger \in \mathcal{H}_3$. The argument "2,1" of the function $\mathbf{a}^{(3)}(2^3;2;1;u)$ indicates that this (third-level adjoint) function corresponds to the mixed second-order sensitivity of the response with respect to the "*second and first*" components, (f_2, f_1), of the feature function $\mathbf{f}(\boldsymbol{\alpha})$.

The third-level adjoint sensitivity function $\mathbf{a}^{(3)}(2^3;2;1;u)$ will be the solution of 3rd-LASS to be constructed in the Hilbert space $\mathcal{H}_3$ using Equation 104 to construct the inner product of $\mathbf{a}^{(3)}(2^3;2;1;u)$ with Equation 102. Constructing this inner product yields the following relation, where the specification $\{\}_{\boldsymbol{\alpha}^0}$ has been omitted to simplify the notation:

$$\begin{aligned}&\langle \mathbf{a}^{(3)}(2^3;2;1;u), \mathbf{V}^{(3)}[2^3\times 2^3;u;\mathbf{f}]\mathbf{v}^{(3)}(2^3;1;1;u)\rangle_3 \\ &= \langle \mathbf{a}^{(3)}(2^3;2;1;u), \mathbf{q}_V^{(3)}[2^3;\mathbf{u}^{(3)}(2^3;u);\mathbf{f};\delta\mathbf{f}]\rangle_3.\end{aligned} \tag{127}$$

The left side of Equation 127 is integrated by parts to obtain the following relation:

$$\begin{aligned}&\langle \mathbf{a}^{(3)}(2^3;2;1;u), \mathbf{V}^{(3)}[2^3\times 2^3;u;\mathbf{f}]\mathbf{v}^{(3)}(2^3;1;1;u)\rangle_3 \\ &= \langle \mathbf{v}^{(3)}(2^3;1;1;u), \mathbf{A}^{(3)}[2^3\times 2^3;u;\mathbf{f}]\mathbf{a}^{(3)}(2^3;2;1;u)\rangle_3,\end{aligned} \tag{128}$$

where the following boundary conditions were imposed on the components $a_i^{(3)}(2;1;u)$, $i=1,...,8$, of the third-level adjoint sensitivity function $\mathbf{a}^{(3)}(2^3;2;1;u)$:

$$\begin{aligned}&a_1^{(3)}(2;1;u_{th})=0;\ a_2^{(3)}(2;1;0)=0;\quad a_3^{(3)}(2;1;0)=0;\\ &a_4^{(3)}(2;1;u_{th})=0; a_5^{(3)}(2;1;0)=0;\ a_6^{(3)}(2;1;u_{th})=0;\\ &a_7^{(3)}(2;1;u_{th})=0;\quad a_8^{(3)}(2;1;0)=0.\end{aligned} \tag{129}$$

The right side of Equation 109 is now required to represent the G-differential $\{\delta R^{(2)}[2;1;\mathbf{u}^{(3)}(2^3;1;1;u);\mathbf{v}^{(3)}(2^3;1;1;u);\mathbf{f}(\boldsymbol{\alpha})]\}_{\boldsymbol{\alpha}^0}$ by imposing the following relation:

$$\mathbf{A}^{(3)}[2^3\times 2^3;u;\mathbf{f}]\mathbf{a}^{(3)}(2^3;2;1;u) = \mathbf{s}_A^{(3)}(2^3;2;1;\mathbf{f}) \triangleq [0,0,0,0,0,\delta(u),0,0]^\dagger. \tag{130}$$

The relations provided in Equations 108, 110 constitute the 3rd-LASS for the third-level adjoint sensitivity function $\mathbf{a}^{(3)}(2^3;1;1;u)$. Using the relations in Equations 99, 102, 103, 108, and 110 yields the following alternative expression for $\{\delta R^{(2)}[2;1;\mathbf{u}^{(3)};\mathbf{a}^{(3)}(2^3;2;1;u);\mathbf{f}(\boldsymbol{\alpha})]\}_{\boldsymbol{\alpha}^0}$, in which the function $\mathbf{v}^{(3)}(2^3;1;1;u)$ has been replaced by the function $\mathbf{a}^{(3)}(2^3;2;1;u)$:

$$\begin{aligned}&\left\{\delta R^{(2)}\left[2;1;\mathbf{u}^{(3)}(2^3;1;1;u);\mathbf{a}^{(3)}(2^3;2;1;u);\mathbf{f}(\boldsymbol{\alpha})\right]\right\}_{\boldsymbol{\alpha}^0} \\ &= \left\{\int_0^{u_{th}} a_1^{(3)}(2;1;u)\left[(\delta f_2)\delta(u)-(\delta f_1)\varphi(u)\right]du\right\}_{\boldsymbol{\alpha}^0} \\ &\quad -\left\{\int_0^{u_{th}} a_2^{(3)}(2;1;u)(\delta f_1)\psi(u)\,du\right\}_{\boldsymbol{\alpha}^0} \\ &\quad -\left\{\int_0^{u_{th}} a_3^{(3)}(2;1;u)(\delta f_1)a_1^{(1)}(u)\,du\right\}_{\boldsymbol{\alpha}^0} \\ &\quad -\left\{\int_0^{u_{th}} a_4^{(3)}(2;1;u)(\delta f_1)a_2^{(1)}(u)\,du\right\}_{\boldsymbol{\alpha}^0} \\ &\quad -\left\{\int_0^{u_{th}} a_5^{(3)}(2;1;u)(\delta f_1)a_1^{(2)}(1;u)\,du\right\}_{\boldsymbol{\alpha}^0} \\ &\quad -\left\{\int_0^{u_{th}} a_6^{(3)}(2;1;u)(\delta f_1)a_2^{(2)}(1;u)\,du\right\}_{\boldsymbol{\alpha}^0} \\ &\quad -\left\{\int_0^{u_{th}} a_7^{(3)}(2;1;u)(\delta f_1)a_3^{(2)}(1;u)\,du\right\}_{\boldsymbol{\alpha}^0} \\ &\quad -\left\{\int_0^{u_{th}} a_8^{(3)}(2;1;u)(\delta f_1)a_4^{(2)}(1;u)\,du\right\}_{\boldsymbol{\alpha}^0}.\end{aligned} \tag{131}$$

The third-order sensitivities stemming from the relation obtained in Equation 131 are the expressions that multiply the respective variations δf_1 and δf_2 and are as follows:

$$\begin{aligned}\partial^3 R_c(\varphi,\psi)\big/\partial f_1 \partial f_2 \partial f_1 = &-\int_0^{u_{th}} a_1^{(3)}(2;1;u)\varphi(u)\,du \\ &-\int_0^{u_{th}} a_2^{(3)}(2;1;u)\psi(u)\,du \\ &-\int_0^{u_{th}} a_3^{(3)}(2;1;u)a_1^{(1)}(u)\,du \\ &-\int_0^{u_{th}} a_4^{(3)}(2;1;u)a_2^{(1)}(u)\,du \\ &-\int_0^{u_{th}} a_5^{(3)}(2;1;u)a_1^{(2)}(1;u)\,du \\ &-\int_0^{u_{th}} a_6^{(3)}(2;1;u)a_2^{(2)}(1;u)\,du \\ &-\int_0^{u_{th}} a_7^{(3)}(2;1;u)a_3^{(2)}(1;u)\,du \\ &-\int_0^{u_{th}} a_8^{(3)}(2;1;u)a_4^{(2)}(1;u)\,du;\end{aligned} \tag{132}$$

$$\partial^3 R_c(\varphi,\psi)\big/\partial f_2 \partial f_2 \partial f_1 = \int_0^{u_{th}} a_1^{(3)}(2;1;u)\delta(u)\,du. \tag{133}$$

The expressions obtained in Equations 132, 133 are to be evaluated at the nominal values of parameters and state functions, but the notation $\{\}_{\boldsymbol{\alpha}^0}$ has been omitted for simplicity.

In component form, the 3rd-LASS for the third-level adjoint sensitivity function $\mathbf{a}^{(3)}(2^3;2;1;u)$ has the following expression, where dots are used to denote zero-elements for better visibility of the structure:

$$\begin{pmatrix} M & \cdot & \cdot & -1 & \cdot & \cdot & 1 & \cdot \\ \cdot & L & -1 & \cdot & \cdot & \cdot & \cdot & 1 \\ \cdot & \cdot & L & \cdot & 1 & \cdot & \cdot & \cdot \\ \cdot & \cdot & \cdot & M & \cdot & 1 & \cdot & \cdot \\ \cdot & \cdot & \cdot & \cdot & L & \cdot & \cdot & \cdot \\ \cdot & \cdot & \cdot & \cdot & \cdot & M & \cdot & \cdot \\ \cdot & \cdot & \cdot & \cdot & \cdot & -1 & M & \cdot \\ \cdot & \cdot & \cdot & \cdot & -1 & \cdot & \cdot & L \end{pmatrix} \begin{pmatrix} a_1^{(3)}(2;1;u) \\ a_2^{(3)}(2;1;u) \\ a_3^{(3)}(2;1;u) \\ a_4^{(3)}(2;1;u) \\ a_5^{(3)}(2;1;u) \\ a_6^{(3)}(2;1;u) \\ a_7^{(3)}(2;1;u) \\ a_8^{(3)}(2;1;u) \end{pmatrix} = \begin{pmatrix} 0 \\ 0 \\ 0 \\ 0 \\ \delta(u) \\ 0 \\ 0 \\ 0 \end{pmatrix}. \tag{134}$$

Solving Equation 134 yields the following expressions for the components of the third-level adjoint sensitivity function $\mathbf{a}^{(3)}(2^3;2;1;u)$:

$$\begin{aligned} & a_1^{(3)}(2;1;u) = a_4^{(3)}(2;1;u) = a_6^{(3)}(2;1;u) = a_7^{(3)}(2;1;u) = 0\,; \\ & a_5^{(3)}(2;1;u) = H(u)\exp[-uf_1(\boldsymbol{\alpha})];\, a_2^{(3)}(2;1;u) \\ & \qquad\qquad = -u^2\exp[-uf_1(\boldsymbol{\alpha})]\,; \\ & a_3^{(3)}(2;1;u) = -u\exp[-uf_1(\boldsymbol{\alpha})] = -a_8^{(3)}(2;1;u). \end{aligned} \tag{135}$$

Using the expressions obtained in Equation 135, substituting them into Equations 132, 133 and performing the respective operations yield the following results:

$$\begin{aligned} \partial^3 R_c(\varphi,\psi)\Big/\partial f_1\partial f_2\partial f_1 = & -\int_0^{u_{th}} a_2^{(3)}(2;1;u)\psi(u)\,du \\ & -\int_0^{u_{th}} a_3^{(3)}(2;1;u)a_1^{(1)}(u)\,du - \int_0^{u_{th}} a_5^{(3)}(2;1;u)a_1^{(2)}(1;u)\,du \\ & -\int_0^{u_{th}} a_8^{(3)}(2;1;u)a_4^{(2)}(1;u)\,du \\ & = u_d^3\exp[-u_d f_1(\boldsymbol{\alpha})] \end{aligned} \tag{136}$$

$$\partial^3 R_c(\varphi,\psi)\Big/\partial f_2\partial f_2\partial f_1 = 0. \tag{137}$$

6 Concluding discussion

This work has presented illustrative applications of the "nth-FASAM-L," which has been specifically developed to be the most efficient methodology for computing exact expressions of sensitivities of responses (of such unique linear models) to features of model parameters and, subsequently, to the model parameters themselves. The efficiency of the nth-FASAM-L stems from the maximal reduction of the number of adjoint computations (which are "large-scale" computations) compared to the extant conventional high-order adjoint sensitivity analysis methodology nth-CASAM-L (Cacuci, 2022). The unique characteristics of the nth-FASAM-L have been illustrated in this work using a paradigm model of a "contributon-flux density response" that occurs in the energy distribution of neutrons stemming from a fission source in a homogeneous mixture of materials. This analytically solvable illustrative paradigm model has been used to demonstrate the following general conclusions regarding the characteristics and applicability of the nth-FASAM-L.

(i) Comparing the mathematical framework of the nth-FASAM-L to that of the nth-CASAM-L indicates that the components $f_i(\boldsymbol{\alpha}), i = 1,...,TF$ of the "feature function" $\mathbf{f}(\boldsymbol{\alpha}) \triangleq [f_1(\boldsymbol{\alpha}),...,f_{TF}(\boldsymbol{\alpha})]^\dagger$ play within the nth-FASAM-L the same role as played by the components $\alpha_j, j = 1,...,TP$ of the "vector of primary model parameters" $\boldsymbol{\alpha} \triangleq (\alpha_1,\ldots,\alpha_{TP})^\dagger$ within the framework of the nth-CASAM-L. It is paramount to underscore, at the outset, that the total number of model parameters is always larger (usually by a wide margin) than the total number of components of the feature function $\mathbf{f}(\boldsymbol{\alpha})$, i.e., $TP \gg TF$. The illustrative paradigm model of "neutron slowing down in a homogeneous mixture of materials" presented in this work comprised a feature function with two components (i.e., $TF = 2$) denoted as $f_1(\boldsymbol{\alpha})$ and $f_2(\boldsymbol{\alpha})$, which were, in turn, functions of $TP \triangleq 3M + 10$ imprecisely known model parameters (where M denotes the number of materials and/or isotopes in the mixture, which is of the order of 20–50 in a nuclear reactor, depending on its service in operation).

(ii) For computing the exact expressions of the *first-order* sensitivities of a model response to the uncertain parameters, boundaries, and internal interfaces of the model, both the 1st-FASAM-L and 1st-CASAM-L require a *single* large-scale "adjoint" computation. This "large-scale" computation using either the 1st-FASAM-L or 1st-CASAM-L involves solving the same operator equations and boundary conditions within the respective 1st-LASS; only the sources for the respective 1st-LASS differ from each other. The 1st-FASAM-L enjoys a slight computational advantage since it requires only TF quadratures (one quadrature per component of the feature function), while the 1st-CASAM-L requires TP quadratures (one quadrature per model parameter). For the illustrative "contributon response of the neutron slowing-down" paradigm model, the computation of the first-order response sensitivities with respect to the model parameters required two quadratures using the 1st-FASAM-L, while the 1st-CASAM-L required TP-quadratures. Within the 1st-FASAM-L, the sensitivities with respect to the primary model parameters are obtained by using the first-order sensitivities $\partial R_c/\partial f_1$ and $\partial R_c/\partial f_2$ (with respect to the components of the feature function) in conjunction with the chain rule of differentiation of the exactly known expressions of the components $f_1(\boldsymbol{\alpha})$ and $f_2(\boldsymbol{\alpha})$ in terms of the primary model parameters.

(iii) Both the 2nd-FASAM-L and 2nd-CASAM-L conceptually determine the *second-order* sensitivities by using the fundamental concept that "the second-order sensitivities are the first-order sensitivities of the first-order sensitivities." For computing the exact expressions of the second-order response sensitivities with respect to the primary model's parameters, the fundamental difference between the 2nd-FASAM-L and 2nd-CASAM-L is obtained as follows: the 2nd-FASAM-L requires as many large-scale "adjoint" computations as there are "feature functions of parameters" $f_i(\boldsymbol{\alpha}), i = 1, ..., TF$ (where TF denotes the total number of feature functions) for solving the left side of the 2nd-LASS with TF distinct sources on its right side. In contradistinction, the 2nd-CASAM-L requires TP (where TP denotes the total number of model parameters or non-zero first-order sensitivities) large-scale computations for solving the same left side of the 2nd-LASS but with TP distinct sources. Remarkably, the types of "large-scale" computations are the same in both the 2nd-FASAM-L and 2nd-CASAM-L since they both solve the same operator equations and boundary conditions within the respective 2nd-LASS systems; only the sources for these adjoint systems differ from each other. Since $TF \ll TP$, the 2nd-FASAM-L is considerably more efficient than the 2nd-CASAM-L for computing the exact expressions of the second-order sensitivities of a model response to the uncertain parameters, boundaries, and internal interfaces of the model. For the illustrative contributon-response paradigm model, the computation of the second-order response sensitivities with respect to the model parameters using the 2nd-FASAM-L requires just two large-scale computations, for solving the two 2nd-LASS that correspond to the first-order sensitivities, $\partial R_c/\partial f_1$ and $\partial R_c/\partial f_2$, of the contributon response with respect to the respective components, $f_1(\boldsymbol{\alpha})$ and $f_2(\boldsymbol{\alpha})$, of the model's "feature function" $f(\boldsymbol{\alpha})$. In contradistinction, computing the second-order sensitivities to the model parameters using the 2nd-CASAM-L requires TP large-scale computations, one for solving each of the 2nd-LASS that corresponds to each one of the distinct first-order sensitivities $\partial R_c/\partial \alpha_i$, $i = 1, ..., TP$, of the response with respect to the TP model parameters. Remarkably, only the unmixed second-order sensitivity $\partial^2 R_c(\varphi, \psi)/\partial f_1 \partial f_1$ and the mixed second-order sensitivity $\partial^2 R_c(\varphi, \psi)/\partial f_1 \partial f_2 = \partial^2 R_c(\varphi, \psi)/\partial f_2 \partial f_1$ are non-zero. The unmixed second-order sensitivity is identically zero, i.e., $\partial^2 R_c(\varphi, \psi)/\partial f_2 \partial f_2 \equiv 0$. In contradistinction, computing the second-order sensitivities to the model parameters using the 2nd-CASAM-L requires TP large-scale computations, one for solving each of the 2nd-LASS that corresponds to one of the distinct TP model parameters. None of the second-order sensitivities with respect to the primary model parameters vanish.

(iv) For computing the exact expressions of the *third-order* response sensitivities with respect to the primary model's parameters, the 3rd-FASAM-L requires at most $TF(TF + 1)/2$ large-scale "adjoint" computations for solving the 3rd-LASS with $TF(TF + 1)/2$ distinct sources, while the 3rd-CASAM-L requires at most $TP(TP + 1)/2$ large-scale computations for solving the 3rd-LASS with $TP(TP + 1)/2$ distinct sources. For the illustrative "contributon response of the neutron slowing-down" paradigm model, the computation of the third-order response sensitivities with respect to the model parameters using the 3rd-FASAM-L requires only *two* large-scale computations for solving the two 3rd-LASS that correspond to the respective non-zero second-order sensitivities $\partial^2 R_c(\varphi, \psi)/\partial f_1 \partial f_1$ and $\partial^2 R_c(\varphi, \psi)/\partial f_1 \partial f_2 = \partial^2 R_c(\varphi, \psi)/\partial f_2 \partial f_1$. Only the unmixed third-order sensitivity $\partial^3 R_c(\varphi, \psi)/\partial f_1 \partial f_1 \partial f_1$ and the mixed third-order sensitivity $\partial^3 R_c(\varphi, \psi)/\partial f_1 \partial f_1 \partial f_2$ are non-zero; all other third-order sensitivities vanish identically. In contradistinction, the 3rd-CASAM-L requires all $TP(TP + 1)/2$ large-scale computations for solving the 3rd-LASS since all of the second-order sensitivities with respect to the primary model parameters are non-zero. Furthermore, all of the third-order response sensitivities with respect to the primary model parameters are non-zero.

(v) The same computational count of "large-scale computations" caries over when computing the fourth- and higher-order sensitivities, i.e., the formula for calculating the "number of large-scale adjoint computations" is formally the same for both the nth-FASAM-N (Cacuci, 2024a, 2024b) and nth-CASAM-N (Cacuci, 2023a), but the "variable" in the formula for determining the number of adjoint computations for the nth-FASAM-N is TF (i.e., total number of feature functions), while the counterpart for the formula for determining the number of adjoint computations for the nth-CASAM-N is TP (i.e., total number of model parameters). Since $TF \ll TP$, it follows that the higher the order of computed sensitivities, the more efficient the nth-FASAM-N (Cacuci, 2024a, 2024b) becomes compared to the nth-CASAM-N (Cacuci, 2023a).

(vi) The probability of encountering vanishing sensitivities is much higher when using the nth-FASAM-L than when using the nth-CASAM-L. For the illustrative "contributon response of the neutron slowing-down" paradigm model, it is evident that the only a few of the response sensitivities of fourth order (and higher order) with respect to the components of the feature function $\mathbf{f}(\boldsymbol{\alpha})$ will *not* vanish, and the non-vanishing sensitivities will all involve the component $f_1(\boldsymbol{\alpha})$ of the feature function since this component appears in an exponential, whereas the other component appears just as a multiplicative factor. In contradistinction, none of the higher-order response sensitivities with respect to the primary model parameters will vanish using the 2nd-CASAM-L.

(vii) When a model has no "feature" functions of parameters, but only comprises primary parameters, the nth-FASAM-L becomes identical to the nth-CASAM-L.

(viii) Both the nth-FASAM-L and nth-CASAM-L are formulated in linearly increasing higher-dimensional Hilbert spaces—as opposed to exponentially increasing parameter-dimensional spaces—thus overcoming the limitation of dimensionality in the sensitivity analysis of linear systems. Both the nth-FASAM-L and nth-

CASAM-L are incomparably more efficient and more accurate than any other method (statistical, finite differences, etc.) for computing the exact expressions of response sensitivities (of any order) with respect to the uncertain parameters, boundaries, and internal interfaces of the model.

Data availability statement

The original contributions presented in the study are included in the article/Supplementary Material; further inquiries can be directed to the corresponding author.

Author contributions

DC: conceptualization, data curation, formal analysis, investigation, methodology, project administration, resources, software, supervision, validation, visualization, writing–original draft, and writing–review and editing.

Funding

The author(s) declare that no financial support was received for the research, authorship, and/or publication of this article.

Conflict of interest

The author declares that the research was conducted in the absence of any commercial or financial relationships that could be construed as a potential conflict of interest.

Publisher's note

References

Cacuci, D. G. (2022). "The nth-order comprehensive adjoint sensitivity analysis methodology (nth-CASAM): overcoming the curse of dimensionality in sensitivity and uncertainty analysis," in *Volume I: Linear systems* (Cham, Switzerland: Springer Nature), 362. doi:10.1007/978-3-030-96364-4

Cacuci, D. G. (2023a). "The nth-order comprehensive adjoint sensitivity analysis methodology (nth-CASAM): overcoming the curse of dimensionality in sensitivity and uncertainty analysis," in *Volume III: Nonlinear Systems* (Cham, Switzerland: Springer Nature), 369. doi:10.1007/978-3-031-22757-8

Cacuci, D. G. (2024a). Introducing the nth-order features adjoint sensitivity analysis methodology for nonlinear systems (nth-FASAM-N): I. Mathematical framework. *Am. J. Comput. Math.* 14, 11–42. doi:10.4236/ajcm.2024.141002

Cacuci, D. G. (2024b). Introducing the nth-order features adjoint sensitivity analysis methodology for nonlinear systems (nth-FASAM-N): II. Illustrative example. *Am. J. Comput. Math.* 14, 43–95. doi:10.4236/ajcm.2024.141003

Cacuci, D. G. (2024c). The nth-order features adjoint sensitivity analysis methodology for response-coupled forward/adjoint linear systems (nth-FASAM-L):I. I. Mathematical framework. *Front. Energy Res.* 12, 1417594. doi:10.3389/fenrg.2024.1417594

Cacuci, D. G., and Fang, R. (2023). "The nth-order comprehensive adjoint sensitivity analysis methodology (nth-CASAM): overcoming the curse of dimensionality in sensitivity and uncertainty analysis," in *Application to a large-scale system* (Nature Switzerland, Cham: Springer), 463. doi:10.1007/978-3-031-19635-5

Lamarsh, J. R. (1966). *Introduction to nuclear reactor theory*. Reading MA, USA: Adison-Wesley Publishing Co., 491–492.

Lewins, J. (1965). *IMPORTANCE: the adjoint function*. Oxford, UK: Pergamon Press Ltd.

Meghreblian, R. V., and Holmes, D. K. (1960). *Reactor analysis*. New York, USA: McGraw-Hill.

Stacey, W. M. (1974). *Variational methods in nuclear reactor physics*. New York, USA: Academic Press.

Stacey, W. M. (2001). *Nuclear reactor physics*. New York. USA: John Wiley and Sons.

Valentine, T. E. (2006). "Polyethylene-reflected plutonium metal sphere subcritical noise measurements, SUB-PU-METMIXED-001," in *International handbook of evaluated criticality safety benchmark experiments, NEA/NSC/DOC(95)03/I-ix, organization for economic Co-operation and development (OECD)*. Paris, France: Nuclear Energy Agency.

Williams, M. L., and Engle, W. W. (1977). The concept of spatial channel theory applied to reactor shielding analysis. *Nucl. Sci. Eng.* 62, 92–104. doi:10.13182/nse77-a26941

Wilson, W. B., Perry, R. T., Shores, E. F., Charlton, W. S., Parish, T. A., Estes, G. P., et al. (2002). "SOURCES4C: a code for calculating (α, n), spontaneous fission, and delayed neutron sources and spectra," in *Proceedings of the American nuclear society/radiation protection and shielding division 12th biennial topical meeting* (Santa Fe, NM, USA), 14–18.

frontiers | Frontiers in Energy Research

TYPE Original Research
PUBLISHED 10 October 2024
DOI 10.3389/fenrg.2024.1437115

OPEN ACCESS

EDITED BY
Jiankai Yu,
Massachusetts Institute of Technology,
United States

REVIEWED BY
Wei Li,
Xi'an Jiaotong University, China
Ivo Kljenak,
Institut Jožef Stefan (IJS), Slovenia

*CORRESPONDENCE
Yazhe Lu,
✉ luyz07@foxmail.com
Xu Ran,
✉ peaceran@163.com

RECEIVED 23 May 2024
ACCEPTED 19 September 2024
PUBLISHED 10 October 2024

CITATION
Lu Y, Ran X and Wei Z (2024) Computational fluid dynamics simulations of spray tests in a multicompartment construction with an Eulerian–Lagrangian approach.
Front. Energy Res. 12:1437115.
doi: 10.3389/fenrg.2024.1437115

Computational fluid dynamics simulations of spray tests in a multicompartment construction with an Eulerian–Lagrangian approach

Yazhe Lu*, Xu Ran* and Zonglan Wei

Science and Technology on Reactor System Design Technology Laboratory, Nuclear Power Institute of China, Chengdu, China

This paper is an investigation of the gas mixing and depressurization effects of containment spray on hydrogen risk during a typical severe accident in a light water reactor (LWR). Two spray tests (ST3_0 and ST3_1) were simulated using the OECD/SETH-2 project frame; the tests were performed with different preconditions in two interconnected vessels of the PANDA facility by focusing on the breaking-up of the stratified helium-rich layer and helium transport between the interconnected vessels with and without heat and mass transfer. The computational fluid dynamics simulations were performed using an Eulerian–Lagrangian approach, in which the dispersed droplets were tracked with a Lagrangian framework and the heat and mass transfer model between the droplets and gas were developed through user-defined functions. The simulation results are in reasonable agreement with the test data and reproduce the main phenomena of the spray tests. Although the proposed approach is adequate for addressing similar problems, some discrepancies still exist in the simulations. Based on these discrepancies, some recommendations are suggested to improve the accuracy of the proposed approach.

KEYWORDS

containment spray, depressurization, mixing, Eulerian–Lagrangian approach, computational fluid dynamics simulation

1 Introduction

During a typical severe accident in a light water reactor (LWR), oxidation of the reactor fuel cladding produces a large amount of hydrogen due to long-term coolant loss. In such cases, hydrogen is released through the cladding break and spreads to the entire containment space, mixing with air and steam. This gas mixture is locally flammable or even explosive and may threaten the containment integrity. Thus, multiple phenomena occur within the containment in the event of a severe accident, including the transport of gases (air, steam, and hydrogen), stratification of gases, and condensation of steam.

The containment spray system is an important safety mechanism used in hypothetical severe accidents and has two main functions: preventing containment overpressure and removing radioactive aerosols. Moreover, sprayed water injection can enhance gas mixing; hence, spray activation causes steam condensation (depressurization), spray droplet evaporation, and gas stratification breakup. This makes the post-accident phenomena more complex; the depressurization induced by the spray reduces the partial pressure of

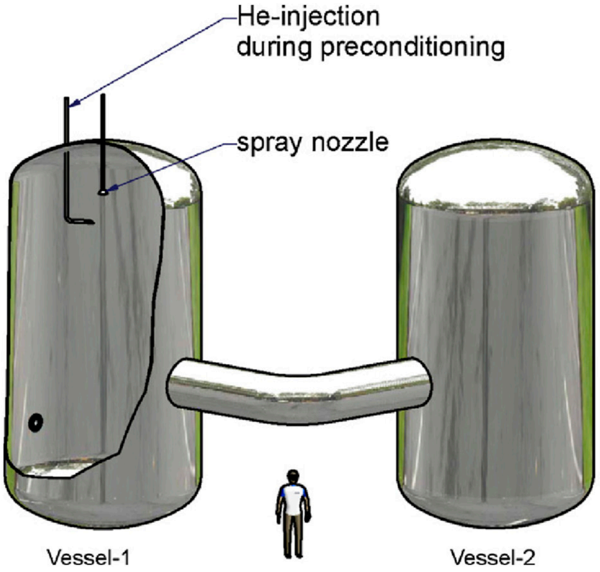

(a) Drywell compartment

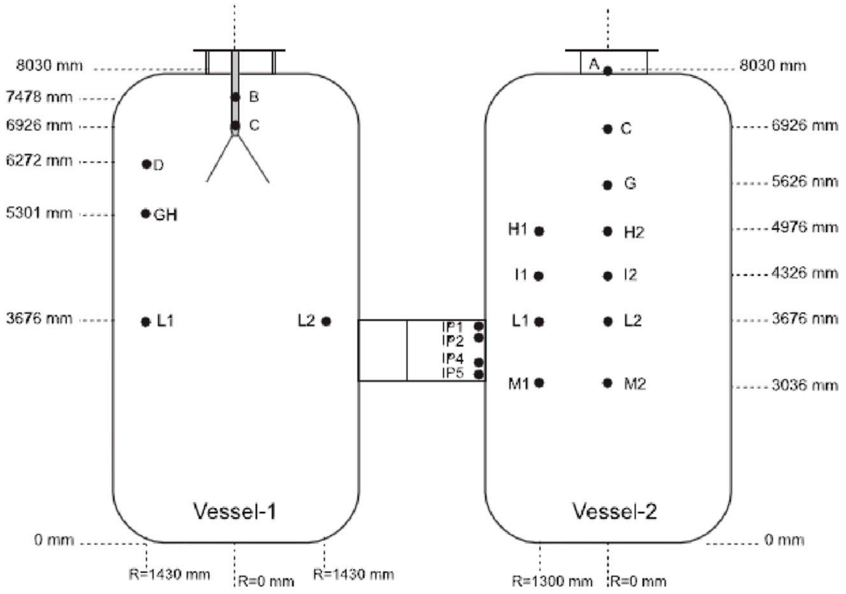

(b) Gas concentration measurement locations

FIGURE 1
PANDA facility: **(A)** drywell compartment and **(B)** gas concentration measurement locations.

steam and enhances the risk of a hydrogen explosion, while the gas stratification break-up suppresses hydrogen accumulation in the head space to reduce the flammability of the gas mixture. Prediction of steam and hydrogen distribution during spray activation is essential for ensuring containment integrity and optimizing the severity of accident mitigation. Numerical analyses of these phenomena caused by the spray require sophisticated analytical tools, such as advanced lumped parameter (LP) and computational fluid dynamics (CFD) codes. Therefore, spray experimental investigations conducted in large-scale facilities are necessary to study these phenomena and provide detailed data for code validation.

In the past, some experimental investigations have been conducted in several test facilities, e.g., TOSQAN (IRSN, France), MISTRA (CEA, France), PANDA (PSI, Switzerland), and SPOT (JSC, Russia). These facilities were characterized by large enclosures (TOSQAN: 7 m^3, MISTRA: 100 m^3, PANDA: 180 m^3, SPOT: 59 m^3) to simulate the typical thermal–hydraulic conditions during an accident in the containment. Furthermore, helium was used to simulate hydrogen in these experiments.

The Severe Accident Research Network (SARNET) spray benchmark (2004–2007) (Wilkening et al., 2008; Babic et al., 2009; Malet et al., 2011) was developed to understand the influences of containment sprays on atmospheric behaviors by

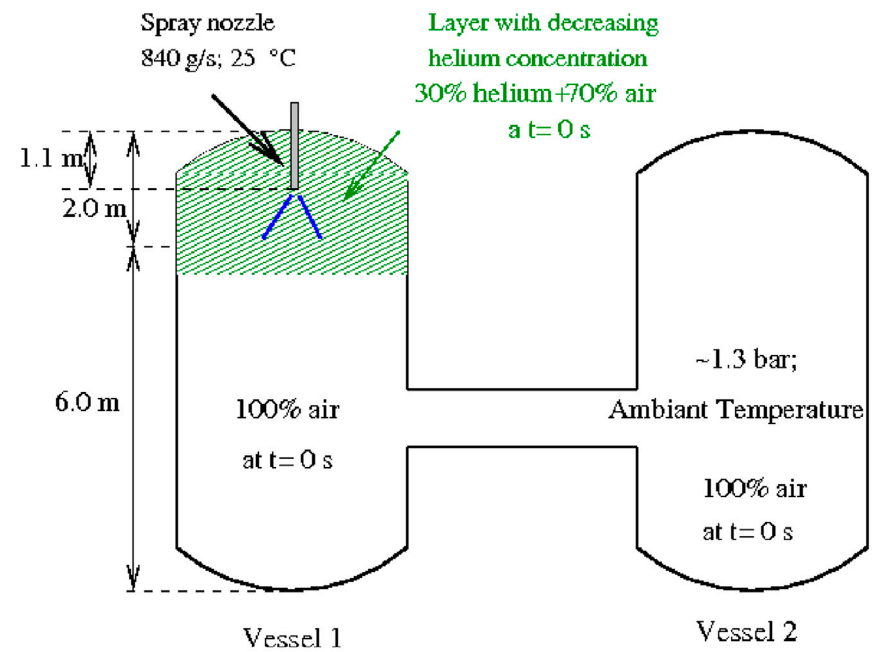

(a) ST3_0

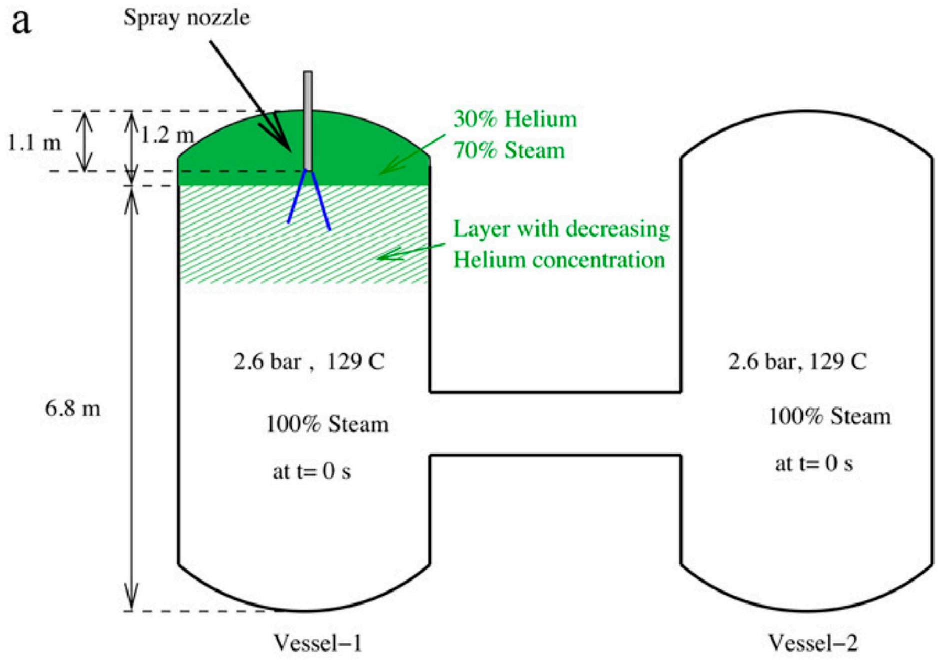

(b) ST3_1

FIGURE 2
Schematic view of the experimental layout and parameters of the **(A)** ST3_0 and **(B)** ST3_1 tests.

using the TOSQAN and MISTRA facilities. The benchmark was divided into two parts as follows: the thermal–hydraulic part concerned with depressurization by the spray (TOSQAN 101 and MISTRA MASPn tests); the dynamic part concerned with light gas stratification break-up by the spray (TOSQAN 113 and MISTRA MARC2b tests) (Malet and Huang, 2015). The spray tests included in the SARNET spray benchmark have been simulated using LP and CFD codes. Comparisons between the simulations and experiments revealed discrepancies in some local domains, such as the spray region and dome above the spray nozzle, despite the good global agreement in terms of pressure, gas temperature, and gas concentration (Malet et al., 2011; Malet et al., 2014). Thus, further investigations are needed to improve the predictability of the spray-related phenomena.

SARNET-2 that was launched in 2009 (Malet et al., 2015a) was the successor to SARNET; under the SARNET-2 framework,

TABLE 1 Test parameters for ST3_0 and ST3_1.

Condition		Test	
		ST3_0	ST3_1
Helium molar fraction in the layer (%)		30	30
Ambient gas component (molar fraction, %)	Air	100	0
	Steam	0	100
Pressure (bar)		1.3	2.6
Temperature (°C)		25	129
Spray flow rate (g/s)		840	840
Spray temperature (°C)		20	40

more detailed investigations have been conducted continually to improve the predictability of the spray-related phenomena. Three benchmarks were included in this framework: 1) heat and mass transfer of a single water droplet; 2) gas entrainment by a real pressurized water reactor spray nozzle; 3) gas entrainment by two real nozzles. CFD simulations accurately predicted the droplet size and velocity below the nozzle but had significant disparities in the gas-phase velocity compared to the corresponding experimental data (Malet et al., 2015a; Malet et al., 2014). In addition, sensitivity analysis showed that the input conditions at the spray boundary, such as the size and velocity distribution of the droplets as well as gas-phase velocity distribution, significantly affected the accuracy of the simulation results.

The OECD/SETH-2 project was launched by OECD/NEA during 2007–2010 (NEA/CSNI/R, 2012); in this project, tests were performed in enclosed facilities involving various conditions like handling light gas stratification as well as erosion of stratification and spray. A series of spray tests were carried out in the MISTRA and PANDA facilities; the MISTRA facility was a multicompartment vessel, and the PANDA facility was composed of two vessels (90 m^3) connected by a pipe. These spray tests differed in their initial conditions for the temperature, pressure, and gas components, and an additional spray test was performed at normal temperature for reference. Mimouni et al. (2013) used the NEPTUNE_CFD code to simulate the reference test and another spray test in which the spray was injected in a typical post-accident condition. For the reference test, the simulation results of helium concentration matched the experimental data very well; for the spray test, the simulated pressure reduction rate was too high while the light gas concentration matched the test data.

The ERCOSAM-SAMARA project was a 4-year research (2010–2014) (Dabbene et al., 2015; Malet et al., 2015b) conducted by the European Union and Russia's nuclear energy agencies; this project investigated the formation of gas stratification under the assumed typical severe accident scenarios and the accident mitigation system steps (sprays, condensers, heaters, etc.) for breaking such gas stratification. Four different volume facilities were utilized (TOSQAN, SPOT, MISTRA, and PANDA) along with the virtual facility HYMIX (3,180 + 3,010 m^3). Tests were performed at these facilities with different volumes and structures to study the impacts of mitigation system activation on gas stratification at various spatial scales to draw general conclusions as well as provide references and inspiration for corresponding research expansion to containment. The tests indicated that the facilities of different scales showed similar phenomena when activating the same mitigation system (Dabbene et al., 2015), with spray being the most effective means of depressurization and atmospheric mixing compared to other mitigation measures. Numerical studies on these tests indicated that the currently available codes have the potential to simulate the thermal–hydraulic conditions of the containment (Malet et al., 2015b); however, optimization approaches are still needed for these simulation methods.

Based on the background and research status, the process of spray-breaking gas stratification in a multicompartment enclosed

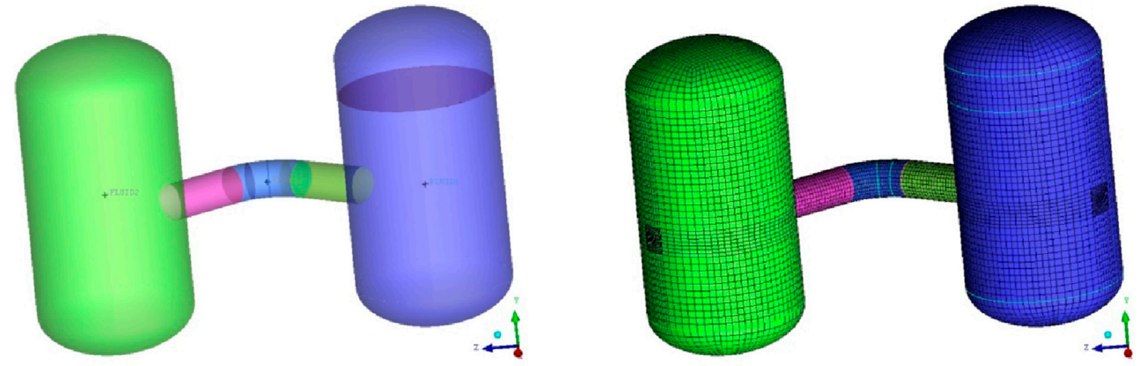
(a) computational domain

(b) computational mesh

FIGURE 3
(A) Computational domain and **(B)** computational mesh of the two-vessel facility.

TABLE 2 Mesh quality comparisons.

	Coarse mesh	Fine mesh
Cell number	228,715	546,738
Node number	234,896	557,060
Minimum orthogonal quality	0.5835	0.5605
Maximum aspect ratio	30.20	36.08

space is studied, and two tests (ST3_0 and ST3_1) conducted in the framework of the OECD/SETH-2 project using the PANDA facility are analyzed in this paper. Here, ST3_0 is the reference test and ST3_1 is the spray test performed under pure hot steam conditions. ANSYS FLUENT v18.0 was chosen as the tool to implement the CFD simulations, and an Eulerian–Lagrangian method was used to simulate the spray droplets by adding models using user-defined functions (UDFs) for some key phenomena during spraying. The following sections describe the spray tests and numerical calculations; then, the simulations are compared with the experiments for the characteristics of the spray phenomena. Finally, some recommendations are provided for more accurate calculations.

2 Description of the spray tests

2.1 Experimental facility

PANDA is a large-scale facility with an overall height of 25 m and a total volume of 515 m^3. It is characterized by multicompartment construction and is equipped with CFD-grade instruments that can be used to investigate various thermal–hydraulic conditions in the LWRs (NEA/CSNI/R, 2012). The spray tests were performed in the drywell compartment of the PANDA facility (Figure 1A); the drywell compartment consists of two vessels (Vessel-1 and Vessel-2), each having a height of 8 m and diameter of 4 m, which are interconnected horizontally by a bent pipe (IP) of 1 m diameter. The spray nozzle is installed in Vessel-1, and its outlet is located 1.1 m from the top of the vessel. The nozzle has an outlet diameter of 6.4 mm, which is oriented vertically downward to produce a conical solid spray with an opening angle of 30°.

There are 261 and 87 K-type thermocouples installed in Vessel-1 and Vessel-2, respectively, for measuring the fluid and wall temperatures. The gas molar fractions are measured using mass spectrometer capillaries located at 59 positions in Vessel-1, 34 positions in Vessel-2, and 15 positions in the IP, as shown in Figure 1B (Erkan et al., 2011).

2.2 Information on the spray tests

Two tests (ST3_0 and ST3_1) were selected for the simulations, and both of them were focused on the spray-erosion of the stratified helium-rich layer at the top of Vessel-1 under different initial conditions. The experimental layout and parameters of the two tests are shown in Figure 2 (Mimouni et al., 2013; Erkan et al., 2011). The test sequence is divided into the preconditioning and spray phases. During the preconditioning phase, a helium-rich layer is formed at the top of Vessel-1; the remaining part of Vessel-1 together with the IP and Vessel-2 was preconditioned with air or steam before being pressurized. Then, in the spray phase, the spraying proceeded at a constant spray flow rate until the end of the test.

For the reference test ST3_0, a helium-rich layer was produced at the top of Vessel-1 while the remaining space was filled with air at room temperature to consider only the hydrodynamic interactions between the droplets and ambient gas. The hot spray test ST3_1 was performed with steam and helium to investigate heat transfer between the spray droplets

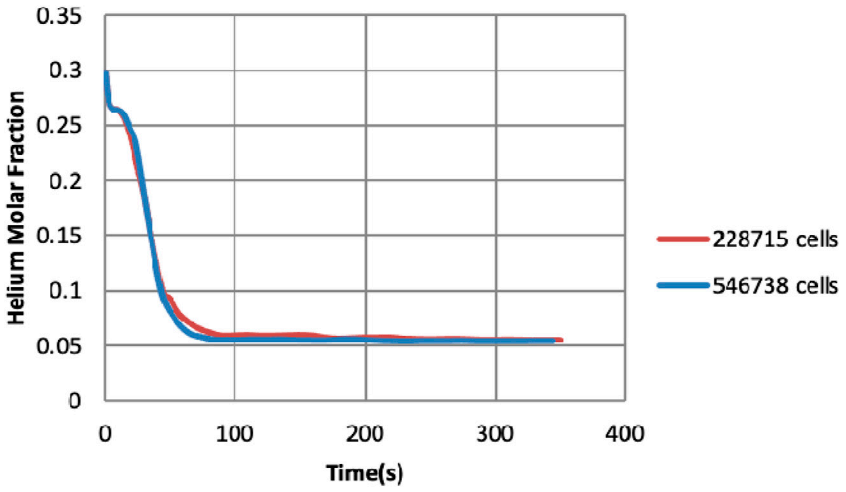

FIGURE 4
Mesh independence test results.

TABLE 3 Positions of the concentration measurement points in the PANDA drywell.

Measurement point	Height (m)	Radial position (m)
Vessel-1 B18	7.478	0.65
Vessel-1 L26	3.676	1.430
Vessel-2 B20	7.478	0

and steam during stratification breakup. Table 1 lists the parameters used for the initial conditions.

3 Numerical calculations

Since the spray droplets occupy a much lower volume fraction than gas during the spray tests, an Eulerian–Lagrangian approach is suitable for simulating the spray process; here, the continuous gas is solved using an Eulerian approach while the dispersed droplets are tracked in a Lagrangian framework. The droplets can exchange mass, momentum, and energy with the gas.

ANSYS Fluent was used for the numerical computations in this paper, and its discrete phase model (DPM) is appropriate for the discrete droplets existing in the fluid field. In particular, the mass and heat transfer models were developed using UDFs, but the interactions between the droplets were neglected.

3.1 Governing equations and physical models

In the DPM, the gas phase was treated as a continuum and solved using the Navier–Stokes equation. Since large numbers of

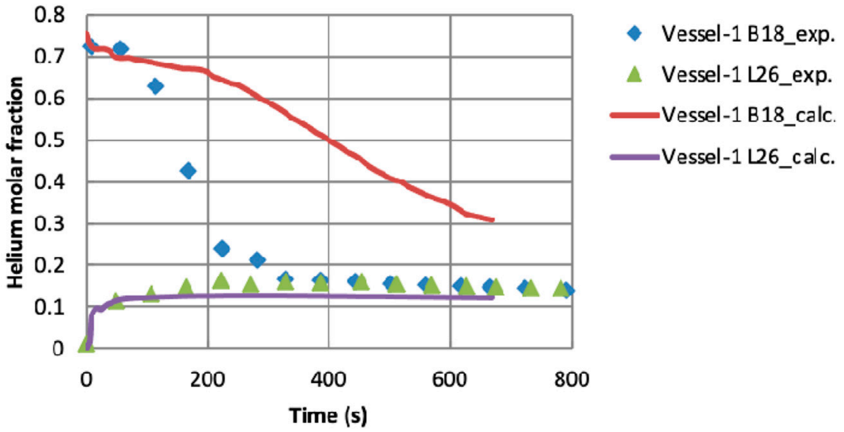

(a) Vessel-1

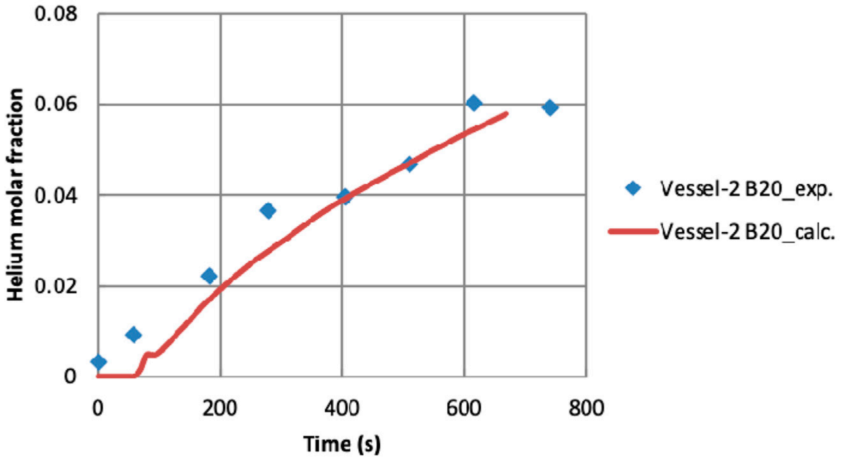

(b) Vessel-2

FIGURE 5
Helium volume fraction time evolutions (PANDA ST3_0 test) in **(A)** Vessel-1 and **(B)** Vessel-2.

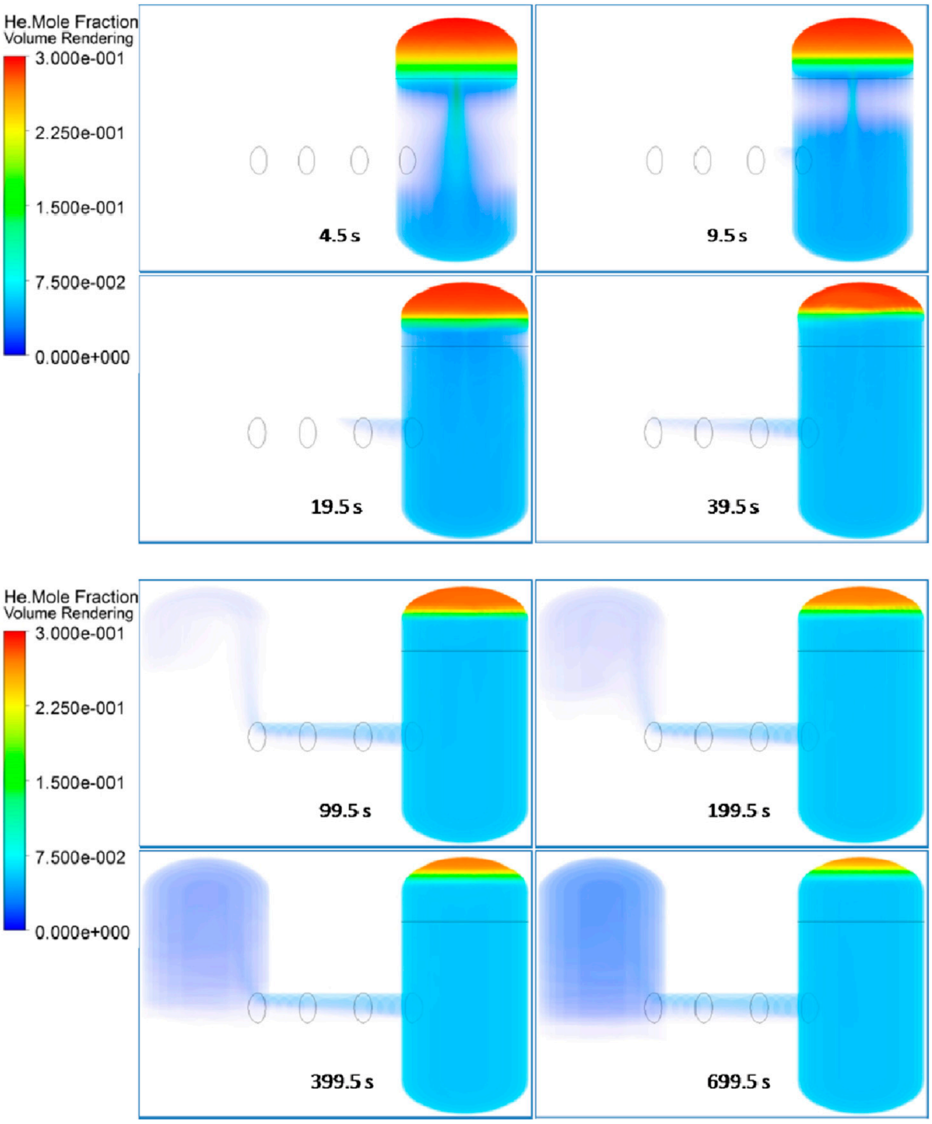

FIGURE 6
Helium molar fractions over time after spray activation (PANDA ST3_0 test, left: Vessel-2; right: Vessel-1).

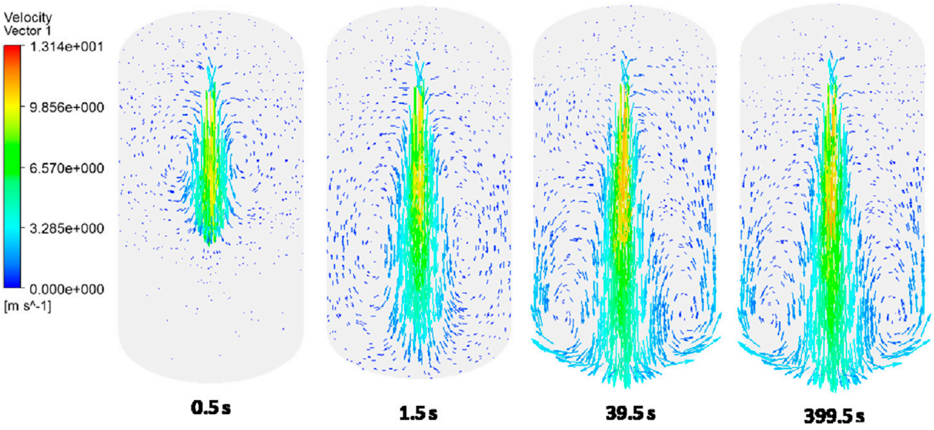

FIGURE 7
Velocity vector field in the vertical section of Vessel-1 (PANDA ST3_0 test).

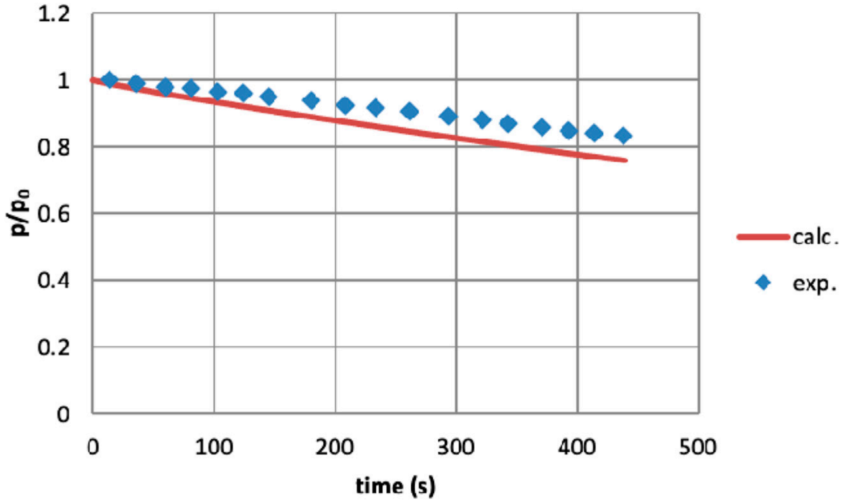

FIGURE 8
Pressure evolution in the vessels (PANDA ST3_1 test).

droplets are injected by the spray, these droplets were divided into a finite number of groups containing droplets of the same sizes, temperatures, and initial velocities to reduce the calculation cost. Then, each group was tracked as a single entity for representation. Equations 2–9 are governing equations of the physical model, which describe mass, momentum and energy conservation.

(1) Momentum equation

$$\frac{d\vec{u}_p}{dt} = \frac{\vec{U}_g - \vec{u}_p}{\tau} + \frac{\vec{g}\left(\rho_p - \rho_g\right)}{\rho_p} + \vec{f}, \tag{1}$$

where $\vec{u}_p$ is the droplet velocity, $\vec{U}_g$ is the gas velocity, ρ_p is the droplet density, ρ_g is the gas density, $\vec{g}$ is the gravitational acceleration, $\vec{f}$ is an additional acceleration term, and $\frac{\vec{U}_g - \vec{u}_p}{\tau}$ is the drag force per unit droplet mass. The droplet relaxation time is

$$\tau = \frac{\rho_p d_p^2}{18\mu_g}\frac{24}{C_D \mathrm{Re}_p}, \tag{2}$$

where d_p is the droplet diameter, μ_g is the molecular viscosity of the gas, and C_D is the drag coefficient. Re_p is the relative Reynolds number defined as

$$\mathrm{Re}_p = \frac{\rho_g d_p \left|\vec{U}_g - \vec{u}_p\right|}{\mu_g}. \tag{3}$$

For the drag coefficient C_D, the spherical drag provided by ANSYS Fluent (ANSYS FLUENT 18, 2016) was used as the drag force acting on the droplets:

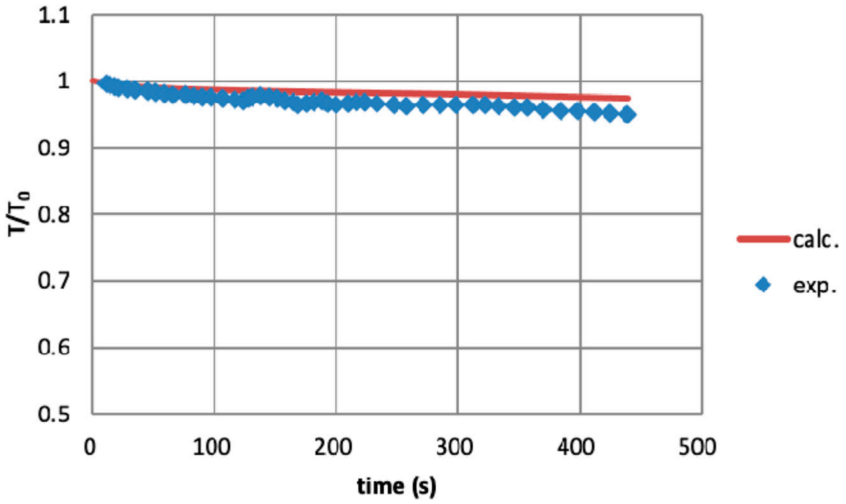

FIGURE 9
Temperature evolution in Vessel-1 (PANDA ST3_1 test).

$$C_D = a_1 + \frac{a_2}{\mathrm{Re}_p} + \frac{a_3}{\mathrm{Re}_p^2}, \tag{4}$$

where a_1, a_2, and a_3 are constants dependent on the Reynolds number; these were defined by Morsi and Alexander (1972) as follows:

$$a_1, a_2, a_3 = \begin{cases} 0, 18, 0 & 0 < \mathrm{Re}_p < 0.1 \\ 3.690, 22.73, 0.0903 & 0.1 \le \mathrm{Re}_p < 1 \\ 1.222, 29.1667, -3.8889 & 1 \le \mathrm{Re}_p < 10 \\ 0.6167, 46.50, -116.67 & 10 \le \mathrm{Re}_p < 100 \\ 0.3644, 98.33, -2778 & 100 \le \mathrm{Re}_p < 1000 \\ 0.357, 148.62, -47500 & 1000 \le \mathrm{Re}_p < 5000 \\ 0.46, -490.546, 578700 & 5000 \le \mathrm{Re}_p < 10000 \\ 0.5190, -1662.5, 5416700 & \mathrm{Re}_p \ge 10000 \end{cases}.$$

In the Lagrangian framework, the droplet position and velocity are updated by integrating the momentum equation (Equation 1) and equation predicting the droplet trajectory:

$$\frac{d\vec{x}_p}{dt} = \vec{u}_p, \tag{5}$$

where x_p is the position of the droplet.

(2) Energy equation

$$m_p c_p \frac{dT_p}{dt} = h_q A_p \left(T_\infty - T_p\right) - \frac{dm_p}{dt} L_{fg}, \tag{6}$$

where c_p is the heat capacity of the droplet, T_p is the droplet temperature, h_q is the convective heat transfer coefficient between the droplet and gas, T_∞ is the temperature of the bulk gas, and L_{fg} is the latent heat.

The convective heat transfer coefficient h_q is related to the Nusselt number as

$$Nu = \frac{h_q d_p}{k_g}, \tag{7}$$

where k_g is the thermal conductivity of the gas phase.

(3) Mass equation

$$\frac{dm_p}{dt} = h_m A_p \left(C_s - C_\infty\right) M_{h2o}, \tag{8}$$

where h_m is the mass transfer coefficient between the droplet and gas, A_p is the surface area of the droplet ($A_p = \pi d_p^2$), C_s is the vapor concentration at the droplet surface, C_∞ is the vapor concentration of the bulk gas, and M_{h2o} is the molar mass of water. The mass transfer coefficient h_m is related to the Sherwood number as

$$Sh = \frac{h_m d_p}{D_{h2o,m}}, \tag{9}$$

where $D_{h2o,m}$ is the diffusion coefficient of vapor in the bulk.

Given the similarity between heat and mass transfer, the Nusselt number Nu and Sherwood number Sh were calculated using the Ranz and Marshall correlations (Sazhin, 2006; Ranz and Marshall, 1952a; Ranz and Marshall, 1952b):

$$Nu = 2 + 0.6\mathrm{Re}_p^{1/2}\mathrm{Pr}_g^{1/3}, \tag{10}$$

$$Sh = 2 + 0.6\mathrm{Re}_p^{1/2}Sc_g^{1/3}. \tag{11}$$

Here, Pr_g is the Prandtl number for the gas phase given by $\mathrm{Pr}_g = \frac{c_{p,g}\mu_g}{k_g}$, and Sc_g is the Schmidt number for the gas phase given by $Sc_g = \frac{\mu_g}{\rho_g D_{h2o,m}}$.

3.2 Computational domain

The fluid domain is the drywell space of the PANDA facility that ignores the internal structures such as the spray nozzle. Figure 3A shows the 3D computational domain; structural meshes were generated using ICEM CFD (Figure 3B) with different numbers of cells. The mesh quality is detailed in Table 2.

3.3 Physical modeling

Using ANSYS Fluent, the turbulence was calculated by the standard k-ε model, and the buoyancy term was included for the transport equation of the rate of dissipation ε. The species transport model describes the mixing and transport of gas components by solving the standard scalar transport equations based on mass fractions. The properties of the gas mixture (steam and helium) were determined using the ideal gas mixing law, while the specific heat and thermal conductivity of each component were calculated using different polynomial laws depending on the gas temperature with the other properties set as constants. The drag force and gravity are considered in (Equation 1). In the DPM, an inert particle was chosen to simulate a droplet, and the mass and heat transfer models for the droplet were embedded in Fluent via UDFs using the Ranz and Marshall correlations in Equations (10, 11). To ensure two-way coupling between the droplets and gas, the corresponding source terms for the gas phase were added separately to the mass, momentum, and energy equations. The droplets were considered to be extracted from the domain as soon as they touched a wall. Neither droplet breakup nor collision was considered in the simulation. Moreover, for the preliminary simulations, collection and evaporation of the spray water in the lower head of Vessel-1 were neglected. For the initial conditions (Table 1), the helium-rich layer was simply set as the region that was 6 m above the bottom of Vessel-1, and the remaining space was considered to be filled with 100% air or steam. The wall condition was set to have a constant temperature that was the same as the initial atmospheric temperature.

4 Simulation results and discussion

4.1 Validation of mesh independence

Based on the ST3_0 test, two meshes (Table 2) were validated for mesh independence. At the C14 measurement point in Vessel-1 (z =

6.926 m, r = 1.430 m), the molar fraction time evolutions of helium calculated from the two meshes are as shown in Figure 4. There was no significant improvement with the mesh containing 546,738 cells; thus, the following results are all based on the mesh comprising 228,715 cells.

4.2 Results for the ST3_0 test

Three measurement points were selected for comparisons with the calculated results and experiment data. These positions are as noted in Table 3. Figure 5 shows the comparison for the time evolution of helium concentration; there is a difference in the comparison at point B18 in Vessel-1, while the simulation results agree well with the test data for the other two measurement points. The reason for this may be the lack of detailed initial data when simulating the ST3_0 test, especially for helium concentration distribution, as its initial conditions were simplified as stepwise changes along the height for calculations (Section 3.3). For the simulation, the initial simplified gas layer has a significant effect on the change in helium concentration.

Figure 6 displays the helium molar fraction distribution over time in the computational domain. As the spray activates, the helium concentration decreases at the top of Vessel-1 because of convection caused by the spray. This process thins the helium-rich layer, resulting in a more homogeneous mixture. Moreover, the difference in concentration causes helium to diffuse into Vessel-2 through the IP. The velocity vector field in Vessel-1 at different moments is shown in Figure 7. It is seen that approximately 40 s after the spray starts, the gas entrainment by the spray becomes strong and develops the flow in Vessel-1. Once the flow develops, stable global circulation is established around the spray zone but the gas is almost stagnant in the space above the nozzle.

4.3 Results for the ST3_1 test

During the ST3_1 test, the spray was injected into hot and pressurized 100% steam. This section discusses the test results for two effects of the spray injection: depressurization and gas mixing.

4.3.1 Depressurization

To analyze the spray effects on the evolutions of the global pressure and average temperature in Vessel-1, these two parameters were normalized using their initial values p_0 and T_0. As shown in Figures 8, 9, both the normalized pressure and temperature decayed with time. Compared with the test data, the simulation results were generally in agreement with the real evolutions; however, the simulations underestimated pressure and overestimated temperature. This is probably because the evaporation of the spray water collected in the lower head of Vessel-1 was neglected.

Figure 10 presents the variations of the calculated temperature contours at the vertical sections of Vessel-1 and Vessel-2. During the ST3_1 test, the hottest point is located at the outlet of the spray nozzle because the droplet density is highest in this domain and steam condensation on the water droplet surface, which is a heat-loss process, heats the surrounding gas. According to temperature contours, in the region away from the spray nozzle in Vessel-1, water droplet evaporation is dominant along with heat absorption, leading to lower temperature. The temperature difference in Vessel-2 causes the cooler gas to settle at the bottom, while the warmer gas collects at the top. With time, the temperature stratification becomes clear in

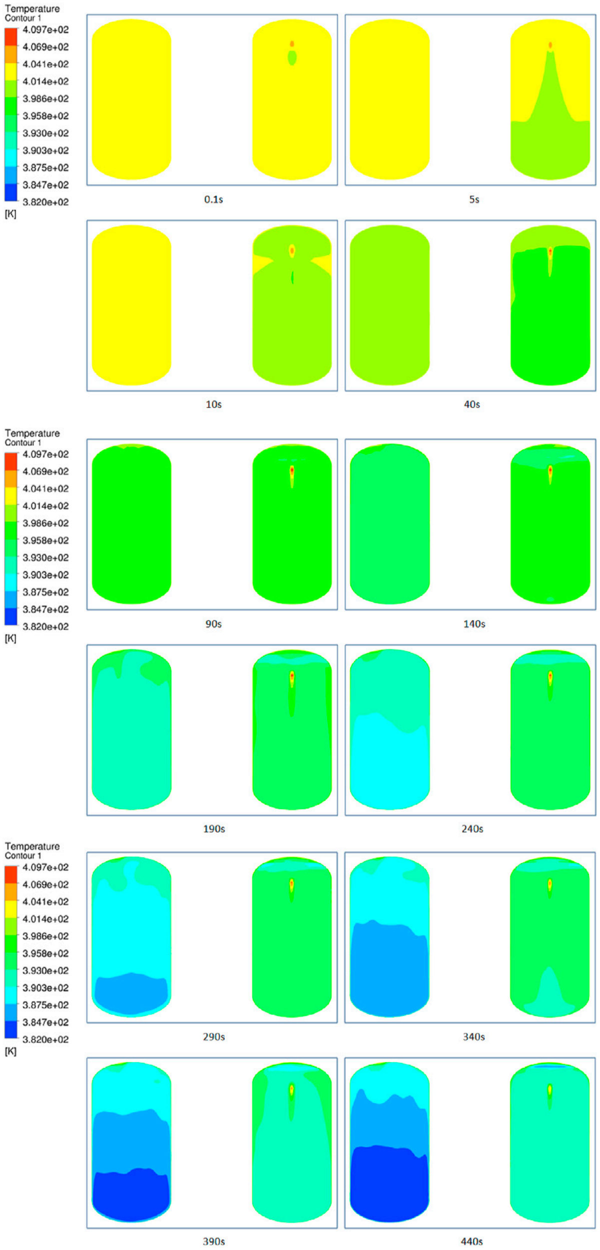

FIGURE 10
Temperature fields in the vertical sections of Vessel-1 and Vessel-2 (PANDA ST3_0 test, left: Vessel-2; right: Vessel-1).

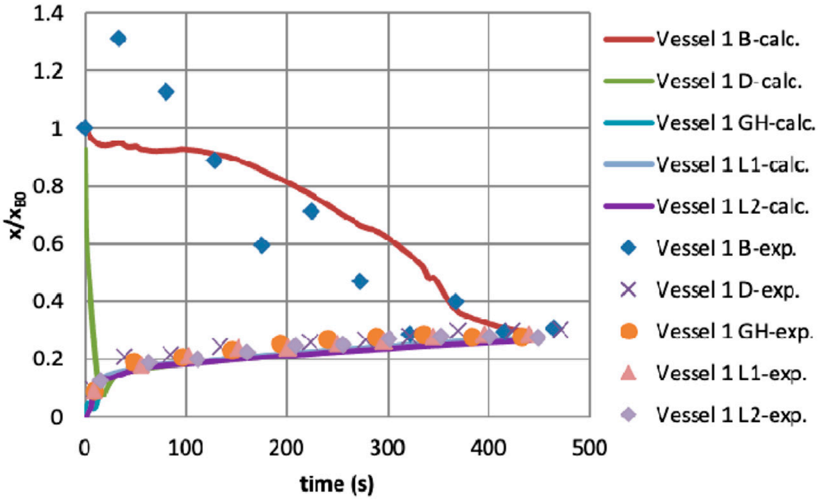

(a) Vessel-1

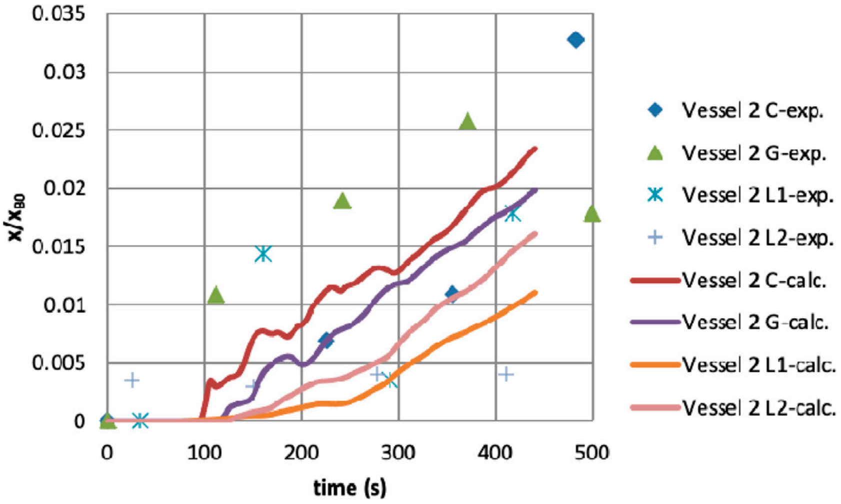

(b) Vessel-2

FIGURE 11
Time-dependent helium molar fractions (PANDA ST3_1 test) in **(A)** Vessel-1 and **(B)** Vessel-2.

Vessel-2, and the average temperature of Vessel-2 is lower than that of Vessel-1.

4.3.2 Gas mixing

Similar to pressure and temperature, the helium concentration and gas mixture density were normalized with the initial values. Figure 11 demonstrates the time-dependent variations of the helium concentrations at some of the measurement points in Figure 1B. For Vessel-1, the numerical results are almost in agreement with the test data, except for the concentration at Point B. Similar to the simulation and experimental comparison for the ST3_0 test, a significant discrepancy is noted in the region above the spray nozzle, possibly owing to the lack of initial helium distribution. For Vessel-2, the simulation roughly follows the real trend but has differences with the test data.

Figure 12 shows the changes in the gas mixture densities in Vessel-1 and Vessel-2 over time; it can be seen that the simulation results agree with the test data. Figure 13 shows the distribution of helium molar fraction in the computational domain at different moments. Similar to the findings of the ST3_0 test, helium gas collected at the top of Vessel-1 upon spray injection is transported downward by spray entrainment, so the helium-rich layer becomes thin. Then, helium enters Vessel-2 through the IP from top to bottom and fills the entire Vessel-2.

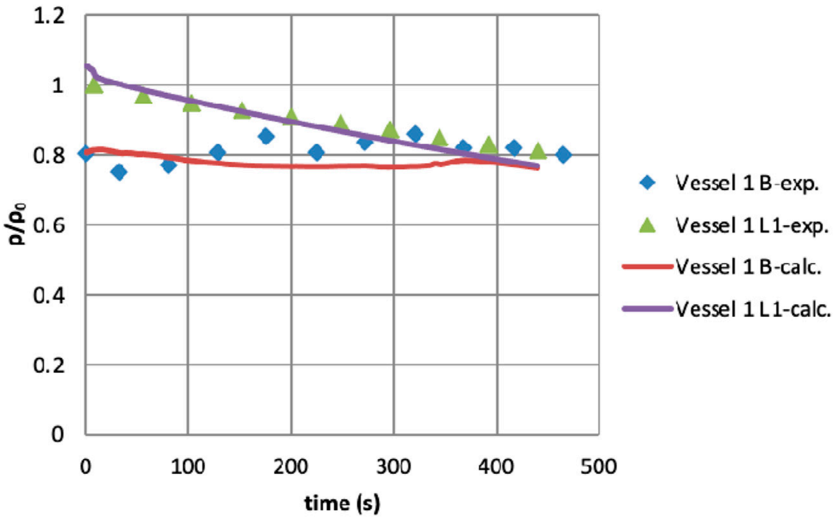

(a) Vessel-1

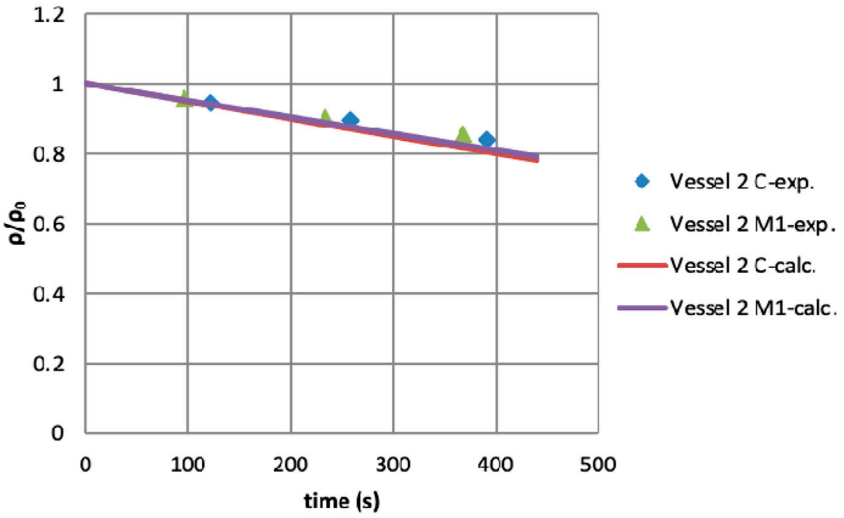

(b) Vessel-2

FIGURE 12
Gas mixture density versus time for the PANDA ST3_1 test in **(A)** Vessel-1 and **(B)** Vessel-2.

5 Conclusion

Two spray tests were performed in the multicompartment PANDA facility with different preconditions and were also simulated; the focus here was on the effects of a spray on the atmosphere of a containment after a typical severe accident. Using an Eulerian–Lagrangian approach in ANSYS Fluent, the dispersed droplets were tracked in a Lagrangian framework for continuous gas solved using an Eulerian approach by considering two-way coupling between the droplets and gas. In particular, the mass and heat transfer models of the droplets were developed using UDFs, but the interactions between the droplets were neglected.

For the reference test ST3_0, comparisons between the simulations and experiments show that the simulation results almost agree with the test data, except for the measurement point above the spray nozzle, possibly because of the simplified initial condition for gas concentration. The simulation reproduces the gas stratification breakup processes upon spray injection and light gas transport in a multicompartment facility; helium penetrates the neighboring compartment upon spray activation.

In the simulation of the ST3_1 test, pressure is underestimated and temperature is overestimated, which is attributable to the neglect of sump re-evaporation. From the mass and heat transfer of the droplets, the calculated results show that the spray cools the entire region except for the outlet zone of the spray nozzle as heat absorption due to droplet evaporation plays a key role. Moreover, in the neighboring compartment, there is temperature stratification with spray activation. The time-dependent variations of the helium concentration calculated using the CFD code are similar to the results of the ST3_0 test. Although the simulation reproduces the

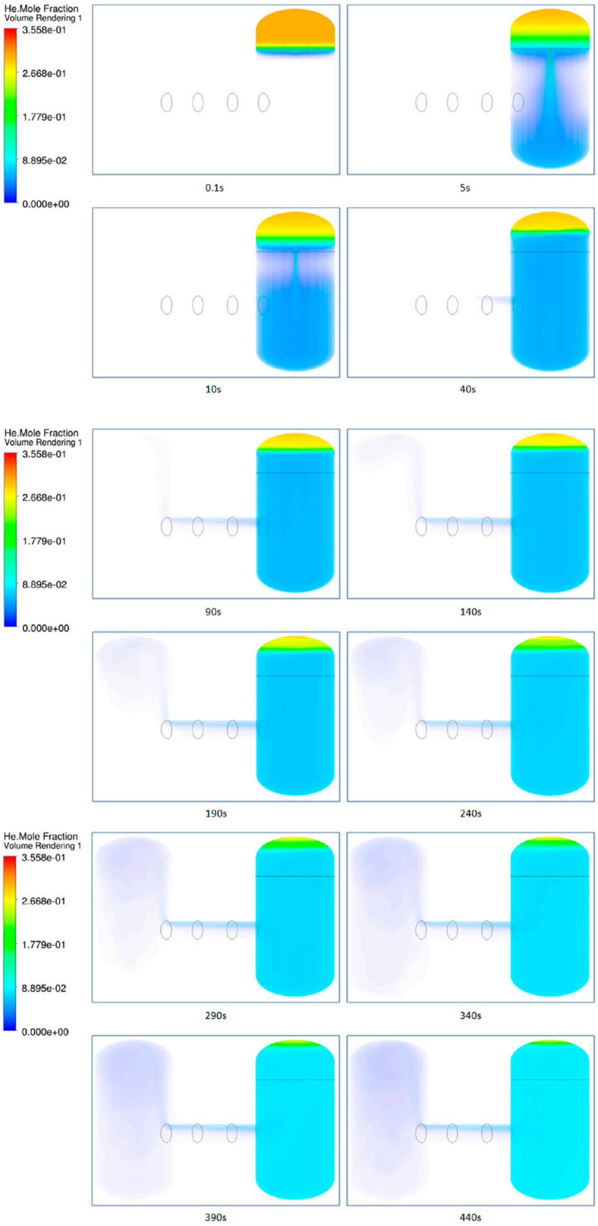

FIGURE 13
Helium molar fractions over time after spray activation (PANDA ST3_1 test, left: Vessel-2; right: Vessel-1).

real evolution of gas concentration, deviations still exist for the region above the spray nozzle.

Despite some discrepancies, there is general agreement between the simulation results and test data, showing that the proposed approach is adequately applicable to similar problems. However, further efforts are needed to improve the accuracy of the simulation, such as consideration of the detailed initial gas concentration distribution, by taking into account the sump re-evaporation.

Data availability statement

The original contributions presented in the study are included in the article/Supplementary Material; further inquiries can be directed to the corresponding authors.

Author contributions

YL: writing–original draft and writing–review and editing. XR: conceptualization, supervision, and writing–review and editing. ZW: validation and writing–review and editing.

Funding

The authors declare that financial support was received for the research, authorship, and/or publication of this article. The authors gratefully acknowledge the support by the Nature Science Foundation of Sichuan province (grant number 2024NSFSC1381) and Nuclear Power Institute of China Innovation Funding of Science and Technology (KJCX-2023-YC1-8).

Conflict of interest

The authors declare that the research was conducted in the absence of any commercial or financial relationships that could be construed as a potential conflict of interest.

Publisher's note

Supplementary material

The Supplementary Material for this article can be found online at: https://www.frontiersin.org/articles/10.3389/fenrg.2024.1437115/full#supplementary-material

References

ANSYS FLUENT 18.0 user's guide[M], 2016.

Babic, M., Kljenak, I., and Mavko, B. (2009). Simulations of TOSQAN containment spray tests with combined Eulerian CFD and droplet-tracking modelling. *Nucl. Eng. Des.* 239, 708–721. doi:10.1016/j.nucengdes.2008.12.022

Dabbene, F., Brinster, J., Abdo, D., Porcheron, E., Lemaitre, P., Mignot, G., et al. (2015). "Experimental activities on stratification and mixing of a gas mixture under the conditions of a severe accident with intervention of mitigation measures performed in the ERCOSAM-SAMARA project," in ICAPP, Nice, France.

Erkan, N., Kapulla, R., Mignot, G., Zboray, R., and Paladino, D. (2011). Experimental investigation of spray induced gas stratification break-up and mixing in two interconnected vessels. *Nucl. Eng. Des.* 241, 3935–3944. doi:10.1016/j.nucengdes.2011.07.025

Malet, J., Blumenfeld, L., Arndt, S., Babic, M., Bentaib, A., Dabbene, F., et al. (2011). Sprays in containment: final results of the SARNET spray benchmark. *Nucl. Eng. Des.* 241, 2162–2171. doi:10.1016/j.nucengdes.2011.03.016

Malet, J., Laissac, R., Bentaib, A., Lemaitre, P., and Porcheron, E. (2015b). "Synthesis of stratification and mixing of a gas mixture under severe accident conditions with intervention of mitigating measures," in ICAPP 2015, Nice, France, May 3–6, 2015 (Acropolis Congress Center).

Malet, J., and Huang, X. (2015). Influence of spray characteristics on local light gas mixing in nuclear containment reactor applications. *Comput. and Fluids* 107, 11–24. doi:10.1016/j.compfluid.2014.10.002

Malet, J., Mimouni, S., Manzini, G., Xiao, J., Vyskocil, L., Siccama, N. B., et al. (2015a). Gas entrainment by one single French PWR spray, SARNET-2 spray benchmark. *Nucl. Eng. Des.* 282, 44–53. doi:10.1016/j.nucengdes.2014.12.008

Malet, J., Parduba, Z., Mimouni, S., and Travis, J. (2014). Achievements of spray activities in nuclear reactor containments during the last decade. *Ann. Nucl. Energy* 74, 134–142. doi:10.1016/j.anucene.2014.05.033

Mimouni, S., Baudry, C., Douce, A., Guingo, M., Hassanaly, M., Lavieville, J., et al. (2013). "Modelling of sprays in a multi-compartment geometry with a CMFD code," in NURETH15, Pisa, Italy.

Morsi, S. A., and Alexander, A. J. (1972). An investigation of particle trajectories in two-phase flow systems. *J. Fluid Mech.* 55 (2), 193–208. doi:10.1017/s0022112072001806

NEA/CSNI/R (2012). *OECD/SETH-2 project PANDA and MISTRA experiments - final summary report*, 5.

Ranz, W. E., and Marshall, W. R., Vaporation from drops, part[J], *Chem. Eng. Prog.*, 48(4): 141–146.

Ranz, W. E., and Marshall, W. R., Vaporation from drops, Part I and Part II, *Chem. Eng. Prog.*, 48(4): 173–180.

Sazhin, S. S. (2006). Advanced models of fuel droplet heating and evaporation. *Prog. Energy Combust. Sci.* 32, 162–214. doi:10.1016/j.pecs.2005.11.001

Wilkening, H., Kljenak, I., Ambrosini, W., Bentaib, A., Blumenfeld, L., Dabbene, F., et al. (2008). *European research on issues concerning hydrogen behaviour in containment within the SARNET Network of excellence, ICAPP 2008*. CA USA: Anaheim.

frontiers | Frontiers in Energy Research

TYPE Original Research
PUBLISHED 18 December 2024
DOI 10.3389/fenrg.2024.1450488

OPEN ACCESS

EDITED BY
Jiankai Yu,
Massachusetts Institute of Technology,
United States

REVIEWED BY
Wei Li,
Xi'an Jiaotong University, China
Yunmei Zhao,
Tongji University, China
Kai Chen,
Shanghai Jiao Tong University, China

*CORRESPONDENCE
Xiao Zhong,
✉ qiumi332@126.com

RECEIVED 17 June 2024
ACCEPTED 25 November 2024
PUBLISHED 18 December 2024

CITATION
Changbing T, Feng Y, Yongjun J, Yong X, Zengping P and Zhong X (2024) Simulation research on the blister evolution behaviors of UMo/Zr monolithic fuel elements. *Front. Energy Res.* 12:1450488. doi: 10.3389/fenrg.2024.1450488

Simulation research on the blister evolution behaviors of UMo/Zr monolithic fuel elements

Tang Changbing, Yan Feng, Jiao Yongjun, Xin Yong, Pu Zengping and Xiao Zhong*

National Key Laboratory of Nuclear Reactor Technology, Nuelear Power Institute of China, Chengdu, China

Blister behavior is one of the main failure modes of UMo/Zr monolithic fuel elements during irradiation. The temperature of fuel elements may increase greatly so that the fuel elements may be destroyed. Post-irradiation annealing tests are used to study the blister behaviors of fuel elements under high temperature. In this study, a simulation method is developed based on the finite element method to study the evolution of blister behaviors of UMo/Zr monolithic fuel elements in the blister tests, taken into considering that the evolution of bubble pressure should be coupled with the deformation of cladding. The influence of creep rate of the cladding on the evolution of blister height is analyzed. The study shows that the unrecoverable creep deformation of the cladding, which occurs under high temperature, is the major factor in the increment of bubble height. The increase of bubble height mainly occurs during the heat preservation process and the initial stage of cooling process. The creep rate of cladding is positively related to the evolution of bubble height.

KEYWORDS

UMo/Zr monolithic fuel element, annealing test, creep rate, blister height, finite element method

1 Introduction

To prevent nuclear proliferation, the Reduced Enrichment for Research and Test Reactors (RERTR) program proposes the use of low-enrichment uranium fuel in research reactors (Burkes et al., 2016; Burkes et al., 2014; Burkes et al., 2015). In this situation, UMo fuel has emerged as one of the most promising candidate fuels for research reactors due to its high equivalent uranium density and stable irradiation performance (Kim et al., 2013). Compared to dispersion-type UMo fuel, monolithic UMo fuel offers a higher equivalent uranium density, meeting the neutron flux requirements of high-performance research reactors (Ozaltun et al., 2015), and is generally clad with Al or Zr alloys (López et al., 2017).

During irradiation, UMo/Zr monolithic fuel elements experience complex thermo-mechanical coupling behaviors (Yan et al., 2019; Zhao et al., 2015; Kong et al., 2018). The fission of UMo fuel generates fission heat and products, leading to intense thermodynamic interactions between the UMo fuel and Zr alloy cladding under irradiation-induced swelling (Zhao et al., 2015). Under transient conditions such as rapid reactor heating, the fuel core near the cladding interface is prone to cracking, releasing fission gases into the cracks, generating pressure, and forming macroscopic blisters on the cladding surface (Wachs et al., 2012; Beeston et al., 1980; Rice et al., 2010). The formation of blisters can obstruct coolant flow channels, affecting the heat dissipation performance of the fuel assemblies and the safety of the reactor

(Hongsheng et al., 2020; Lijun et al., 2012). In severe cases, it can lead to the burnout of the fuel elements. Therefore, blister behavior is a critical consideration in the design of fuel elements.

To investigate the formation and evolution of blisters, annealing tests are currently employed, wherein irradiated fuel elements are heated to observe the formation of blisters on their surface (Rice et al., 2010; Ozaltun et al., 2012; Zhouzhi et al., 2024). Annealing tests help identify the temperature and location of blister formation but do not allow continuous observation of the evolution of blisters. Gao et al. analyzed the mechanism of blister formation in plate-type fuel element (Lijun et al., 2012). Long et al. developed a method to predict the crack behaviors of nuclear materials (Chongsheng et al., 2014; Hongsheng et al., 2020). However, the mechanism of blister formation is still unclear and worthy studying. For monolithic fuel elements, considering the main thermo-mechanical behaviors during annealing tests and the coupling between gas pressure and crack volume, a numerical simulation method for the evolution of blisters is established. This helps identify the contributions of various mechanical behaviors to the growth of blister height and explore the key factors influencing blister evolution.

This study focuses on UMo/Zr monolithic fuel elements with localized cracking, establishing a 2D finite element geometric model with a pre-cracked zone. Considering the coupling relationship between gas pressure, the number of gas atoms, and the volume of the crack zone, a corresponding simulation method is developed, achieving numerical simulation of gas pressure evolution behavior. For the cladding material, the main thermo-mechanical behaviors during the annealing process are considered, combining cladding deformation with the evolution of gas pressure to achieve numerical simulation of the evolution behavior of blisters during annealing tests. The evolution law of blister height with temperature is obtained, and the influence of creep rate on blister behavior is investigated.

2 Material models

2.1 Thermal conductivity model

The thermal conductivity of zirconium alloy from room temperature to its melting point is given by (MacDonald and Thompson, 1976):

$$k = 7.51 + 2.09 \times 10^{-2}T - 1.45 \times 10^{-5}T^2 + 7.67 \times 10^{-9}T^3 \tag{1}$$

where k is the thermal conductivity in W/m·K shown as Equation 1 and T is the temperature in K.

2.2 Thermal expansion coefficient

The thermal expansion coefficient of zirconium alloy is 5.58×10^{-6}/K (MacDonald and Thompson, 1976).

2.3 Elastic constants

The elastic modulus and Poisson's ratio of zirconium alloy are given by the Fisher model (Fisher and Renken, 1964):

$$E = \left[9.9 \times 10^5 - 566.9 \times (T - 273.15)\right] \times 9.8067 \times 10^4 \tag{2}$$

$$\nu = 0.3033 + 8.376 \times 10^{-5}(T - 273.15) \tag{3}$$

where E is the elastic modulus in Pa shown as Equation 2; T is the temperature in K; and ν is the Poisson's ratio shown as Equation 3.

Under irradiation conditions, the elastic modulus of zirconium alloy increases. The elastic modulus under irradiation can be expressed as (Hagrman and Reymann, 1979):

$$E = \left[9.9 \times 10^5 - 566.9 \times (T - 273.15)\right] \times 9.8067 \times 10^4 / k_1 \tag{4}$$

$$k_1 = 0.88 + 0.12\exp\left(-\frac{\phi \times t}{10^{25}}\right) \tag{5}$$

in Equations 4, 5 k_1 is a dimensionless correction factor considering the effect of fast neutrons on the elastic modulus; and $\phi \times t$ is the fast neutron flux in n/m^2.

2.4 Plasticity model

The stress-strain curve for non-irradiated zirconium alloy is given by (Hagrman and Reymann, 1979):

$$\begin{aligned}\sigma &= K\varepsilon^n \cdot \left(\frac{\dot{\varepsilon}}{10^{-3}}\right)^m\\ K &= 1.17628 \times 10^9 + T\left[4.54859 \times 10^5 + T\left(-3.28185 \times 10^3 + 1.72752T\right)\right]\\ n &= -9.49 \times 10^{-2} + T\left[1.165\times10^{-3} + T\left(-1.992\times10^{-6} + 9.588 \times 10^{-10}T\right)\right]\end{aligned} \tag{6}$$

in Equation 6 σ is the true stress in Pa; ε is the true strain; K is the strength coefficient; n is the strain hardening exponent; $\dot{\varepsilon}$ is the true plastic strain rate, which is given as $\dot{\varepsilon} = 10^{-5}$/s, if $\dot{\varepsilon} < 10^{-5}$/s; m is the strain rate sensitivity index, which is 0.02; T is the temperature in K.

To account for the irradiation effects of fast neutrons, the strength coefficient K is modified by a correction factor k_2 shown as Equation 7:

$$k_2 = 5.54 \times 10^{-18}\phi \cdot t \tag{7}$$

Similarly, the strain hardening exponent n is adjusted by a dimensionless correction factor k_3 shown as Equation 8:

$$k_3 = 1.369 + 0.032 \times 10^{-25}\phi \cdot t \tag{8}$$

where $\phi \times t$ is the fast neutron flux in n/m^2.

2.5 Creep model

During the annealing process, the high-temperature creep behavior of zirconium alloy is modeled by (Suzuki and Saitou, 2006):

$$\dot{\varepsilon}^{cr} = 2000\alpha\sigma^{5.32} \cdot \exp\left(-\frac{34220}{T}\right) \tag{9}$$

where $\dot{\varepsilon}^{cr}$ is the creep rate in s^{-1}; σ is the Mises stress in MPa shown as Equation 9 T is the temperature in K; Q is the activation energy for creep; α is the creep amplification factor, typically set to 1.

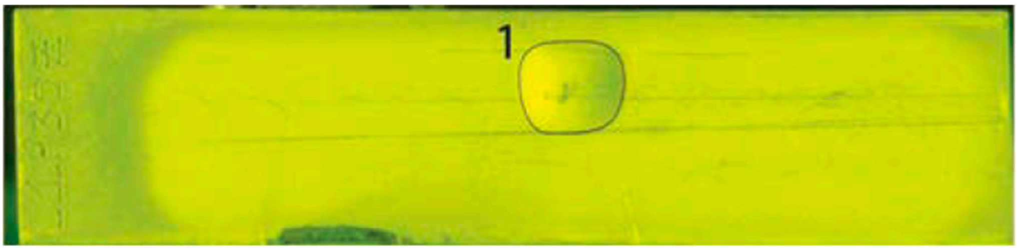

FIGURE 1
Blister formed on the surface of fuel plates (Meyer et al., 2012).

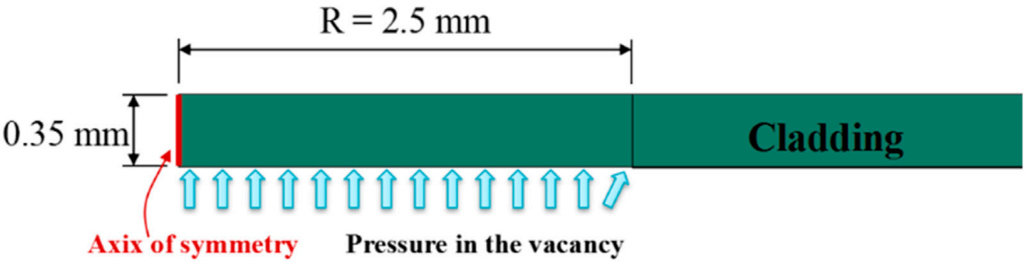

FIGURE 2
Finite element model for simulating blistering behavior.

3 Numerical simulation methods

3.1 Finite element geometric model

Results from annealing tests indicate that the core section near the interface is most prone to cracking, forming crack cavities. The fission gas products generated during irradiation are released into these crack cavities, generating pressure that causes the cladding above the crack cavities to deform, forming macroscopic blisters on the surface of the fuel elements, as shown in Figure 1. The size of these blisters ranges from approximately 3–5 mm (Meyer et al., 2012).

To simulate the blistering behavior of fuel elements during annealing tests, a finite element geometric model, as shown in Figure 2, was established. This model is axisymmetric, with the axis of symmetry indicated by the red line in the figure. The cladding part of the finite element geometric model has a thickness of 0.35 mm (Yan et al., 2018), a crack cavity radius of 2.5 mm, and an initial height of 0.005 mm. The finite element model is discretized into 4,820 elements using the axisymmetric element CAX4T in ABAQUS. The outer surface of the cladding is subjected to atmospheric pressure, applying a pressure load of 0.1 MPa. The thickness of the fuel meat is 0.20 mm, the fission density of fuel meat is 4.0×10^{18} fissions/mm^3, and the number of fission gas atoms produced per fission is 0.3. Assuming that 80% of the fission gas atoms produced by the fuel particles beneath the crack are released into the crack cavity, the number of gas atoms in the crack cavity is 1.896×10^{18}. The initial gas pressure in the crack cavity is determined to be 80 MPa. The fast neutron flux of the fuel plate is 2.0×10^{19} n/mm^2.

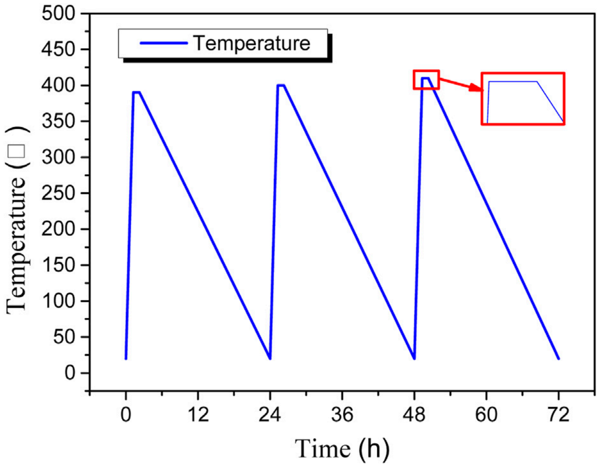

FIGURE 3
Schematic diagram of temperature evolution during annealing tests.

3.2 Temperature variation during the annealing process

The annealing test consists of 24-h cycles. Each cycle starts from room temperature, heats up to the target temperature, holds for 1 hour at the target temperature (Miller et al., 2012), and then returns to room temperature. The target temperature for the first annealing cycle is 400°C. Each subsequent cycle increases the target temperature by 10°C, up to a maximum of 600°C.

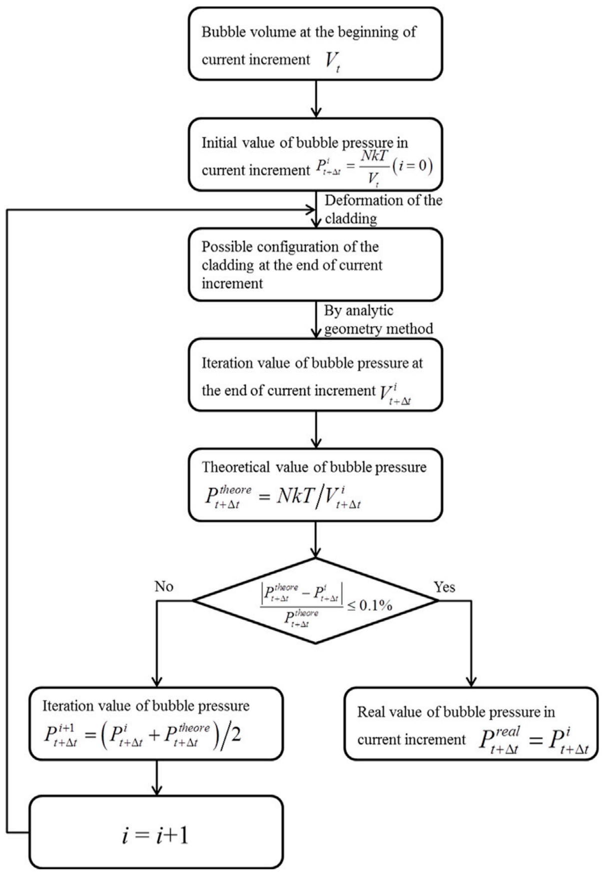

FIGURE 4
Schematic diagram of temperature evolution during annealing tests.

The temperature variation during the annealing tests is illustrated in Figure 3. It is important to note that Figure 3 only shows the temperature changes for the first three annealing cycles, while the actual numerical simulation considers a total of 21 annealing cycles.

3.3 Simulation method for blistering behavior

Due to the relatively large volume of the crack cavities formed by cracking, the gas pressure within these cavities is relatively low. The behavior of the gas within the crack cavities can be described using the ideal gas law:

$$P \cdot V = NkT \tag{10}$$

where P is the gas pressure in Pa; V is the volume of the crack cavity in m^3; N is the number of gas atoms; $k = 1.38 \times 10^{-23}$ J/K is the Boltzmann constant; T is the temperature in K.

During the bubble evolution process of fuel elements, the cladding continuously deforms under the pressure within the crack cavity, causing changes in the volume of the crack cavity. According to the ideal gas law, shown as Equation 10, the volume change of the cavity affects the pressure, indicating a coupled relationship between the two. To study the bubble evolution behavior of the fuel element, an iterative calculation method was employed, as shown in Figure 4. For a typical increment step $[t, t + \Delta t]$, the gas cavity volume V_t at the beginning of the step and the temperature $T_{t+\Delta t}$ at the end of the step are used to calculate the initial iteration value of pressure $P^0_{t+\Delta t} = \frac{NkT_{t+\Delta t}}{V_t}$. The iterative value of pressure $P^i_{t+\Delta t}$ ($i = 0,1,2,3\ldots$) applied to the cladding causes further deformation of the cladding. Using analytical geometry methods, the gas cavity volume $V^i_{t+\Delta t}$ can be calculated, and the theoretical value of pressure $P^{theore}_{t+\Delta t} = \frac{NkT_{t+\Delta t}}{V^i_{t+\Delta t}}$ can be obtained by substituting it into the gas law equation. If the error between the theoretical value and the iterative value of pressure is less than 0.1%, the real gas pressure $P^{real}_{t+\Delta t}$ at the end of the increment step is considered to be obtained; otherwise, the iterative pressure value is updated to $P^{i+1}_{t+\Delta t} = \frac{P^i_{t+\Delta t}+P^{theore}_{t+\Delta t}}{2}$, and the cladding deformation is recalculated until the pressure converges.

3.4 Stress update algorithm

To simulate the bubble evolution process of the cladding material during the annealing test, the primary thermo-mechanical behavior of the cladding material must be considered. This involves establishing a three-dimensional large deformation incremental constitutive relation in a rotating coordinate system, deriving the stress update algorithm, and consistent stiffness matrix, and writing a UMAT subroutine for implementation on the commercial finite element platform ABAQUS.

During the annealing test, the contributions of elastic strain, thermal expansion strain, plastic strain, and creep strain of the cladding material are primarily considered:

$$\Delta\varepsilon^e_{ij} = \Delta\varepsilon^{total}_{ij} - \Delta\varepsilon^{th}_{ij} - \Delta\varepsilon^{pl}_{ij} - \Delta\varepsilon^{creep}_{ij} \tag{11}$$

where $\Delta\varepsilon^{total}_{ij}$ is the total strain increment; $\Delta\varepsilon^e_{ij}$ is the elastic strain increment; $\Delta\varepsilon^{th}_{ij}$ is the thermal expansion strain increment; $\Delta\varepsilon^{pl}_{ij}$ is the plastic strain increment; and $\Delta\varepsilon^{creep}_{ij}$ is the creep strain increment. The specific stress update algorithm is referenced from the literature (Zhao et al., 2014).

4 Results and discussion

4.1 Study on the mechanism of bubble height evolution

Figure 5 shows the displacement contour plot of the cladding at the end of the annealing cycle at a target temperature of 500°C. It can be observed that, at this temperature, the bubble height on the cladding reaches approximately 0.294 mm, forming a notable bubble. As the annealing test progresses, the bubble height on the cladding will continue to increase, which can significantly obstruct coolant flow if severe.

The annealing test consists of multiple annealing cycles. To investigate the mechanism of bubble height evolution within a single annealing cycle, a cycle with a target temperature of 500°C was selected. It is the eleventh cycle during the annealing process, which starts at 264 h and ends at 288 h. The bubble

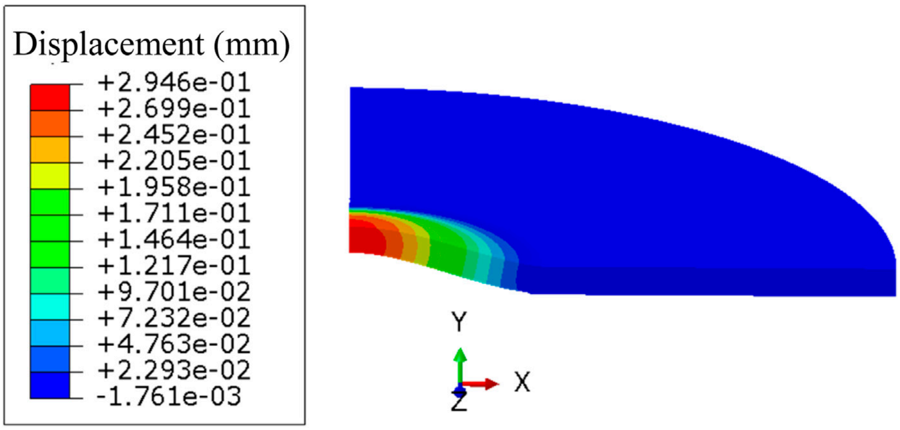

FIGURE 5
Contour plot of displacement in cladding at the end of the annealing cycle at 500°C.

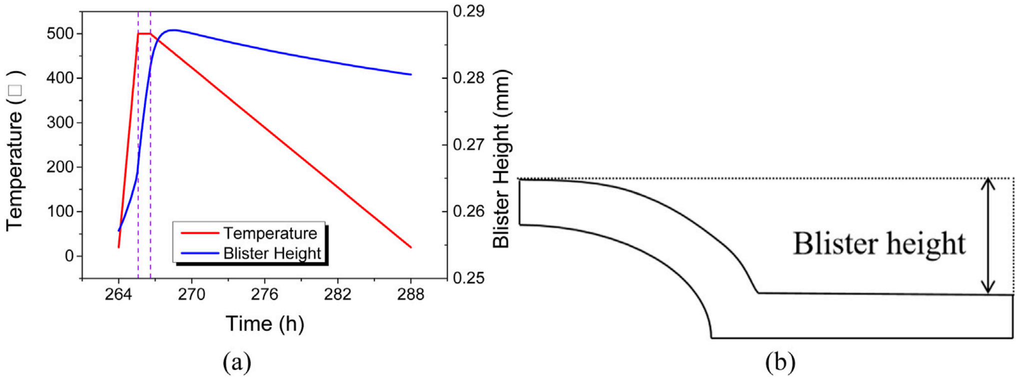

FIGURE 6
(A) Evolution of Temperature and Bubble Height during the Annealing Cycle at 500°C; **(B)** The sketch of blister height.

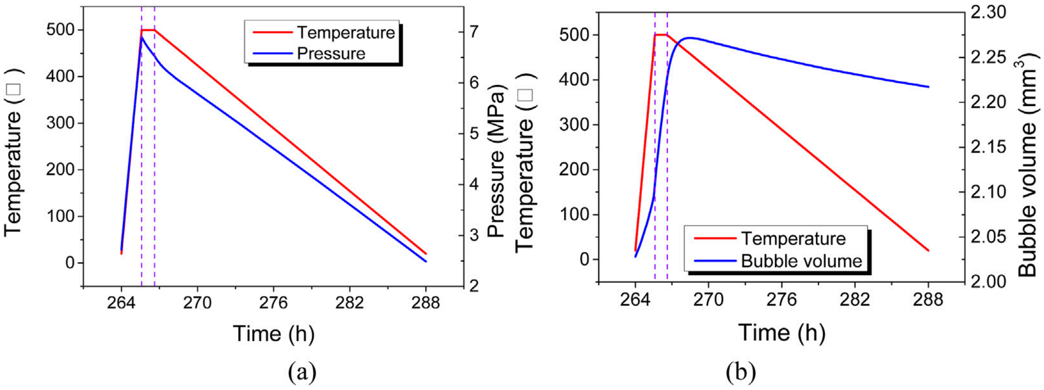

FIGURE 7
Evolution of **(A)** bubble pressure and **(B)** bubble volume during the annealing cycle at 500°C.

height variation process is shown in Figure 6A. The bubble height could be calculated by the displacement of the cladding, as shown in Figure 6B. At the beginning of this annealing cycle, the bubble height is approximately 0.257 mm. During the heating and holding processes, the bubble height gradually increases with the progression of the annealing test. In the

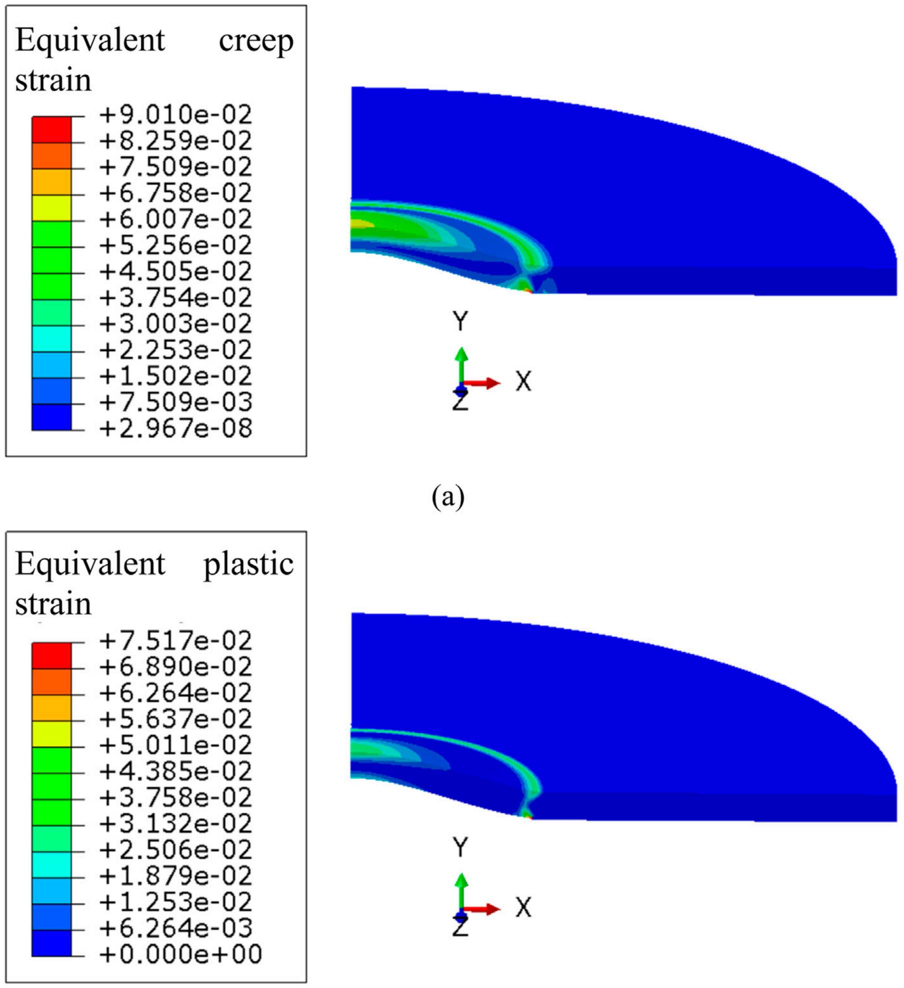

(a)

(b)

FIGURE 8
Contour plot of **(A)** Equivalent creep strain and **(B)** Equivalent plastic strain at the end of the annealing cycle at 500°C.

early stage of the cooling process, the bubble height continues to increase due to the high temperature of the fuel plate. About 2 hours after the cooling process starts, the bubble height reaches a maximum of approximately 0.287 mm and then slowly decreases to around 0.281 mm. Compared to the initial stage, the bubble height in this annealing cycle increases by about 0.024 mm.

The variation of bubble height during the annealing cycle is influenced not only by temperature but also by the coupled gas pressure inside the bubble. Figure 7A shows the gas pressure variation during the 500°C annealing cycle. During the heating process, the temperature rise rate is high, and according to Equation 1, the gas pressure inside the bubble increases rapidly, causing continuous deformation of the cladding under the gas pressure, manifested macroscopically as a continuous increase in bubble height. During the holding and initial cooling processes, as the temperature stops rising and starts to decrease slowly, the gas pressure decreases accordingly. However, the gas pressure still remains around 6–7 MPa, higher than the external environmental pressure, leading to continued creep deformation of the cladding under pressure, which macroscopically appears as a continuous increase in bubble height. According to Equation 1, the increase in bubble volume will result in a decrease in gas pressure. After about 2 hours of cooling, the gas pressure drops to a level insufficient to drive further outward deformation of the cladding, leading to a reduction in bubble height and gas pressure as the temperature decreases. Figure 7B shows the evolution of gas cavity volume. During the 500°C annealing cycle, the evolution pattern of the gas cavity volume is similar to that of the bubble height, indicating that the bubble height variation reflects the changes in gas cavity volume.

Within the temperature range of the annealing test, the elastic and thermal expansion strains of the cladding material are relatively small and insufficient to cause significant bubbling in the fuel element. Therefore, the distribution and evolution of equivalent creep strain and equivalent plastic strain in the cladding during the annealing test are the focus. Figure 8 shows the contour plots of equivalent creep strain and equivalent plastic strain at the end of the 500°C annealing cycle. Significant creep strain and plastic strain

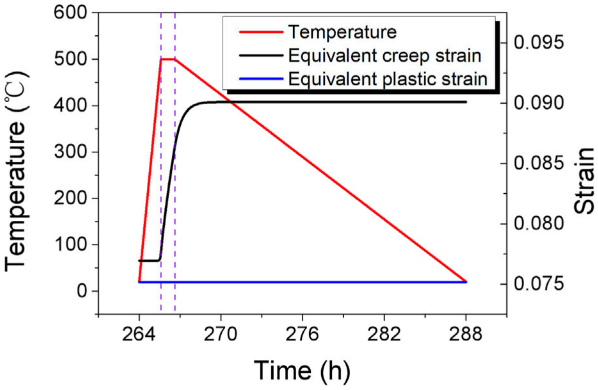

FIGURE 9
Evolution of equivalent creep strain and equivalent plastic strain of cladding during the annealing cycle at 500°C.

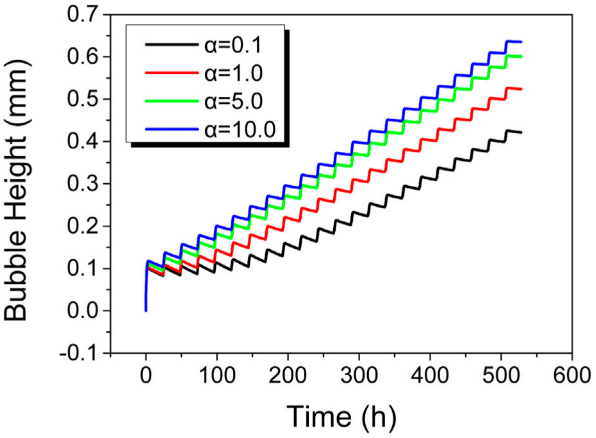

FIGURE 10
Effects of creep rate on the evolution of bubble height.

occur in the cladding, with maximum values located at the base of the bubble.

Figure 9 illustrates the variation of maximum equivalent creep strain and equivalent plastic strain in the cladding during the 500°C annealing cycle. During the heating process, the accumulated creep strain remains largely unchanged, with bubble height variations mainly caused by elastic deformation and thermal expansion due to temperature increase. During the holding process, equivalent creep strain in the cladding rises rapidly, while during the cooling process, equivalent creep strain initially increases and then stabilizes. Comparing Figures 6, 9, the period of increased equivalent creep strain aligns with the period of increased bubble height, indicating that the bubble height increase primarily results from creep strain during the holding and initial cooling stages, with a minor contribution from elastic strain and thermal expansion. According to Equation 7, the cladding material exhibits high creep rates at elevated temperatures. Prolonging the holding period would result in continuous creep strain increase in the cladding, further increasing bubble height until cladding rupture or gas pressure reduction halts further deformation.

After more than 2 hours of cooling, the cladding creep rate approaches zero due to lower temperatures, as per Equation 7, resulting in stable creep strain. During this period, thermal expansion strain decreases with temperature, leading to a reduction in bubble height due to combined thermal expansion and elastic strain effects. However, since creep strain remains unchanged, the bubble height at the end of the annealing cycle remains higher than at the initial stage.

Figure 9 also shows that equivalent plastic strain in the cladding remains unchanged throughout the annealing cycle. This indicates that creep strain predominates over plastic strain in the bubble evolution process, with plastic deformation mainly occurring in the initial stage of bubble evolution. The next section will examine the evolution patterns of creep and plastic strains in the cladding throughout the entire annealing test.

4.2 Effect of creep rate on bubble evolution

The previous analysis indicates that bubble growth is mainly influenced by creep, and the creep behavior of the cladding material significantly impacts its growth. To further investigate the effect of creep rate on bubble growth, the original cladding creep model, shown as Equation 7, was modified to examine bubble evolution under different creep magnification factors: 0.1, 1.0, 5.0, and 10.0.

Figure 10 shows the variation in bubble height of the fuel element under different creep rates. As seen in Figure 10, higher creep rates result in faster bubble height growth during the heating process. Ultimately, models with higher creep rates exhibit greater final bubble heights after undergoing the same bubble test temperature profile.

Figure 11A shows the variation in maximum equivalent creep strain of the cladding over time for different creep rates. As shown in Figure 11A, the trend of creep strain variation is similar to that of bubble height, with higher creep rates corresponding to greater creep strain. However, the differences in creep strain do not scale linearly with creep rate. This is because higher creep rates lead to greater bubble heights, which in turn reduce gas pressure inside the bubble. Consequently, although bubbles with higher creep rates reach greater heights, their internal pressures are lower, leading to non-linear relationships between creep rate and the resulting creep strain and bubble height.

Figure 11B illustrates the evolution of maximum equivalent plastic strain of the cladding under different creep rates. At the initial stage of the annealing test, significant equivalent plastic strain is observed in the cladding. This is due to the low temperature and low creep rate at the beginning of the annealing test, making significant creep deformation difficult. During this stage, bubble height growth mainly results from plastic deformation of the cladding. After a certain period of the annealing test, equivalent plastic strain in the cladding stabilizes, while equivalent creep strain continues to increase. After more than 400 h of the annealing test, equivalent creep strain in the cladding significantly exceeds equivalent plastic strain, indicating that creep deformation primarily contributes to bubble height growth.

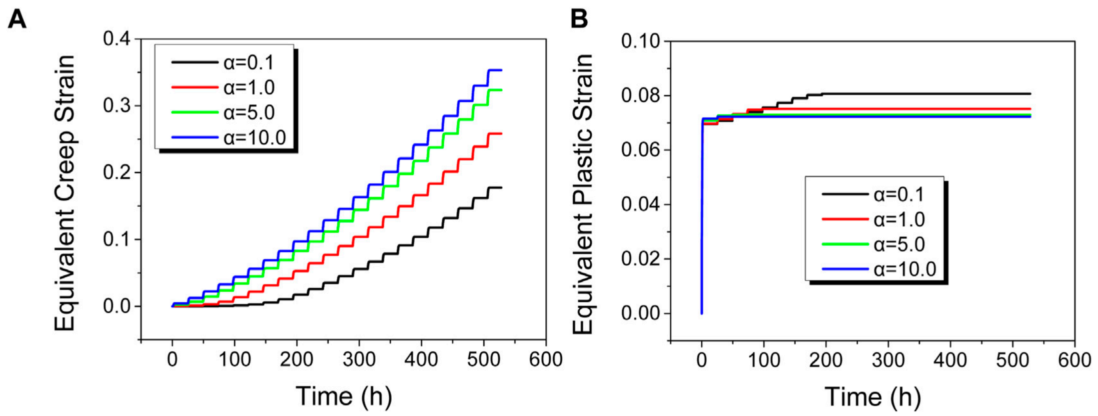

FIGURE 11
Effects of creep rate on the evolution of **(A)** maximum equivalent creep strain and **(B)** maximum equivalent plastic strain of cladding.

5 Conclusion

This study establishes a simulation method for bubble evolution in the annealing test of UMo/Zr monolithic fuel elements that exhibit local cracking, considering the primary thermo-mechanical behavior of the cladding material, and the evolution of crack cavity pressure and volume. The following key conclusions are drawn regarding the influence of cladding creep rate on bubble height:

(1) Cladding plastic deformation mainly affects the initial slight bubbling, while the subsequent increase in bubble height is primarily due to creep, with plastic deformation having a relatively limited impact.
(2) The duration of the holding period significantly affects bubble height. Longer high-temperature stages result in greater bubble height increments. In a specific annealing cycle, the accumulation of bubble height mainly arises from the holding period, with a minor contribution from the initial stage of the cooling period.
(3) Reducing the creep rate of the cladding material helps to suppress the growth of bubble height, but the effect is relatively small. Improving the creep properties of the material to slow down the growth of bubbles during the process has a relatively limited impact.
(4) The evolution of bubble height is driven by bubble pressure. It is supposed that the coolant pressure has an negative effect on bubble height, which should be considered in engineering practices.

Data availability statement

The original contributions presented in the study are included in the article/supplementary material, further inquiries can be directed to the corresponding author.

Author contributions

TC: Funding acquisition, Software, Supervision, Writing–original draft, Writing–review and editing. YF: Investigation, Software, Writing–review and editing. JY: Project administration, Supervision, Writing–review and editing. XY: Supervision, Writing–review and editing. PZ: Formal Analysis, Supervision, Writing–review and editing. XZ: Conceptualization, Project administration, Supervision, Writing–review and editing.

Funding

The author(s) declare that financial support was received for the research, authorship, and/or publication of this article. The authors thank for the supports of Natural Science Foundation of Sichuan Province (2023NSFSC1316) and Young Talents Program of CNNC.

Conflict of interest

The authors declare that the research was conducted in the absence of any commercial or financial relationships that could be construed as a potential conflict of interest.

Publisher's note

References

Beeston, J. M., Hobbins, R. R., Gibson, G. W., and Francis, W. C. (1980). Development and irradiation performance of uranium aluminide fuels in test reactors. *Nucl. Technol.* 49 (1), 136–149. doi:10.13182/nt80-a32515

Burkes, D. E., Casella, A. J., and Casella, A. M. (2016). Measurement of fission gas release from irradiated U Mo dispersion fuel samples. *J. Nucl. Mater* 478, 365–374. doi:10.1016/j.jnucmat.2016.05.039

Burkes, D. E., Casella, A. M., Buck, E. C., Casella, A. J., Edwards, M. K., MacFarlan, P. J., et al. (2014). Development and validation of capabilities to measure thermal properties of layered monolithic U-Mo alloy plate-type fuel. *Int. J. Thermophys.* 35 (8), 1476–1500. doi:10.1007/s10765-014-1683-4

Burkes, D. E., Casella, A. M., and Huber, T. K. (2015). Modeling the influence of interaction layer formation on thermal conductivity of U-Mo dispersion fuel. *J. Alloy Compd.* 618, 7–13. doi:10.1016/j.jallcom.2014.08.123

Chongsheng, L., Yi, Z., Wen, G., Hongxing, X., and Tianguo, W. (2014). A model for cracking of ceramic fuel particles in dispersion fuel. *Nucl. Power Eng.* 35 (1).

Fisher, E. S., and Renken, C. J. (1964). Single-crystal elastic moduli and the hcp → bcc transformation in Ti, Zr, and Hf. *Phys. Rev.* 135 (2A), 482–494. doi:10.1103/physrev.135.a482

Hagrman, D. L., and Reymann, G. A. C. (1979). *MATPRO-Version 11: a handbook of materials properties for use in the analysis of light water reactor fuel rod behavior*. United States.

Hongsheng, C., Chongsheng, L., and Hongjun, X. (2020a). Crack characteristic model of metal matrix induced by dispersion fuel. *Atomic Energy Sci. Technol.* 54 (02), 334–339.

Kim, Y. S., Hofman, G. L., Cheon, J. S., Robinson, A. B., and Wachs, D. M. (2013). Fission induced swelling and creep of U-Mo alloy fuel. *J. Nucl. Mater* 437 (1-3), 37–46. doi:10.1016/j.jnucmat.2013.01.346

Kong, X., Ding, S., and Tian, X. (2018). Research on in-pile thermal-mechanical behavior of UMo/Zr monolithic fuel plates. *Nucl. Power Eng.* 39 (02), 109–113. doi:10.1515/eng-2018-0029

Lijun, G., Bingde, C., Shengyao, J., Zhong, X., Jiyang, Y., Lin, Z., et al. (2012). Analysis of blistering mechanism for dispersion-type fuel plates during irradiation. *Atomic Energy Sci. Technol.* 46, 819–825.

López, M., Picchetti, B., and Taboada, H. (2017). Influence of temperature and compressive stress on the UMo/Zry-4 interdiffusion layer. *Prog. Nucl. Energ* 94, 101–105. doi:10.1016/j.pnucene.2016.10.006

MacDonald, P. E., and Thompson, L. B. (1976). Matpro - a handbook of materials properties for use in the analysis of light water reactor. *Fuel Rod. Behav.*

Meyer, M. K., Moore, G. A., Jue, J. F., and Keiser, D. D. (2012). *Investigation of the cause of low blister threshold temperatures in the RERTR-12 and AFIP-4 experiments. Report*. ID, USA: Idaho National Laboratory.

Miller, S. J., and Ozaltun, H. (2012). “Evaluation of U10Mo fuel plate irradiation behavior via numerical and experimental benchmarking,” in *Imece 2012*. Editors S. J. Miller and H. Ozaltun (Houston, Texas: ASME).

Ozaltun, H., Medvedev, P. G., and Rabin, B. H. (2015). Effects of the foil flatness on irradiation performance of U10Mo monolithic mini-plates. *J. Nucl. Eng. and Radiat. Sci.* 1. doi:10.1115/1.4030982

Ozaltun, H., and Miller, S. J. (2012). “Evaluation of blister behavior for U10Mo mini fuel plates with cold rolled foils,” in *International mechanical engineering congress and exposition*. Editors H. Ozaltun and S. J. Miller (Houston, Texas, USA).

Rice, F. J., Wachs, D. M., Robinson, A. B., Keiser, D. D., and Jue, J. F. (2010). *U-Mo plate blister anneal interim report. Report*. Lisboa, Portugal: Idaho National Laboratory.

Suzuki, M., and Saitou, H. (2006). Light water reactor fuel analysis code FEMAXI-6 (Ver.1); Detailed structure and user’s manual. *Report*.

Wachs, D., Rice, F., Glagalenko, I., Robinson, A., Rabin, B., and Meyer, M. (2012). “Blister threshold based thermal limits for the U-Mo monolithic fuel system,” in *International meeting on reduced enrichment for research and test reactors*. Editors D. Wachs, F. Rice, I. Glagalenko, A. Robinson, B. Rabin, and M. Meyer (Warsaw, Poland).

Yan, F., Ding, S., Yuanming, L., Zhou, Y., Tang, C., and Yong, X. (2018). Numerical simulation of blistering behavior in UMo/Zr monolithic fuel plate. *Atomic Energy Sci. Technol.* 52, 1063–1069. 06.

Yan, F., Kong, X., Ding, S., He, D., Li, Y., Chen, P., et al. (2019). Effects of porous fuel structure on the irradiation-induced thermo-mechanical coupling behavior in monolithic fuel plates. *Sci. Sinica Phys. Mech. and Astronomica* 49 (11), 114606. doi:10.1360/SSPMA2018-00297

Zhao, Y., Gong, X., and Ding, S. (2015). Simulation of the irradiation-induced thermo-mechanical behaviors evolution in monolithic U-Mo/Zr fuel plates under a heterogeneous irradiation condition. *Nucl. Eng. Des.* 285, 84–97. doi:10.1016/j.nucengdes.2014.12.030

Zhao, Y., Gong, X., Ding, S., and Huo, Y. (2014). A numerical method for simulating the non-homogeneous irradiation effects in full-sized dispersion nuclear fuel plates. *Int. J. Mech. Sci.* 81, 174–183. doi:10.1016/j.ijmecsci.2014.02.012

Zhouzhi, W., Kun, Z., Yanpei, W., Hongxing, Y., Lin, Z., Liang, H., et al. (2024). Research on high temperature oxidation behavior of zirconium alloy for fuel element based on MOOSE platform. *Nucl. Power Eng.* 45 (1), 84–89.

Frontiers in
Energy Research

Advances and innovation in sustainable, reliable and affordable energy

Explores sustainable and environmental developments in energy. It focuses on technological advances supporting Sustainable Development Goal 7: access to affordable, reliable, sustainable and modern energy for all.

Discover the latest Research Topics

See more →

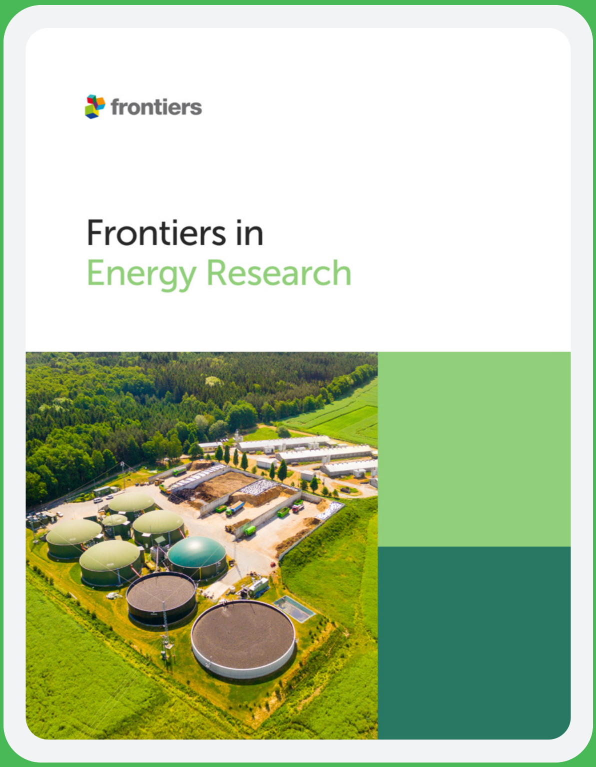
frontiers

Frontiers in
Energy Research

Frontiers

Avenue du Tribunal-Fédéral 34
1005 Lausanne, Switzerland
frontiersin.org

Contact us

+41 (0)21 510 17 00
frontiersin.org/about/contact